Colectia Manifestări științifice

cce2017

Computational Civil Engineering

International Symposium
Iasi, Romania, May 26, 2017

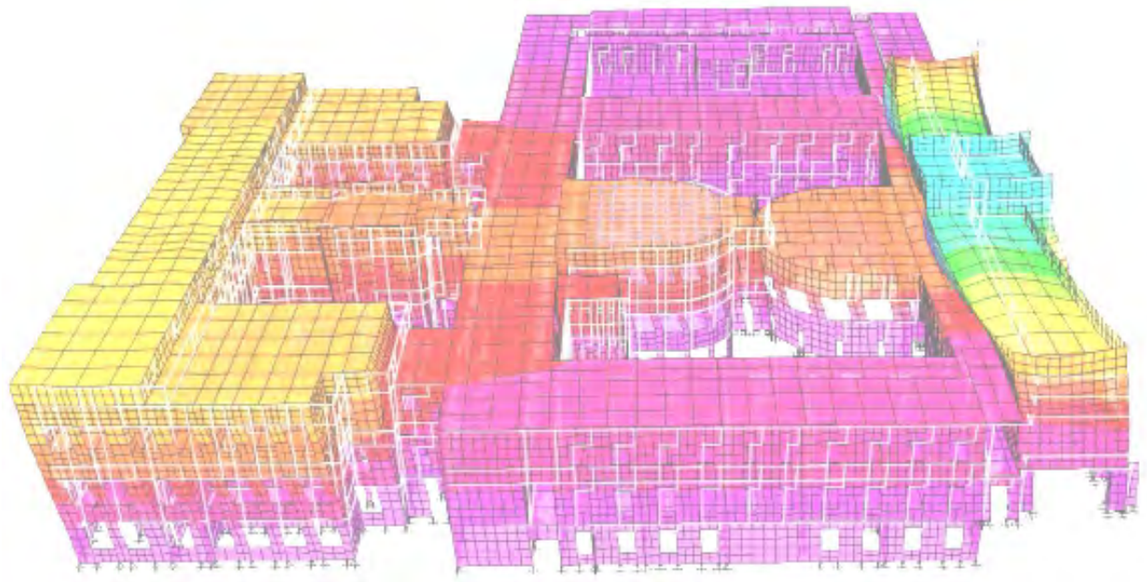

CCE 2017 - International Symposium Iasi, Romania, May 26, 2017

ISSN 2285-2735

Editura Societății Academice “Matei-Teiu Botez” IAȘI
2017

COMPUTATIONAL CIVIL ENGINEERING 2017

Editura Societăţii Academice "MATEI -TEIU BOTEZ"

Proceedings of the 14th International Symposium

“Computational Civil Engineering”

Iasi, Romania - May 26th, 2017

Scientific publication

Descrierea CIP a Bibliotecii Nationale a României
Proceedings of the 14th International Symposium “Computational Civil Engineering” / ed.: Gabriela Covatariu, Mircea-Vasile Venghiac - Iasi : Editura Societatii Academice "Matei - Teiu Botez", 2017. ISSN 2285-2735, ISSN-L 2285-2735
I. Covatariu, Gabriela (ed.)
II. Mircea-Vasile Venghiac (ed.)
624

THE 14th INTERNATIONAL SYMPOSIUM

"COMPUTATIONAL CIVIL ENGINEERING 2017"

ORGANIZERS

Faculty of Civil Engineering and Building Services - "Gheorghe Asachi" Echnical University from IASI, Romania
Academic Society "Matei - Teiu Botez", IASI, Romania
The International Center for Numerical Methods in Engineering (CIMNE) - Barcelona, Spain

Co-ordination committee

Prof. Eng. **Constantin Ionescu**, PhD
Prof. Eng. **Alex. Horia Barbat**, PhD
Prof. Eng. **Mihai Budescu**, PhD

Scientific commission

Daniel Aelenei - *Universidade Nova de Lisboa*, Portugal
Melito A. Baccay - *Technological University of the Philippines*, The Philippines
Sergiu Baetu - "*Gheorghe Asachi" Technical University of Iasi*, Romania
Cristina Câmpian - *Technical University of Cluj-Napoca*, Romania
Jan Červenka - *Červenka Consulting*, Czech Republic
Miguel Cervera - *CIMNE - Universitat Politecnica de Catalunya*, Spain
Piero Colajanni - *Università degli Studi di Palermo*, Italy
Cristina Cosma - *Wentworth Institute of Technology*, USA
Anca-Mihaela Costin - *University of East London*, UK
Daniel Covatariu - *"Gheorghe Asachi" Technical University of Iasi*, Romania
Sorin Codruț Floruț - *Polytechnic University of Timisoara*, Romania
Ștefan Guțiu - *Technical University of Cluj-Napoca*, Romania
Mihail Iancovici - *Technical University of Civil Engineering of Bucharest*, Romania
João C. Gonçalves Lanzinha - *Universidade da Beira Interior*, Portugal

Silviu Melenciuc - *"Gheorghe Asachi" Technical University of Iasi*, Romania
Gunther Meschke - *Ruhr Uni Bochum*, Germany
Kamran M. Nemati - *University of Washigton*, USA
Ioana Olteanu - *"Gheorghe Asachi" Technical University of Iasi*, Romania
Eugenio Oñate - *CIMNE -Universitat Politecnica de Catalunya*, Spain
Gabriel Oprișan - *"Gheorghe Asachi" Technical University of Iasi*, Romania
Viorel Popa - *Technical University of Civil Engineering of Bucharest*, Romania
Filippo Giammaria Pratico' - *Universita Mediterranea di Reggio Calabria*, Italy
Victor-Octavian Roșca - *"Gheorghe Asachi" Technical University of Iasi*, Romania
Thanasis C. Triantafillou - *University of Patras*, Greece
Lusa Tuleasca - *Unitech Institute of Technology*, New Zealand
Juan Carlos Vielma - *Universidad Centroccidental Lisandro Alvarado*, Venezuela
Mauricio Toledo Villegas - *Universidad Andres Bello*, Chile
Hiroshi Yokota - *Hokkaido University*, Japan

Organizing commission

Daniela Manea –*Technical University of Cluj-Napoca*
Valeriu Stoian - *"Politehnica" University of Timisoara*
Radu Vacareanu - *Technical University of Civil Engineering Bucharest*
"Gheorghe Asachi" Technical University of Iasi
Dorina-Nicolina Isopescu
Vasilica Ciocan
Mihai Petru
Ionut-Ovidiu Toma
Gabriela Covatariu
Mircea-Vasile Venghiac
Rodian Scînteie - *Regional Directorate of Roads and Bridges, Iasi*

CONTENTS

Investigation of Thermal Effects on Retrofitted Bosphorus Bridge: Comparison between Diagonal and Vertical Hanger Configurations

M. Mert Eyupgiller[1] and Cagri Mollamahmutoglu[2]
[1]*Civil Eng. Dept., F.M.V. Isik University, Istanbul, 34980, Turkey*
[2] *Civil Eng. Dept., Yildiz Technical University, Istanbul, 34220, Turkey*

Summary

Bosphorus Bridge which was constructed in 1973 recently has undergone a retrofitting process. In the process, original diagonal hanger configuration has changed into the vertical configuration. Literature includes numerous studies which address almost every aspect of the structural analysis of the diagonal case but lacks any study concerning the recent vertical configuration. In this study, an advanced 3D finite element model (FEM) of the complete bridge has been developed with intricate details. The model includes detailed structural components such as stiffeners with realistic 3D towers and also incorporates a frictional contact model for the cable saddle interaction – a unique feature among the model realm. Both diagonal and vertical configurations are taken into consideration with an automated script in the framework of a commercial FEM package. In order to demonstrate the effectiveness and usefulness of the model, we have opted to work on thermal effects on the bridge among various other possible research directions which can be tractable by the model such as vehicle interactions, forced vibrations, fatigue etc. We have studied the effects of homogeneous heating of the deck structure and various parts of the towers for both configurations. Variations on the stress distributions of the deck structure and cable forces are investigated. It is seen that diagonal configuration is more sensitive to the thermal effects and thus the related fatigue.

KEYWORDS: Bosphorus Suspension Bridge, 15th July Martyrs' Bridge, Finite-Element Method, Thermal Effects.

1. INTRODUCTION

Istanbul, the capital of Eastern Roman Empire and Ottoman Empire, is currently locomotive of the economy of Turkey, and meanwhile is one of the most crowded cities around the world. It is located on flanks of the strait, named the Bosphorus,

which allows the passage from Mediterranean to Black Sea. This strait is defined as a border between continental Europe and Asia, dividing the city into two over these continents. The Bosphorus has an average depth of about 50 m and its width varies from 0.7 to 3.5 km [1].

The first suspension bridge, namely the Bosphorus Bridge (a.k.a. 15th July Martyrs' Bridge), over this strait was opened in 1973. A recent retrofitting project on the bridge has changed some major components, such as its hangers. Although there are numerous studies on the former configuration of the Bosphorus Bridge, its new design has not been studied yet.

In this study, an advanced 3D finite element model (FEM) of the complete bridge has been developed with intricate details. The model includes detailed structural components such as stiffeners with realistic 3D towers and also incorporates a frictional contact model for the cable saddle interaction – a unique feature among the model realm. Both diagonal and vertical configurations are taken into consideration with an automated script in the framework of a commercial FEM package. In order to demonstrate the effectiveness and usefulness of the model, we have opted to work on thermal effects on the bridge among various other possible research directions which can be tractable by the model such as vehicle interactions, forced vibrations, fatigue etc. We have studied the effects of homogeneous heating of the deck structure and various parts of the towers for both configurations. Variations on the stress distributions of the deck structure and cable forces are investigated.

2. DESCRIPTION OF THE BOSPHORUS BRIDGE

The Bosphorus Bridge, located between Ortaköy and Beylerbeyi villages in Istanbul, is a single-span, two-hinged stiffening girder, with vertical hangers (diagonal hangers before retrofitting) and externally-anchored (gravity anchored) bridge. It has a portal type of main tower skeleton and main cables made of parallel wire strands [2]. As a linking element between the main cables and the deck, there are hangers (spiral rope), which are basically groups of wires of 5 mm approximate diameter. The reason for choosing strands instead of a truss is not only to improve strength but also to decrease ductility. A wire is typically four times as strong as a mild steel, while, being much less ductile [3]. In the Bosphorus Bridge (figure 1), the hangers are built inclined in order to restrict longitudinal displacement of the deck. This special constraint type in such a long bridge can also be observed in the Humber Bridge in England. Although it has not had a complication arising from its inclined hangers for over 40 years, this rarely preferred design went through a retrofitting.

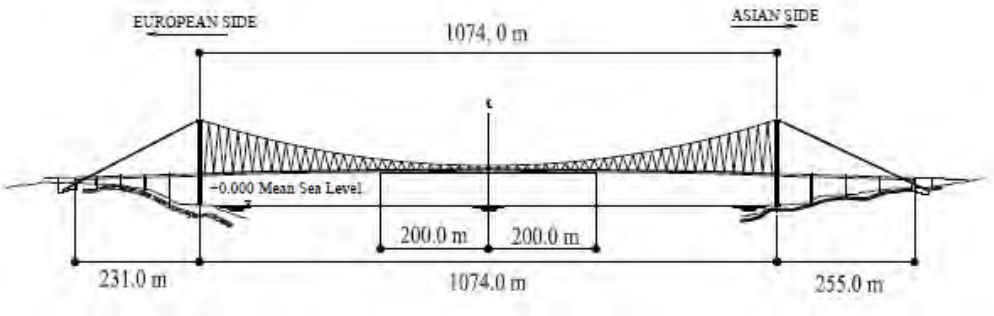

Figure 1. General arrangement of the Bosphorus Bridge [4]

The retrofitting project might have redesigned many characteristics of the bridge but its main components are still in use as they were. The hangers and the rocker bearings at the ends of the deck were changed, in new configuration hangers are vertically aligned and paired, while dampers were added to the ends of the deck. However, the deck superstructure and main cables had only been under maintenance renovations and the principal dimensions of the bridge remained the same.

Table 1: Material properties and some element dimensions

Young's modulus	200 GPa	Plate thicknesses	Towers	17-22 mm
Poisson's ratio	0.25		Deck	6-12 mm
Yielding stress of the cables	1500 MPa	Sectional area of cables	Main cables (backstay)	0.219 m^2
Yielding stress of the structural steel	320 MPa		Main cables (span)	0.205 m^2
			Hangers (both Diagonal and Vertical)	0.00196 m^2

Principal Dimensions [5]

Span Length	: 1074 m
Length of Approach Viaducts- (Ortaköy)	: 231 m
(Beylerbeyi)	: 255 m
Length of the Main Span	: 400 m
Clearance of the Main Span	: 64 m
Height of the Towers	: 165 m

Main Cable Sagging	: 93 m
Height of the Standard Deck Unit	: 3 m
Width of the Standard Deck Unit (w/o side plates)	: 28 m
Some Quantities about the Construction	
Excavation	: 63 000 m3
Concrete	: 71 000 m3
Concrete reinforcement	: 4 000 tons
Steel	: 17 000 tons
Cables	: 6 000 tons
Cost of the bridge (Turkish Lira)	: 191 785 265 TL
	23 213 666 USD

3. FINITE ELEMENT MODELING OF THE BOSPHORUS BRIDGE

In order to compare the thermal effects on former and the current configurations of the Bosphorus Bridge, two different three-dimensional (3D) finite element (FE) models were created in finite element analysis program ABAQUS. It is the first work that includes 3D FE model of both configurations of the Bosphorus Bridge. It is also unique because of the elements used. Instead of using equivalent beam elements for towers and the deck, these components were also modelled in 3D space and no additional restraints were assigned.

3.1 Finite Element Modelling of the Diagonal Configuration

The construction project of the bridge had been drawn regarding the conclusive state of the bridge (Figure 2). In other words, the cables had been loaded with the stress that they were going to resist, and then they were cut in their design lengths. Therefore, in modelling phase, the bridge model was designed as in the projects and the calculated stresses were assigned in the first step. If the bridge was to be loaded with these stresses in the initial state, it would go out of balance in dynamic step. However, it was totally balanced and had deflections around ±10 cm, when it was loaded gradually with the calculated stresses and the gravitational acceleration.

The deck and the towers are composed of thin plates made of steel. Thickness of the plates differs as their positions. The deck structure was built by plates with the thickness of 6 mm to 12 mm, and in the towers that range is 15 to 22 mm. These plates forming the components of the bridge were modelled with S3R and mostly S4R, which are, respectably, triangular and quadrilateral shell elements. The main cables and hangers were modeled with T3D2 elements. This element type is ideal for modelling cables or rods under the axial loads. In this model, 152495 nodes and 114653 elements were used.

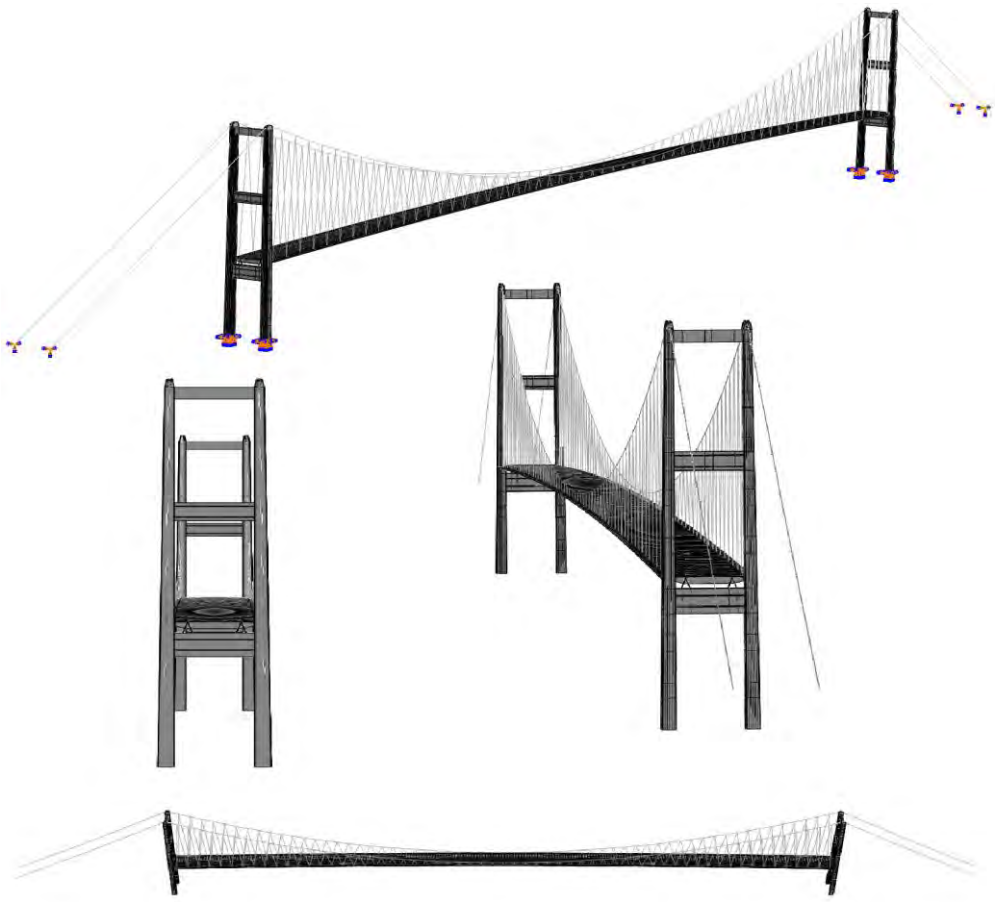

Figure.2. The 3D FE model of diagonal configuration of the Bosphorus Bridge

3.1.1 Validation of the Model

For the purpose of checking the validity, the analysis results obtained from the model were compared to the outcomes of past experimental studies. The first five

lateral, vertical and torsional modes of the FE model are listed below, in comparison to the results of Brownjohn et al. [6]. "Relative error" (R.E.) stands for:

$$\text{R.E.} = \frac{\text{ABS(FE Model Result - Experiment al Result)}}{\text{Experiment al Result}} \tag{1}$$

Table 2: Comparison of frequencies between the model and the results from the experimental studies [6]

Lateral modes		Experimental frequency-Brownjohn et al.	Relative Error
mode 1	0.072429	0.07	3.47%
mode 2	0.21433	0.209	2.55%
mode 3	0.27855	0.284	1.92%
mode 4	0.29164	0.294	0.80%
mode 5	0.36499	0.365	0.00%
Vertical modes		**Experimental frequency-Brownjohn et al.**	**Relative Error**
mode 1	0.12695	0.129	1.59%
mode 2	0.16784	0.16	4.90%
mode 3	0.23161	0.217	6.73%
mode 4	0.2888	0.277	4.26%
mode 5	0.38163	0.362	5.42%
Torsional modes		**Experimental frequency-Brownjohn et al.**	**Relative Error**
mode 1	0.33356	0.324	2.95%
mode 2	0.49833	0.474	5.13%
mode 3	0.49915	0.492	1.45%
mode 4	0.6705	0.649	3.31%
mode 5	0.89433	0.877	1.98%

3.2 Finite Element Modelling of the Vertical Configuration

Most of the structural components remained from the diagonal configuration. However, the hanger configuration was changed in this model, dampers were placed and, the towers were strengthened as in the retrofitting project. In this model, 152445 nodes and 114539 elements were used. It can be seen that the difference of element numbers between two models was relatively small (Figure 3).

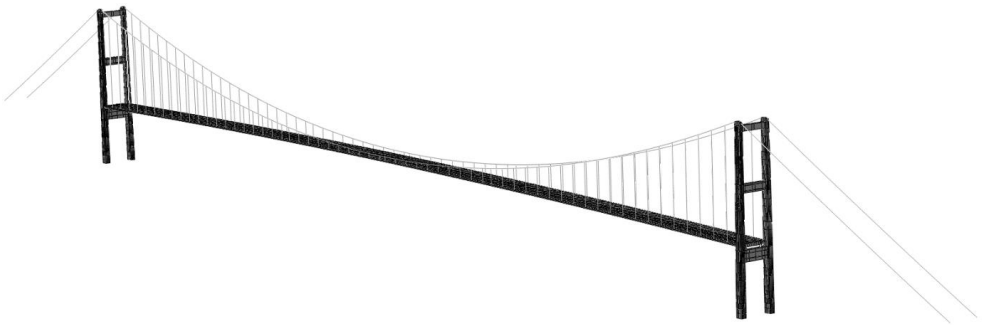

Figure 3. The 3D FE model of vertical configuration of the Bosphorus Bridge

4. COMPARISON BETWEEN THE TWO MODELS

Different temperatures were affected to both models and their responses were recorded. The extremum temperatures of weather are -16.1^{o}C and 41.1^{o}C [7]. Therefore, the models were exposed to ±30 ^{o}C temperature changes. The responses of the models were compared in various aspects.

4.1 Comparison of Displacements of the Deck

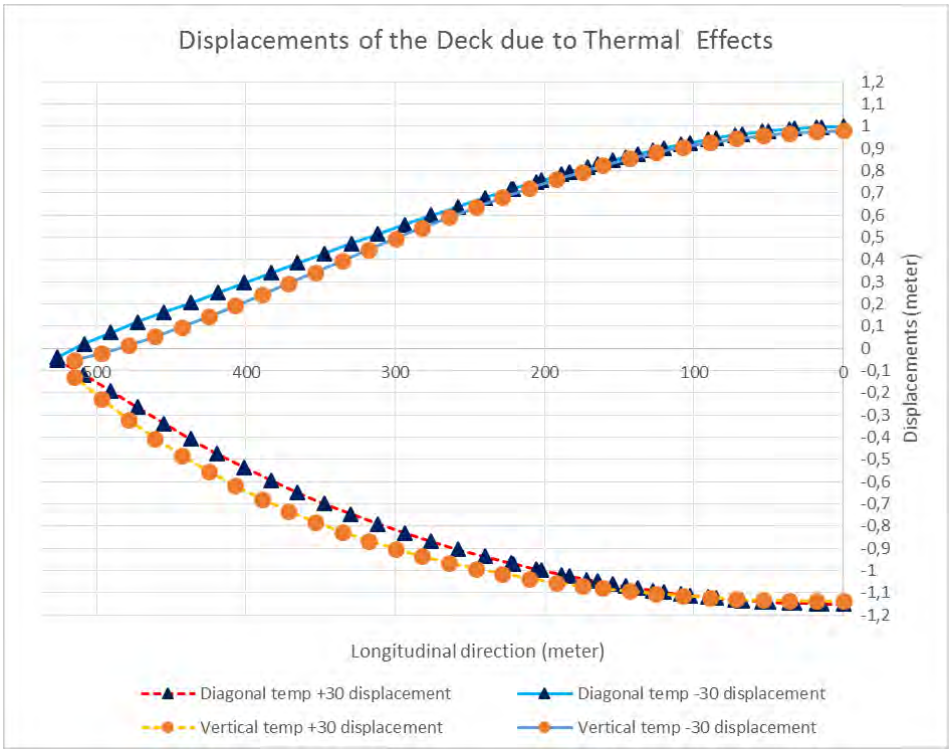

Figure 4: Displacements of the deck due to Thermal Effects

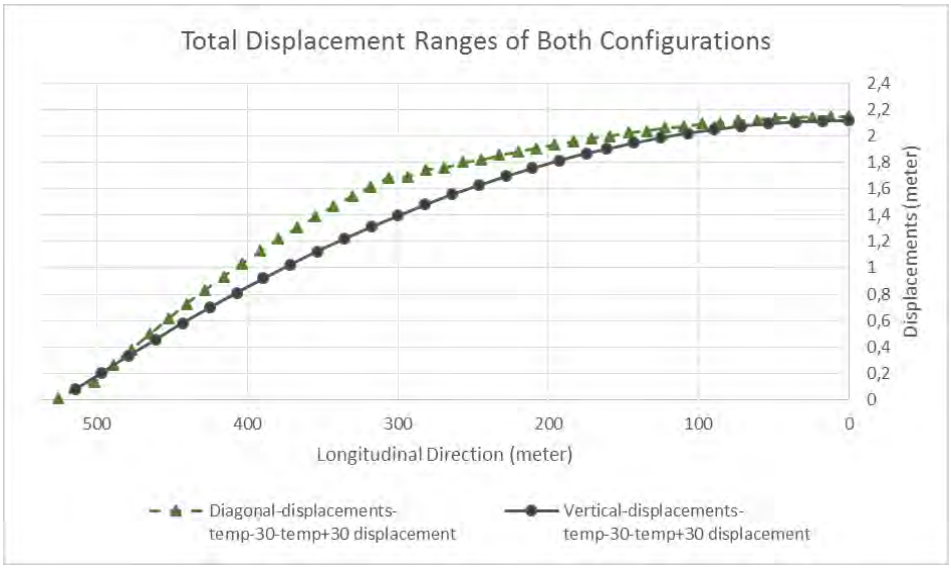

Figure 5. Total displacement ranges of both configurations under thermal effects

4.1 Comparison of Stresses on Hangers

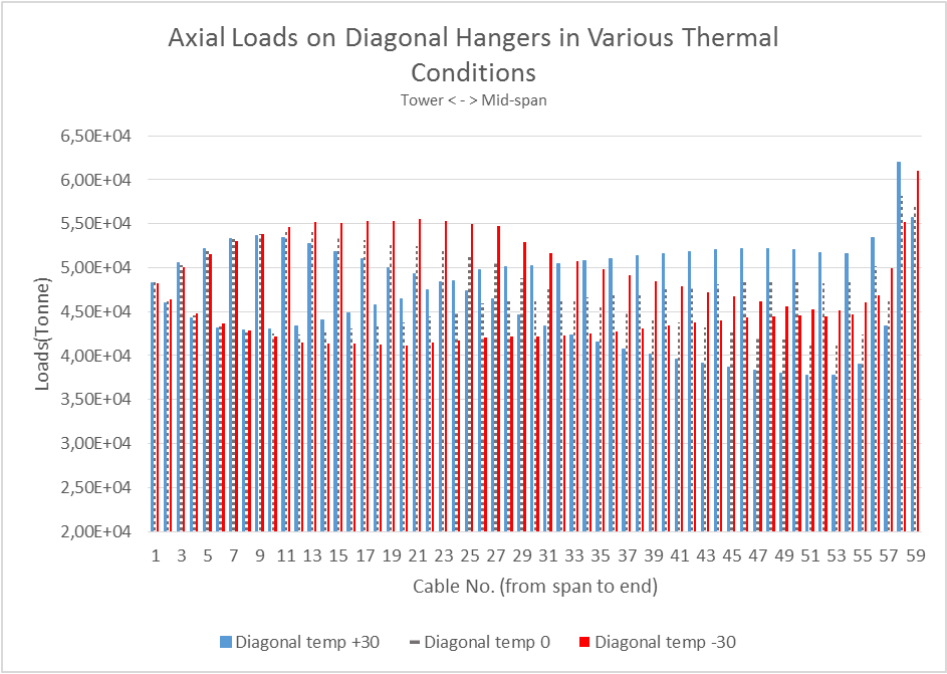

Figure 6. Axial stresses on diagonal hangers in various thermal conditions

5 CONCLUSIONS

The comparison of the experimental results and the FE model of diagonal configuration indicated the accuracy of the model. Then, the study proceeded to comparing thermal responses of two different hanger configurations of the Bosphorus Bridge. These comparisons showed that, under thermal effects, the displacements of the Bosphorus Bridge does not change drastically after the retrofitting on cable configurations. However, the model with diagonal hangers was found to be affected more than the model of vertical hangers did. The axial stresses on the diagonal hangers closer to the mid-span were changed noticeably due to thermal effects. In the high temperature environment, the cables that are inclined toward the centerline of the bridge, tended to get higher loads. In contrast, the load on them decreased as the model cooled down. The percentage of change, the hangers faced during heating and cooling, showed that the diagonal configuration was more prone to fatigue failure than the vertical configuration of the hangers.

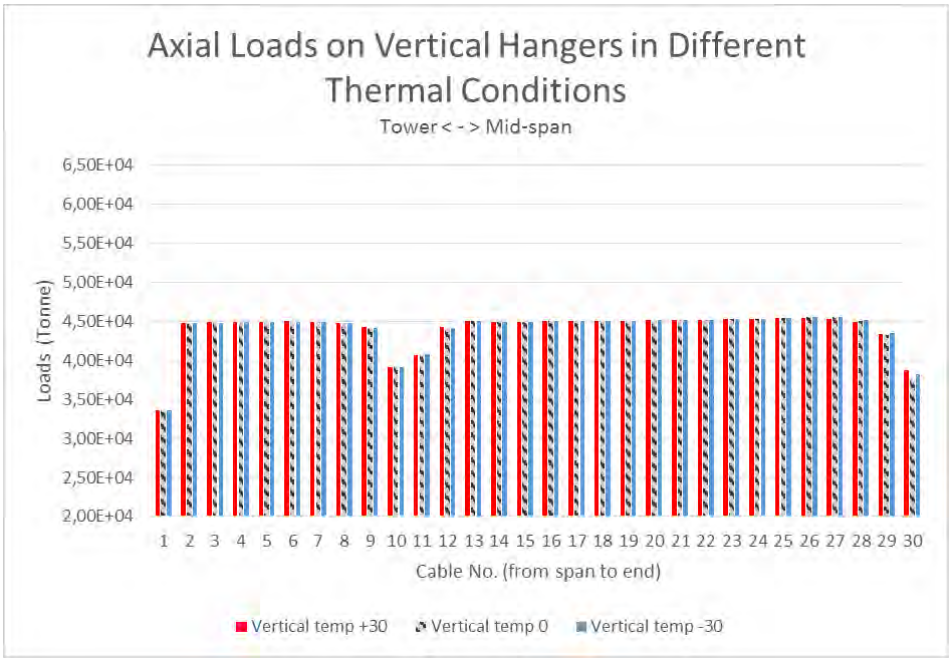

Figure 7. Axial stresses on vertical hangers in various thermal conditions

References

1. Yucel Y. (2007). *Morphotectonic Development of the Southern Black Sea Region and the Bosphorus Channel*. In Yanko-Hombach, V., & Gilbert, A. S. (Eds.). *The Black sea flood question: changes in coastline, climate, and human settlement*. Dordrecht: Springer.
2. Chen, W., & Duan, L. (2014). *Bridge engineering handbook*. Boca Raton: CRC Press.
3. Blockley, D. (2012). *Bridges: the science and art of the world's most inspiring structures*. Oxford: Oxford University Press.
4. Bas S., Apaydin N., Catbas N. (2016). *Considerations for Finite Element Modeling of the Bosphorus Suspension Bridge*. In Istanbul Bridge Conference 2016
5. General Directorate of Highways, Turkey, (1973). Record book: *Istanbul Bogazici Koprusu* (Bosporus Suspension Bridge), Istanbul: KGM matbaasi.
6. Brownjohn J., Dumanoglu A., Severn R., Blakeborough A. (1989). *Ambient Vibration Survey of the Bosphorus Suspension Bridge*. Earthquake Engineering and Structural Dynamics, Volume 18, pp. 263-83.
7. *İllerimize Ait İstatistik Verileri* (Statistical Data of Turkish Cities) (2017, May) Retrieved from https://www.mgm.gov.tr/veridegerlendirme/il-ve-ilceler-istatistik.aspx?m=ISTANBUL

Landslides hazard analysis based on deterministic models using different scenarios of groundwater and seismic acceleration

Cristina Magdalena Coman[1], Sanda Manea[2], Ernest Olinic[3]
[1]*Department of Geotechnical and Foundation Engineering, Technical University of Civil Engineering, Bucharest, 020396, Romania*
[2] *Department of Geotechnical and Foundation Engineering, Technical University of Civil Engineering, Bucharest, 020396, Romania*
[3] *Department of Geotechnical and Foundation Engineering, Technical University of Civil Engineering, Bucharest, 020396, Romania*

Summary

The main indicator of the steady state of slopes is the safety factor, which can be physically expressed by comparing the stress conditions in the natural earthen slopes. The safety factor can vary between the critical value, the minimum value which marks the limit of the stable condition, and large and very large values, theoretically infinite.

The leading aim of this framework is to create a deterministic model for landslides hazard analysis based on direct evaluation of safety factor, under different degrees of soil saturation and considering different scenarios of seismic acceleration. The slope stability assessment will be done using infinite slope model.

This analysis can be approached in geographic information systems taking into account a pixel basis. Therefore, the factors and parameters that trigger the slope fail and those that prevent the slope for failing will be expressed as individual maps (thematic maps). These maps will be overlaid using a created GIS function, according to the mathematical formula of the safety factor.

The proposed model has been tested in a geographic information system environment in the Bucium Hill area, located on the south-east side of the Romanian city, Iasi.

The thematic maps engine used as main input data: digital terrain model and the results of geotechnical laboratory tests from 25 bore holes (friction angle, cohesion, unit weight).

The final result will be a quantitative hazard map of failure probability assessment. The calibration will be done by comparing with other maps obtained from two different approaches.

KEYWORDS: landslide, hazard, infinite slope, safety factor, GIS

1. INTRODUCTION

The purpose of the authors' work is twofold: providing a theoretical and practical overview of landslides hazard assessment based on the infinite slope stability model and also providing pragmatic and purposeful suggestions for its utilisation.

The infinite slope model can be implemented in GIS systems by creating a two-dimensional model that divides the analysis range into discrete elements of a pixel size. Thus, using the GIS tools, the stability factor for each pixel is calculated. The effect of the neighbouring pixels is ignored.

The stability factor maps will be designed by overlapping the parameter maps, according to the mathematical formula given by the infinite stability slope model, considering four scenarios: completely dry soil, completely saturated soil, dry soil under seismic loads and saturated soil under seismic load.

The relative size of the areas that are found to be stable, critical or unstable slopes will result from the reclassification process of the final maps according to the minimum values required for the stability factor.

The practical work for landslide hazard assessment using infinite slope model, on GIS systems was built for the geographical area of the Bucium Hill and hydrographic basin of Vamasoaia River, located in Iasi City, on the south side of the Bahlui River.

The Iasi City represents a very geomorphological-active region from Romania which is certified by a large number of landslides registered over time. Predisposing, preparing and triggering factors such as intense slope, soil saturation, erosion processes and human actions are overlapping and leading to a wide variety of geomorphic phenomena.

The natural landforms extracted from digital elevation model indicate maximal altitudes between 100 – 370 m and general slopes between 10 – 20 degrees

The built model uses geotechnical data obtained in laboratory tests on samples from 25 geotechnical boreholes with depths between 2 and 10 m, executed in the field and topographic data consisting of a digital terrain model with 1m resolution. This type of models requires very high accuracy data.

In the end, two more landslides hazard maps will be presented, achieved for the same study area, using different approaches such as the bivariate statistical method and the national methodology. The way these maps are obtained will not be the subject of this paper work, but they allow comparing the final results.

2. THE PECULIARITY OF THE NATURAL LANDSLIDE HAZARD

The natural hazard of landslides is a potentially destructive physical event in which circumstances can cause property destruction, a negative social and economic impact, environmental degradation, and even injuries or loss of life. Slides of landslides may have natural triggers or may occur due to human activities [1]. Landslides hazard zonation allows delineation between stable areas and instable or potential instable area.

In the research literature, at the national and international level, can be found valuable documents and studies regarding landslide hazard assessment and its mapping methods. However, there is not a standardised method for achieving these types of maps. The landslides hazard maps can be designed using different approaches depending on user requirements, assessment purposes, mapping scale factor and very important, the quality of the available data.

Also called instability map or failure probability map, the landslides hazard map is a site plan to a conveniently chosen scale performed in a study area, which divides the entire area in polygons characterised by the same instability degree.

The first landslide hazard maps have been developed in the proximity of 1970 [2] [3].

The scientific community reveals a range of landslide hazard assessment methods. Those methods involve either qualitative evaluation such as inventory-based methods and knowledge-driven methods, either quantitative evaluation such as data-driven methods and physically based methods [4].

Very large used and recommended methods for data-driven landslide hazard assessment are bivariate statistical methods, multivariate statistical methods and artificial neural networks. The statistical methods, they are strictly dependent on landslides inventories.

Physically based methods are relayed on landslide hazard assessment using the modelling of slope failure processes. Examples of methods for physically based landslide assessment are GIS-based limit equilibrium methods (e.g. static infinite slope modelling), kinematic analysis for rock slopes, 2-D limit equilibrium methods, 3-D limit equilibrium methods and numerical modelling.

In the last three decades, collecting and processing data using automatic systems have been recorded significant developments and great progress. Now, there are available for large use many computer programs, able to process high complexity operations.

3. NATURAL AND ANTHROPIC CONDITIONS INFLUENCING NATURAL LANDSLIDE HAZARD

The natural landscapes of Iasi constitute of high fields bordered by hills or interfluvial hills with maximum altitudes between 100 and 370 m (Figure 1), developing steep slopes, some affected by erosions and landslide processes characterised by an extremely active morphodynamic.

The vulnerability of the study area, located in the Moldavian Plain reveals an area with the high potential of landslides manifestation, sometimes with great magnitude and generating significant damage.

The eastern side of the Copou Hill, the segment between Sararie and Ticau, the right overbank of the Cacaina River, the Bucium Hill, the Galata and Niculina districts are only a few examples which have registered numerous areas with high landslides occurrence. The morphodynamic activity attained a higher intensity in the early twentieth century, most likely with the beginning of slope deforestation and development of the inhabited area. The human intervention on the natural slopes and the large removal of the forest are two of the main causes of the instability slope increasing.

In the recent decades, the municipality has completed extensive work to reduce the landslides risk for Iasi city and yet the instability potential is still high.

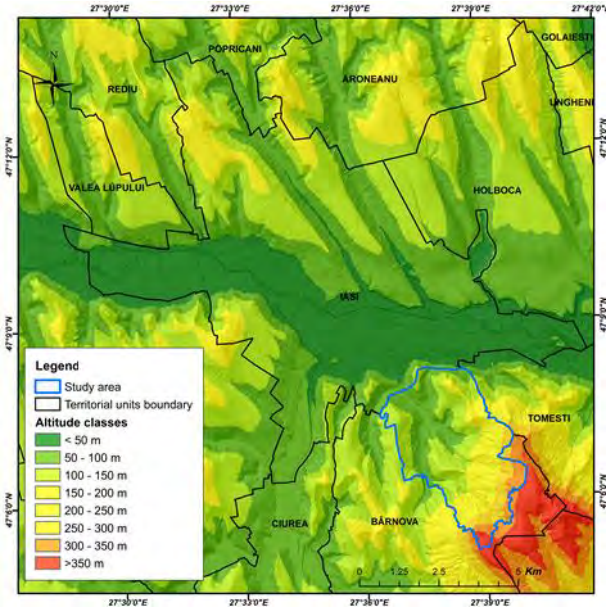

Figure 1. Terrain altitude map

From the geotechnical point of view, the soils layered in the Bucium Hill area have the following general stratification: under a filling layer with the maximum thickness of about 3 m, distinguish a succession of cohesive materials like clay, silty clay or silt with clay fractions, sandy clays, being in a mostly semi-solid consistency and plastic consistency, placed on a sandstone outline bedrock.

Sandy clay, silty clay or clay with small sands lens are generally found in the floodplains of the rivers. Clay and silty clays, with plastic consistency, are generally found in the hilly areas. Through its physical and mechanical properties, silty clay is considered a conducive environment for slip surface occurrence and slope failure.

The main trigger factor of slope failure is the presence of water (groundwater or surface water) by increasing tangential forces along the sliding plane.

The annual rainfall conditions are represented by the continental climate regime, with multi-annual averages of 518.9 mm at Airport Station and 514.8 mm at High School Negruzzi Station, with the minimum in February (25.9 mm) and March (23.8 mm) and a maximum in June (70.4 and 76.7 mm). The highest average daily amount of rainfall was recorded in June (2.2 mm) and the lowest in March (0.8 mm) and December (0.9 mm). In most years, snow has reduced thickness, in the winter of 1931-1932 was recorded the highest accumulated snow thickness (195 cm). The average annual temperature is about 9-10 degrees.

The rainfalls with long periods and slow discharge, the large melt of snow accumulations and the freeze - thaw processes are the major causes generating landslides.

4. INFINITE SLOPE STABILITY MODEL

The equilibrium state of a natural earthen slope can be assessed based on the estimation of the stability factor, a factor whose physical significance is expressed by comparing the stress conditions along the potential slip surface.

Therefore, the stability factor is determined as the ratio between the soil shear strength and the induced tangential forces as shown in Equation (1).

$$F_s = \frac{\tau_f}{\tau} \tag{1}$$

Acceptable values of safety factor which define the stability ranges are 1.5 for dry conditions, 1.3 for saturated conditions and 1.1 for infrequent loading conditions such as seismic acceleration. Lower values than 1 indicate unstable slopes. Values

ranging between 1 to the acceptable minimum values indicate critical slope. The stable slopes are characterised by values higher than acceptable values.

The proposed model in this paper evaluates the stability factor based on the infinite slope model.

The infinite slope stability model is a high degree simplified model, which oversees the destabilising components of gravity in relation to the resistance components given by cohesion and friction along a failure plane, considered parallel to the natural ground surface (Figure 2).

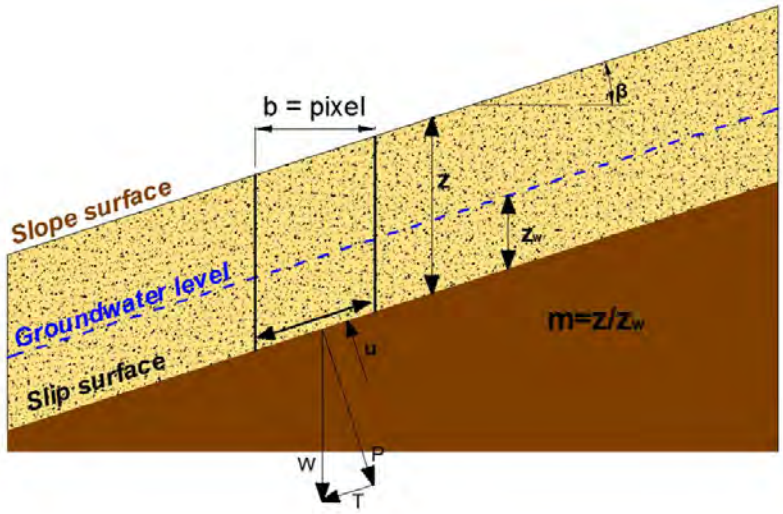

Figure 2. Infinite slope model

The infinite slope model takes into account an infinite sliding plan and calculates the stability factor according to Equation 2 [5].

$$F_s = \frac{c' + (\gamma - \frac{z}{z_w}\gamma_w) z \cos^2 \beta \tan \phi'}{\gamma z \sin \beta \cos \beta} \quad (2)$$

Where

c' effective cohesion (Pa);

ϕ' effective internal friction angle (°);

γ unit weight of soil (N/m^3);

γ_w unit weight of water (N/m^3);

z depth of slip surface (m);

z_w height of groundwater table above slip surface (m);

β terrain slope (°).

The calculation of the stability factor under seismic conditions uses the mathematical formula given by Equation 3 [5].

$$F_s = \frac{c' + (z\gamma \cos^2 \beta - z\rho\alpha \sin \beta \cos \beta - z_w \gamma_w \cos^2 \beta) \tan \phi'}{\gamma z \sin \beta \cos \beta + z\rho\alpha \cos^2 \beta} \quad (3)$$

Where

ρ bulk density (kg/m^3);

α peak ground acceleration (m/s^2);

The geotechnical (physical-mechanical soil parameters) and morphological parameters are the ones that determine the construction of the model and they are most often measurable and can be considered state variables that have a unique value at a given point in time and space.

The model accounts for different trigger factors such as the transient groundwater response of the slopes and/or the effect of earthquake excitation.

The soil moisture leads to the increase of water pore pressure and the decreasing of the effective normal stress, which through the internal friction angle is related to the shear strength of soil (Mohr-Coulomb failure criteria). The edge effects are considered negligible.

The infinite slope model approach applies over large areas when the geological and geotechnical conditions can be considered relatively homogeneous. It is intended to be used at a local scale, for shallow landslides (less than a few meters in depth), generally for translational sliding. It does not apply to deep-seated instability phenomena, only for simple landslide types.

It is also applicable to areas with nonexistent or incomplete landslide inventories when other methods (such as statistical methods) cannot be implemented because of their dependence of historical landslides locations map.

Infinite slope stability model has a higher predictive capability and provides more suitable and consistent results than heuristic and statistical models, which picture the underlying physical parameters leading up to the phenomena being modelled.

The disadvantages of the model are the high degree of simplification involved and the required for large field input data.

The main advantage of the proposed model is the ability to calculate the quantitative values of stability (safety factors or probability of failure).

5. SPATIAL DISTRIBUTION OF THE STABILITY FACTOR IN THE STUDY AREA

5.1. Site characterization

Bucium Hill and hydrographic basin of Vamasoaia River are located on the south side of Iasi city, in an area characterised by a monoclinic geological structure, the slopes surface being affected by land terraces erosion and sliding occurrence.

The area is generally occupied by forests, grasslands, orchards, vineyards and inhabited areas.

From the geological point of view, the study area is entirely in the Bessarabian Deposits (bs), the oldest deposits in the region and with the widest spread (Figure 3).

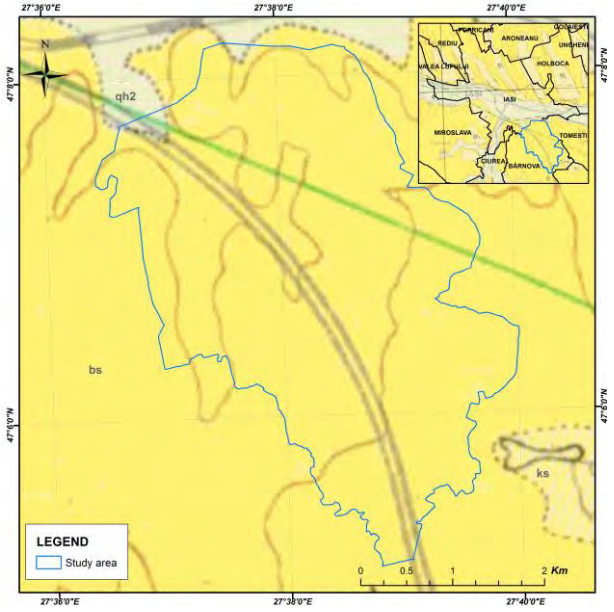

Figure 3. Geological map

Seismic activity of the study area is characterised by a peak ground acceleration value of 0.25g for earthquakes with the mean recurrence interval 225 years and the control period (corner seismic period) 0.7 sec (according to the "Seismic design code - Part I - Design provisions for buildings"- indicative P 100-1/2013).

The groundwater level intercepted in the 25 boreholes, indicates depths between 5 and 7,5 m for the high areas of the Bucium Hill and depths between 1 to 3 m depths for the Vamasoaia valley.

The soils and rocks layered in the study area have the following general stratification: under a filling layer with the maximum thickness of about 3 m, distinguish a succession of cohesive materials like clay, silty clay or silt with clay fractions, sandy clays, being in a mostly semi-solid consistency and plastic consistency, placed on sandstone outline bedrock.

Through its physical and mechanical properties, silty clay is considered a conducive environment for slip surface occurrence and slope failure.

5.2. The structure of the database used for the model construction and data processing

The database used to create the model consists of different types of data such as:

- tabular data (Table 1) that includes information from the study area, stratification description, specific geotechnical parameters (determined in the laboratory tests);
- vector data represented by "shapefile" files, representing points or polygons of the geographic location for study area and boreholes (the vector data will be used to create raster data);
- raster data represented by the digital terrain model (Figure 1), the terrain slopes maps, maps with a spatial distribution of the geotechnical parameters resulted in the interpolation/extrapolation of 25 points measured data (Figure 4).

Table 1. Geotechnical parameters determined in the laboratory tests

Borehole	Borehole depth [m]	Layer depth [m]	Groundwater table [m]	γ [kN/m^3]	γd [kN/m^3]	c [kPa]	φ [°]
FG1	6	1.4	-	18.4	15.0	78.3	21.5
FG2	6	2.5	1.7	18.6	15.2	55.0	22.0
FG3	10	2.7	3.1	19.2	15.6	64.4	21.9
FG4	10	2.8	-	18.4	15.0	78.3	21.5
FG5	6	2.8	-	19.4	16.0	39.1	30.4
FG26	6	1.4	-	18.6	15.7	70.0	25.0
FG37	6	2.4	2.4	18.5	14.6	55.4	13.5
FG38	6	3	-	17.8	14.9	53.1	28.4

Borehole	Borehole depth	Layer depth	Groundwater table	γ	γd	c	φ
FG39	6	2	-	18.8	15.2	48.0	18.0
FG40	6	1.4	-	18.5	14.6	55.4	13.5
FG53	6	1.6	1.8	18.4	15.1	39.2	17.5
FG54	6	5.4	1.8	18.9	15.1	23.0	21.7
FG55	6	2.6	1.2	18.8	15.2	48.0	18.0
FG11	2.2	2.2	-	18.7	16.0	53.7	29.8
FG12	5.2	5.2	-	18.5	15.2	66.7	24.1
FG13	10	5.3	7.5	17.9	14.9	96.3	26.8
FG14	4.7	3	-	18.6	16.2	75.3	25.7
FG15	1	1	-	18.6	15.7	70.0	25.0
FG16	1.7	1.7	-	17.7	15.7	60.0	27.0
FG17	9	1.4	6	20.1	17.7	14.8	21.7
FG18	10	2.2	-	18.4	14.8	50.7	27.9
FG19	3.2	1.8	-	18.6	15.7	70.0	25.0
FG20	3.2	2.3	-	15.7	14.7	65.0	25.0
FG21	1.3	1.2	-	18.7	16.0	53.7	29.8

All used data and built maps are raster format and following the Stereo 70, S42 Romania coordinate system.

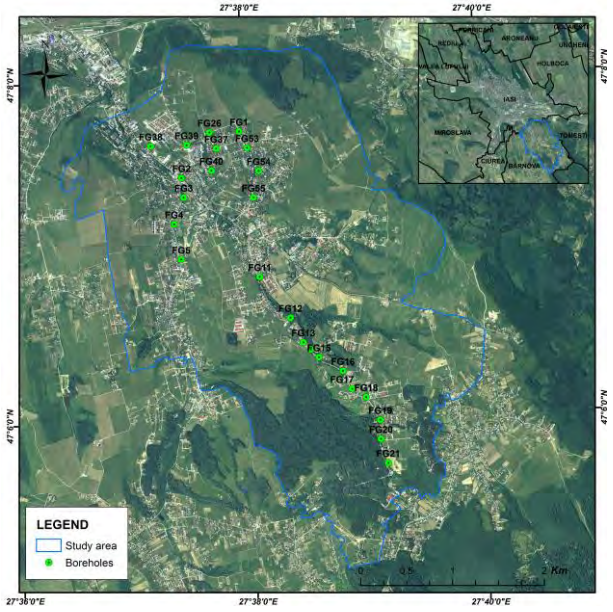

Figure 4. Geotechnical boreholes location

The maps representing the spatial distribution of geotechnical parameters like cohesion map (Figure 5.a), internal friction angle (Figure 5.b), dry soil weight map

(Figure 5.c) and soil depth (Figure 5.d), were built by interpolating the measured data.

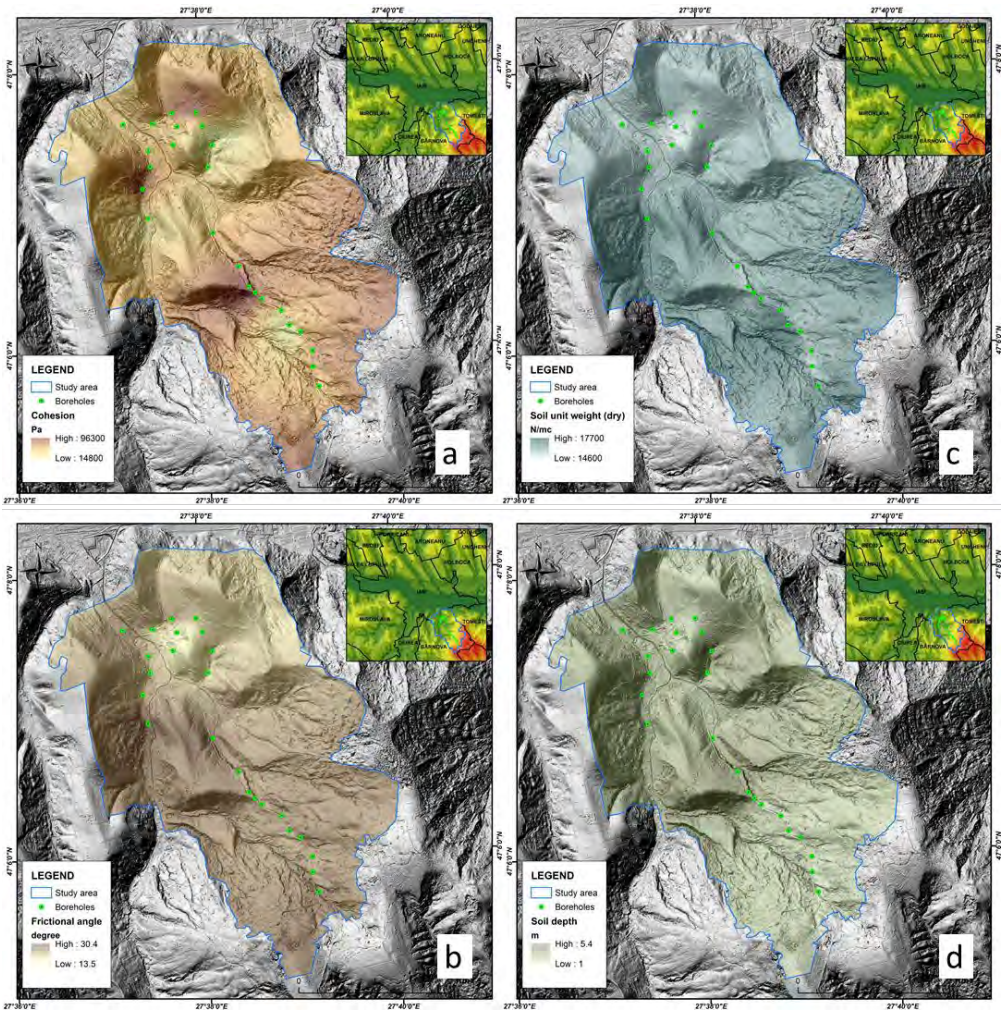

Figure 5. Spatial distribution of soil parameters: a. cohesion, b. internal frictional angle, c. soil unit weight, d. soil depth

The terrain slope expressed in degrees (Figure 6.a), well as the sinus function (Figure 6.b) and cosine (Figure 6.c) function applied to the slope, result from the digital terrain model with 1m precision, using the GIS tools.

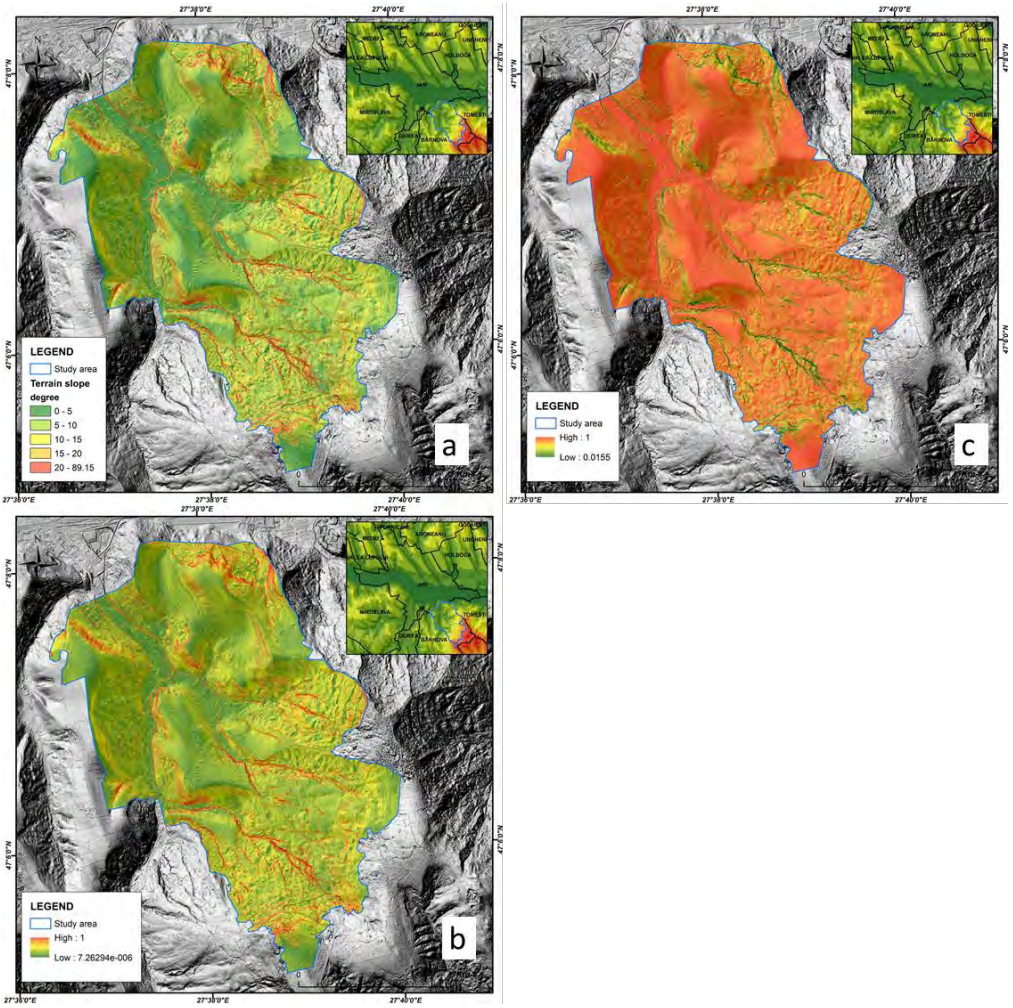

Figure 6. Terrain slope: a. slope (β), b. sin (β), c. cos (β)

5.3. Stability factor assessment

Applying Equation 2 and Equation 3 on the GIS parameter maps presented above, will outcome the spatial distribution maps of the stability factor, for different scenarios of groundwater and seismic acceleration. The stability model is generated as GIS functions. The four different scenarios are calculated by changing the variables of these functions.

5.3.1. Scenario 1 – Spatial distribution map of the stability factor considering dry conditions

The safety factor is evaluated under the assumption the soil is completely dry, so the groundwater table is equal to 0. The completely dry scenario is an extreme situation and may not occur in a region such as Iasi.

In these conditions, the Equation 5 substitutes the Equation 2, by replacing the parameter given by Equation 4.

$$z_w = 0 \tag{4}$$

$$F_s = \frac{c' + \gamma z \cos^2 \beta \tan \phi'}{\gamma z \sin \beta \cos \beta} \tag{5}$$

Applying Equation 5 in GIS platform outcomes the factor stability maps as shown in Figure 7.

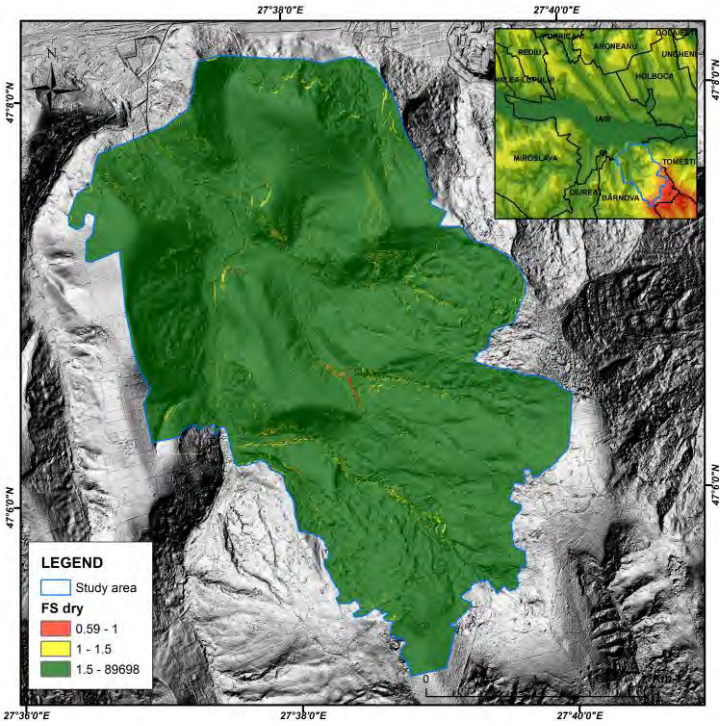

Figure 7. Spatial distribution of stability factor considering dry conditions

The completely dry scenario result indicates the most stable situation.

5.3.2. *Scenario 2 – Spatial distribution map of the stability factor considering saturated conditions*

The second scenario aims the stability assessment under the assumption the soil is completely saturated. This requires a diminution of the shear resistance parameters (cohesion and internal friction angle).

The Equation 7 substitutes the Equation 2, by replacing the parameters given by Equation 6.

$$z_w = z \tag{6}$$

$$F_s = \frac{c' + (\gamma - \gamma_w) z \cos^2 \beta \tan \phi'}{\gamma z \sin \beta \cos \beta} \tag{7}$$

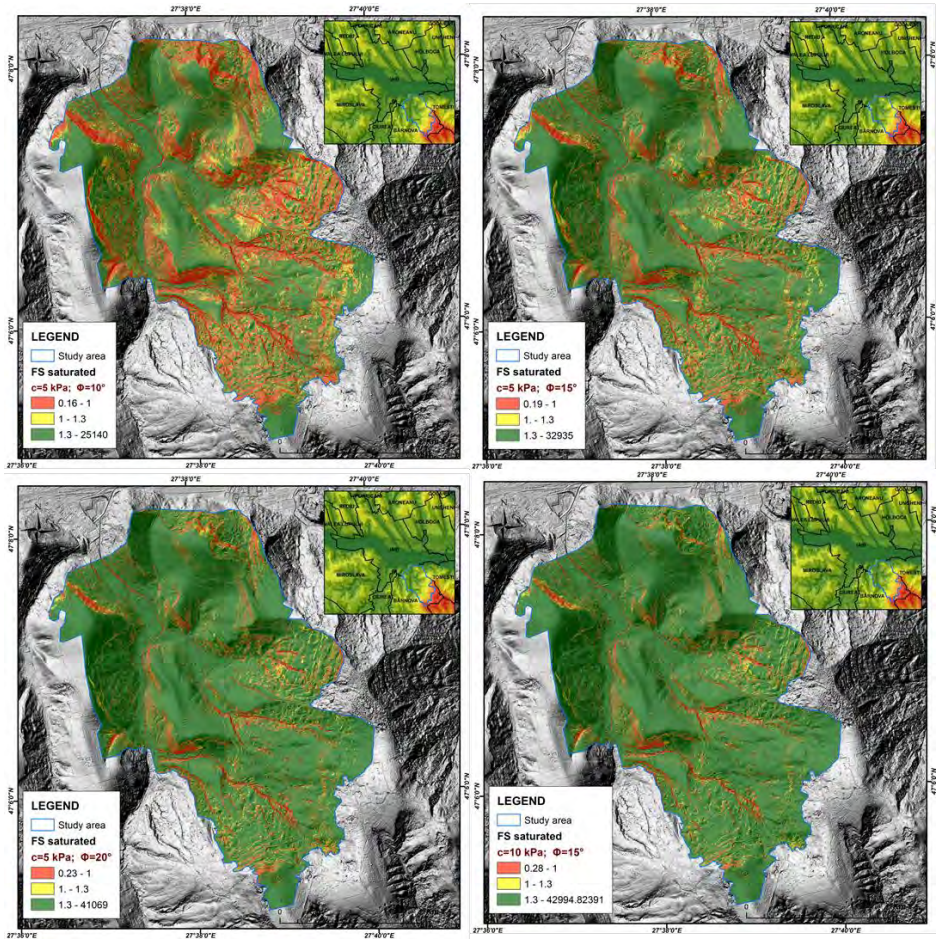

Figure 8. Spatial distribution of stability factor considering saturated conditions

Applying Equation 7 in GIS platform outcomes the factor stability maps as shown in Figure 8.

It is noticed that the presence of the groundwater table does not produce a significant increase in the potentially unstable surfaces and the study area surface remains still generally stable or partially stable.

5.3.3. Scenario 3 – Spatial distribution map of the stability factor considering dry conditions and seismic action

The third scenario assesses the stability factor considering completely dry conditions and seismic loads, associated with the peak horizontal ground acceleration.

In these conditions, the Equation 8 substitutes Equation 3, by replacing the parameters given by Equation 4 and considering the peak ground acceleration equal to 0.25g.

$$F_s = \frac{c' + (z\gamma \cos^2 \beta - z\rho\alpha \sin \beta \cos \beta) \tan \phi'}{\gamma z \sin \beta \cos \beta + z\rho\alpha \cos^2 \beta} \tag{8}$$

Overlapping the parameter maps according to the Equation 8 will disclose the stability factor maps as shown in Figure 9.

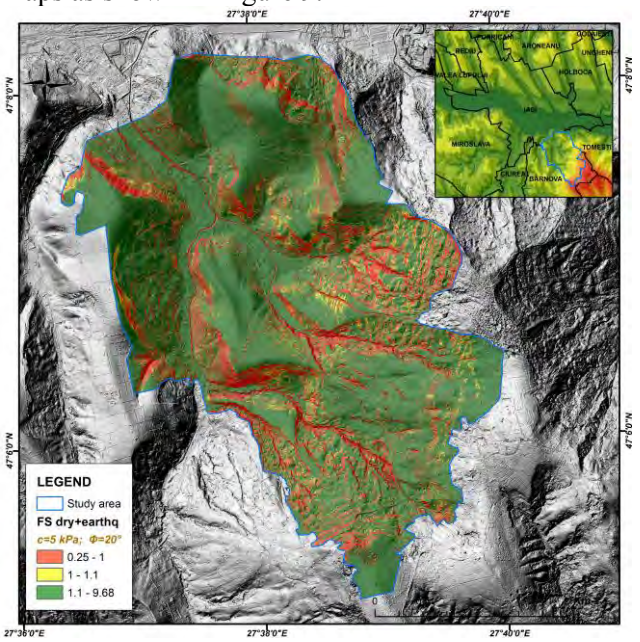

Figure 9. Spatial distribution of stability factor considering dry conditions and seismic action

The influence of the seismic acceleration has led to enlarged unstable surfaces than the unloaded situation simulated by scenario 1.

5.3.4. Scenario 4 – Spatial distribution map of the stability factor considering saturated conditions and seismic action

Considering completely saturated soil and seismic loads associated with the peak horizontal ground acceleration are not very realistic conditions but gives the most pessimistic situation.

Applying Equation 3 on the parameter maps outcomes the factor stability maps as shown in Figure 10.

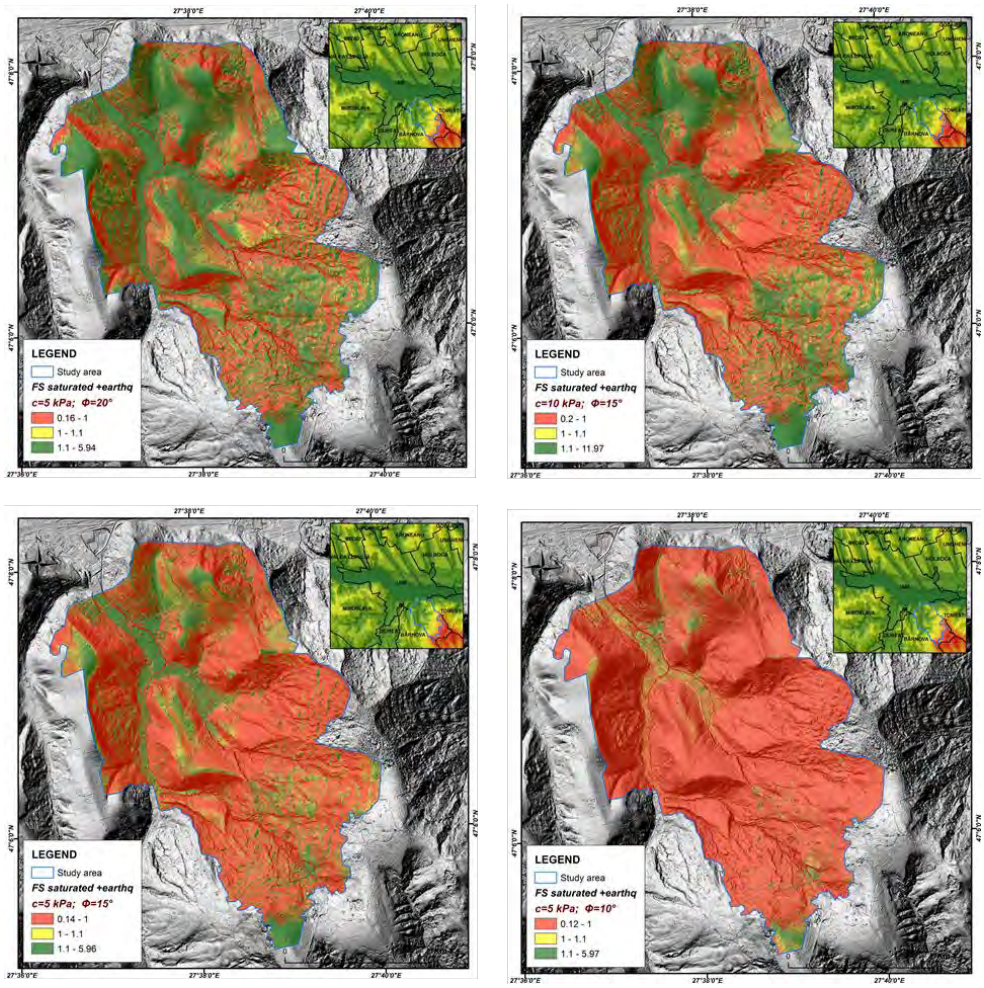

Figure 10. Spatial distribution of stability factor considering saturated conditions and seismic action

3. CONCLUSIONS

The results of the analyses indicate the values of the stability factors, calculated according to four scenarios: completely dry conditions, completely saturated conditions, dry conditions and seismic action, saturated conditions and seismic action.

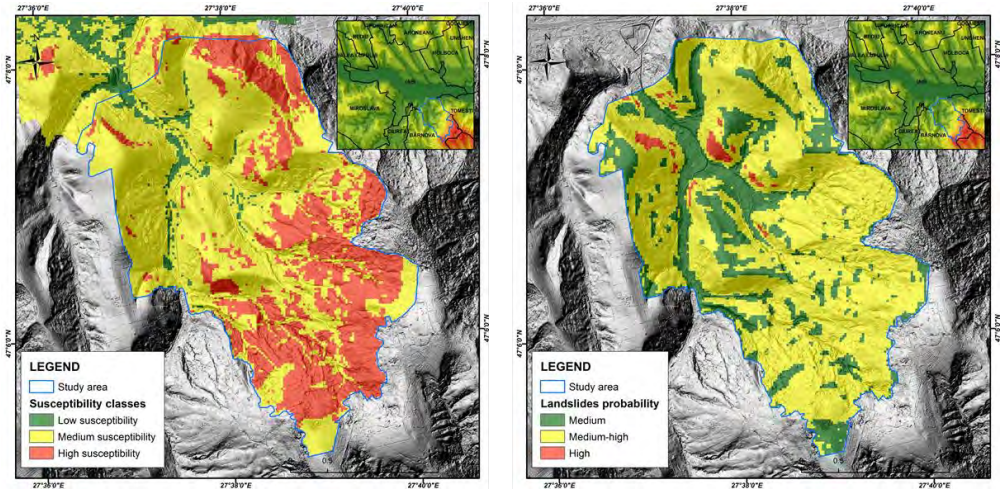

Figure 11. Landslides hazard maps: a. bivariate statistical method, b. national methodology

The landslides hazard assessment using slope stability models, similar to the one created in this paper, have higher prediction capability than other qualitative or quantitative methods (Figure 11), for example statistical methods, because it evaluates the potential slip following a calculation based on the parameters measured in the field, while the other quantitative methods are based on historical data (landslides inventories), and this can lead to results with high degrees of uncertainty.

These types of analyses are more suitable for soil layers less than a few meters in depth, with high superficial landslides occurrence and which are characterised by the presence of cohesionless soils or poorly cohesive soils.

One disadvantage of using the method is the high degree of simplification of the slope failure mechanism.

The landslides hazard assessment based on the stability factor is preferable to be used for local analyses. It can hardly be applied at national scales due to the variability of geotechnical data and the difficulty of building a national geotechnical database with high precision.

The stability factor maps keep the purpose and the quality of the hazard maps and will not serve the constructions design activities.

References

1. Manea, S., *Evaluarea riscului de alunecare a versanților*, Conpress, Bucharest, 2009.
2. Brabb E.E., Pampeyan E.H., Bonilla M.G., *Landslide susceptibility in San Mateo County, California*. Misc. Field Studies, map MF-360, scale 1: 62,500, US Geological Survey, Reston, 1972.
3. Kienholz H., *Map of geomorphology and natural hazards of Grindelwald*, Switzerland, scale 1: 10,000. Artic Alp Res 10:169–184, 1978.
4. Corominas, J., van Westen, C.J., Frattini, P., Cascini, L., Malet, J.-P., Fotopoulou, S., Catani, F., Van Den Eeckhaut, M., Mavrouli, O., Agliardi F., Pitilakis, K., Winter, M. G., Pastor, M., Ferlisi, S., Tofani, V., Herva´s, J., Smith J. T., *Recommendations for the quantitative analysis of landslide risk,* 2014
5. Brunsden, D., Prior, D. B., *Slope instability*, Wiley, Chichester, 1984.

Analytical differences between seven prediction models and the description of the rail track deterioration process through these methods

Richard Nagy
Department of Transport Infrastructure, Széchenyi István University, Győr 9024 Hungary

Summary

The quality of the rail track is one of the most important indicators to manage a reliable maintenance system so that plan the costs and the technical interventions. In this study, the track state will be defined by the qualifying numbers of the track, which shows the geometrical condition of a given rail section. More than one million measured data with the car (FMK-004) were processed than analysed and defined by configuring and programming a new regression method. The aim was the perfection of an analytic examination, which describes the differences between models of the track deterioration process, through characterized the correspondences more precisely and better to use in practice. Seven models were built and tested for prediction of the track qualifying numbers. One conventional non-linear regression model based on Vaszary's model using VBA, four new model using basic predictable equations, one new model using linear regression in VBA and one new model using an artificial neural network in MATLAB. When compare the predictions of models, the result shows that exist some basic models with more accurate predictions than a complex model.

KEYWORDS: rail geometric deterioration, track dimensioning factor, measuring and qualifying numbers, curve fitting, linear and non-linear regression, artificial neural network, visual basic, MATLAB

1. INTRODUCTION

The paper starts with a presentation of predictions models problems that shows a solution for this question. Furthermore, seven prediction model will be presented and these prediction values models will be compared with the real degradation values. Finally, it will be shown results and suggestions regarding some remark about the differences between the old and some new investigated methods.

There are two geometrical denominations in connection with rail tracks. The first one is the absolute geometry, which is planned by the rail designing engineer in case of newly-built rails or rail reconstructions with plot data, cross segment data

and length segment data and realises based on geodetic alignment [1], [2]. The second denomination is the relative rail geometry, which describes the position of rails to each other and to the basic lines and plane, so it shows the deviation compared to the error-free position [3]-[5]. The deterioration process of relative geometry is affected by several factors, which mostly come from traffic on it and from environmental effects [6]-[11]. The deterioration of the track without any regulation works can be described with the following equation:

$$C = C_0 \cdot e^{\alpha\, m\, v^2}, \tag{1}$$

where, C is the general characteristic of the geometric condition of the rail; C_0 is the number describing the initial condition; α is the so-called track dimensioning factor depending on the structural formation; m is the rolling load in tonnes and v is the equivalent speed.

From a technical point of view, this quality deterioration is firstly due to the interaction between the running rail vehicle and the rail track, secondly to the effect of the weather. The condition of the rail track suffers structural deterioration from the implementation time. As a result of the rolling friction the wheels and rails wear away, the tight rail fastenings loosen because of the sinking - rising movements of the track, the sleepers are pushed increasingly into the ballast bed, the rail ballast granules are forced into the protection layer or if there is no one, into the subgrade. In the case of the superposing of all these effects there will be size differences and later on, location errors evolve in the rail. The relative geometry of the rail track is described with three quantities along with others:

- alignment;
- longitudinal level;
- track twist.

Using the measuring numbers created for these three quantities, the Summary qualifying number weighted with ADded track twist (SAD) qualifying number describes the general geometric condition of the track. It is calculated to a given qualifying length (earlier 500 m, currently 200 m).

2. CRITICAL OBSERVATIONS

Until now in the literature, the model was given by the equation (1) created by Dr. Vaszary Pál [12] (Fig. 1). This is a clear model, the process is undisturbed by operational interferences, but differs from reality more and more as it is moved forward along the axis. The condition of the rail track cannot deteriorate forever, sometime later the deterioration function has to be tended asymptotically towards a border condition characterised by Ch value.

In reality, the geometric deterioration of the track is not an undisturbed process, because from time to time regulation work has to be performed on the line as a function of the condition (Fig. 2).

In connection with Vaszary’s formula, equation (1), it must be stated that the product is difficult to describe numerically in a lack of values of α factor, and the condition of the substructure also plays a huge role in the rail track deterioration process.

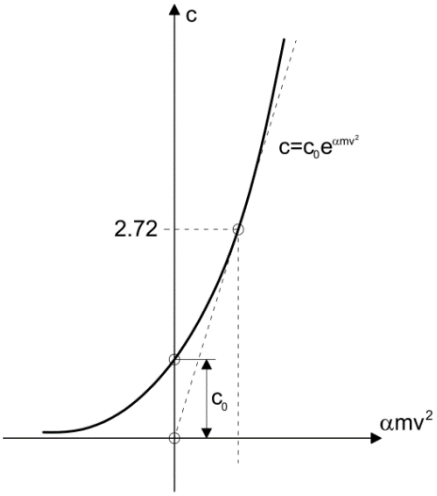

Figure 1. The equation of the track geometric deterioration according to [6]

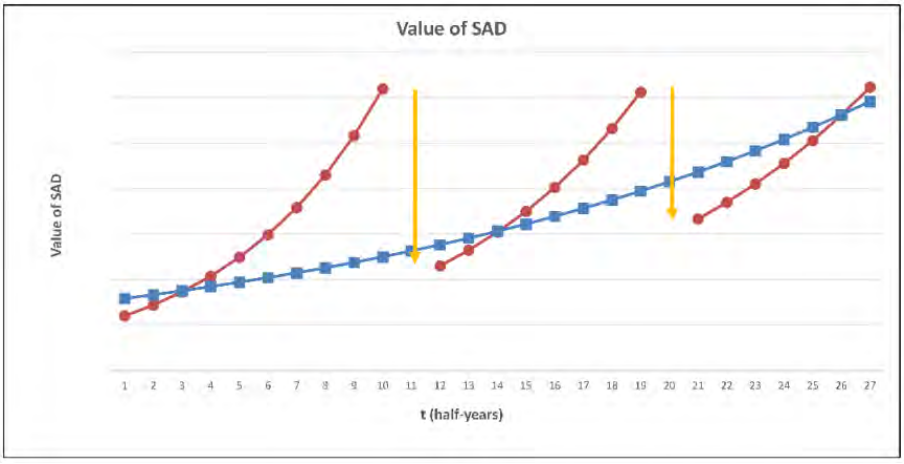

Figure 2. The effect of the track regulation works on the deterioration process

3. CREATING A NEW PROCEDURE

The FMK-004 measuring car of Hungarian State Railways Central Superstructure Examiner Ltd (MÁV KFV Ltd) provided measuring and qualifying numbers about the railway tracks at a stated frequency from the 2nd half of 1999 until the 2nd half of 2013. In the year 2013, the evaluation system has been changed, so the work with long data series is possible only with values, which were processed by FMK-004 measuring car until this year. Measuring and qualifying numbers are provided for each 500 meter length of the tracks. In Hungarian railway network there are 16.250 pieces qualifying sections with 500 meter length and altogether the data of 29 terms are available - counting with 2 measurements a year. That is 471.250 data to each measuring and qualifying number, and altogether (longitudinal level, alignment, twist and SAD) 1.885.000 data, which shows the extensiveness of the examination. After optimising the data chart and removing the incomplete lines there are 1.072.420 data remained for analysis.

It can easily be understood that it is an impossible task to analyse this amount of data with manual methods. So a method of progress was created, which correctly and valuably handles and processes this huge amount of data in a controlled way with given initial figures and boundary conditions.

3.1 The bases of the procedure

As mentioned earlier, the product factors cannot be handled numerically correctly in the model, described by equation (1), so the model of the rail geometric deterioration is reformed according to the theory used at the Technical University of Graz [13], [14]:

$$C_{SAD_i} = C_{SAD_0} \cdot e^{bt} \tag{2}$$

where C value is the qualifying number C=SAD; C0 is the value of the qualifying number determined during the first measurement after maintenance.

Instead of the product $\alpha m v^2$ should be used $b t$, where b value is dimensioned factor, which depends on the super-structural parameters (e.g. rail profile, sleepers type and distance, ballast thickness) and the sub-structural parameters (e.g. E2 bearing capacity values on protection layer/sub-base) [15]-[17]; t value has elapsed time. (It should be mentioned that the worse the quality of track geometry, the deterioration process is the faster. Due to low financing of maintenance of railway tracks in Hungary, all the track faults cannot be eliminated. The extant track faults will be deteriorated forward due to the cancelled (or delayed) maintenance, and other new faults can be evolved. In case the size of the track faults exceeds the prescribed value contained the maintenance regulations related to railway tracks

speed restrictions have to be used, i.e. a reduced speed is allowed in this section. At the end of this kind of sections, additional acceleration energy demand comes forward as compared to state if the train can be driven with constant speed [18]).

3.2 The course of the procedure

A large Excel table was created which contains all the measuring and qualifying numbers of each rail line in Hungary recorded with the FMK-004 measuring car from the second half of 1999 to the second half of 2013. The compiled large table was reduced to 1.072.420 data due to the changes mentioned above, which is the number of data taken into account.

The process of the automatic procedure

The automatic procedure (program henceforth) makes a catalogue of the lines found in the large table. It collects the initial and the final segments of the given line, the row-number of the initial and final segment in the large table and provides the number of the 500-meter sections in the given line. From this catalogue, the program knows, which fields to read when it analyses the given rail line. After reading the first line it analyses the data related to the 500-meter sections according to the description in the paragraph beginning with the analysis process of a 500-meter long qualifying section. If the analysis is completed the program goes on to the next 500-meter section.

When the last 500-meter section is analysed, all the regression equations are completed for the b dimensioned factor related to all qualifying sections.

The program is able to calculate the curve fitting with regression according to linear, exponential, power or natural based logarithm deterioration.

The program draws the distribution (n and m) of the equation parameters according to the type of curve fitting with regression one by one.

The result of linear regression calculation in parametrically:

$$y_i = n_i x + m_i \,. \tag{3}$$

The result of exponential regression calculation parametrically:

$$y_i = m_i \, e^{n_i x} \,. \tag{4}$$

The result of power regression calculation parametrically:

$$y_i = m_i \, x^{n_i} \,. \tag{5}$$

The result of naturally based logarithm calculation parametrically:

$$y_i = n_i \ln(x) + m_i \,. \tag{6}$$

Currently, the examinations are continuing according to the exponential fitting.

Distribution of the results of exponential regression calculation

The program calculates the (2)-(5) equations for each 500-meter section of the indicated line and describes them in a frequency histogram, where there are data from at least 7 consecutive terms without track regulation.

In *Fig. 3* and *Fig. 4* the frequency diagrams of parameters *n* and *m* in the exponential deterioration equations of SAD values can be seen. It was measured along the railway line No. 1, where sections were built with track system 54.

In *Fig. 5* and *Fig. 6* there are the frequency diagrams of parameters *n* and *m* in the exponential deterioration equations of SAD values measured along the railway line No. 1, where sections were built with track system 60.

There are differences between the examined sections not only in the rail systems (54E1 and 60E1), but in the sleeper types (LM and LW) and the types of rail fastenings (Skl-3 and Skl-1).

In the functions, the value of parameter *n* is the *b* dimensioned factor itself, while parameter *m* shows where the function crosses *y* axis so that it gives the value of SAD_0.

When the function describing the geometric deterioration process of a given railway track is unknown, it is mostly the speed of deterioration depending on the type of the curve fitting with regression is what we look for. The parameter *n* shows the deterioration speed in linear and non-linear cases as well.

The parameter *m* also provides interesting information, it shows the condition of the given rail track as a result of the regulation work.

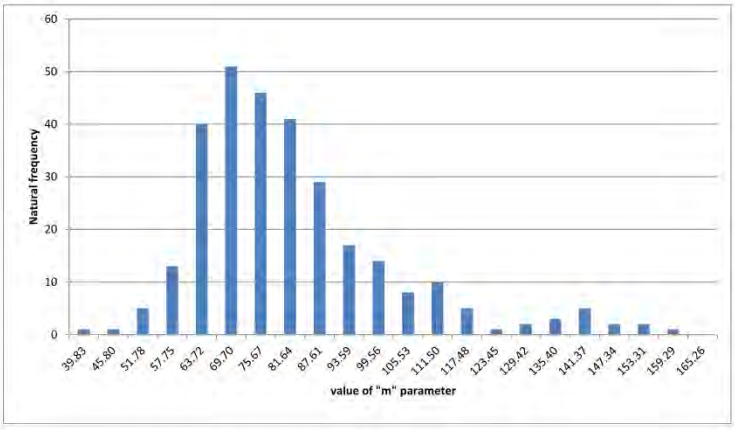

Figure 3. The natural frequency diagram of parameter m in the exponential deterioration equation for railway line No. 1, where sections were built with track system 54

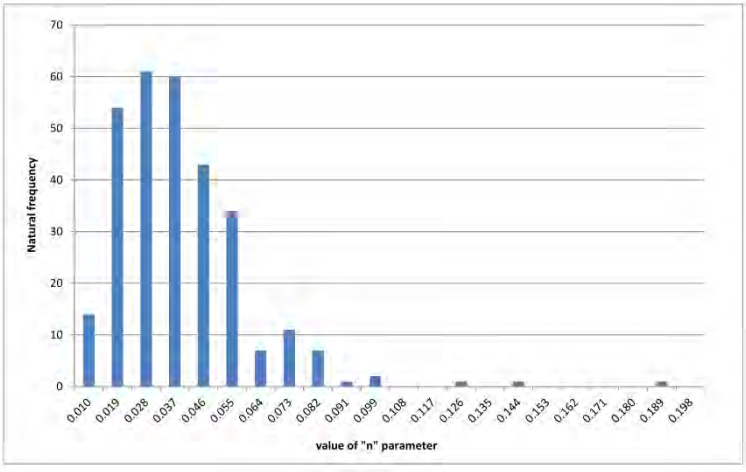

Figure 4. The natural frequency diagram of parameter n in the exponential deterioration equation for railway line No. 1, where sections were built with track system 54

To continue the evaluation, the values belonging to n parameter are selected, which are used by the program to calculate a more exact result.

After appointing the value set the program draws up the distribution of the given parameter. After this, the mean value of the given parameter weighted with R2 value can be calculated with the narrowed value set.

The program collects the mathematical and graphic results in a separate file, gives a name to the file, deletes the chart and calls in for the data of the following line with the help of a catalogue and the analysis starts again.

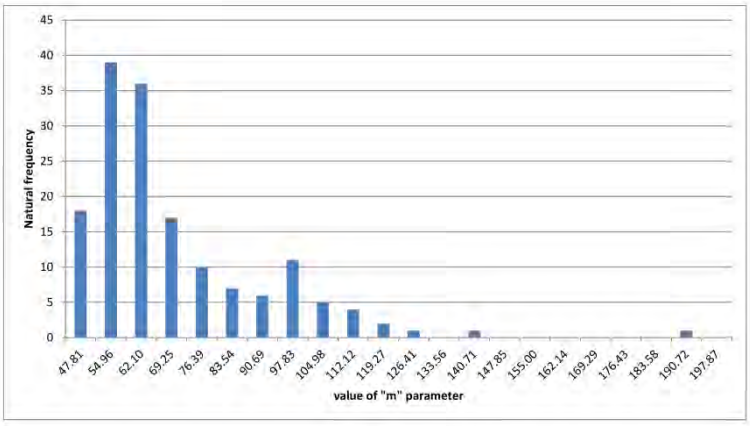

Figure 5. The natural frequency diagram of parameter m in the exponential deterioration equation for railway line No. 1, where sections were built with track system 60

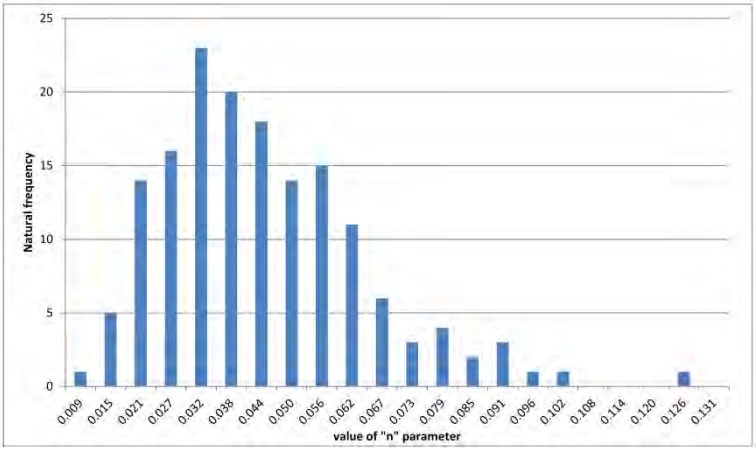

Figure 6. The natural frequency diagram of parameter in the exponential deterioration equation for railway line No. 1, where sections were built with track system 60

The analysis process of a 500-meter long qualifying section

The process starts with the program looking for consecutive terms without regulation work in the given 500-meter section. It can be determined separately how many consecutive operation-free terms should be the minimum that the

program takes into account during the analysis. The program indexes each inspected datum related to the term with 0 where there is a condition improvement (characterised by SAD value) higher than 5% compared to the previous term. This value indexed with 0 will be the SAD0 value during the analysis when the examination of the qualifying number is described.

Transforming the formula above (2) the b sub- and super-structural dimensioned factors are received as

$$b = \frac{\ln\left(C_{SAD_i} / C_{SAD_0}\right)}{t}. \tag{7}$$

Based on the SAD numbers the program determines the equation of the given data series and the determination coefficient describing the rate of the fitting by the setting of linear (2) and non-linear (3), (4), (5) regression functions.

Hereinafter only the regression equations having a determination coefficient of

$$R^2=0.75, \tag{8}$$

or higher will be taken into consideration.

As the program completes the analysis of a 500-meter section, it continues with the next 500-meter rail section.

When the last 500-meter track section has been already analysed and the analysis has been completed according to the scheme in Fig. 7, the program goes on to the next line.

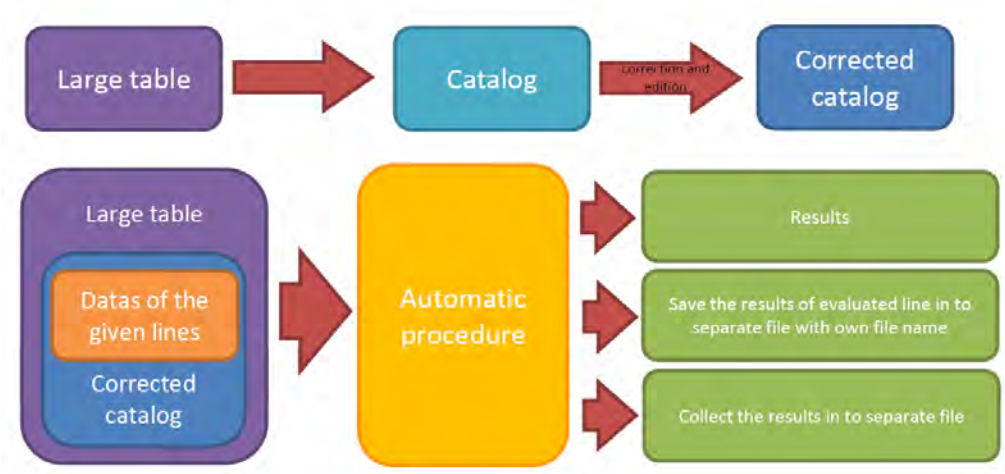

Figure. 7. The automatization figure of the program

Assigning other parameters

The procedure described above determines the deterioration equation of the given line on the basis of the unfiltered data.

It is a fact that a lot of parameters are available for the examined lines, including horizontal geometry, speed, the track system, the rail system, the type of sleeper, the sleeper spacing and the ballast thickness, etc. Despite this, there are factors in the analysis that the program cannot take into account.

The parameters mentioned above must be assigned to the 500-meter rail sections of the lines examined, which required separate programming and procedure creation over again. The following Table I provides the information for railway line No. 1 about the diversity of rail system, currently, it would be 70 rows. It can be simplified with creating a separate program.

Table 1. Sections of rail systems

Zone	Initial section	Zone	Final section	Rail system
1	0	1	1340	MÁV48,5 normal
1	1340	1	11800	54E1 normal
1	11800	1	12300	60E1 normal
1	12300	1	17299	54E1 normal
1	17299	1	17600	60E1 normal
…	…	…	…	…
3	188370	3	188495	60E1 normal
3	188495	3	189115	54E1 normal
3	189115	3	189476	60E1 normal
3	189476	3	192720	54E1 normal

If this assignment has been completed, it is possible to call the 500-meter long railway track sections that should be evaluated into the program according to the filtered parameters.

The results of the linear and the exponential regression from this program are going to be countered in the followings.

4 PREDICTION MODELS

Four simple model was created for control, two regression model and the artificial neural network was built to overcome the more simple models.

It can be seen that a higher orders model is endured if it predicts more precise data than more simple models.

Basic models show that some simple model can predict processes, although it is proved that a complex model has better prediction values.

4.1 Basic models

All of the basic models are linear and low ordered, meanwhile, it is necessary to compare with the higher ordered models.

Basic model 1

$$SAD_{t=n+1} = SAD_{t=n} + \frac{(SAD_{t=n} - SAD_{t=1})}{n} \tag{9}$$

Basic model 2

$$SAD_{t=n+1} = SAD_{t=n} + (SDA_{t=n} - SAD_{t=n-1}) \tag{10}$$

Basic model 3

$$SAD_{t=n+1} = SAD_{t=n} + \frac{(SAD_{t=n} - SAD_{t=n-1})}{2} + \frac{(SAD_{t=n-1} - SAD_{t=n-2})}{2} \tag{11}$$

Basic model 4

$$SAD_{t=n+1} = SAD_{t=n} + \frac{(SAD_{t=n} - SAD_{t=n-1})}{4} + \frac{(SAD_{t=n-1} - SAD_{t=n-2})}{4} + \frac{(SAD_{t=n-2} - SAD_{t=n-3})}{4} + \frac{(SAD_{t=n-3} - SAD_{t=n-4})}{4} \tag{12}$$

where $SAD_{t=n+1}$ is the value of the next half year’s qualifying number.

4.2 Regression models

Hereinafter only the given railway line’s regression equations having a determination coefficient of R2=0.75 or higher will be taken into consideration.

Linear regression

general equation: $$y_i = \alpha + \beta x_i + u_i \tag{13}$$

current equation: $$SAD_t = SAD_0 + \mathrm{bt} \tag{14}$$

where the

SAD_t is the predicted SAD value in the tth half year,

SAD_0 is the predicted value of the qualifying number after maintenance

b is the degradation gradient (here it is the dimensioned factor),

t is the number of elapsed terms since the last maintenance.

Exponential regression

general equation: $$y_i = \alpha + e^{\beta x_i} + u_i \quad (15)$$

current equation: $$SAD_t = SAD_0 + e^{bt} \quad (16)$$

where the

SAD_t is the predicted SAD value in the tth half year,

SAD_0 is the predicted value of the qualifying number after maintenance

b is the degradation gradient (here it is the dimensioned factor),

t is the number of elapsed terms since the last maintenance.

4.3 Artificial Neural Networks

Artificial Neural Networks (ANNs) known as connectionist models are systems that try to make use of some of the known or expected organising principles of the human brain. They consist of a number of independent, simple processors - the neurons. These neurons communicate with each other via weighted connections - the synaptic weights.

An ANN is such a mapping device, which assigns to each input exactly one output (both input and output may be vectors of values). The function is determined by the network's weights which are set while training the network. A neural network is trained, roughly, as follows. The network is shown a set of examples, each consisting of inputs and outputs. It learns the connections among them by assigning weights to connections. This is done by continuously changing weights to get closer to the desired outputs [19].

The X matrix was pre-ordained in order to the correct comparability, only the regression equations were used having a determination coefficient of R2=0.75 or higher, what caused the reduction of the input matrix to 1490 rows. The aim vector is always the value of the next missing half year; the hidden neurons number are three.

The examined railway line

Such a railway line had to be found in which the time between two maintenance is long enough to examine the model’s predictions.

In order to find this railway line, the author program was used with some modifications. It countered the number of the half years between two maintenance line by line.

After the examination, the line No.60 (Pécs to Gyékényes) had been chosen because this line has the longest periods without maintenance, which provided long degradation processes to test the models.

This line has many 500 meter sections in which the time between two maintenance is more than 15 half years.

The learning sources and the validation process of the models are shown in Table 2. The first seven half years after the maintenance are the learning SAD values, while from the eighth half year the predicted and the real values were compared to count the difference.

Table 2. SAD values of a given model

	Learning SAD values							Predicted SAD values			
Number of the 500 meter long sections	half years										
	1	2	3	4	5	6	7	8	9	…	16
1	Real SAD values							Real SAD values			
1								Predicted SAD values			
1								The value of the error			
2	Real SAD values							Real SAD values			
2								Predicted SAD values			
2											
…	…							…			
1490	Real SAD values							Real SAD values			
1490								Predicted SAD values			
1490								The value of the error			

The differences between the real and the predicted values are countered with the [1] equation, then these values are averaged to the given half years.

$$\sqrt{\frac{1}{n}\sum_{i=i}^{n}(SAD_i - \widehat{SAD_i})^2} \tag{17}$$

This process was run for all seven models, the root mean squared error values are shown in the 3rd table.

Table 3. RMSE values

	8th half-year	9th half-year	10th half-year	11th half-year	12th half-year	13th half-year	14th half-year	15th half-year	16th half-year
Basic 1	10,67	15,94	17,28	24,30	33,51	17,95	28,41	34,24	43,22
Basic 2	14,53	21,27	26,87	38,55	40,58	60,89	55,55	66,74	79,25
Basic 3	12,64	15,71	18,82	24,56	22,10	30,81	33,88	30,30	52,11
Basic 3	11,84	14,83	17,90	21,47	20,99	28,53	34,04	33,96	45,25
Linear regression	10,49	14,83	15,49	20,66	26,28	19,05	28,75	36,13	48,98
Exponential regression	17,11	29,48	39,71	52,42	85,28	44,21	70,72	85,10	47,88
Artificial neural network	10,86	11,54	12,71	17,17	17,29	19,95	22,47	18,95	26,46

The next figures (8. to 11.) show the root mean squared error values of the prediction models as a function of the number of terms.

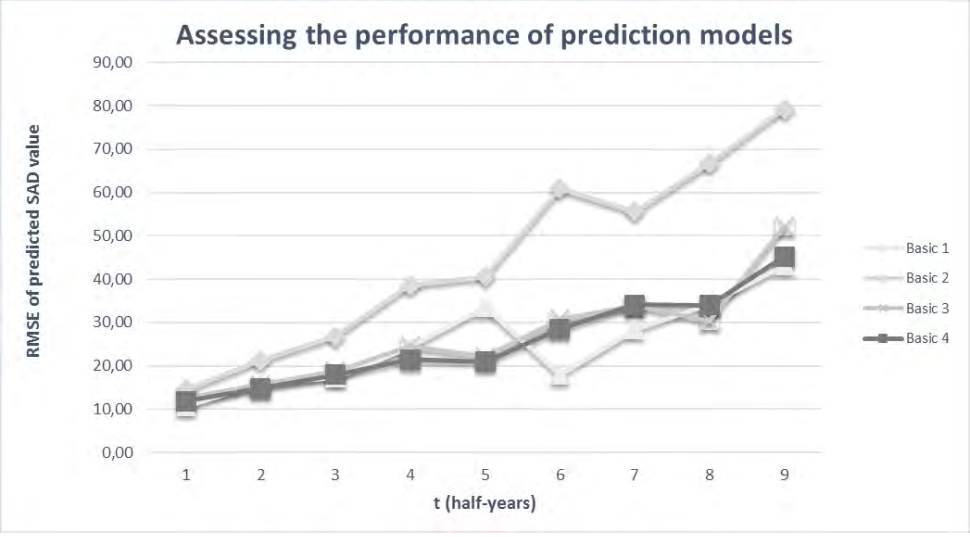

Figure 8. Basic models

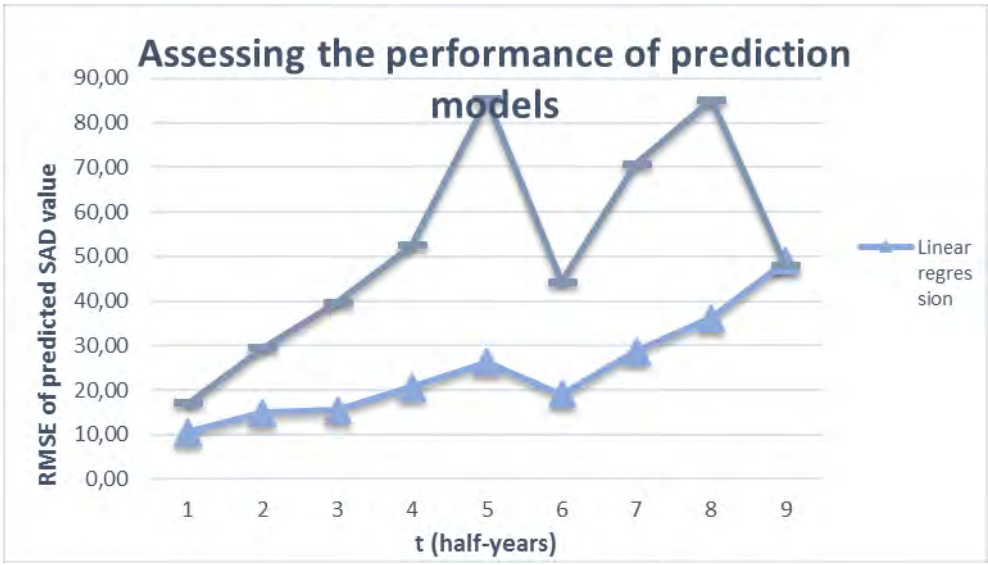

Figure 9. Regression models

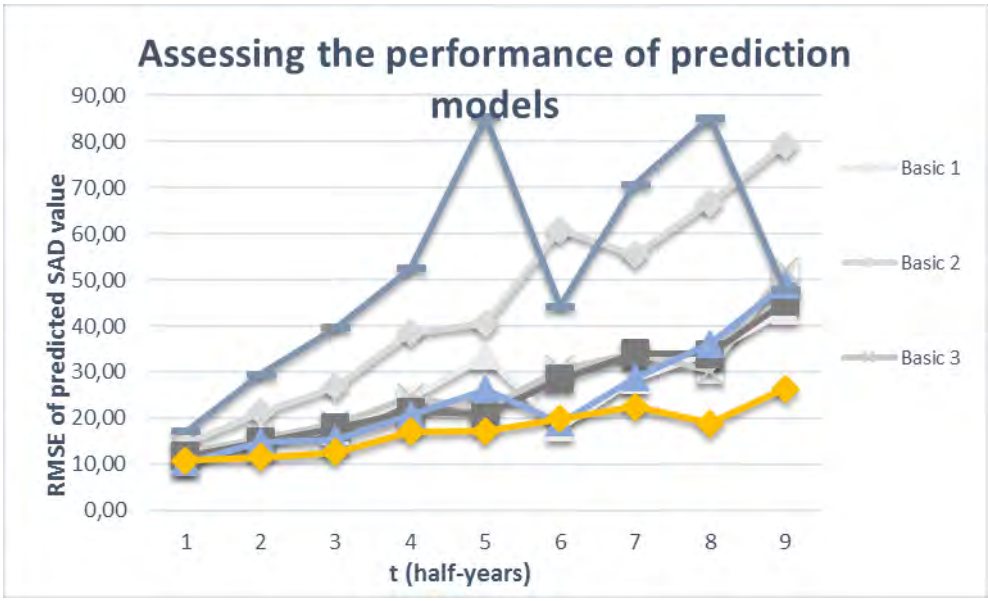

Figure 10. Prediction models

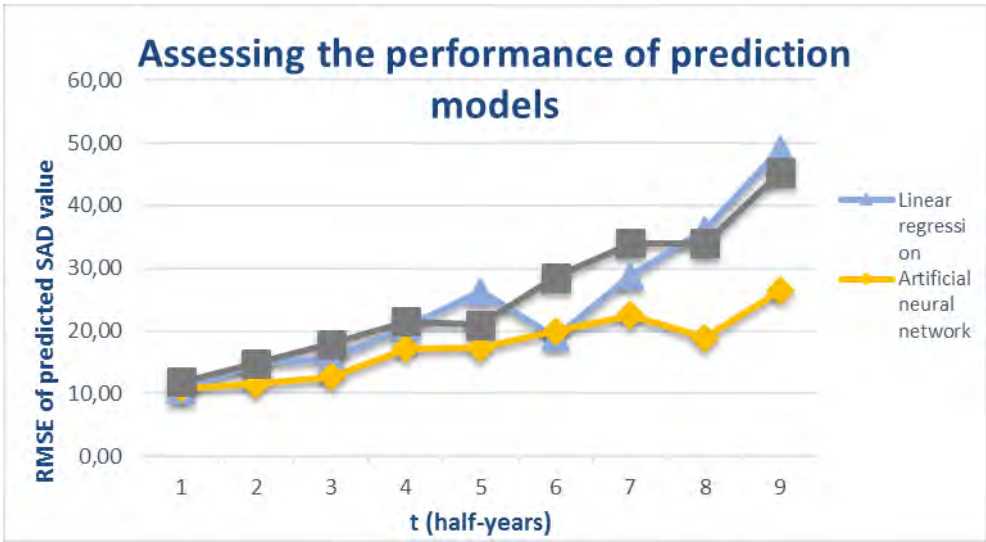

Figure 11. The chosen models

The root mean squared error values (RMSE) of the models relative to each other are shown with numbers in the 4th table.

Table 4. Excess error compare

Excess error compared to the linear regression model										
Half years	1	2	3	4	5	6	7	8	9	cumulatively
Basic 4	1,34	0	2,41	0,81	-5,29	9,48	5,29	-2,17	-3,73	8,14
Neural Network	0,37	-3,28	-2,78	-3,49	-8,99	0,89	-6,27	-17,17	-22,53	-63,25
Cumulatively:										-55,11
Excess error compared to the Basic 4 model										
Half years	1	2	3	4	5	6	7	8	9	cumulatively
Basic 4	-1,34	0	-2,41	-0,81	5,29	-9,48	-5,29	2,17	3,73	-8,14
Neural Network	-0,97	-3,29	-5,19	-4,29	-3,7	-8,59	-11,56	-15	-18,79	-71,39
Cumulatively:										-79,53
Excess error compared to the neural network model										
Half years	1	2	3	4	5	6	7	8	9	cumulatively
Basic 4	0,97	3,29	5,19	4,29	3,7	8,59	11,56	15	18,79	71,39
Neural Network	-0,37	3,28	2,78	3,49	8,99	-0,89	6,27	17,17	22,53	63,25
Cumulatively:										134,64

The frequency of RMSE values of the predictions models is shown in the next figures (12th -14th figure).

These box plot diagrams show that the frequency of the predicted data has almost the same value. Thus the neural network model has a better prediction than the others.

It has to be mentioned that generally known box plot diagram was used to setup in the following figures.

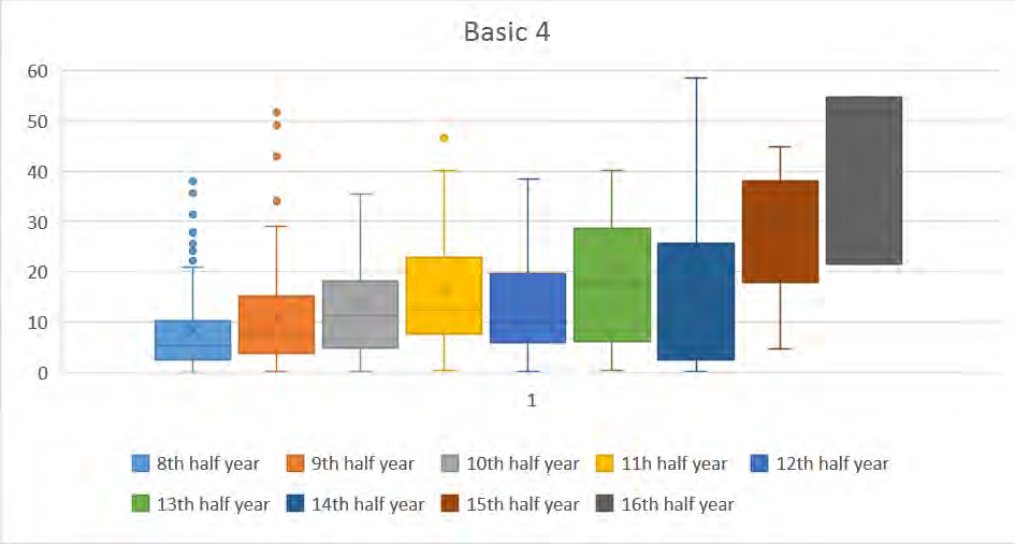

Figures 12. The frequency of the predicted values of the Basic 4 model

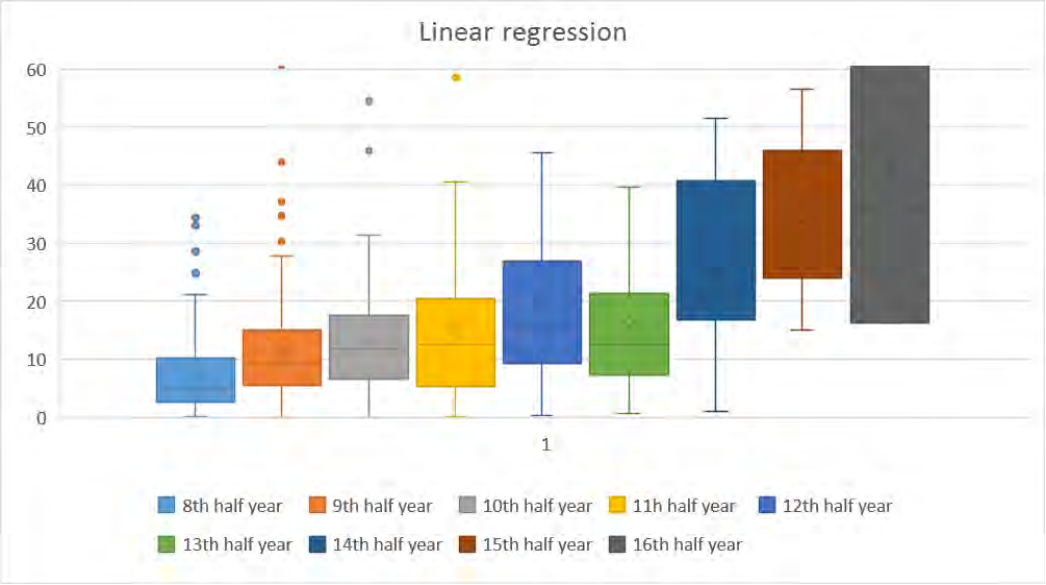

Figures 13. The frequency of the predicted values of the Linear regression model

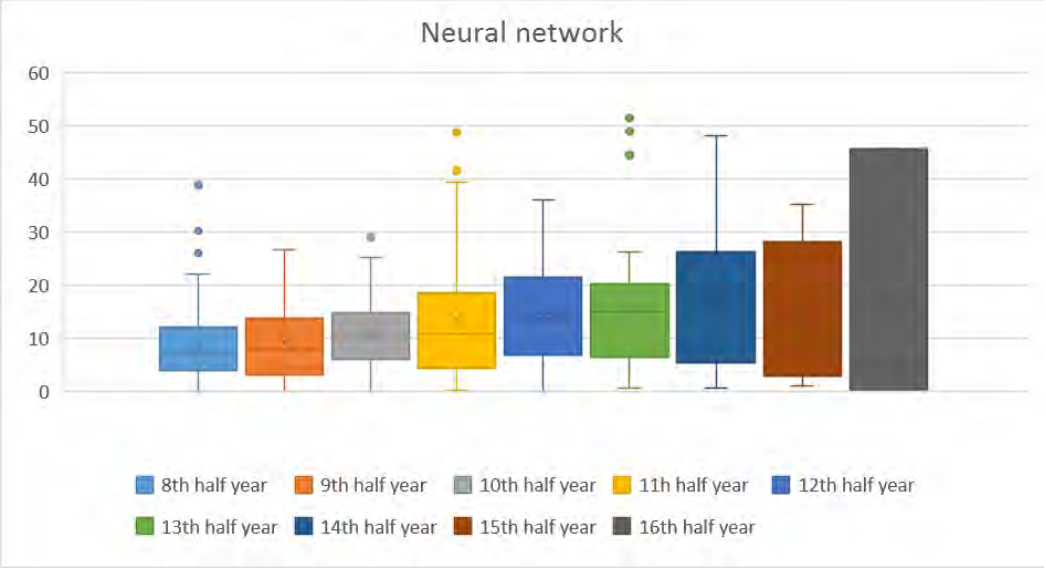

Figures 14. The frequency of the predicted values of the Neural network model

It can be seen that the artificial neural network is the model, among the others, which has the lowest RMSE values in long term prediction in the line No. 60.

5 CONCLUSION

On the one hand by analysing the deterioration processes the date of the required intervention (practices or restriction) became plan-able in an exact way. On the other hand it supports the creating of economical calculations, which is significant when decisions are taken between investment and maintenance. The reviewed procedure calculates this progress automatically with the modern computing devices.

6 ACKNOWLEDGEMENTS

The journey and the accommodation are granted by EFOP-3.6.1-16-2016-00017 “Internationalization, initiatives to establish a new source of researchers and graduates, and development of knowledge and technological transfer as instruments of intelligent specializations at Szechenyi University”

References

1. Fischer Sz. Comparison of railway track transition curves, Pollack Periodica, Vol. 4, No. 3, 2009, pp. 99−110.
2. Horvát F. The railway geometry progress from the beginning to nowadays (in Hungarian) Indóház, Vasúti Magazin, Vol. 9, No. 4, 2013, pp. 2−7.
3. Fischer Sz., Horvát F. Superstructure Stabilization of Ballast Bedded Railway Tracks with Geogrids, Hungarian Journal of Industrial Chemistry, Vol. 39, No. 1, 2011, pp. 101−106.
4. Šestáková J., Mečár M. Evaluation of track design and track geometry of the track with unconventional structure of railway superstructure, Procedia Engineering, Vol. 111, 2015, pp. 709–716.
5. Lestoille N., Soize C., Funfschilling C. Stochastic prediction of high-speed train dynamics to long-term evolution of track irregularities, Mechanics Research Communications, Vol. 75, 2016, pp. 29–39.
6. Vinkó Á. Monitoring and condition assessment of tramway track using in-service vehicle, Pollack Periodica, Vo. 11, No. 3, 2016, pp. 73–82.
7. Papp H., Liegner N. Investigation of internal forces in the rail due to the interaction of CWR tracks and steel railway bridges with ballasted track superstructure, Pollack Periodica, Vol. 11, No. 2, 2016, pp. 65–74.
8. Cárdenas-Galloa I., Sarmientoa C. A., Moralesa G. A., Bolivara M. A., Akhavan-Tabatabaeia R. An ensemble classifier to predict track geometry degradation, Reliability Engineering & System Safety, Vol. 161, 2017, pp. 53–60.
9. Andradea A. R., Teixeirab P. F. Statistical modeling of railway track geometry degradation using Hierarchical Bayesian models, Reliability Engineering & System Safety, Vol. 142, 2015, pp. 169–183.
10. Lestoille N., Soize C., Funfschilling C. Stochastic prediction of high-speed train dynamics to long-term evolution of track irregularities, Mechanics Research Communications, Vol. 75, 2016, pp. 29–39.
11. Lee J. S., Choi I. Y., Kim S. H., Moon D. S. Kinematic modeling of a track geometry using an unscented Kalman filter, Measurement, Vol. 94, 2016, pp. 707–716.

12. Vaszary P. The theory of the track degradation, in I. Mezei and F. Horváth (Eds.) Railway construction and maintenance, Part II., Magyar Államvasutak Ltd. Budapest, 1999.
13. Veit P. Rail steel grades in track, Europien Railway Preview, Vol. 19, No. 4, 2013, pp. 32−36.
14. Veit P. The sustainability of railways (in Hungarian), Sinek Világa, No. 2, 2015, pp. 2−7.
15. Fischer Sz. Investigation of inner shear resistance of geogrids built under granular protection layers and railway ballast, Nauka ta Progres Transportu, Vol. 59, No. 5, 2015, pp. 97−106.
16. Fischer Sz., Szatmári T. Investigation of the geogrid-granular soil combination layer with laboratory multi-level shear box test, 6th European Geosynthetics Congress, Eurogeo6, Ljubljana, Slovenia, 25-28 September 2016, pp. 439−448.
17. Esveld C. Modern railway track, Second Edition, MRT-Productions, Zaltbommel, Netherlands, 2001.
18. Fischer Sz. Traction Energy Consumption of Electric Locomotives and Electric Multiple Units at Speed Restrictions, Acta Technica Jaurinensis, Vol. 8, No. 3, 2015, pp. 240−256.
19. Y. Shafahi, P Masoudi, R Hakhamaneshi Track Degradation Prediction Models, Using Markov Chain, Artificial Neural and Neuro-Fuzzy Network https://www.researchgate.net/publication/268011897_Track_Degradation_Prediction_Models_Using_Markov_Chain_Artificial_Neural_and_Neuro-Fuzzy_Network

Tools and models for testing the capacity, level of functionality and performances for two-lane roundabout

Rodica Dorina Cadar, Gavril Hoda, Rozalia Melania Boitor and George Moga
Department of Railways, Roads and Bridges, Technical University of Cluj-Napoca, 72-74 Observatorului Street, Cluj-Napoca, Romania

Summary

Starting with the first decade of the XXth century, the first signs of interest appear for the arrangement of circular crossroads in America and in Europe as well. A history of the evolution of such types of arrangements is presented up until modern endorsements from our days.

This paper presents a case study for a two-lane roundabout, positioned in the Municipality of Cluj-Napoca, Romania. The capacity of circulation, the level of functionality and the performance of the crossroad are analysed by using the analytical and empirical models.

Moreover, the relationship between entry flow and the circulating flow is analysed, based on the observations made within 15 minutes intervals at the morning and the afternoon peaks of the traffic from the area

KEYWORDS: roundabout capacity, gap-acceptance theory, empirical theory.

1. INTRODUCTION

The concept of a roundabout was introduced both in America and Europe in the early 1900s, being developed over the course of 100 years, many countries and researchers from all over the world contributing to today's degree of knowledge.

The design of these intersections was based initially on heuristic models in which the experience and the logical rules of appreciation were used.

The first concept of roundabout arrangement was introduced in Paris (1907) by architect Eugene Alfred Henard.

According to [1] the first use of the British word, "roundabout" was adopted by the UK Transport Ministry. The US and Canadian names of this type of intersection are "traffic circle" or "rotary" in the case of generic geometric arrangements that offered long weaving sections. In the US, the first design guide for these types of fittings was published in 1945 by the American Association of State Highway Officials (AASHO).

After this period of beginning, the old concept of weaving capacities was replaced with the modern concept of the entry capacities. Designing modern roundabouts uses different principles. The key decision was to change circulating traffic priority and began designing roundabouts with smaller diameters to determine the driver to focus on critical access time and follow-up time.

According to [2], since 1966 the British have adopted the "priority-to-the-circle" rule or "YELD" sign at entries. Also, a number of measures have been adopted to reduce the number of accidents, for example, the deflection of traffic through the use of properly designed approaches and exits being one of the characteristics that distinguish the modern roundabout from a traffic circle. A feature of modern roundabouts is the high traffic capacity that is obtained by slightly widening the road at the entry points.

The results of UK researchers have been extended to many countries, including the US. According to [2], the first word of “roundabout” arrived in Michigan in 1995 and [3], the California Department of Transportation converted the Long Beach traffic circle to a modern roundabout in 1993. This conversion was the first of its kind in the US and involved modifications to all entries.

In our country, the roundabouts have seen a widespread development in the last decade both in urban and extra urban areas. The first rule adopted in Romania, dealing with the roundabout intersections [4] provides a method for calculating roundabout circulation capacity with one traffic lane on the ring road, taken from the HCM 2000 (Highway Capacity Manual 2000) [5], and two alternative methods. In order to calculate the circulation capacity of a roundabout with two lanes on the ring road, the Romanian norm wanted to adopt the formula provided by HCM 2010 (Highway Capacity Manual 2010) [6], but this was transcribed erroneously, being impossible to be applied in the norm Offered by the current Romanian standard. This study wants to provide the clarifications needed to apply this formula in good condition.

In Romania, prior to this regulation [4], [7] was used to for designing and analysing the geometry of the traffic capacity of these types of intersections.

At present, the most ambitious achievement in this field in our country is the first suspended roundabout in Romania, inaugurated in May 2016, on the Blejoi locality in Prahova county, at the exit from Ploiesti to Paulesti. The suspended roundabout, which has a unique architecture in Romania, is about one kilometre long and a height of about 7 meters.

2. ANALYSIS METHODS

According to [5], intersection analysis models generally fall into two categories. Empirical models rely on field data to develop relationships between geometric design features and performance measures such as capacity and delay. Analytical models are based on the concept of gap acceptance theory.

We chose for this paper to present five methods for roundabout circulation analysis that can be grouped into analytical models based on the principle of "gap acceptance theory" and empirically based on the "regression model" principle for the two-lane circulating model. The methods used for this research are described below (Case i … v). Each model equation is presented taking into account the general characteristics of each arm.

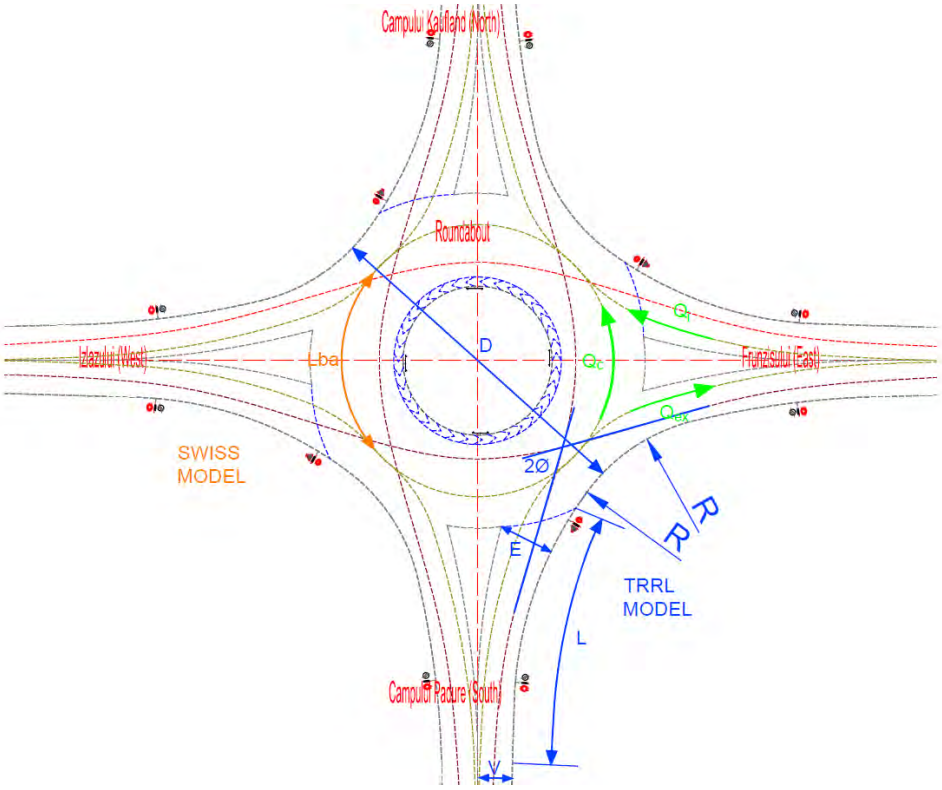

Figure 1. Geometric parameters

2.1. Case i

Case i - R.L.Kimber [8] with the Transport Research Laboratory (T.R.R.L.) development of a capacity model for roundabouts in the U.K. Prediction of entering flow or capacity was found to correlate to circulating flow and six geometric parameters:

- entry width (e)
- approach width (v)
- flare length (ℓ, ℓ' - the length over which local widening of the approach is developed)
- entry angle (φ)
- inscribed circle diameter (D)
- the radius of the curb at entry (r)

This formula ("11 Equation") yields a linear relationship between the capacity and the opposing flow. The capacity obtained when the opposing flow is null is named "geometric capacity".

$$Cap = F - f_c * Q_c \tag{11}$$

where:

- Cap is the entry flow or capacity in pcu/h;
- Q_c is the circulating flow in pcu/h;
- F is the y intercept
- f_c is the slope of the linear regression, are positive constants determined by the equations listed below.

$$k = 1 - 0.00347(\emptyset - 30) - 0.978((1/r) - 0.05)$$

$$F=303x_2$$

$$f_c = 0.210t_d(1 + 0.2x_2)$$

$$t_D = 1 + 0.5/(1 + \exp((D - 60)/10))$$

$$x_2 = v + (e - v)/(1 + 2S)$$

$$S = (e - v)/\ell = 1.6(e - v)/\ell$$

where e, v, ℓ, ℓ', D, r are in meters and φ in degrees.

2.2. Case ii

Case ii - The following equations (“12 Equation and13 Equation”) presented in the Swiss guide on roundabout design[9] are used to calculate the capacity of the roundabout.

$$Cap = k[1500 - (8/9) * Q_g] \tag{12}$$

$$Q_g = (\beta * Q_c + \alpha * Q_{ex}) \tag{13}$$

where:

- Cap is the entry flow or capacity in pcu/h;
- Q_c is the circulating flow in pcu/h;
- Q_{ex} is the flow leave the roundabout by the previous exit in pcu/h;
- α is a parameter reflecting the degree of vehicles in the entry disturbed by the vehicles exiting at the same branch, determined based on L_{ba} which is the distance between the diverging point at an exit and converging point at entry;
- κ in this case is 1.4 and it depends on the number of lanes in the entry and
- β is a parameter taking account of multi-lanes in the circulating carriageways, in this case, is 0.7.

These two models can be considered empirical, the other tools presented below belong to the group of analytical models based on the concept of gap acceptance theory.

2.3. Case iii

Case iii - The model presented in the German Highway Capacity Manual (HBS 2001) [10] uses gap acceptance theory with critical gap access (t_c) and follow-up headway (t_f) as the main parameters: number of circulating lanes (n_c), number of entry lanes (n_e) and minimum gap between succeeding circulating vehicles (t_{min}). The resulting capacity equation (“14 Equation”) is:

$$Cap = 3600\left(1 - \frac{t_{min}Q_c}{3600n_c}\right)^{n_c}\frac{n_e}{t_f}e^{-\frac{Q_c}{3600}\left(t_c - \frac{t_f}{2} - t_{min}\right)} \tag{14}$$

where

- Cap is the entry flow or capacity in pcu/h;
- Q_c is the circulating flow in pcu/h;
- critical gap (t_c)
- follow-up headway (t_f)
- minimum gap between succeeding circulating vehicles (t_{min}) are in seconds (s).

According to [11] it has come to this solution after considering many approaches, the proposed formula uses Tanner's [12] equation in a form which was adjusted to the necessities of roundabout analysis approach by Wu [13].

2.4. Case iv

Case iv – According to [6], equation (15) gives the capacity of the lanes, respectively, of a two-lane roundabout entry conflicted by two circulating lanes.

$$Cap_{right} = 1{,}130e^{(-0.7\times10^{-3})Q_c} \tag{15}$$

This model has been developed in the U.S. and it is recommended to be calibrated according to the area in which the roundabout is located and to familiarise users with these types of arrangements. Depending on this, its capacity may increase or decrease.

2.5. Case v

Case v – A simplified formula of eq. 14 in which t_{min} is considered = 0, known as Siegloch's capacity equation [14], has been adopted by the normative frame from Romania [4].

$$Cap = 3600 \cdot \frac{n_g}{t_f} \cdot e^{-\frac{Q_c}{3600}(t_c - \frac{t_f}{2})} \tag{16}$$

The last two equations are exponential and the parameters have the same meaning as in the first three formulas.

The extensive documentation on the models developed over time, used in the case study presented in the next chapter, is included in "Table 1". This synthetic analysis includes parameters of each model equation used in microsimulation to highlight the similarities and differences between them.

Table 1. Simulation case

Case	Capacity Equation for two-lane circulating model – Capacity entering flow rate Cap (pcu/h)	Model Equation parameters
Case i	Formula of T.R.R.L. - Empirical Regression Capacity Equation	Circulating flow rate Q_C (pcu/h) Geometric parameters
Case ii	Formula of CETUR	Circulating flow rate Q_C (pcu/h) Exit flow rate Q_{ex} (pcu/h) Distance between diverging point at exit and converging

		point at entry Number of entry lanes
Case iii	Formula of German Highway Capacity Manual (HBS 2001)	Circulating flow rate Q_C (pcu/h) Number of circulating lanes Number of entry lanes Follow-up headway Gap acceptance (critical gap and minimum gap)
Case iv	Formula of NCHRP 572 / HCM 2010	Circulating flow rate Q_C (pcu/h)
Case v	Siegloch's capacity equation	Circulating flow rate Q_C (pcu/h) Number of circulating lanes Follow-up headway Critical gap

One can notice that all models use the circulating flow rate as the input date within the circulating capacity calculation formula.

3. COMPARISONS ALTERNATIVE MODELING TOOLS

The roundabout hereinafter referred to as "Câmpului", is located in an urbanised area of Cluj-Napoca in Romania.

The intersection geometry analysed is explained in Table 2.

Table 2. Geometric parameters

Arm	Geometric parameters					
	e (m)	V (m)	l' (m)	D (m)	Φ (°)	r (m)
Arm 1-Frunzisului (East)	5.96	3.5	7.24	36	27.13	20
Arm 2-Campului Padure (South)	5.96	3.5	7.24	36	27.13	20
Arm 3-Izlazului (West)	5.96	3.5	7.24	37	27.13	20
Arm 4- Campului Kaufland (North)	5.97	3.5	7.19	38.26	38.26	20

The modeling was reported in all five cases to the same traffic data in "Table 3", during the peak period of the day set in the range (17.00-18.00), considering the critical gap (t_c= 4,1 s), follow-up headway (t_f = 2,9 s) and minimum gap between succeeding circulating vehicles (t_{min}= 2,1 s).

Table 3. Traffic data

	Entry flow rate Q_i (pcu/h)	Conflicting flow rate Q_C (pcu/h)	Exit flow rate Q_{ex} (pcu/h)	Entry lanes	Number of circulating lanes
Arm 1	602	987	824	2	2
Arm 2	1001	425	723	1	2
Arm 3	733	991	972	2	2
Arm 4	997	708	592	2	2

In this research, all models behaved similarly with the use of similar traffic data. A slight reserve of traffic capacity was highlighted in the first two cases.

Table 4. Level of service based on Degree of saturation only

		Capacity	Degree of saturation (V_i/Cap ratio)	Level of service
Case i	Arm 1	832.47	0.72	C
	Arm 2	1165.64	0.86	D
	Arm 3	831.70	0.88	D
	Arm 4	1000.08	1.00	E
Case ii	Arm 1	789.78	0.76	C
	Arm 2	369.80	2.71	F
	Arm 3	810.34	0.90	D
	Arm 4	566.64	1.76	F
Case iii	Arm 1	49.01	12.28	F
	Arm 2	295.70	3.39	F
	Arm 3	52.04	14.08	F
	Arm 4	67.46	14.78	F
Case iv	Arm 1	421.14	1.43	F
	Arm 2	738.76	1.35	F
	Arm 3	419.46	1.75	F
	Arm 4	556.67	1.79	F
Case v	Arm 1	536.68	1.12	F
	Arm 2	941.43	1.06	F
	Arm 3	534.54	1.37	E
	Arm 4	709.38	1.41	F

One of the questions that require a response as a result of this modelling is how the user behaves in the future. Do the following parameters change: gap acceptance (critical gap and minimum gap) and follow-up headway so that capability estimates are based on minimum, maximum, or average values? Clearly, there are several issues that require careful thinking to improve waiting times and provide a better

understanding of drivers over the prospects of exploiting these types of intersections that will lead to increased traffic and safety.

Data aggregation from the five approaches studied for the "Câmpului" roundabout allowed the determination of control delays for each arm and the determination of the intersection service level, depending on this parameter.

Table 5. Level of service based on Delay only

		Control delay (sec/veh)	Level of service for lane	Delay for the intersection (sec/veh)	Level of service for the intersection
Case i	Arm 1	18.99	B	44.88	D
	Arm 2	24.95	C		
	Arm 3	37.11	D		
	Arm 4	86.23	F		
Case ii	Arm 1	22.52	C	1362.18	F
	Arm 2	3102.46	F		
	Arm 3	43.95	D		
	Arm 4	1393.01	F		
Case iii	Arm 1	20468.54	F	17662.54	F
	Arm 2	4327.69	F		
	Arm 3	23700.78	F		
	Arm 4	24917.26	F		
Case iv	Arm 1	231.97	F	293.15	F
	Arm 2	186.44	F		
	Arm 3	368.94	F		
	Arm 4	381.51	F		
Case v	Arm 1	103.41	F	145.73	F
	Arm 2	68.14	F		
	Arm 3	200.79	F		
	Arm 4	208.68	F		

During this study, many problems have been identified that require further research, especially with regard to control delays where it has not really been proven that there is a related queue of this length to justify the values obtained from modelling. Even long queues tended to advance so there are questions about defining delays.

4. CONCLUSIONS

Given the significant traffic increase in Romania, the use of roundabouts has become one of the most attractive types of intersections in both urban and extra urban areas.

The implementation of this type of arrangement requires the choice of the most suitable instrument, calibrated according to the area in which the roundabout is located, the geometric elements of the arrangement and familiarization of the users with this type of intersection, for the calculation of the traffic capacity.

In chapter 2 we present five procedures for analysing roundabouts, introduces the unique characteristics of roundabout capacity and presents terminology specific to roundabouts.

Due to the in-depth analysis, we have been able to determine the transcription error, existing in the formula presented by the normative framework in Romania and we make suggestions, on this occasion, to remedy it.

Both models known in the literature: Regression models and Analytical models were described and then used as modelling tools in chapter 3 of the study for the "Câmpului" roundabout in Cluj-Napoca.

All models use the circulating flow rate as the input data within the circulating flow calculation formula. Slightly permissive results from the point of view of the circulation capacity were obtained with the empirical models. During this study, identified problem, especially with regard to control delays where it has not really been proven that there is a related queue of this length to justify the values obtained from modelling.

This research provides a scientific perspective regarding the optimal tool for calculating the circulation capacity of the roundabouts, but choosing the direction of the analysis is a complex decision that depends on several factors and needs to be well managed.

References

1. Weiqi W., Xiaokuan Y., *Research on Capacity of Roundabouts in Beijing*, 8th International Conference on Traffic and Transportation Studies (ICTTS) , Procedia - Social and Behavioral Sciences, Edited by Baohua Mao, Zongzhong Tian, Haijun Huang and Ziyou Gao, Volume 43, Pages 1-848, 2012.
2. Waddell E., *Evolution of roundabout technology: a history based literature review*, Compendium of Technical Papers, 67th annual meeting, Institute of Transportation Engineers, Boston, August 1997.
3. Gates T., Maki R., *Converting old traffic circles to modern roundabouts*: Michigan State University case study, Department of Civil and Environmental Engineering. East Lansing, MI: Michigan State University, 2000.

4. AND 600-2010, *Normativ pentru amenajarea intersecţiilor la nivel pe drumurile publice*, Buletinul Tehnic Rutier nr. 4 / 2010. (in Romanian).
5. *Highway Capacity Manual* 2000. Transportation Research Board, 2000.
6. *Highway Capacity Manual* 2010. Transportation Research Board, 2010.
7. *Norme tehnice privind intersecţiile giratorii la acelasi nivel pe drumurile din afara oraşelor*, Administraţia Naţională a Drumurilor, Centrul de Studii Rutiere şi Informatică, BOMACO. (in Romanian).
8. Kimber R. M., *The Traffic Capacity of Roundabouts. Laboratory Report* 942. Transport and Road Research Laboratory, Crowthorne, Berkshire, United Kingdom, 1980.
9. Bovy Ph. (ed.) (1991) *Guide Suisse des Giratoires*. Lausanne, Suisse, 1991.
10. FGSV. *Handbuch für die Bemessung von Straßenverkehrsanlagen* (German Highway Capacity Manual). Forschungsgesellschaft für Straßen- and Verkehrswesen (Hrsg.), No. 299. FGSV Verlag GmbH, Koln, Germany, 2001(in German).
11. Brilon, W. Roundabouts: *A State of the Art in Germany*. Presented at the National Roundabout Conference. Vail, Colorado. May 22-25, 2005.
12. Tanner, J.C., *The capacity of an uncontrolled intersection*. Biometrica, 54 (3 and 4), pp. 657 – 658, 1967.
13. Brilon, W.; Bondzio, L.; Wu, N., *Unsignalized Intersections in Germany - a State of the Art*, 2nd International Symposium for Unsignalized Intersections, Portland/Oregon, 1997.
14. Siegloch, W., *Die Leistungsermittlung an Knotenpunkten ohne Lichtsignalsteuerung* (Capacity of unsignalized intersections), Series Strassenbau und Strassenverkehrstechnik, No. 154, 1973.

"Computational Civil Engineering 2017", International Symposium
Iasi, Romania, May 26, 2017

Numerical Modelling of a Masonry Wall Strengthened with GFRP Strip

George Taranu
Department of Structural Mechanics, "Gheorghe Asachi" Technical University of Iasi, Iasi, 700050

Summary

This paper presents a study based on a comparison of multiple FEM analysis of a 604x240x115 mm masonry element subjected to out of plane bending. The behaviour of materials was changed in terms of stiffness to simulate the damaging effect. One strip of glass fibre reinforced polymer composite material was added at the bottom of masonry element. The results show the influence of the GFRP strip on the behaviour and the strength of the masonry. All the analyses were performed by ANSYS software.

KEYWORDS: GFRP strips, masonry wall, FEM

1. INTRODUCTION

The strengthening techniques of the masonry buildings have evolved continuously. Some of these are composite materials. These solutions have different requirements and different behaviour. Their advantages like lightweight or the application procedures make them favourite for some masonry buildings. After few experimental tests of multiple samples, a numerical model was necessary.

The study in the present paper shows ten numerical analyses. The objective was the understanding of the behaviour of a GFRP strengthened masonry element subjected to out of plane bending [1], [2], [3].

Seeing the stress or the displacement map distribution and their maximum values, in numerical modelling help future design scenarios. The approaching of the mortar layer stiffness is the key of FEM in this study because these layers are weaker than bricks in tension and the brick failure occurring due to mortar weakness.

2. MATERIALS AND NUMERICAL MODEL

For a more realistic modelling, all the components of the masonry and GFRP strip are solid parts. Each component is a unique block and simulates bricks, mortar layers and GFRP strip. Figure 1 presents the solid parts of the masonry beam,

which have four end supports and one GFRP strip at the bottom side. Figure 2 shows the finite element discretization and loading scheme.

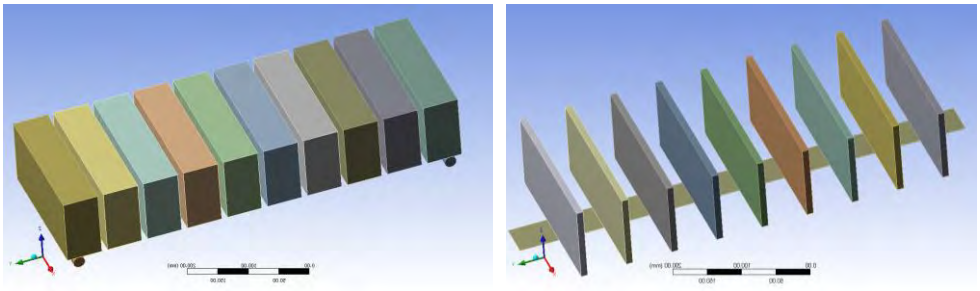

a b

Figure 1. The component parts of the masonry model:
a - bricks and end supports; b- mortar layers and GFRP strip

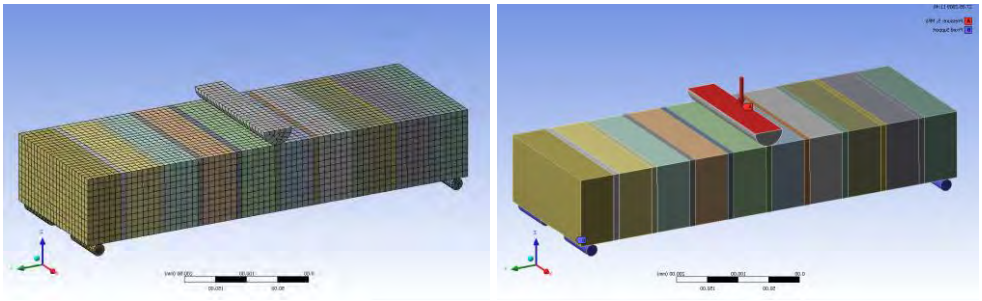

a b

Figure 2. a- finite elements discretization; b- loading scheme

Each of the numerical analysis uses material properties previously obtained from an experimental program. The mortar was labelled from Mortar 100%E to Mortar 5%E depending on the value of Young’s modulus, which was reduced in 10 steps with 10%. Table 1 presents all the mechanical properties of the materials used in analyses.

Table 1. Materials properties

	Young's modulus (MPa)	Poison coefficient	Density (kg/m³)	Tensile Strength (MPa)	Compressive Strength (MPa)
Mortar 100%E	10000	0.18	2100	-	8
Mortar 90%E	9000	0.18	2100	-	8
Mortar 80%E	8000	0.18	2100	-	8
Mortar 70%E	7000	0.18	2100	-	8
Mortar 60%E	6000	0.18	2100	-	8
Mortar 50%E	5000	0.18	2100	-	8
Mortar 40%E	4000	0.18	2100	-	8
Mortar 30%E	3000	0.18	2100	-	8
Mortar 20%E	2000	0.18	2100	-	8
Mortar 10%E	1000	0.18	2100	-	8
Mortar 5%E	500	0.18	2100	-	8
GFRP strip	77000	0.28	2600	1500	-
Brick	18000	0.20	1900	-	20

The decreasing of mortar stiffness simulate the real behaviour and damage which occur in mortar layers.

3. RESULTS AND DISCUSSION

After the performing of the analyses, records of the overall behaviour and systematic results show variation at the interface between GFRP strip and masonry model. In terms of stress and displacement map distribution, figure 3 presents the maximum principal stress and strain meanwhile figure 4 present maximum vertical displacement and interface behaviour. In this step, mortar stiffness has Young's modulus of 10000 MPa. The first analysis results show that the maximum principal stress has a value of 48 MPa and is a tensile stress. This occurs in GFRP strip. The maximum displacement is 0.43mm in the middle of the model. At the interface of strip and masonry, there are two types of behaviour sliding with yellow colour and sticking with orange colour. The orange colour is exactly on the bricks surfaces, which means that the adherence is better on the bricks than the mortar.

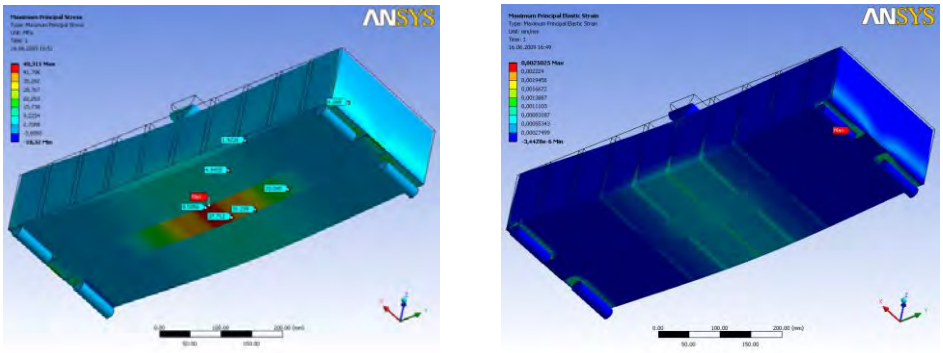

a b

Figure 3. First analysis results - E_m=10000 MPa:
a- maximum principal stress; b- maximum principal strain.

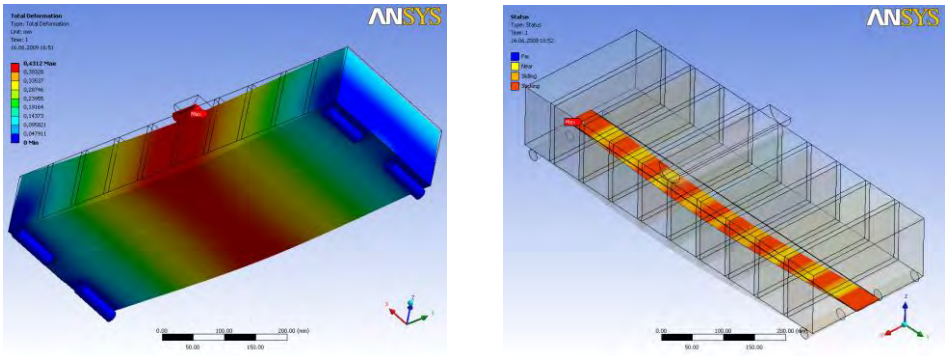

a b

Figure 4. First analysis’ results - E_m=10000 MPa:
a- maximum vertical displacements; b- interface status.

Figure 5.a show the frictional stress distribution map on the GFRP strip interface side. Their distribution has a maximum tensile value of 1.5 MPa at the ends and 0.75 MPa in the middle. Another result consists in the mortar central layer pressure, at the interface between mortar and brick. The compressive value is 10 MPa and the tensile value is 8.8 MPa.

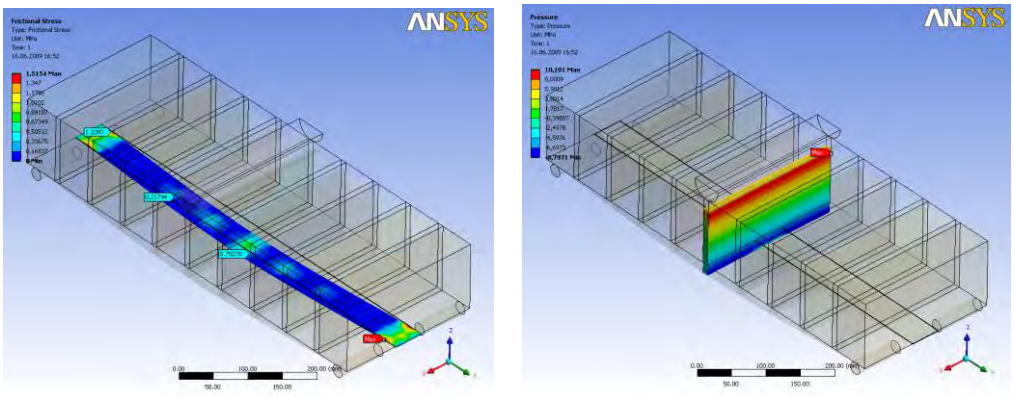

a b

Figure 5. First analysis' results - E_m=10000 MPa:
a- frictional stress distribution map; b- pressure on the mortar layer interface.

The reducing of the mortar stiffness almost ten times shows an increase of three times of the maximum value of maximum principal stress in the GFRP strip. In addition, the maximum principal strain occurs in the central mortar. Figure 6 shows their distribution map.

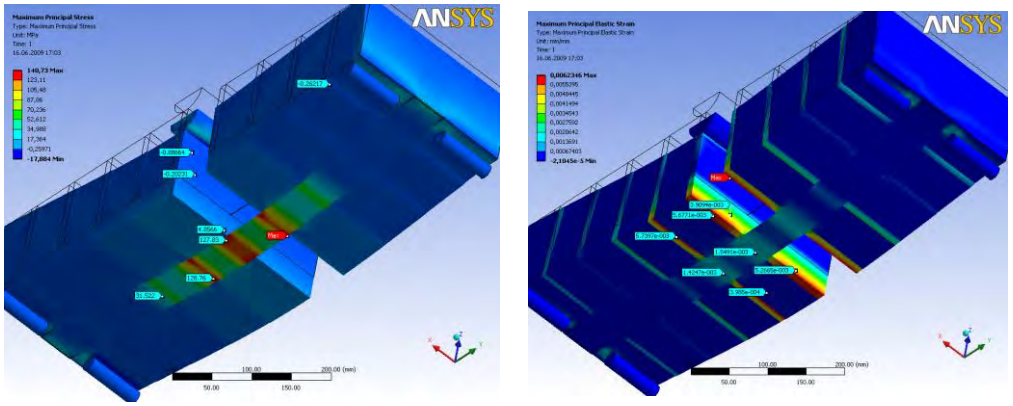

a b

Figure 6. The tenth analysis' results - E_m=1000 MPa:
a- maximum principal stress; b- maximum principal strain.

The frictional stress has an increase of 280% in the GFRP strip interface. In the same areas where the frictional stress are distributed the sliding distance occurs with a maximum value of 0.0001mm. Figure 7 presents the distribution map of these results.

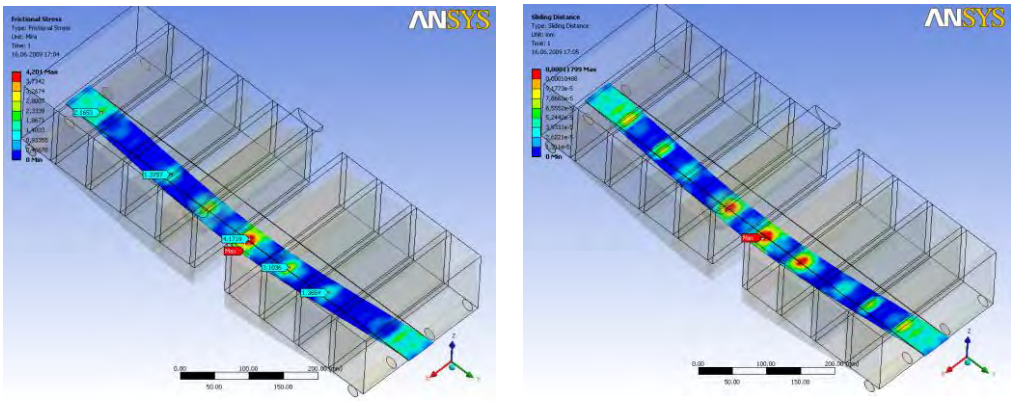

a b

Figure 6. The tenth analysis’ results - E_m=1000 MPa:
a- frictional stress distribution map; b- pressure on the mortar layer interface.

The variation of mortar stiffness was reported to the maximum principal stress and frictional stress. Figure 7 presents these variation curves.

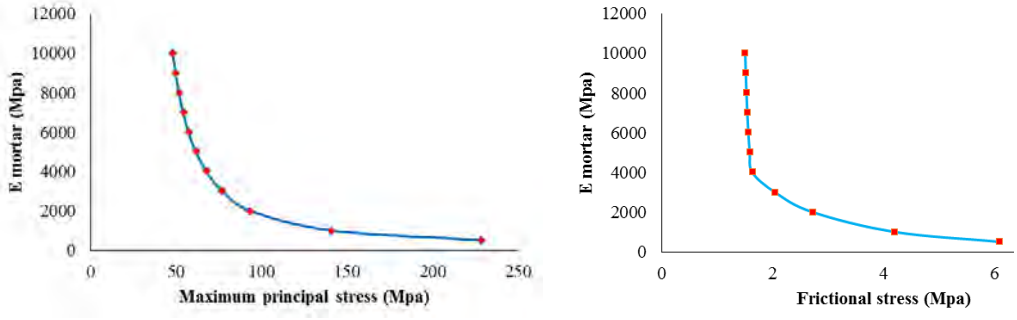

a b

Figure 7. The curve variation of stiffness reported to maximum principal stress and frictional stress at the GFRP strip interface

From these curves, it can be observed that the GFRP strip has an important role in the strength of the masonry wall element. This significantly occurs when the mortar was damaged and no tensile strength is present between bricks and mortar layers. The entire tensile stress is present in GFRP strip and in the interface area. The increasing of the maxim principal stress in the GFRP strip begins immediately, which means that the influence of strengthening is compatible with masonry. The vertical displacements are not significantly reduced by the presence of the strip, as was seen from the numerical analyses.

4. CONCLUSIONS

The strengthening techniques for masonry walls is a permanent research subject due to massive masonry buildings and their importance. The preservation of these buildings which, sometimes are historical monuments, is important for each nation, especially for those, which have seismic areas. The use of GFRP composite materials is conducted by the strength, efficiency, lightness and minimum structural intervention.

This study presents an incremental analysis of the influence of a GFRP strip on a masonry element. These results show a good structural behaviour considering the worst scenario when the wall is subjected to out of plane bending and the mortar layer lost the tensile strength capacity. The adherence between bricks and GFRP strip is almost a bonded contact and the frictional stress, which occurs, can be taken by the adhesive strength. These results can be used for future design work in a masonry building rehabilitation project.

References

1. Taranu, G., Masonry arches and vaults composite materials strengthening at historical buildings, PhD Thesis, T.U. Iasi (2009)
2. Lourenço, P.B.; Rots J.G., A multi-surface interface model for the analysis of masonry structures. J. Eng. Mech., ASCE, 123(7), pp. 660-668, 1997.
3. Giordano, A., Mele, E., De Luca., A., Modelling of historical masonry structures: comparison of different approaches trough a case study, Engineering Structures 24 (2002) 1057-1069.

Numerical Investigations of Stresses and Damage Distributions on the Layers of a Sandwich Beam with Composite Laminated Faces Subjected to Bending

Iuliana Dupir (Hudișteanu), Nicolae Țăranu, Cristina Vlădoiu and Dragoș Ungureanu
Department of Civil and Industrial Engineering, Technical University "Gheorghe Asachi", Iasi, Zip code 700050, Romania

Summary

The sandwich elements are multi-layered structures made of two strong and stiff thin exterior faces, bonded by a lightweight thick core, such that the structural properties of the entire assembly are superior to those of the separate components.

The composite laminates are build up by stacking two or more unidirectional fibre reinforced composite laminas, with different or same fibre orientation angles, thicknesses and materials constituents.

The design flexibility of composite structures is a great challenge since the advantage of orienting the composite laminas in the needed directions leads to improved structural properties of the whole assembly.

The paper presents the flexural response of a sandwich beam with exterior layers made of laminated composites with different fibre orientations. The results are presented in terms of distribution of stresses on the layers of the composite sandwich beam. The failure and the damage occurrence on the plies of the laminated facings are investigated according to the maximum strain failure criterion and to the modified Puck failure criterion.

KEYWORDS: sandwich beam, composite laminate facings, stresses distributions, fibre orientations.

1. INTRODUCTION

When compared to the traditional materials, composites have improved performances, such as high stiffness and strength, low density, high fatigue endurance, corrosion and wear resistance, environmental stability, tailoring advantages and adaptability to the intended function and requirements of the structure [1].

The unidirectional composite lamina is the simplest element of the composite material, formed by unidirectional fibres embedded in a matrix [2]. Moreover, a

lamina can be considered an elementary layer of a composite laminate, which is made by stacking two or more plies, with different fibre orientation angles. The most important aspect of using composite laminates is the possibility of tailoring the stiffness and strength in the needed direction, through the suitable selection of the fibre orientations and stacking sequences [3].

The simplest types of sandwich elements are those which are composed of two strong and stiff thin exterior layers, separated by a low density continuous thick core [4-6]. The main functions of the faces of the sandwich beam are to take over the direct stresses, to provide the bending stiffness of the structure and to ensure the general stability of the element. The core should be stiff enough in order to provide the shear strength and to ensure that the exterior layers do not slide over each other [7-8]. Combining the advantages of the sandwich beams and of the composite laminates respectively, an improved element can be achieved, such as a sandwich beam with composite laminated faces.

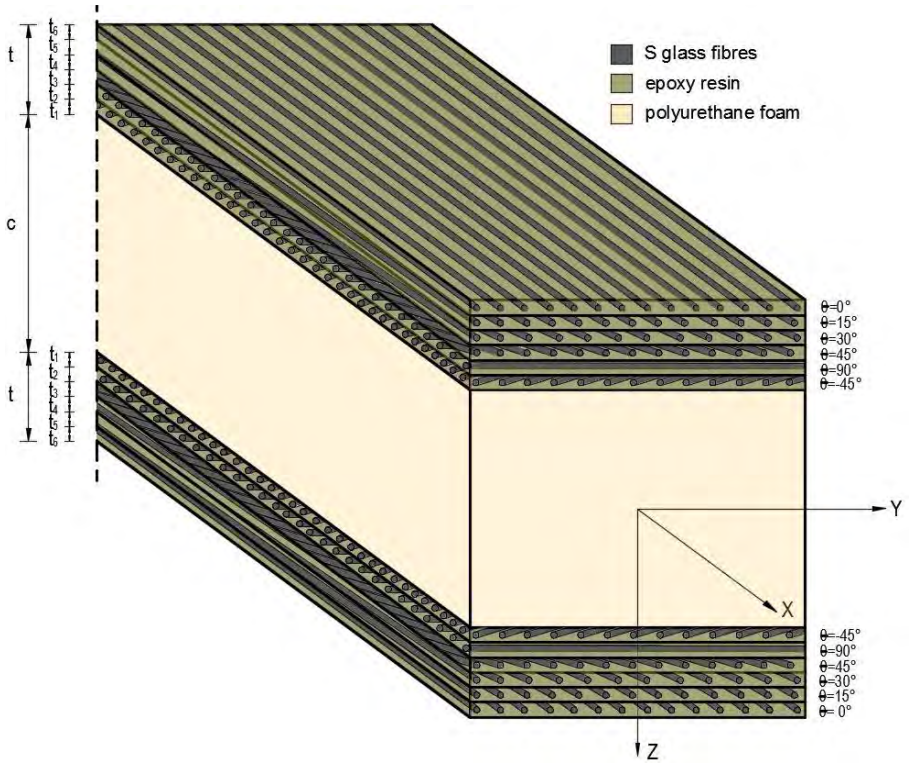

Figure 1. Sandwich beam with laminated composite facings

The present paper is focused on the study of the stresses distributions on the layers of a continuous core sandwich beam with exterior layers made of laminated composites, subjected to bending. The analysis is based on a symmetrically

balanced composite laminate with the following stacking sequence $[0/15/30/45/90/-45]_s$, which has been previously proven [9] to have a gradual failure when subjected to uniaxial loads, due to the different fibres orientation angles. A continuous core is disposed of as an intermediate layer between the laminated composite facings, such that the sandwich effect can be achieved, as shown in Fig. 1.

Each layer of the composite laminates has 0.25 mm thickness and it is made of S-glass fibres embedded in an epoxy resin, while the core is realised of polyurethane foam, with a thickness of 60 mm. The in-plane dimensions of the sandwich beam have been selected as 100 mm wide and 400 mm long, according to ASTM C393 [8, 10]. The total height of the analysed layered element has resulted equal to 63 mm. The simply supported beam is subjected to bending produced by an equivalent load of 45 kN, uniformly distributed on the upper face of the sandwich element.

The mechanical properties of the unidirectional lamina and the elastic modulus of the polyurethane foam core are presented in Table 1.

Table 1. Mechanical properties of the materials [11]

	S glass_epoxy lamina				polyurethane foam
Stiffness properties	Longitudinal modulus	Transverse modulus	Shear modulus	Poisson's ratio	Elastic modulus
	E_1 [GPa]	E_2 [GPa]	G_{12} [GPa]	ν_{12}	E [MPa]
	52.94	13.93	5.07	0.292	37.9
	S glass_epoxy lamina				
Strength properties	Longitudinal tensile strength	Longitudinal compressive strength	Transverse tensile strength	Transverse compressive strength	In-plane shear strength
	f_{Lt} [MPa]	f_{Lc} [MPa]	f_{Tt} [MPa]	f_{Tc} [MPa]	F_{LTs} [MPa]
	2836	1122	62.53	125.1	58.29

The main purpose of the paper is to evaluate the damage localisations on the layers of the sandwich facings, which have different orientation angles. The plies sequence failure predictions of the composite exterior layers subjected to bending can be considered a serious concern.

2. FAILURE CRITERIA APPLIED IN THIS STUDY

The investigation of the failure index in each layer of the laminated composite is a necessity in order to verify that the plies contribute to the overall stiffness of the sandwich element or they have to be discounted from the calculation of the

assembled stiffness matrix of the laminate, at a given loading. Different failure modes can be associated with composite elements, such as fibres rupture (tension of the fibres), fibres kinking (compression of the fibres), matrix cracking (tension of the matrix), matrix crushing (compression of the matrix) or interface delamination [12, 13].

The failure criteria selected in the study are the maximum strain failure criterion and the modified Puck failure criterion.

2.1. Maximum strain failure criterion

According to the maximum strain failure criterion, the failure occurs in the composite lamina when the strains along any principal material directions exceed the corresponding ultimate strains, as follows [14]:

$$\begin{aligned} -\varepsilon_{Lc} < \varepsilon_1 < \varepsilon_{Lt} \\ -\varepsilon_{Tc} < \varepsilon_2 < \varepsilon_{Tt} \\ -\gamma_{LTf} < \gamma_{12} < \gamma_{LTf} \end{aligned} \tag{1}$$

where:

$\varepsilon_{Lt}, \varepsilon_{Lc}$ - the ultimate tensile and compressive strains in the longitudinal direction;
ε_{Tt}, ε_{Tc} - the ultimate tensile and compressive strains in the transverse direction;
γ_{LTf} represent the ultimate in-plane shear strain.

The strains along the principal material directions ($\varepsilon_1, \varepsilon_2$, γ_{12}), which corresponds to a stress σ_x, can be determined according to Eq. (2):

$$\begin{aligned} \varepsilon_1 &= \frac{\sigma_x}{E_1}\left(\cos^2\theta - \nu_{12}\sin^2\theta\right) \\ \varepsilon_2 &= \frac{\sigma_x}{E_2}\left(\sin^2\theta - \nu_{21}\cos^2\theta\right) \\ \gamma_{12} &= \frac{\sigma_x}{G_{12}}\sin\theta\cos\theta \end{aligned} \tag{2}$$

where:
θ is the fibre orientation angle;
E_1, E_2 and G_{12} represent the elastic engineering constants along the principal material axes.

For the maximum strain failure criterion, the stresses interaction is not considered, except for the effect of Poisson's coefficient.

This failure criterion identifies three types of possible failure modes, such as longitudinal failure, transverse failure and shear failure.

2.2. Puck failure criterion

The greatest advantage of using Puck failure criteria leads to the distinguish between fibre failure and matrix failure.

2.2.1. Fibre Failure

The failure in the fibre direction is evaluated similar with the maximum stress failure criterion (Eq. 3a) or according to the maximum strain failure criterion, as it was previously presented (Eq. 3b):

$$-\sigma_{Lc} < \sigma_1 < \sigma_{Lt} \tag{3a}$$

or

$$-\varepsilon_{Lc} < \varepsilon_1 < \varepsilon_{Lt} \tag{3b}$$

where

$\sigma_{Lc} = f_{Lc}$,

$\sigma_{Lt} = f_{Lt}$ and

σ_1 is stress in the fibre direction.

2.2.2.a Matrix Failure (Simple Puck failure criterion)

According to the simple Puck failure criterion, the failure occurs in the matrix when the left-hand side of the Eq. (4) reaches 1, as follows [15]:

$$\left(\frac{\sigma_2}{f_T}\right)^2 + \left(\frac{\tau_{12}}{f_{LTs}}\right)^2 = 1 \tag{4}$$

where σ_2 and τ_{12} are the in-plane stresses along the principal material directions, f_T refers to both compressive f_{Tc} and tensile f_{Tt} failure stresses, depending on the stress state, and f_{LTs} represents the in-plane shear strength.

2.2.2.b Matrix Failure (Modified Puck failure criterion)

The modified Puck failure criterion is different from the simple Puck formulation, only in case of matrix failure. An improvement of the relation criterion consists in the simultaneous implication of both compression and tensile stresses [15]:

$$\frac{\sigma_2^2}{f_{Tt} \cdot f_{Tc}} + \frac{\tau_{12}^2}{f_{LTs}^2} + \left(\frac{1}{f_{Tt}} + \frac{1}{f_{Tc}} \right) \cdot \sigma_2 = 1 \tag{5}$$

For the failure analysis performed in the numerical modelling, the modified Puck criterion was considered.

3. NUMERICAL MODELLING

The flexural response of the composite sandwich beam is carried out in ANSYS Composite Prep/Post, in order to define the stacking sequence of the laminated facings and of the sandwich element, respectively. Moreover, the results can be visualised in terms of plies groups, depending on the fibres orientation angles.

3.1. Failure index evaluation

The evaluation of the failure index was carried out for each layer of the laminated composite facing, with respect to both failure criteria. The distributions of the failure index for the inferior laminate composite face are presented in Fig. 2 and Fig. 3.

A failure index greater than 1 indicates that the breakage of the composite lamina has occurred. According to the results obtained by maximum strain criteria, the shear failure occurs in the plies with the fibre orientation angles of 15°, 30° and 45°, while the ply 5 (90°) fails due to transverse stresses. Moreover, the failure of the layer with 45° fibres orientation is caused by both shear and transverse stresses.

The critical failure mode that has occurred according to Puck criterion is caused by the failure of the matrix. However, the fibres orientation angles have a major influence on the distribution of principal stresses.

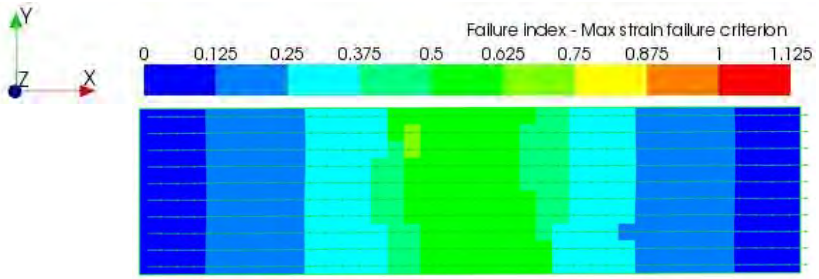

a) ply 1, 0° fibre orientation

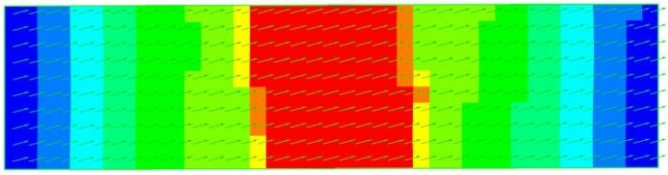

b) ply 2, 15° fibre orientation

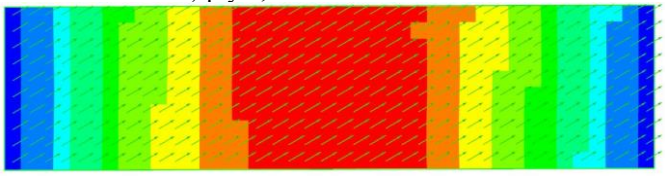

c) ply 3, 30° fibre orientation

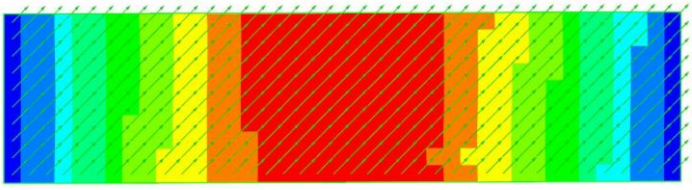

d) ply 4, 45° fibre orientation

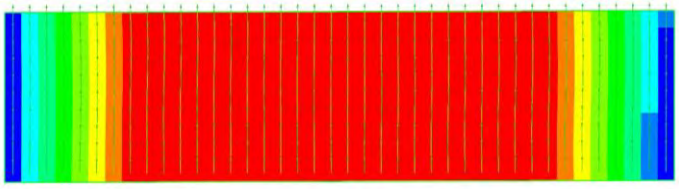

e) ply 5, 90° fibre orientation

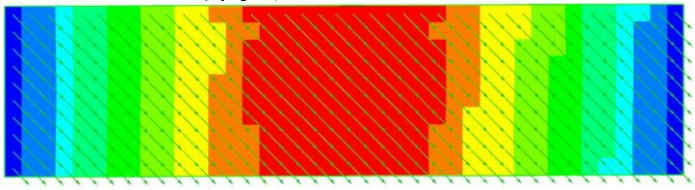

f) ply 6, -45° fibre orientation

Figure 2 Failure index on the inferior facing layers, according to maximum strain failure criterion

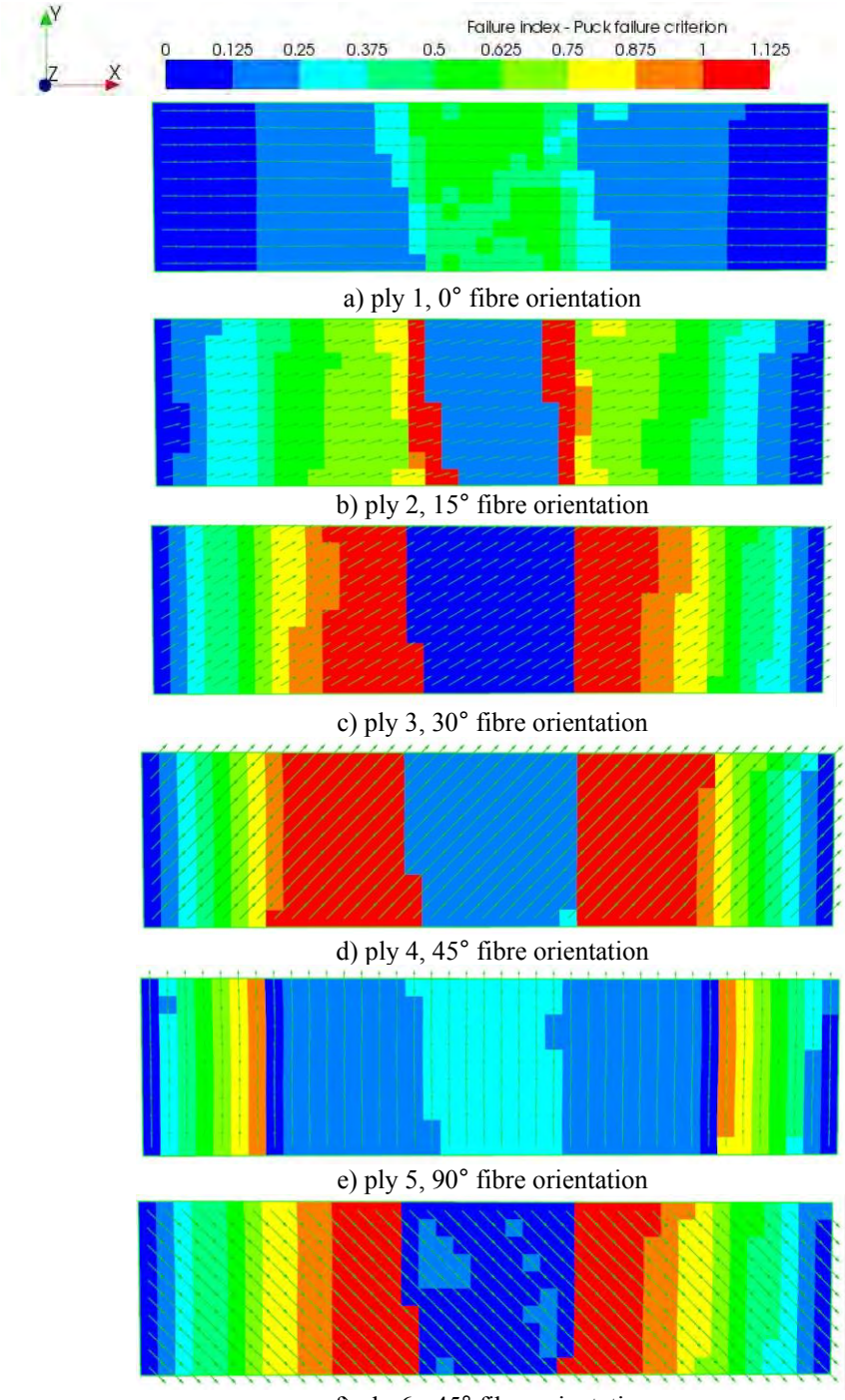

a) ply 1, 0° fibre orientation

b) ply 2, 15° fibre orientation

c) ply 3, 30° fibre orientation

d) ply 4, 45° fibre orientation

e) ply 5, 90° fibre orientation

f) ply 6, -45° fibre orientation

Figure 3 Failure index on the inferior face layers, according to Puck failure criterion

3.2. Direct stresses distribution

The distribution of the direct stresses of the sandwich beam is illustrated in Fig. 4, both for the inferior facing made of multi-layered composite and for the core of the sandwich beam.

The influence of the fibre orientation angles on the variation of direct stresses of the composite laminate facing can be noticed according to the stresses distribution reflected in each layer with a different orientation.

According to the analogy between the sandwich beam and a double T beam, the obtained results confirmed that the exterior layers have to withstand the maximum direct stresses, while the normal stresses in the core are negligible.

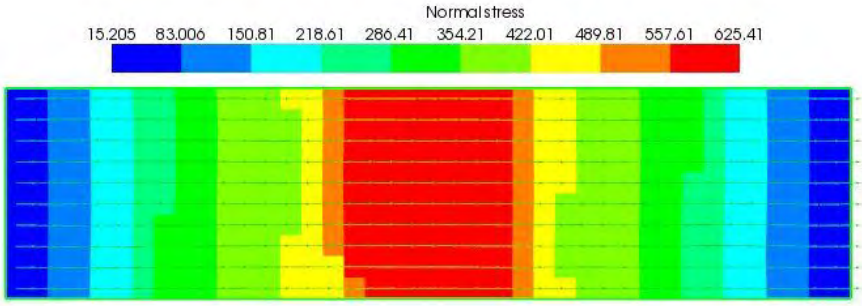

a) ply 1, 0° fibre orientation

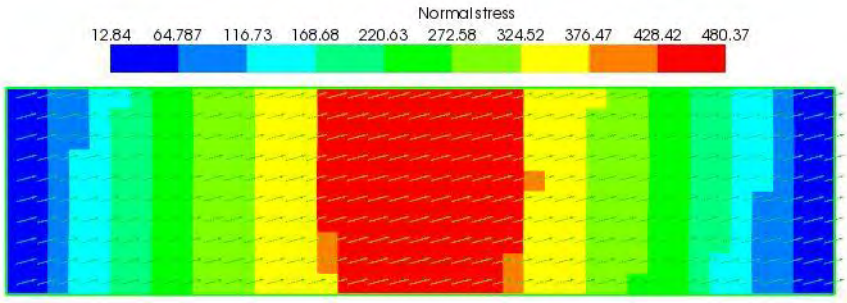

b) ply 2, 15° fibre orientation

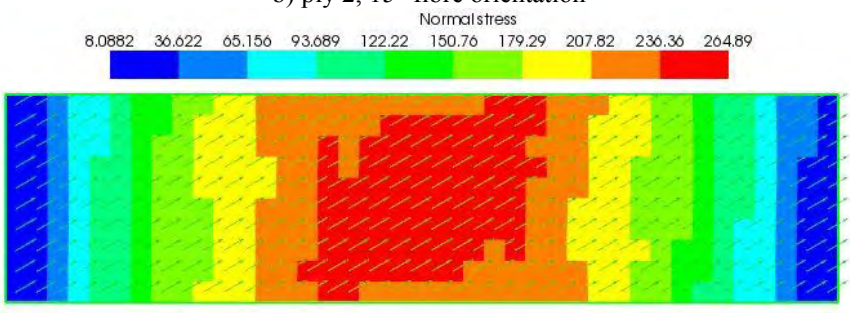

c) ply 3, 30° fibre orientation

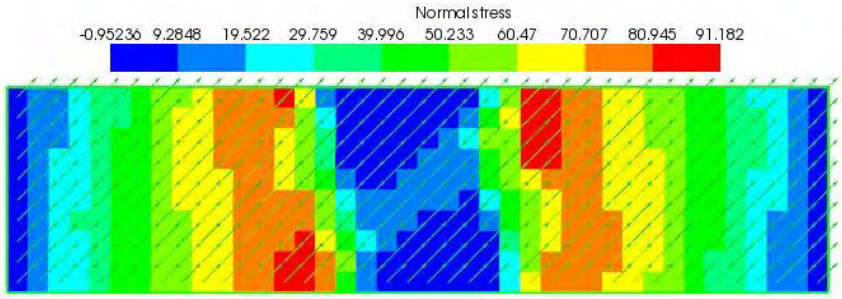

d) ply 4, 45° fibre orientation

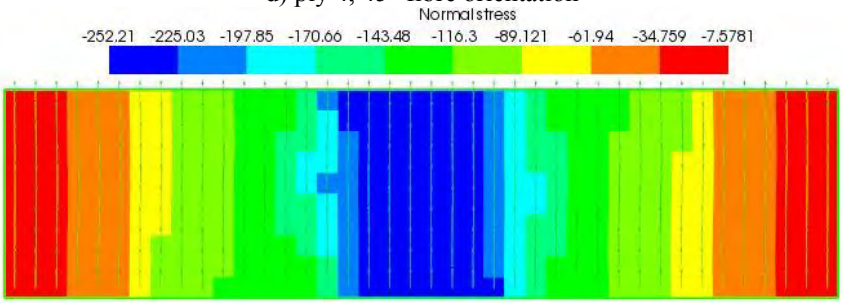

e) ply 5, 90° fibre orientation

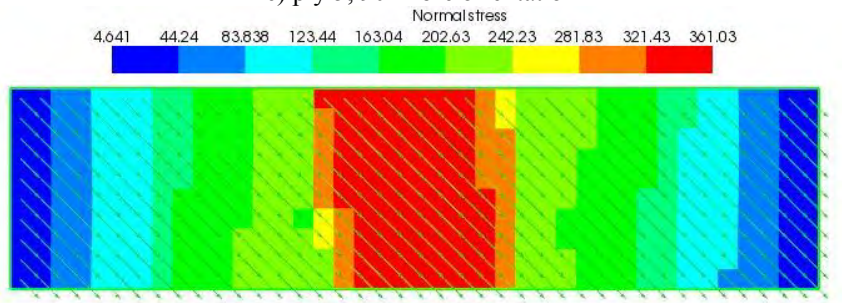

f) ply 6, -45° fibre orientation

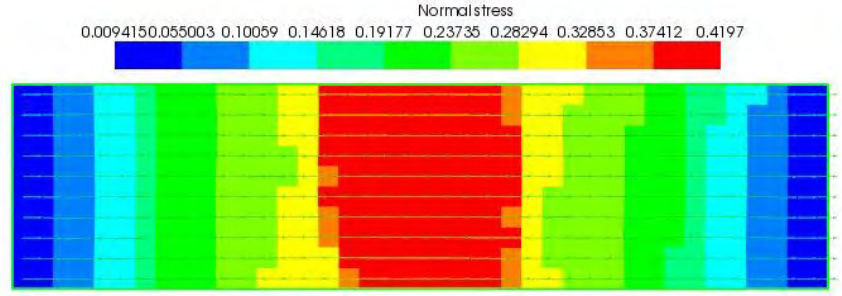

g) core layer

Figure 4 Normal stresses distributions on the layers of the sandwich beam

3.3. Damage identification

The identification and progression of damages are generally performed based on failure criteria and a damage evolution law. The progressive failure analysis carried out in this paper is based on both proposed failure criteria. Moreover, the considered damage evolution method is the material property degradation procedure. The selected coefficient of stiffness degradation is 0.9, which means that the composite material can be degraded up to 90%.

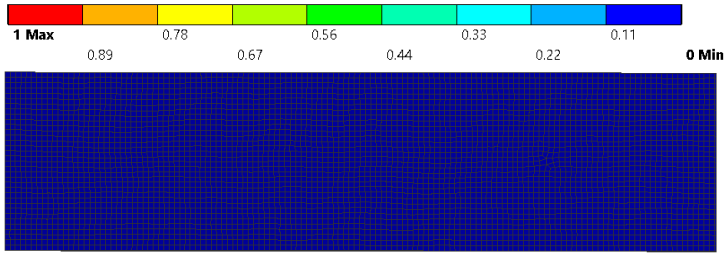

a) ply 1, 0° fibre orientation

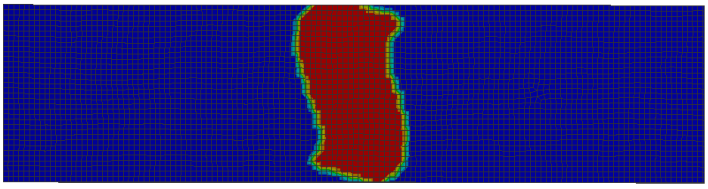

b) ply 2, 15° fibre orientation

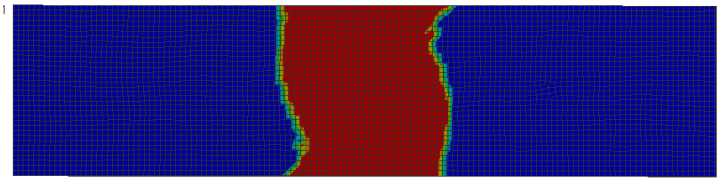

c) ply 3, 30° fibre orientation

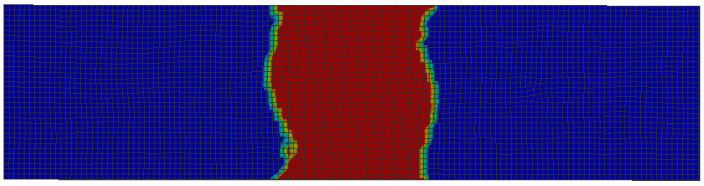

d) ply 4, 45° fibre orientation

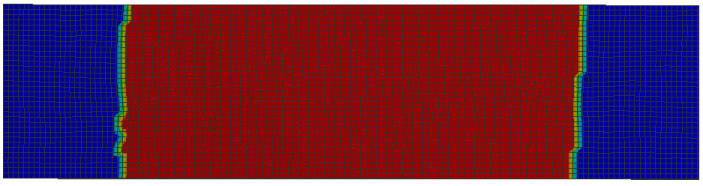

e) ply 5, 90° fibre orientation

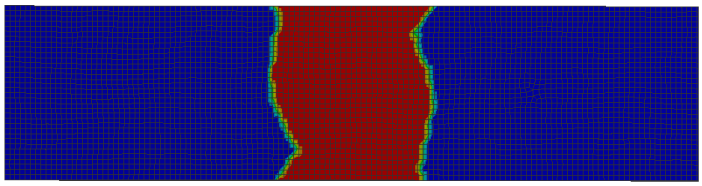

f) ply 6, -45° fibre orientation

Figure 6 Damage distributions on the layers of the sandwich beam according to maximum strain failure criterion

Figs. 6-7 show the damage distributions on the laminated composite facing with layers of different fibre orientations, where *0* means undamaged and *1* is completely damaged.

The most affected layers in the composite laminate facings are those with the fibre orientation of 90º because the transverse properties of the unidirectional reinforced laminas are much lower compared to the longitudinal ones. Reversely, the ply 1 (with 0° fibre orientation angle) is undamaged and it is the layer which withstands the highest stresses up to failure.

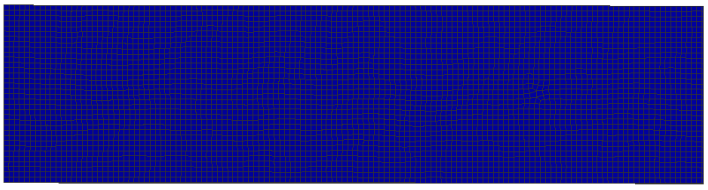

a) ply 1, 0° fibre orientation

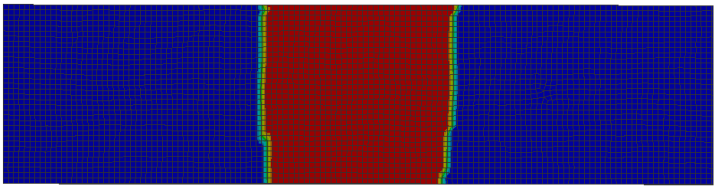

b) ply 2, 15° fibre orientation

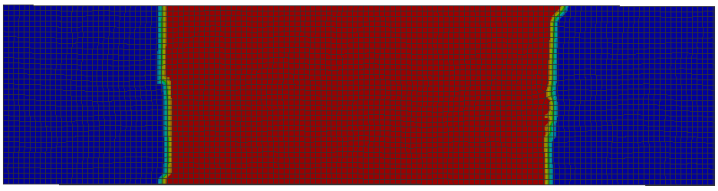

c) ply 3, 30° fibre orientation

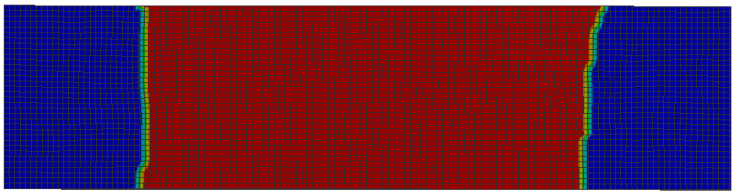

d) ply 4, 45° fibre orientation

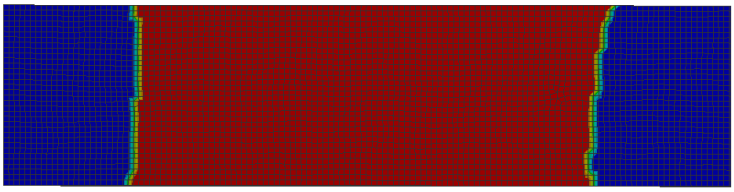

e) ply 5, 90° fibre orientation

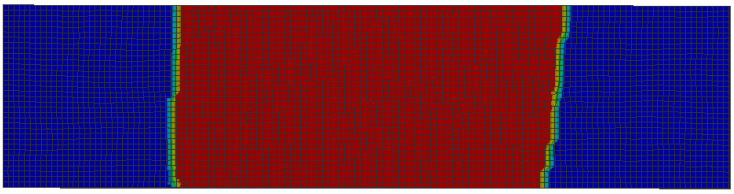

f) ply 6, -45° fibre orientation

Figure 7 Damage distributions on the layers of the sandwich beam according to Puck failure criterion

The comparison of the analysed failure criteria leads to the conclusion that the Puck failure criterion is more restrictive than the maximum strain condition since largest areas are affected according to Puck failure criterion.

4. CONCLUSIONS

A numerical study was performed in this paper, in order to investigate the flexural response of a sandwich beam with multi-layered composite facings. The direct stresses distributions were evaluated on the exterior layers and core, respectively. The failure index and the damages occurrence were identified on each layer of the composite laminate. Two failure criteria, namely the maximum strain criterion and Puck failure criterion were selected to establish the damage evolution law,

The results confirmed the analogy of the sandwich beam with an I beam and lead to significant direct stresses in the faces compared to those in the core. Moreover, the progressive failure of the balanced laminate facings is caused due to the different fibres orientation angles of the laminas. The damages evaluated with maximum strain failure criteria were caused by the transverse and shear failure,

while in the case of the Puck failure criteria, the damages occur due to the failure of the matrix.

References

1. Daniel, I.M., Ishai, O., *Engineering mechanics of composite materials*. *Second Edition*, Oxford University Press, 2006.
2. Vasiliev. V.V., Morozov E., *Advanced Mechanics of Composite Materials and Structural Elements, Third Edition*, Elsevier, 2013.
3. Hudișteanu, I., Țăranu, N., Ențuc, I.-S., Maxineasa, S.G., *Comparative analysis of the engineering constants of composite laminates*, Rev Rom Mat, 46(2), 232-241, 2016.
4. Țăranu, N., *Elemente portante din materiale plastice*, PhD thesis, Institutul Politehnic, Iași, 1978.
5. Zenkert, D., *An Introduction to Sandwich Construction*, Chameleon Press Ltd., London, United Kingdom, 1995.
6. Davies, J.M., *Lightweight Sandwich Construction*, Blackwell Science, London, 2001.
7. Allen, H., *Analysis and design of structural sandwich panels*, Pergamon Press, Oxford, 1969.
8. Marta C. L. *Optimizarea multicriterială a elementelor de închidere pentru construcţii industriale*, PhD thesis, Iaşi, 2007.
9. Dupir (Hudișteanu), I., Țăranu, N., Lupăşteanu,V., Ungureanu, D., *Comparative analysis of first ply failure and progressive failure for symmetric composite laminates*, XVI International Scientific Conference VSU'2016, II 134-139, 2016.
10. ASTM C393/C393M-16, *Standard Test Method for Core Shear Properties of Sandwich Constructions by Beam Flexure,* ASTM International, West Conshohocken, PA, 2016 .
11. Hudișteanu, I., Țăranu, N., Isopescu, D.N., Bejan, L., Axinte, A., Ungureanu, D., *Improving the mechanical properties of composite laminates through the suitable selection of the corresponding materials and configurations*, Rev Rom Mat, 47(2), accepted for publication, 2017.
12. Barbero, E.J., *Introduction to Composite Materials Design. Second edition*, CRC Press, Taylor and Francis Group, 2011.
13. Doughett, A., Asnarez, P., *Composite Laminates: Properties, Performance and Applications*, Materials Science and Technologies Series, Nova Science Publishers, Inc., New York, 2010.
14. Țăranu, N., Bejan, L., Cozmanciuc, R., Hohan, R., *Materiale şi elemente compozite I. Prelegeri şi aplicaţii*, Ed. Politehnium, Iaşi, 2013.
15. ANSYS® Workbench & ANSYS® Composite Prep/Post, User manual, ANSYS, Inc.

Influence of spew fillets geometry on the bond strength of adhesively bonded FRP composite elements

Dragoș Ungureanu[1], Nicolae Țăranu[2], Vlad Lupășteanu[3]
and Iuliana Dupir (Hudișteanu)[4]
Department of Civil and Industrial Engineering, Technical University "Gheorghe Asachi", Iași, Zip code 700050, Romania

Summary

The adhesive bonding is a suitable joining technique for structural assemblies made of composite materials. Adhesive bonding of fibre reinforced polymer (FRP) composite elements is utilised in several applications, including surface repairing for various composite materials, strengthening/retrofitting techniques and, as a sustainable alternative/replacement, when mechanical fastening methods are not suitable.

This paper focuses on some specific aspects related to the influence of stress reduction methods using various spew fillets on the structural response of adhesively bonded FRP composite elements. Also, this paper presents the influence of the adhesive spew fillet geometry on the peak values and on the distributions of the shear and the normal stresses in adhesively bonded FRP composite members.

KEYWORDS: FRP composites, adhesive bonding; adhesive spew fillets, numerical analysis.

1. INTRODUCTION

Nowadays, fibre reinforced polymer (FRP) composite elements represent a feasible alternative to structural elements made of traditional materials (*i.e.* concrete, steel, wood, aluminium) [1], offering substantial advantages in terms of high mechanical strengths, low weight, tailorability of properties and corrosion resistance [2]. For some particular applications, connections between different FRP elements are required in order to design and construct complex structural assemblies. Thus, the designers must select from several alternatives ranging from mechanical connections (using screws, bolts or rivets) to adhesive bonding [3].

The main disadvantage of mechanical connections refers to the necessity of drilling the FRP composite members that are being assembled which usually leads to discontinuities in the internal reinforcing fibres and significant stress concentrations [4]. The adhesively bonded connections are more suitable for FRP composites materials since the stress transfer through the elements is more

uniform. However, stress concentrations may still arise in FRP adhesively bonded joints, when the thicknesses of the adhesive and the adherents change and due to the differences of the elastic moduli [5].

The most common configuration for FRP adhesively bonded connections subjected to tensile forces is the single lap joint (SLJ). The distributions of the shear and normal stresses in SLJs are influenced by two critical features [6]. The first one refers to the offset of the adherents which produces a bending moment in the joint, adding the corresponding peeling stress component. The second important feature of SLJs relates to the fact that the stresses distributions in the lap are not constant along the bond length since the peak values concentrate at the ends of the overlap.

The peak values of the shear stresses and the normal (peeling) stresses can be diminished by the presence of an overflow of the adhesive at the ends of the overlap region. The spew fillet is defined as the fraction of the adhesive that is squeezed from the overlap ends as the two FRP composite elements are joined. Thus, a smooth transition in bond geometry significantly increases the joint strength. Many investigations have been conducted in order to identify the effect of shaping the edges of the adhesive layer (*i.e* chamfering, rounding, grading) upon the stress state in the adhesively bonded joints [7, 8, 9, 10, 11]. Based on these studies, it has been concluded that the spew fillet shaping is one of the most suitable techniques for reducing the peak values of stresses in FRP adhesively bonded connections.

The main objective of this study is to numerically investigate and compare the stresses distributions for several configurations of SLJs composed of FRP composite elements. All the specimens were conceived using the same adhesive and a constant bond-line length, the variable parameter being the angle of the triangular adhesive spew (*i.e.* 15°, 30°, 45°, 90°).

2. TYPICAL STRESS-STRAIN STATE OF FRP COMPOSITES ADHESIVELY BONDED JOINTS

For any structural application of adhesively bonded joints, the main stress components that develop along the bond length are the shear stresses (τ) and the normal stresses (σ), respectively [12]. The shear stresses are induced by forces acting parallel to the adhesive layer, while the normal stresses are the result of forces acting perpendicularly to it. The shear stresses generate diagonal deformation, known as shear strains (γ), while the normal stresses develop normal strains (ε). The typical stress flow for FRP composite adhesively bonded joints [12] is illustrated in Fig.1.

In adhesively bonded FRP connections subjected to tensile forces, the main function of the adhesive layer is to transfer the load from one adherent to the other. Thus, the adhesive is mainly subjected to shear stresses and the maximum values are concentrated near the extremities of the bond length. However, when relatively thick and stiff FRP composite elements are connected in single lap joint configuration, the final mechanical characteristics of the bond are mainly influenced by the intensity of the through-thickness normal stresses.

The shear force acting at the interface level between the FRP composite element and the adhesive is balanced by the axial force in the adherent. The shear force and the axial force are coupled by a lever arm which is the distance measured from the mid-thickness of the FRP composite element to the adhesive-adherent interface (Fig. 1). The bending moment is counterbalanced by the through-thickness forces in the adhesive layer. The latter is generally referred to as peeling forces. These forces generate through-thickness normal stresses (peeling stresses) in the adhesive layer.

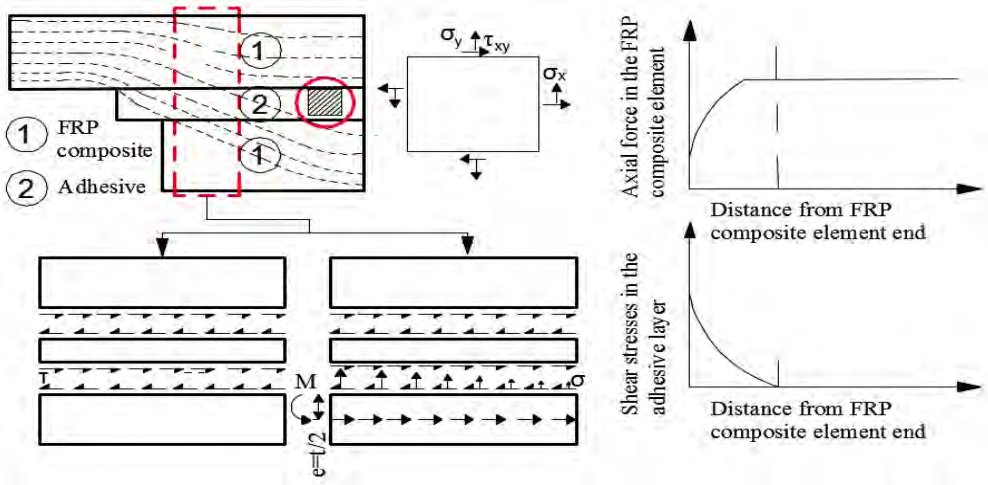

Figure 1. Typically stress flow through adhesively bonded FRP connections (adapted from [12])

3. MATERIAL PROPERTIES AND SPECIMENS GEOMETRY

3.1. Material property

3.1.1 GFRP composite material

For the numerical analysis in this study, the adherents were modelled according to the properties of Fiberline structural plate profiles made up of glass fibre reinforced polymer (GFRP) composite. The FRP composite elements are made of E-glass fibres embedded in an isophthalic polyester resin. The physical and mechanical properties of the GFRP plates are given in Tables 1 to 3. The main directions for strength and stiffness are presented in Fig. 2 [13]. The longitudinal direction is indicated as 0° and the transversal direction is indicated as 90°.

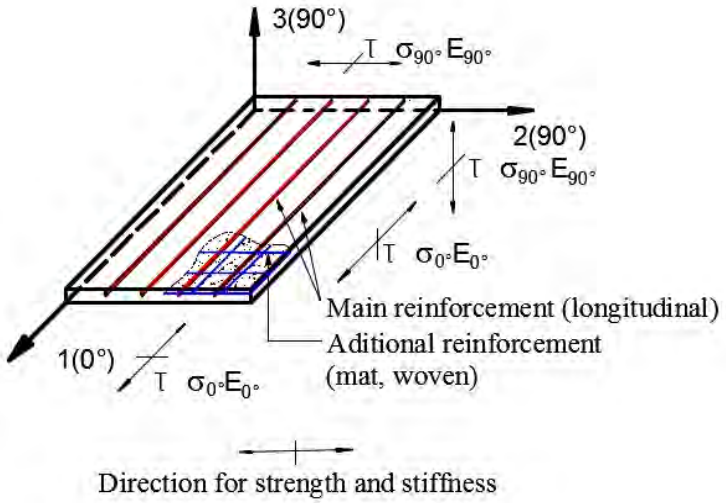

Figure 2. Indication of directions for strength and stiffness [13]

Table 1. Fiberline GFRP composite strip. Physical characteristics [14]

Density [kg/m^3]	Operating temperature [C°]	Fibre volume fraction [%]
1500	-20 ~ +80	>60

Table 2. Fiberline GFRP composite strip. Typical stiffnesses [14]

Longitudinal elasticity modulus [MPa]	Transversal elasticity modulus [MPa]	Modulus in shear [MPa]	Poisson's ratio, 0°, 90°	Poisson's ratio, 90°, 0°
23000	8500	3000	0.23	0.09

Table 3. Fiberline GFRP composite strip. Mechanical characteristics – Strength values [14]

Tensile strength, 0° [MPa]	Tensile strength, 90° [MPa]	Compressive strength, 0° [MPa]	Compressive strength, 90° [MPa]
240	50	240	70

3.1.2 Adhesive

The GFRP composite strips are considered to be bonded with a structural, two-part epoxy adhesive Sikadur30. The adhesive properties are presented in Table. 4

Table 4. Properties of the adhesive [15]

Density [kg/m^3]	Elasticity modulus [MPa]	Compressive strength [MPa]	Shear strength [MPa]	Tensile strength [MPa]
1650	12800	70-80	20	25-28

3.2. Specimens geometry

The SLJ considered in this study is presented in Fig. 3. For comparison purposes, a benchmark joint configuration was maintained throughout the study. The benchmark dimensions consist of a 2 mm adhesive thickness (t_a), 6 mm substrate thickness (t_s), 170 mm length and 25 mm width of the GFRP strip and 70 mm bond length. In order to be easily identified and appealed to, when the results will be analysed and compared, each specimen was marked with a nominal code (Table 5).

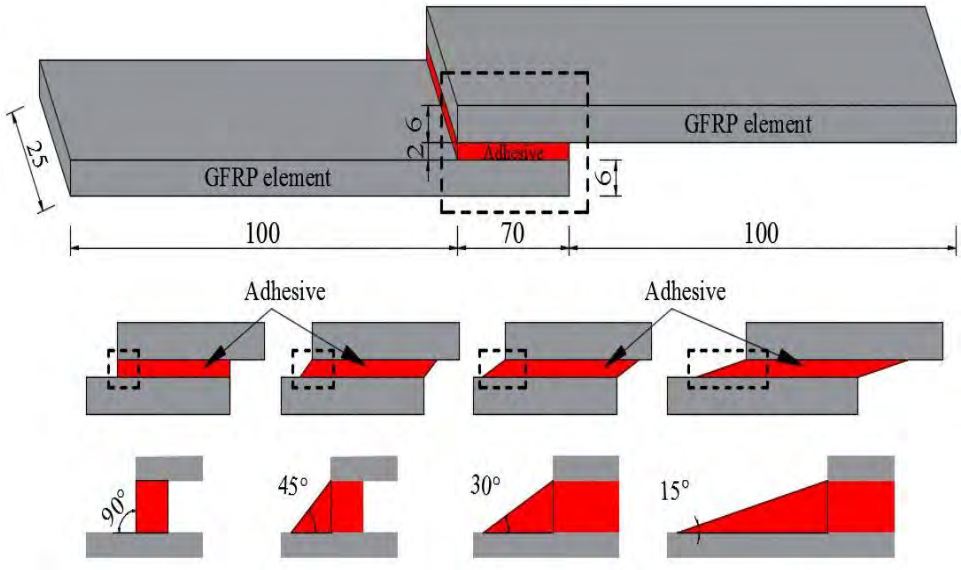

Figure 3. Model geometry in mm (Not at scale)

Table 5. Specimen notation

Specimen name	Specimen description
NSP	Benchmark geometry
SP15	15° triangular spew fillet
SP30	30° triangular spew fillet
SP45	45° triangular spew fillet

4. FINITE ELEMENT MODELLING

In this study, finite element models (FEMs) were used to perform tensile testing simulation on SLJs with and without spew fillets. The simulations were implemented using commercially available ANSYS Workbench software. The GFRP strips have been modelled as being linear elastic orthotropic materials, while the adhesive was modelled as a linear elastic isotropic material.

Each model consisted in three primitives of parallelepiped shape connected together to match the specimen geometric specifications. For each node, the parameters of position and connectivity have been defined. The final models were meshed using rectangular elements for the GFRP strips and triangular elements for the adhesive layer (Fig. 4) [6, 11]. Two refinement levels were used for the model

meshing. The first one was defined for the adhesive layer and consisted in triangular mesh elements of 1 mm while the second one was defined for the edges of the adhesive layer and for the spew fillet, having triangular mesh elements of 0.1 mm. These particular areas of the mesh are usually used to closely monitor the distributions of stresses and to track down any sudden change in stresses magnitudes. Also, a smooth transition region was considered in order to avoid mesh discontinuities. The specimens were considered as simply supported and the tensile loads (5 kN) were applied at the ends of the GFRP strips. The loading conditions are presented in Fig. 5.

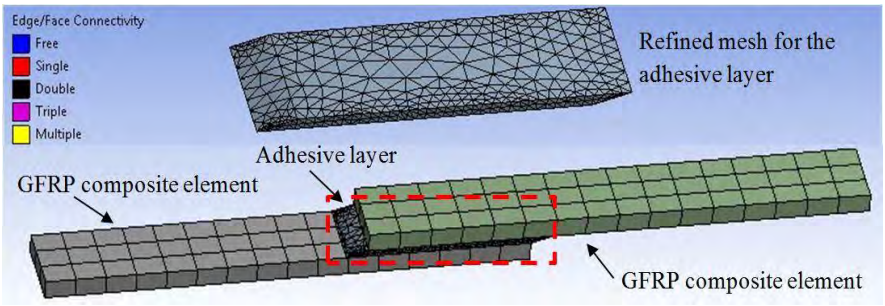

Figure 4. Meshing procedures

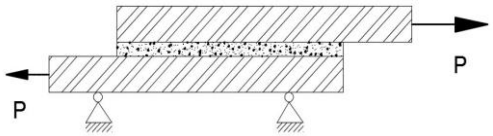

Figure 5. Loading conditions

5. RESULTS

The initial investigation has consisted in the stress state analysis in a square ended SLJ without any spew. The purpose of this investigation is to provide a benchmark for comparing SLJs with different spew configurations. The numerical analysis predicted that the shear stresses and the normal (peeling) stress in the adhesive layer are symmetrical with respect to the centre of the bond line and their peak values are at end of the bond line. However, the distributions of stresses across the thickness of the adhesive are more irregular with respect to the centre of the overlap, being much larger at the interface level. Thus, the shear stresses and the normal stresses distributions were investigated at the interface level between the GFRP strips and the adhesive. The shear stresses and normal stresses maps of the

specimens are presented in Figs. 6 to 13. Also, the comparison between the stresses distribution for the proposed models is graphically depicted in Fig. 14 and Fig. 15.

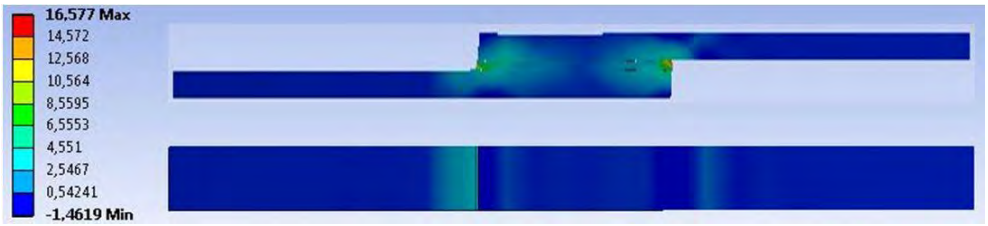

Figure 6. NSP model - Shear stress map [MPa]

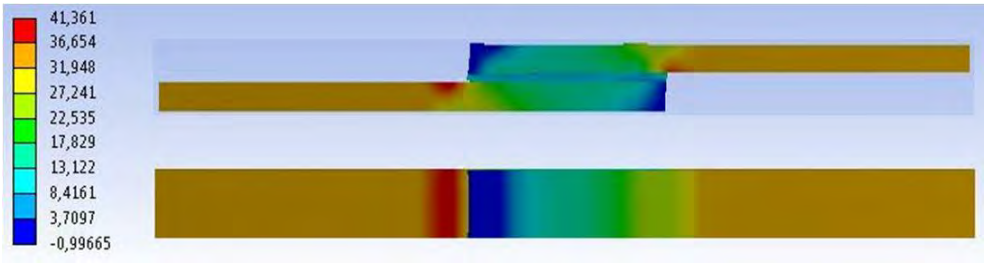

Figure 7. NSP model - Normal stress map [MPa]

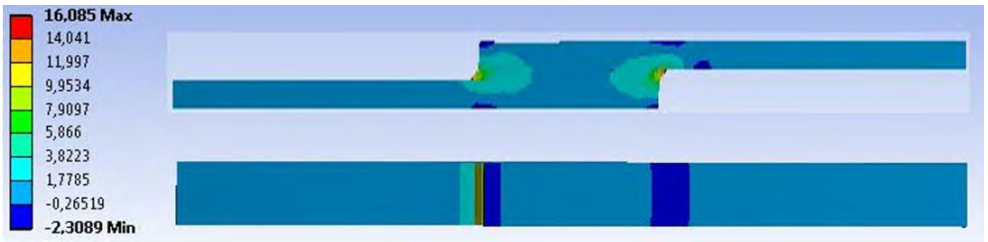

Figure 8. SP 45 model – Shear stress map [MPa]

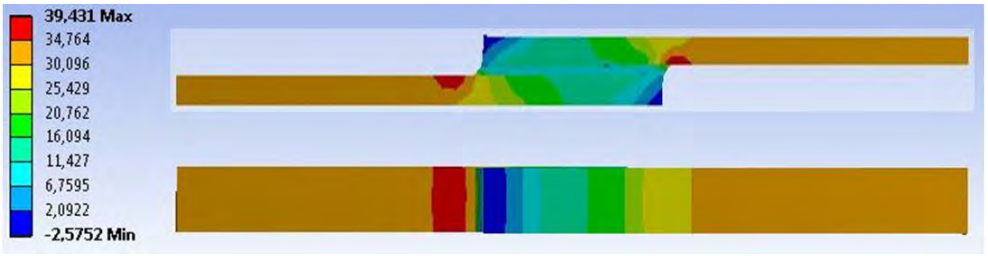

Figure 9. SP 45 model - Normal stress map [MPa]

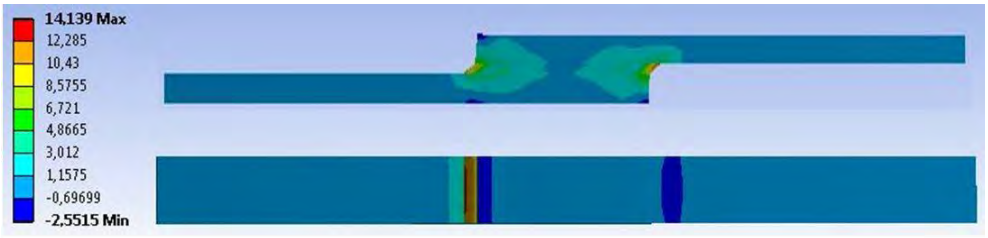

Figure 10. SP 30 model - Shear stress map [MPa]

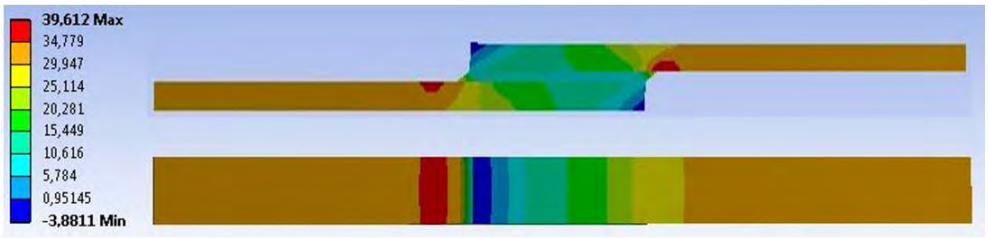

Figure 11. SP 30 model - Normal stress map [MPa]

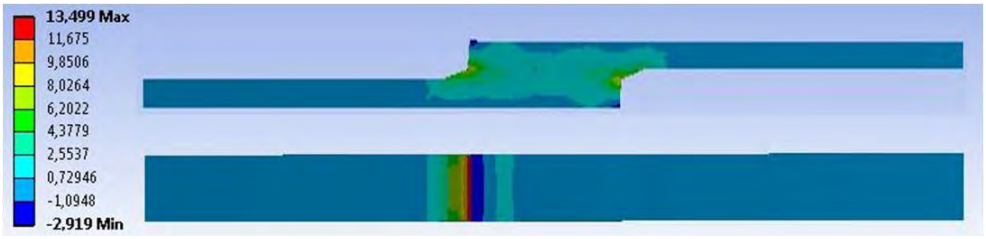

Figure 12. SP 15 model - Shear stress map [MPa]

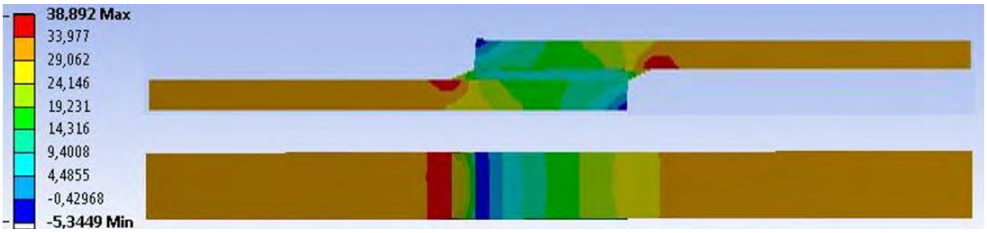

Figure 13. SP 15 model - Normal stress map [MPa]

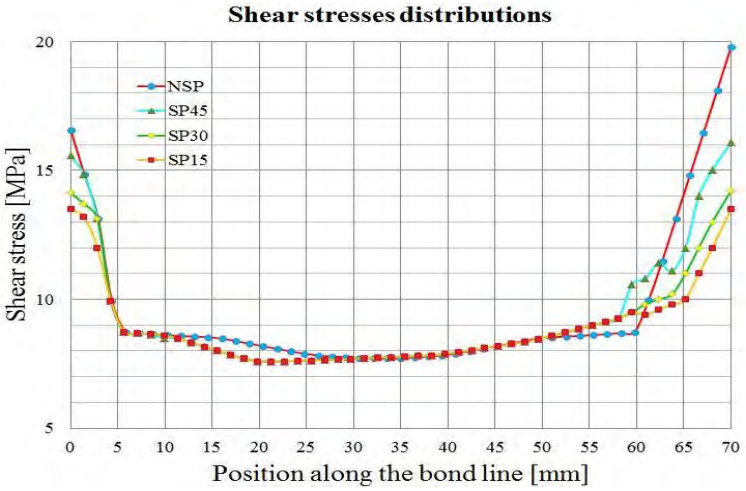

Figure 14. Spew effect on the adhesive shear stress distribution

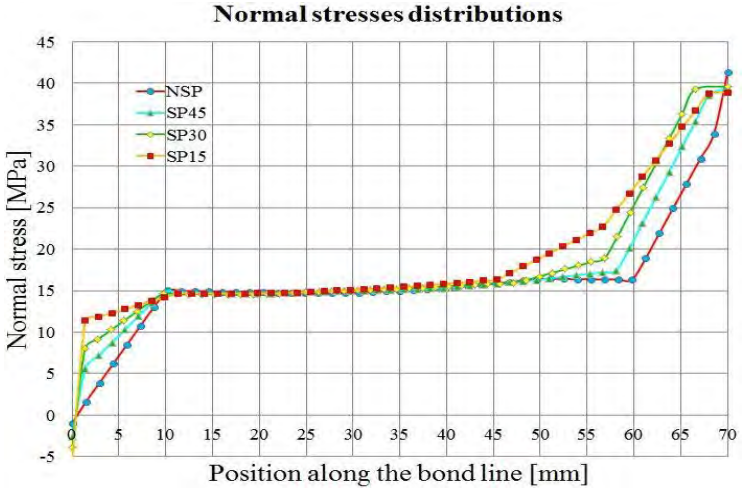

Figure 15. Spew effect on the adhesive normal stress distribution

6 DISCUSSION OF THE RESULTS

The influence of the adhesive spew geometry on shear stresses and normal stresses was investigated by considering the variation of stresses along the top interface between the GFRP strip and the adhesive. It can be noticed that all specimens have similar stress distribution patterns, but display different magnitudes of stresses.

Due to the presence of spews, the peak shear stresses are diminished with 3% for a 15° entry angle (SP15), 15% for a 30° entry angle (SP30) and up to 20% for the 45° entry angle (SP45), respectively. However, the percent reduction in peak normal stresses is lower than that of the peak shear stresses. This may be explained by the disadvantageous geometry features of the SLJs and of the adherents in particular (thick GFRP strips). For the SP15 and the SP30 models, the peak shear stresses diminished with only 4.3% and 5% when compared to the model with square ended adhesive (NSP). For SP15, a slight change in the graph pattern was observed (Fig. 15), tending to shift the location of the maximum normal stresses from the end of the overlap. However, the peak normal stresses were reduced with almost 6.5% when compared to the benchmark model.

7. CONCLUSIONS

This paper presented the outcomes of a numerical study that was conducted in order to determine the effect of adhesive spew geometry on the stress state in FRP adhesively bonded connections. Several triangular spew geometries consisted in different entry angles *(i.e.* 15°, 30°, 45°) had been considered. Based on the investigation of the distributions of the shear stresses and the normal stresses, the following conclusions can be drawn:

- The adhesive spew fillet significantly reduces the stress level in SLJs of bonded FRP composite elements.
- For triangular spew fillets, the lower entry angles cause larger reduction of peak stresses.
- The larger size spew fillets cause a higher reduction of shear stresses and normal stresses.
- The study has pointed out that for the proposed SLJs configurations, the most appropriate triangular spew fillet has a 15° entry angle.
- With respect to other stress reduction solution (*i.e.* rounding), the triangular spew fillets are feasible and simple to assemble.

References

1. Oprișan, G., Țăranu, N., Mihai, P., Ențuc, I., S., Maxineasa, S., G., Lupășteanu V., Structural response of pultruded GFRP profiles subjected to bending, Bulletin of the Polytechnic Institute of Jassy, vol 62(66), 3, 2016.
2. Lupășteanu, V., Țăranu, N., Mihai, P., Oprișan G., Lupășteanu, R., Ungureanu, D., Behaviour of CFRP-to-steel interfaces in adhesively bonded joints, Rev Rom Mat, 44, 4, 2016.

3. Rispler, A., R., Tong, L., Steven, G., P., Wisnom, M., R., Shape optimization of adhesive fillets, International Journal of Adhesion & Adhesives, 20, 2000.
4. Ungureanu, D., Țăranu, N., Lupășteanu, V., Mihai, P., Dupir (Hudișteanu), I., Behaviour of composite-to-composite interface for adhesively bonded joints. Experimental set-up, Bulletin of the Polytechnic Institute of Jassy, vol 62(66), 3, 2016.
5. Tong, L., Steven, G., P., Analysis and design of structural bonded joints, Dordrecht, Kluwer, Netherland, 1999.
6. Belingardi, G., Goglio, L., Tarditi, A., Investigating the effect of spew and chamfer size on the stresses in metal/plastic adhesive joints, International Journal of Adhesion & Adhesives, 22, 2002.
7. Tsai, M., Y., Morton, J., The effect of a spew fillet on adhesive stress distributions in laminated composite single-lap joints, Composite Structures, 32, 1995.
8. Akpinar, S., Doru, M., O., Ozel, A., Aydin M., D., Jahanpasand H., G., The effect of the spew fillet on an adhesively bonded single-lap joint subjected to bending moment, Composites Part B, 55, 2013.
9. Vallee, T., Tannert, T., Murcia-Delso, J., Quinn, D., J., Influence of stress-reduction methods on the strength of adhesively bonded joints composed of orthotropic brittle adherents, International Journal of Adhesion & Adhesives, 30, 2010.
10. Rispler, A., R., Tong, L., Steven, G., P., Wisnom, M., R., Shape optimization of adhesive fillets, International Journal of Adhesion & Adhesives, 20, 2000.
11. Kilic, B., Madenci, E., Ambur, D., R., Influence of adhesive spew in bonded single-lap joints, Engineering Fracture Mechanics, 73, 2006.
12. R., Haghani, Finite element modelling of adhesive bonds joining fibre-reinforced polymer (FRP) composites to steel in Karbhari, V., M., (editor) Rehabilitation of metallic civil infrastructure using fiber reinforced polymer (FRP) composites, Woodhead Publishing, Texas, SUA, 2014.
13. Ungureanu, D., Țăranu, N., Dupir (Hudișteanu), I., Florența, I., Lupășteanu, V., Shear structural response of adhesive joints for FRP composites, Advanced Engineering Forum, 21, 2016.
14. H. Thorning, Fiberline Design manual, Flat profiles, plates and sheets, Chapman & Hall, London, UK, 2012.
15. Technical data sheet - Sikadur – 30, Id no. 02 04 01 04 001 000001, 21,01,2008, Brașov.

"Computational Civil Engineering 2017", International Symposium
Iasi, Romania, May 26, 2017

Parametric Study on the Structural Behaviour of AAC-Reinforced Concrete Hybrid Lintels

Dorina-Nicolina Isopescu, Cristina Lanivschi and Oana Neculai
Department of Civil and Industrial Engineering, Gheorghe Asachi University, Iasi, 700050, Romania

Summary

The paper contains a numerical analysis on AAC-RC hybrid lintels structural behaviour, considering a variation in components heights, for the same overall cross-sectional area. The parametric study focused on the evaluation of deflections and stresses in lintel components and at AAC-concrete interface, for two types of contact behaviours: perfectly bonded and frictional.

KEYWORDS: hybrid lintels, AAC, contact behaviour, interface, frictional.

1. INTRODUCTION

There is a number of scientific papers on structural elements obtained by combining aerated autoclaved concrete (AAC) with reinforced concrete (RC), but the research on the AAC-RC interface is limited and parametric studies on the ratio between the two components are scarce, [1, 2, 3, 4].

The current paper contains part of a research programme requested by the producer of these hybrid AAC-RC lintels, with the purpose to evaluate the structural behaviour of these elements, [5].

The research presented hereinafter represents a parametric numerical analysis on hybrid lintels made of an upper layer of RC and a lower layer of AAC, considering a constant overall cross-sectional area for the element, but varying the height of each component.

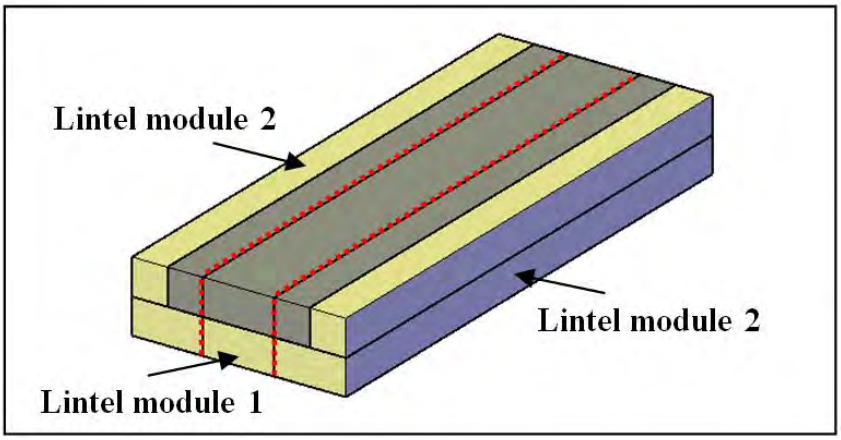

Figure1. Example of compound element made of lintel modules

The analysed lintels have 0.1 x 0.1 m cross-sections and represent part of a larger compound structural element, made of two types of lintel modules, as presented in Fig.1.The main advantage in using lintel modules is that there are theoretically no limits in the compound lintels widths, their dimensions being modulated to 0.1 m. Lintel module 1 is the focus of the current paper.

The purpose of the parametric study was to evaluate stresses in all components of hybrid lintel module 1 and their maximum deflections, for two different approaches on contact behaviour, in order to draw conclusions regarding the influence of the concrete-reinforcement and concrete-AAC bonds for the structural response of the lintel.

The final aim of the analysis was to determine the most advantageous configuration for the lintel cross-section from economical, strength and stiffness points of view.

2. FINITE ELEMENT ANALYSIS OF THE HYBRID LINTELS

The finite element analysis was performed using ANSYS Workbench V15.0, starting from a reference model that was validated in a previous research stage, when the simulation results were confirmed by analytical calculus, [6, 7].

The models consisted of an upper layer made of C20/25 concrete reinforced with longitudinal S500H steel bars and triangular stirrups and a lower AAC layer.

Two different approaches were analysed, related to RC-AAC contact behaviour. An “ideal” model was defined by considering perfectly bonded RC-AAC contact behaviour. Considering that in reality such compatibility between components cannot be achieved, a different scenario was used.

To describe the weak bond between the two components, a Coulomb friction model was introduced by assigning a friction coefficient of only 0.001. This value was chosen to be very small, considering that a real bond between concrete and AAC is not possible due to the fabrication process of the lintels.

2.1. Geometry and material properties

The hybrid lintels cross-section overall dimensions are 0.1 x 0.1 m and length of 2.75 m, consisting of three components: AAC blocks with standardized compressive strength of f_b = 3.50 MPa, C20/25 strength class concrete and S500H steel reinforcement, consisting of three longitudinal bars of Ø4 mm diameter and triangular stirrups of Ø3 mm diameter, spaced at 15 cm lengthwise.

There are 11 lintel models, with the same length and cross-section dimensions, but with different heights for the AAC and RC layers, varying from 0.0 cm to 10 cm, using a step of 0.5 cm, as shown Table 1. For a more intuitive understanding of the models' names, the dimensions are measured in cm.

Table 1. Definition of models and component layers heights

Lintel model	Model name	AAC layer height hAAC, [cm]	RC layer height hRC, [cm]
1	M0.0	0.0	10
2	M0.5	0.5	9.5
3	M1.0	1.0	9.0
4	M1.5	1.5	8.5
5	M2.0	2.0	8.0
6	M2.5	2.5	7.5
7	M3.0	3.0	7.0
8	M3.5	3.5	6.5
9	M4.0	4.0	6.0
10	M4.5	4.5	5.5
11	M5.0	5.0	5.0

The models are denoted with an initial M for "model" followed by the thickness of AAC layer, in cm, and by a superscript "b" – for bonded and "f" – for frictional, M $h_{AAC}^{b/f}$, as shown Figure 2.

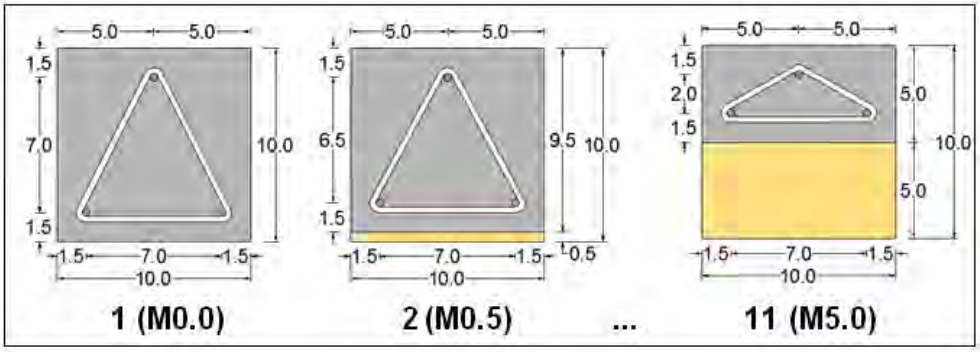

Figure 2. Models cross-sections and notations, measured in cm

The materials models used in the analyses were defined as linear isotropic, their mechanical properties are presented in Table 2.

Table 2. Geometrical and material properties of hybrid lintel components

Component	Cross-section [m]	Density [kg/m^3]	Poisson's ratio	Modulus of elasticity, [GPa]
Concrete	0.10x0.10...0.10x0.05	2300	0.20	30
AAC	0.10x0.005...0.10x0.05	520	0.18	2
Reinforcement	Φ4	7850	0.30	210
Stirrups	Φ3	7850	0.30	210

2.2. Finite element mesh

The meshes were automatically generated and consisted in a number of solid elements varying between 100035 and 110608, associated to 139059 and148950 nodes, as shown in Figure 3.

The finite elements were defined as SOLID185, therefore the mesh consisted in three-dimensional solid elements of 0.0015 - 0.025 m sides, defined by 8 nodes and permitting translations on all three global axes directions.

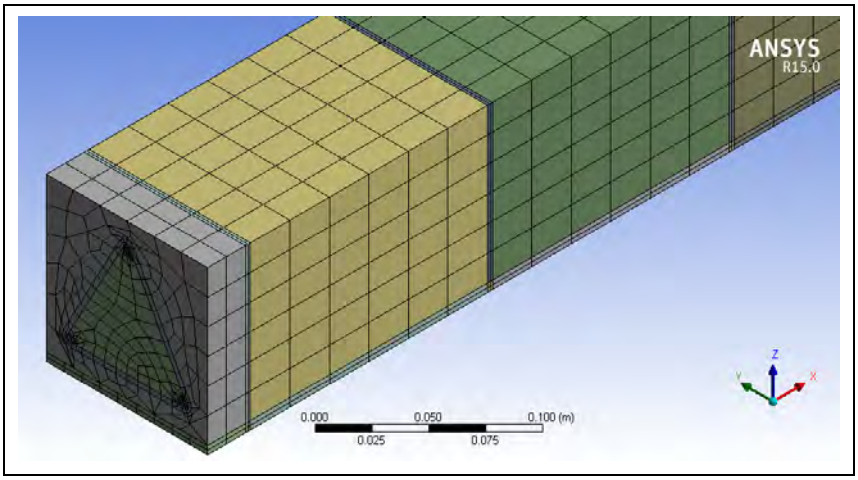

Figure 3. Example of meshing for model number 2

The RC-AAC contact pairs were assigned CONTA174 contact element for the lower part of concrete and TARGE170 target element for the upper part of AAC. Hence, the limits of the deformable bodies were defined using this type of contact pair [8].

2.3. Contact definition

In the case of *bonded RC-AAC interface model* all connections between the components of the hybrid lintel, steel reinforcement-concrete and AAC-RC are considered perfectly bonded, therefore no separation or detachment may occur between them.

In the case of the *frictional RC-AAC interface model,* a weak bond between concrete and AAC blocks was assumed by using a friction coefficient of 0.001. Therefore, the contact behaviour is simulated by the Coulomb friction model that also takes into account the shear stresses developed by the two contacting surfaces. This friction model considers that the contact and target surfaces can slide relative to each other. Sliding occurs when shear stresses at interface exceed a certain limit frictional stress, [8]. According to Coulomb friction model and since no cohesion is considered between the two components, the resulted contact frictional stresses are computed by multiplying the friction coefficient with the obtained contact normal pressure.

2.4. Loads and boundary conditions

The loads and boundary conditions are according to serviceability limit state. The lintel has the function to create the needed space for openings of doors and windows and to supports the wall structure placed on it. The maximum deflection of the lintel subjected to transverse loads must be very small, so that not to affect the frames of the openings. The deflection at mid-span was imposed to 1 mm. The applied loads consisted in the automatically generated self-weight of the components and an external load of 1051.8 N, representing three layers of AAC blocks supported by the hybrid element and distributed over the upper surface of the lintel.

The lintel ends were considered fixed, as they are tightly enclosed into the brick wall.

3. NUMERICAL ANALYSIS RESULTS AND DISCUSSION

The results were recorded and analysed in a benchmark for the two contact behaviour approaches. As expected, maximum deflections were obtained at mid-span, while the maximum normal stresses were identified close to the bearing area.

3.1. Normal stresses

All the results regarding normal stresses are introduced in Tables 3, 4 and 5. The results are the extreme values determined in the nodes from the upper and lower edges of the lintel cross-section, both in bearings and mid-span.

When comparing the maximum normal stresses in all lintel components, the highest values were obtained in the concrete layer.

In the case of *bonded models*, in *bearing area*, the tensile stresses in concrete ranged between 2.61 to 5.32 MPa, while the values recorded in the compressed part of the cross-section resulted slightly lower, of -2.63 to -4.23 MPa, see Figure 4.a.

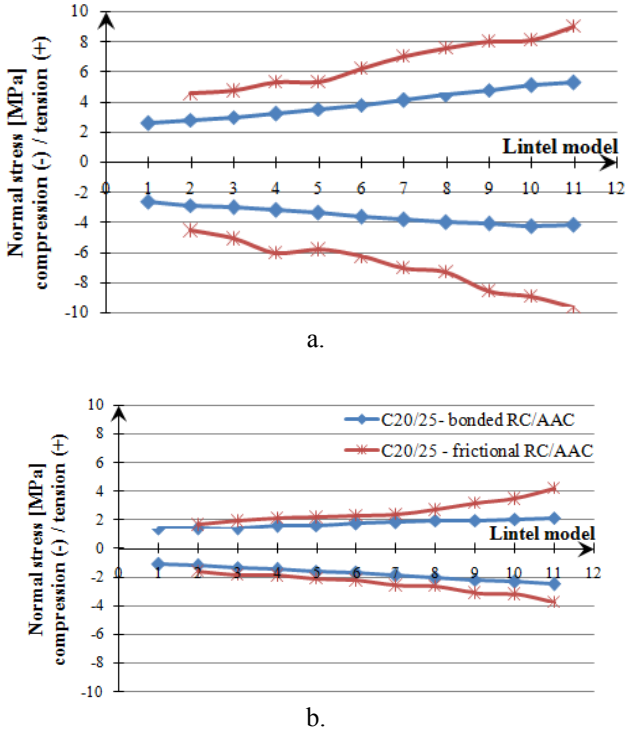

Figure 4. Normal stresses in concrete component for bonded vs. frictional RC/AAC interface: a. results recorded in bearings and b. results recorded at mid-span

The AAC component carries out compression with magnitudes ranging from -0.21 to -0.96 MPa for results recorded in bearings, Fig. 5.a, and tension with magnitudes ranging from 0.10 to 0.40 for results recorded at mid-span.

In the case of bonded models, at *mid-span*, the stresses measured resulted with values of 1.38 to 2.13 MPa at the bottom, and of -1.13 to -2.47 MPa at the upper part of the reinforced concrete cross-section, Fig. 4.b. The stress difference between the tensile and compressed parts of the lintel cross-section at mid-span is also balanced by the stresses developed in the AAC component, which is loaded solely in tension, with values ranging from 0.093 to 0.40 MPa, Fig. 5.b. As expected, due to the bonded interface, the stresses transfer is uniform between components, so that the stress values in the tensile and compressed parts of the cross-section are approximately equal, resulting in a stress difference of only 2.37%.

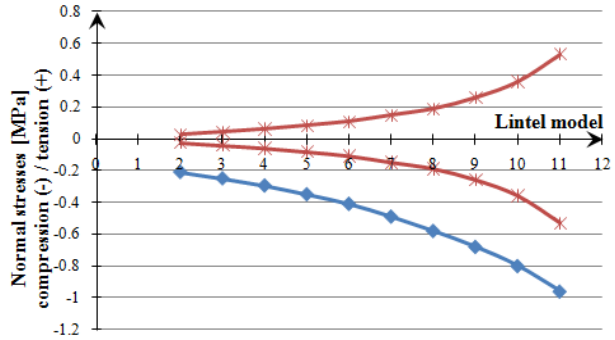

a.

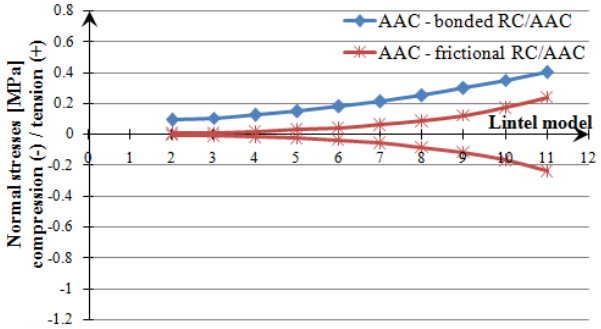

b.

Figure 5. Normal stresses in autoclaved aerated concrete component for bonded vs. frictional RC/AAC interface:
a. results recorded in bearings and b. results recorded at mid-span

Table 3. Normal stresses resulted in concrete

Lintel model	Bonded		Frictional	
	σb bearing [MPa]	σb mid-span [MPa]	σf bearing [MPa]	σf mid-span [MPa]
1	2.61	1.38	-	-
	-2.63	-1.13	-	-
2	2.81	1.42	4.56	1.66
	-2.85	-1.21	-4.54	-1.62
3	3.01	1.38	4.75	1.92
	-2.99	-1.31	-5.08	-1.83
4	3.25	1.57	5.33	2.12
	-3.18	-1.44	-6.03	-1.89
5	3.53	1.61	5.34	2.16
	-3.35	-1.59	-5.82	-2.11
6	3.81	1.72	6.24	2.29
	-3.6	-1.71	-6.27	-2.24

Lintel model	Bonded		Frictional	
	σb bearing [MPa]	σb mid-span [MPa]	σf bearing [MPa]	σf mid-span [MPa]
7	4.15	1.86	7.03	2.36
	-3.83	-1.88	-7.04	-2.59
8	4.46	1.96	7.57	2.69
	-3.99	-2.05	-7.29	-2.65
9	4.8	1.97	8.02	3.19
	-4.09	-2.2	-8.57	-3.12
10	5.09	2.06	8.11	3.47
	-4.23	-2.33	-8.89	-3.195
11	5.32	2.13	9	4.18
	-4.16	-2.47	-9.62	-3.75

For the compressed sides of the concrete component, the maximum compressive stresses resulted of -4.16 MPa and are much lower than the compressive strength of concrete, which is 20 MPa, Fig. 6.a. The colour legend suggests that the red areas show where the maximum stresses appear and they get lower towards the green areas.

The normal compression stresses in AAC component measured in bearings vary from -0.21 to -0.96 MPa and do not exceed the compression strength of the material, Table 4. Nevertheless, at mid-span where AAC is only loaded in tension, the tensile strength of AAC is exceeded for models M4.5-6.5^{b} and M5-5^{b}, having the highest value of 0.40 MPa, Fig. 6.b.

Differently from the bonded models, in the *frictional* RC-AAC interface, due to the low bond strength between components, the concrete and AAC carry out stresses individually, both in tension and compression, Figure 7.

Thus, normal stresses in concrete resulted with higher values, both in bearings and at mid-span, varying in *bearings* from 4.56 to 9.00 MPa in tension, and -4.54 to -9.62 in compression, Figure 4.a, and at *mid-span* with values between 1.66 and 4.18 MPa in tension and between -1.62 and -3.75 MPa in compression, Figure 4.b.

Differently from the bonded models, in the *frictional* RC-AAC interface, due to the low bond strength between components, the concrete and AAC carry out stresses individually, both in tension and compression, Figure 7.

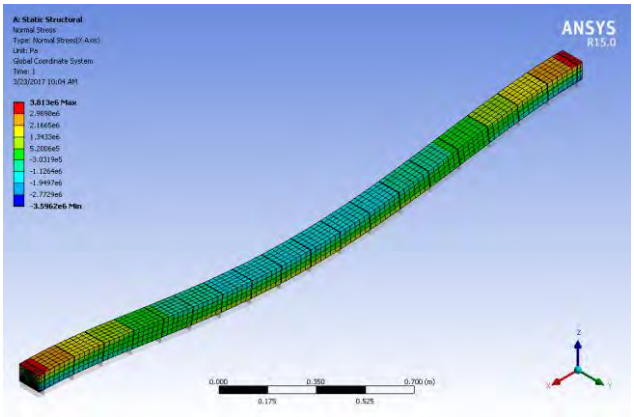

a.

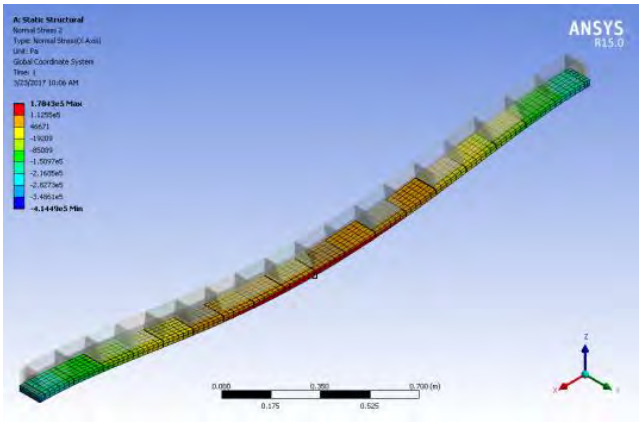

b.

Figure 6. An example of: a. normal stress distribution in concrete and b. in AAC component for bonded contact behaviour

Table 4. Normal stresses resulted in AAC component

Lintel model	Bonded		Frictional	
	σb bearing [MPa]	σb mid-span [MPa]	σf bearing [MPa]	σf mid-span [MPa]
1	-	-	-	-
	-	-	-	-
2	-	0.093	0.027	0.005
	-0.21	-	-0.027	-0.0049
3	-	0.105	0.044	0.011
	-0.25	-	-0.044	-0.011
4	-	0.125	0.062	0.018
	-0.295	-	-0.061	-0.018

Lintel model	Bonded		Frictional	
	σb bearing [MPa]	σb mid-span [MPa]	σf bearing [MPa]	σf mid-span [MPa]
5	-	0.15	0.085	0.028
	-0.35	-	-0.084	-0.028
6	-	0.18	0.11	0.041
	-0.41	-	-0.11	-0.041
7	-	0.21	0.15	0.059
	-0.49	-	-0.15	-0.059
8	-	0.25	0.19	0.084
	-0.58	-	-0.19	-0.084
9	-	0.3	0.26	0.12
	-0.68	-	-0.26	-0.12
10	-	0.35	0.36	0.17
	-0.8	-	-0.36	-0.17
11	-	0.4	0.53	0.24
	-0.96	-	-0.53	-0.24

Thus, normal stresses in concrete resulted with higher values, both in bearings and at mid-span, varying in *bearings* from 4.56 to 9.00 MPa in tension, and -4.54 to -9.62 in compression, Figure 4.a, and at *mid-span* with values between 1.66 and 4.18 MPa in tension and between -1.62 and -3.75 MPa in compression, Figure 4.b.

The AAC component presented reduced values for normal stresses at the interface, when compared to those obtained in bonded models, of only 0.027 to 0.53 MPa both in tension and compression in bearings and of 0.005 to 0.24 MPa, both in tension and compression, measured at lintel mid-span, Figure 5.b.

These values are lower than those obtained on bonded models, measured at mid-span, while models $M4.5^f$ and $M5.0^f$ presented tensile stresses in bearings higher than the tensile strength of AAC. This phenomenon occurs due to the lack of interconnection between the components, both being directly influenced by the different modules of elasticity of the materials and to the fact that components deflect differently and leading to a steeper difference between the stresses overtaken by concrete versus AAC.

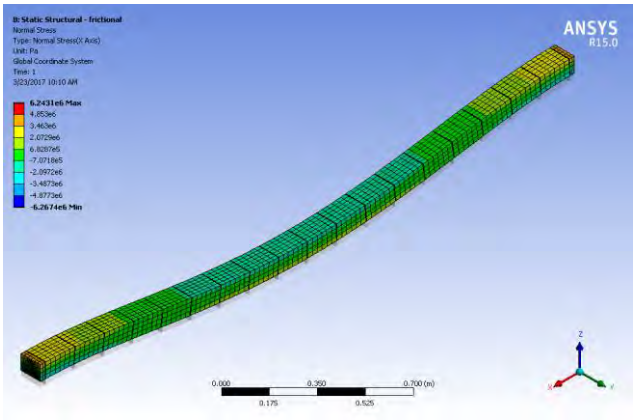

a.

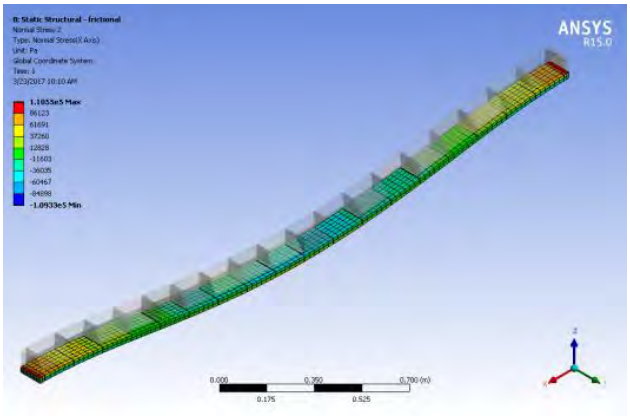

b.

Figure 7. An example of: a. normal stress distribution in concrete and b. in AAC component for frictional contact behaviour

The stresses in steel reinforcement were computed in all three longitudinal bars, and recorded in the upper part of the only longitudinal bar and in the case of the lower part, for the maximum value between both longitudinal bars, Fig. 2. The tensile strength of concrete is exceeded in all models on the upper side of the element and tensile stresses are overtaken instead by the steel reinforcement, Table 5.

The maximum tensile stresses in the steel longitudinal bars are of 25.04 MPa in the case of bonded models and of 26.95 MPa for frictional RC-AAC interface models, and are much lower than the tensile yield strength of 500 MPa, Figure 8.

Table 5. Normal stresses resulted in steel reinforcement

Lintel model	Bonded		Frictional	
	σb bearing [MPa]	σb mid-span [MPa]	σf bearing [MPa]	σf mid-span [MPa]
1	13.85	6.93	-	-
	-13.74	-7.02	-	-
2	15.43	7.721	13.3	6.5
	-14.46	-7.96	-13.37	-6.61
3	16.1	8.29	14.33	6.94
	-15.52	-8.5	-14.25	-7.11
4	16.81	8.43	15.46	7.46
	-15.96	-8.85	-15.3	-7.64
5	18.45	9.08	16.57	8.02
	-17.17	-9.67	-16.36	-8.23
6	19.39	9.7	18.07	8.85
	-18.31	-10.19	-17.72	-9.1
7	20.48	9.58	19.62	9.64
	-18.67	-10.63	-19.13	-9.88
8	22.34	9.77	21.26	10.54
	-19.15	-11.69	-20.67	-10.99
9	23.06	10.03	23.19	11.58
	-19.33	-11.97	-22.13	-11.91
10	24.92	9.37	25.1	12.72
	-18.99	-12.98	-23.49	-13.11
11	25.04	8.69	26.95	13.61
	-17.12	-13.37	-24.64	-14.34

In the *bonded model*, as the two components are not allowed to separate or slide relative to each other, the *interface stresses* are greater than in the case of the frictional contact behaviour models, having values of 0.028 to 0.076 MPa for normal contact stresses and 0.052 to 0.089 MPa for tangential contact stresses, Fig. 9.

In the *frictional model*, the interface stresses resulted with lower values, of 0.006 to 0.028 MPa for normal contact stresses. The tangential contact stresses resulted in 0.1% of the normal contact stresses.

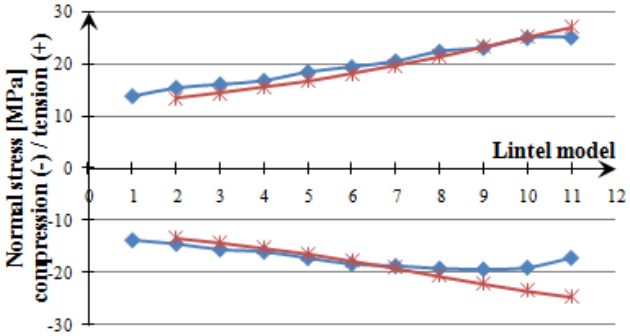

a.

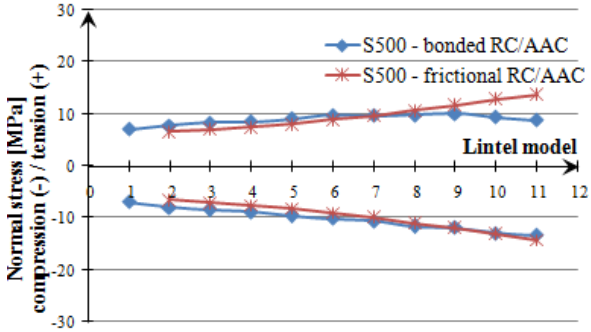

b.

Fig. 8. Normal stresses in steel reinforcement for bonded vs. frictional RC-AAC interface: a. results recorded in bearings and b. results recorded at mid-span

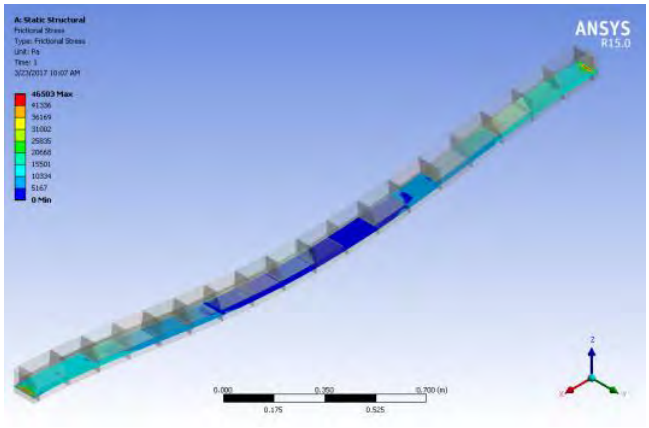

a.

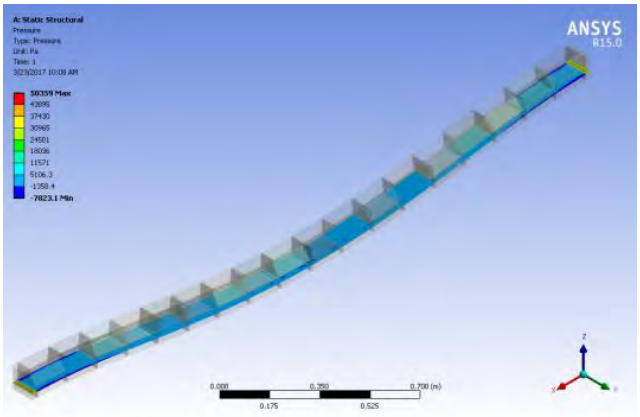

b.

Figure 9. An example of: a. tangential stresses and
b. normal contact stresses at RC-AAC interface for bonded M2.5^{b} model

3.2. Maximum deflections

In the *bonded models*, since no discontinuities develop at the RC-AAC interface, the two components deform uniformly, the concrete component restraining the AAC component to deflect differently. The obtained maximum deflection was of 1.35 mm, Fig. 10, and is higher than the allowable deflection, considered of 1 mm, [6, 7].

Otherwise, in the *frictional models*, the maximum deflections measured at the mid-span were varying from 0.4 to 2.27 mm, with up to 40.53% higher than in the case of a perfect bond between the components.

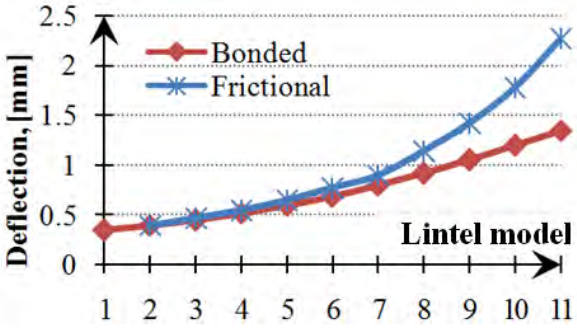

Figure 10. Deflection of lintel measured at mid-span

3.3. Sliding distances and gaps between components

In the *bonded models*, since no discontinuities develop at the RC-AAC interface, the two components deform uniformly, the concrete component restraining the AAC component to deflect differently. The maximum deflection obtained for this analysis was of 1.35 mm, Figure 10, and is higher than the allowable deflection, considered of 1 mm, [6, 7]. In the case of *frictional models*, certain sliding or detachment can occur between RC and AAC layers. Therefore, two effects were analysed at the interface between the concrete and AAC layer: the gap and the sliding distance, Figure 11.a and b.

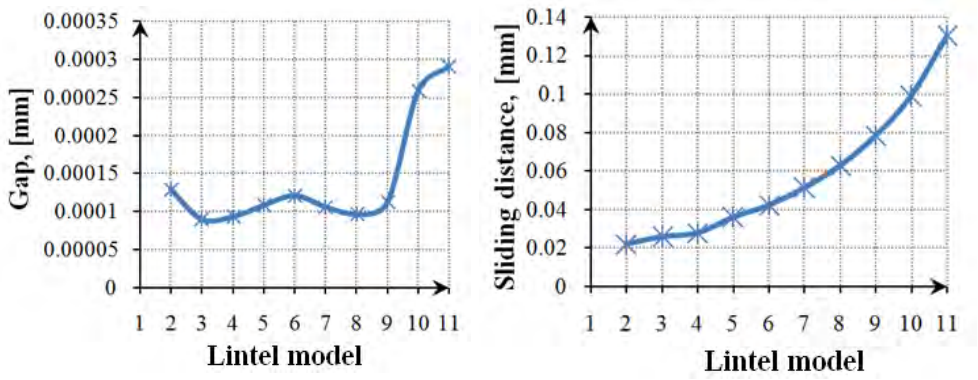

a. b.

Fig. 11. Results obtained for frictional models:
a. gap and b. sliding distance at RC-AAC interface

The gap varies from 0.00013 to 0.00029 mm, presenting an overall increase as the layer of AAC thickens, while the layer of RC is thinner, Fig. 12.a. This appears as a direct consequence of the difference between the stiffness properties of the materials.

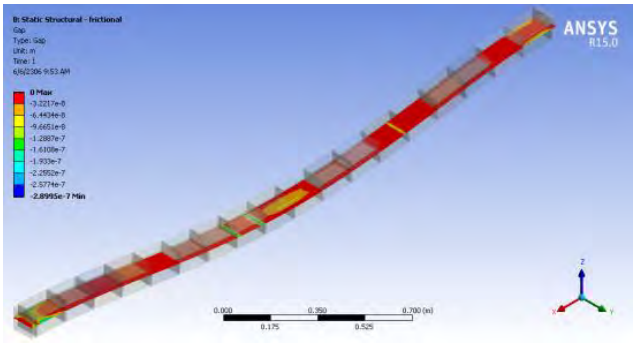

a.

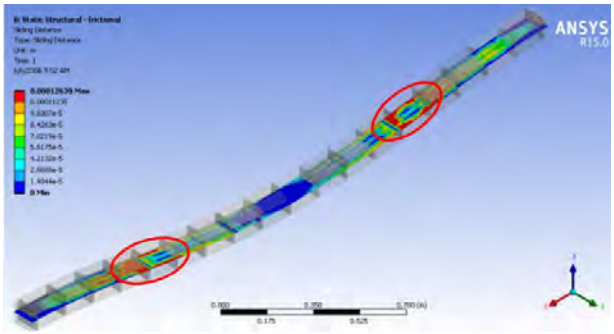

b.

Fig. 12. Example for frictional model M5.0^{f} of:
a. gap at RC-AAC interface, b. sliding distance at RC-AAC interface

The sliding distance maps provide a clear view of the most dangerous areas at RC-AAC interface, where sliding may occur. This sliding distance is larger with the increase in AAC component height. The maximum values are obtained in the areas of inflexion, suggested by the red circles in Fig. 12.b. The sliding distance ranges between 0.0222 and 0.13 mm, and it also raises with the increase in AAC height, for the same reasons as the gap, Fig.12.b. These values are only 0.004% for the lintel span, therefore the two components are still working together.

4. FINAL CONCLUSIONS

When selecting the most advantageous configuration for the hybrid lintel, there are certain criteria that must be considered:

- the normal stresses in all components should not exceed the strengths of the individual materials;

- the maximum deflection at mid-span must be lower than the imposed deflection of 1 mm;
- the lowest values for gap and sliding distance at RC-AAC interface are considered the most desirable.

Because all components are subjected to bending, the stresses developed in each of them are both of tension and compression. Since the compressive stresses obtained in all models and in all components do not overcome the compression strength of materials that constitute the lintel, none of bonded and frictional models fail from compressive stresses.

Analysing the AAC layer at mid-span, the last two bonded models ($M4.5^b$ and $M5.0^b$) recorded tensile stresses higher than the AAC tensile strength, considered 10% from its standardised compressive strength of 3.50 MPa. In addition, the AAC components fail in bearing, in the case of the last two frictional models ($M4.5^f$ and $M5.0^f$).

The allowable deflection of 1 mm for the hybrid lintel was exceeded both in bonded and frictional models by the last three ($M4.0^b$, $M4.5^b$, $M5.0^b$) and four models ($M3.5^f$, $M4.0^f$, $M4.5^f$, $M5.0^f$), respectively.

Regarding the gap at the interface for the frictional models, the lower its value, the better the behaviour of the hybrid lintel is considered. Thus, models $M1.0^f$, $M1.5^f$, $M2.0^f$, $M3.0^f$ and $M3.5^f$ present the most advantageous configuration. Nevertheless, $M3.5^f$ does not meet the maximum deflection condition; therefore this configuration should be avoided.

All frictional lintels present very low sliding distances, thus it can be considered that this condition is met by all models.

In conclusion, the configurations that meet all the above-mentioned criteria are M0.5 to M3.0.

In addition, taking into account the fulfilment of the durability requirements and, at the same time, the removal of the thermal bridges and the provision of the thermal transfer resistance of the structural elements in the buildings, the most recommended model is M3.0, meaning that the AAC component should not exceed 30% of the overall cross-section height.

ACKNOWLEDGEMENTS

The authors acknowledge the contribution and thank SC MACON SA Deva which supported the research of these originally products.

This paper was realised in the framework of the project EFECON – ECO-INNOVATIVE PRODUCTS AND TECHNOLOGIES FOR ENERGY EFFICIENCY IN CONSTRUCTION, POC/71/1/4 - Knowledge Transfer Partnership, Cod MySMIS: 105524, ID: P_40_295, Project co-financed by the European Regional Development Fund.

REFERENCES

1. H. Bagheri, *The BCE (Block Composed Element) building system. A conceptual study*, Licentiate Thesis, Royal Institute of Technology, School of Architecture and Built Environment, Stockholm, ISBN 91-7178-441-1 (2016).
2. B.G. Hellers, O. Lundvall, *Aerated concrete used in composite action with ordinary concrete – from block to element*. Advances in Autoclaved Aerated Concrete, Balkema, Rotterdam, ISBN 90-5410-086-9, pp.201-207 (1992).
3. V. Vimonsatit, A.S. Wahyuni, H. Nikraz, *Reinforced concrete beams with lightweight concrete infill*, Scientific Research and Essays, Vol. 7(27), pp.2370-2379 (2012).
4. T. Subramari, D. Sakthi Kumar, S. Badrinarayanan, *FEM Modelling and Analysis of Reinforced Concrete Section with Light Weight Blocks Infill*, Journal of Engineering Research and Application, Vol. 4, Issue 6, pp.142-149 (2014).
5. Information on http://www.macon.ro.
6. O. Neculai, C. Lanivschi, D.-N. Isopescu, I.-O.Toma, I. Zăpodeanu, *Parametric Study of Structural Performance of Innovative Solutions for Hybrid Lintels* - Part 1: Input Data for FEM Analysis, Advanced Engineering Forum, Trans Tech Publications, Switzerland, Vol. 21, pp. 255-261, ISSN: 2234-991X, doi:10.4028/www.scientific.net/AEF.21.255 (2017).
7. C. Lanivschi, O. Neculai, D.-N. Isopescu, *Structural Behaviour Evaluation by Numerical Simulations for Innovative Solutions of Hybrid Lintels* - Part 2: FEM Analysis, Advanced Engineering Forum, Trans Tech Publications, Switzerland, Vol. 21, pp. 286-293, ISSN: 2234-991X, doi:10.4028/ www.scientific.net/AEF.21.286 (2017).
8. Information on: http://148.204.81.206/Ansys/readme.html.

Comparative study on the design of a condominium residential building with structural masonry walls located in Romania / Republic of Moldova

Marian Pruteanu[1], Ion Sococol[1] and Maricica Vasilache[1]
[1]*Department of Civil and Industrial Engineering, "Gheorghe Asachi" Technical University of Iași, Iași, 700050, Romania*

Summary

For buildings with confined masonry structural walls, both European norms and Romanian codes that regulate their design require architectural-structural compliance and a mode of calculation which involves – in areas with high risk of earthquake – the use of high concrete and steel amounts. By taking into account the essential performance requirements of strength, stability, and economy of resources, the question of justifying these consumptions arises.

Thus, the authors propose to assess the need of excessive confinement of masonry walls in these seismic areas through a comparative study on designing a building with structural walls of solid brick confined masonry – placed simultaneously in Romania and in the Republic of Moldova – at such a distance that earthquake effect is similar, using the numerical program ETABS 2016.

Finally, in order to quantify the excess of material required, an estimated economic analysis regarding the cost of superstructures in the two cases analysed was performed.

Key words: confined masonry, strength and stability, economy of resources, buildings regulation, Etabs 2016

1. INTRODUCTION

Romania and the Republic of Moldova are two neighbouring countries that use different norms/standards for structural design, although certain areas of the two countries are similar concerning the effect of seismic action and that of wind or snow loads. Concerning the structural compliance of structural masonry walls, this is a topic of great actuality, taking into account that – on both banks of the Prut River – these buildings account for over 60% of the national built fund [4] and that the norms regulating this activity in the two countries impose different approaches [1, 2, 3]. The authors believe that the requirements of the Romanian Code – including the multiplication of tie-columns in areas with design ground acceleration $a_g > 0{,}25g$ – lead to high consumption of concrete and steel, which is

sometimes irrational. In order to highlight such forced consumption in Romania (a Member-State of the European Union) it was proposed a fictional placement of a building on both banks of the Prut River. It has been kept the same function, but with the change of the load-bearing frame compliance, pursuant to the technical regulations in effect in the two countries.

Hence, the purpose of this paper was to design a condominium residential building with structural masonry walls, located in the county of Vaslui and in the department of Ungheni, two border regions chosen because we want to meet the three essential requirements:

- Similar seismic area (Figure 1) and similar foundation base with identical stratification;
- Geographic area of the same nature that involves equal Load participations on the two banks of the Prut River.

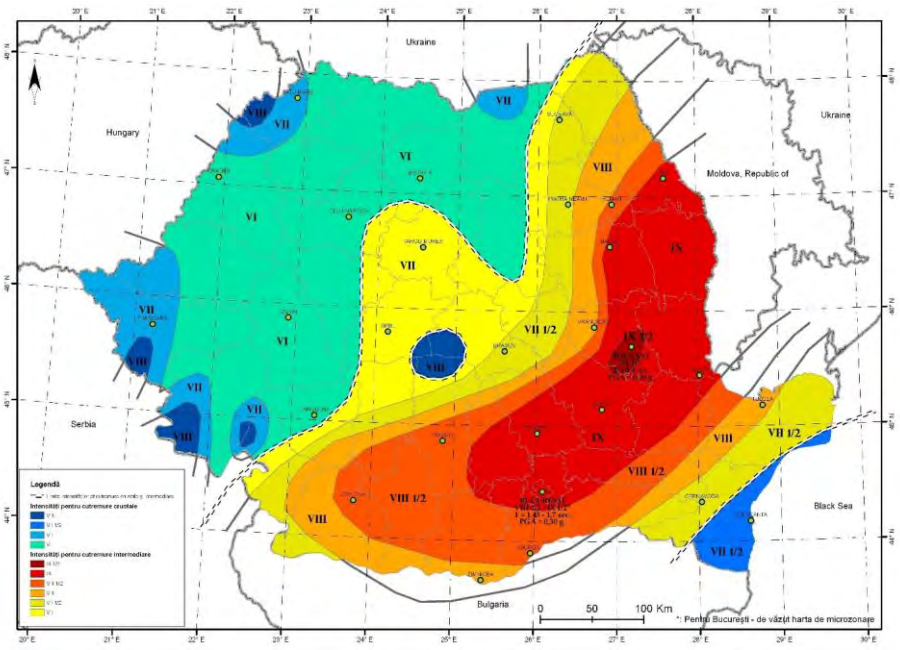

Figure 1. Map featuring earthquake intensities in Romania/The Republic of Moldova [10]

2. CALCULATION OF STRUCTURES

The preliminary compliance of the building was conducted in order to meet the rules imposed by both the CR6:2013 (Design Code for Structural Masonry Walls), P100-1:2013 (Seismic Deign Code), and by the NCM F.03.02-2005 (Moldovan Norms for the Design of Structural Masonry Walls). The height regime is GF (groundfloor) +2S (storeys), H_{storey} = 3 (m), S = 296 (m^2). The current floor plan for the two cases is represented by Figure 2 and Figure 4.

The calculation of section design internal forces was conducted in both cases by using the numerical program ETABS 2016 [9] and the design strengths were calculated manually. In order to conduct these calculations it was used in both cases the Romanian Design Norms [1],[2].

Thus, starting from two structural walls of solid brick masonry (Table 2) with different preliminary compliance (Table 1) we compared resistances and design efforts. We have also analyzed the work method of structures, the structural-spatial cooperation, and the optimal use of construction materials [1],[3].

Table 1. Differences in structural components

Main differences	RO	MDA
Number of tie-columns	93	43
Reinforcement of tie-columns	4 Ø 16 PC52	4Ø20 PC52
Reinforcement of tie-beams (long.)	4Ø16 PC52	4Ø14 PC52
Reinforcement of tie-beams (trans.)	Stirrups Ø8 OB37	Stirrups Ø6 OB37
Girdle sizes	25x30 cm	25x40 cm
Flooring thickness	13 cm	10 cm
Filling door and window spaces	Yes	No

Table 2. Load-bearing elements and materials used for the studied structures

Roof	roof framework
Structural walls	solid brick confined masonry walls 240x115x63 mm
Section of tie-columns	25x25 cm
Concrete	C 16/20

2.1. Assessment of active walls density on the two directions

This assessment was conducted according to CR6:2013 and P100-1:2013, and thus we obtained:

$p\% = \min (p\%_{(transv.)}; p\%_{(long.)}) = \min (6.66; 5.638)\ \% = 5.638\ \%$

Hence, $p\%_{min\ adm} = 5\%$, for $a_g = 0.30g$ one can admit $n_{niv} = 3$ (GF+2S) [1],[2],[4].

2.2. Load participation

Load participation and load combinations were conducted pursuant to SR EN 1991-1-1:2004/NA-2006, SR EN 1991-1-3:2005/NA-2006, P100-1:2013, and they are illustrated in Tables 3, 4, 5 [2],[6],[7].

Table 3. Permanent and variable load participation

Load type	Value
Superstructure weight	1.125 kN/m^2
Roof framework weight	1 kN/m^2
Roofing weight	0.7 kN/m^2
Live loads:	
-roof:	0.75 kN/m^2
-floorings:	2.5 kN/m^2
Snow	1.91 kN/m^2

Table 4. Seismic design parameters

γ_{Is}	1	Third importance class
a_g	0.30g	Design ground acceleration
T_C	0.7 s	Control period (corners)
T_D	3.0 s	Control period (corners)
T_B	0.14 s	Control period (corners)
q	2.8125	Structure behaviour factor

Table 5. Load combinations

1	Fundamental 1	1.35P + 1.5U + 1.05Z
2	Fundamental 2	1.35P + 1.05U + 1.5Z
3	Earthquake Sx	1P + 0,4U + 0.4Z + 1Sx + 0Sy
4	Earthquake Sy	1P + 0.4U + 0.4Z + 0Sx + 1Sy
5	Modal	1P + 0.4U + 0.4Z

2.3. Calculation of design internal forces and strengths

We defined the masonry embrasures:

- for the structure placed in the county of Vaslui (Romania) – Figure 2, 3 [4]
- for the structure placed in the department of Ungheni (The Republic of Moldova) – Figure 4, 5 [3]

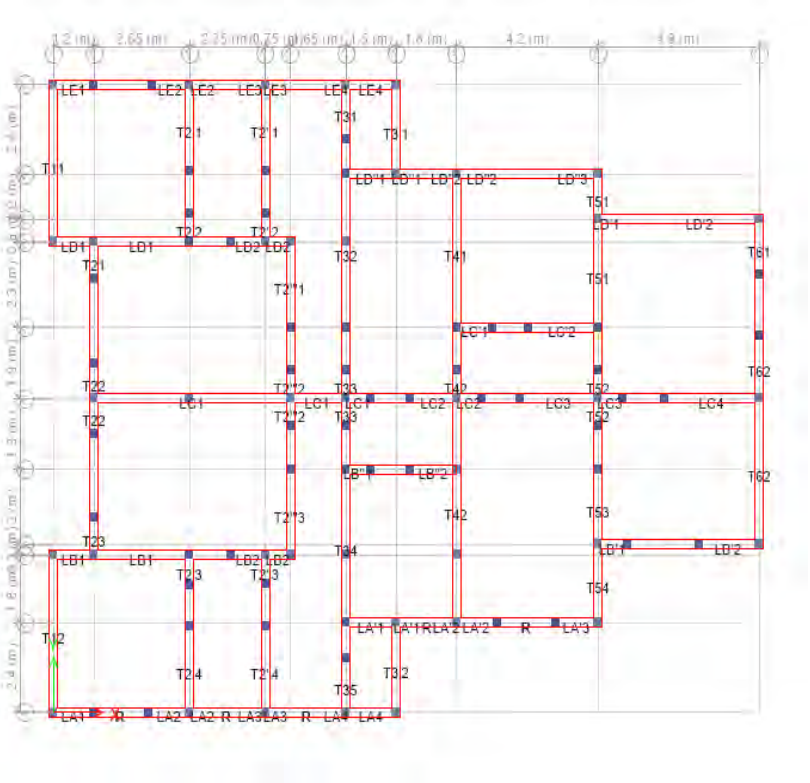

Figure 2. Current floor plan (placed in Romania – county of Vaslui). ETABS Model

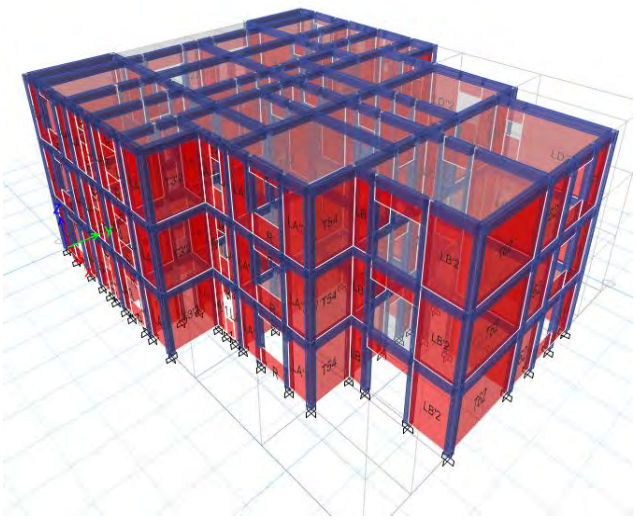

Figure 3. 3D structure representation (placed in Romania – county of Iași). Model ETABS

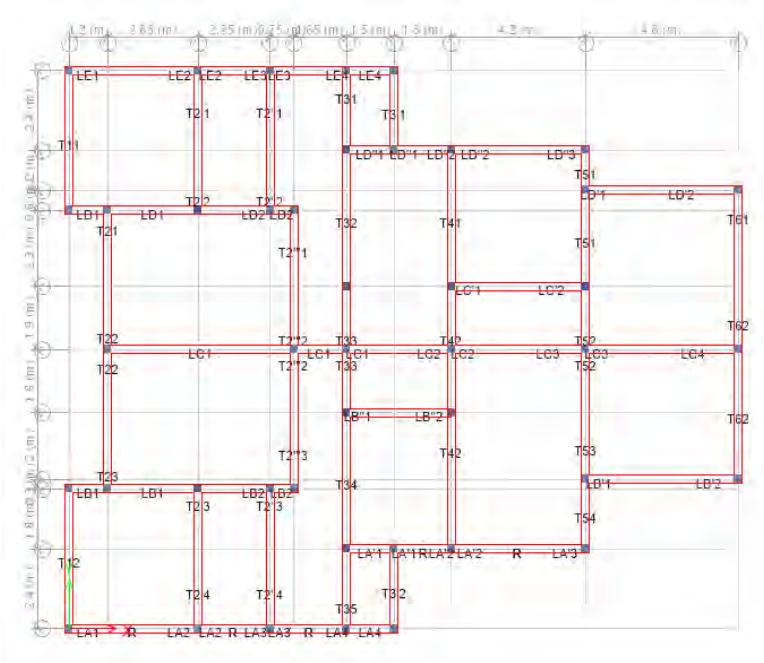

Figure 4. Current floor plan (placed in The Republic of Moldova – department of Ungheni). ETABS Model

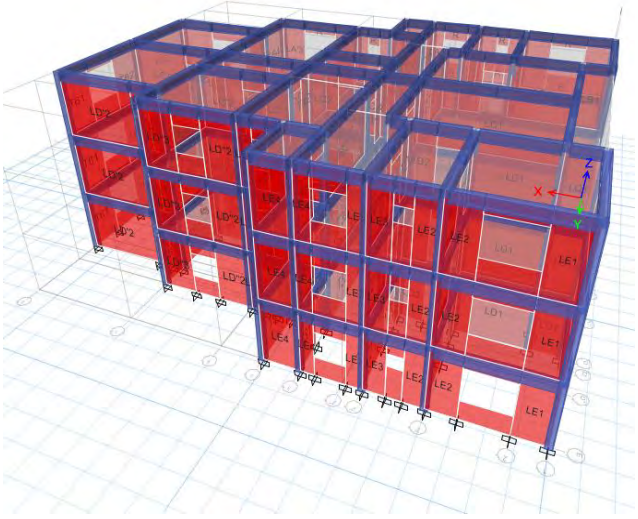

Figure 5. 3D structure representation (placed in The Republic of Moldova – department of Ungheni). ETABS Model

The dynamic characteristics of confined structural masonry walls were represented for each case in Tables 6 and 7 [5],[11].

Table 6. Modal periods, frequencies, and drift

	Case	Mode	Period sec	Frequency cyc/sec	UX mm	UY mm
RO	Modal	1	0.094	10.587	0.7415	0.0505
RO	Modal	2	0.091	10.958	0.0814	0.6238
RO	Modal	3	0.081	12,295	0.0066	0.1476
MDA	Modal	1	0.097	10.261	0.4873	0.1996
MDA	Modal	2	0.095	10.573	0.3207	0.4263
MDA	Modal	3	0.084	11,882	0.0172	0.1911

Table 7. Modal load participation ratios

	Case	Item type	Item	Static %	Dynamic %
RO	Modal	Acceleration	UX	99.85	93.66
RO	Modal	Acceleration	UY	99.86	93.8
MDA	Modal	Acceleration	UX	99.83	93.19
MDA	Modal	Acceleration	UY	99.86	93.61

The final results of section design internal forces and of design strengths on the two directions (longitudinal, transverse) for both researched structures stand to show that both structures successfully bear both gravitational and horizontal loads from the seismic action.

3. ECONOMIC ANALYSIS ESTIMATED FOR SUPERSTRUCTURE COST

In order to highlight the additional consumption of resources, we calculated for the two buildings the consumption of materials (concrete, masonry, steel) necessary for the superstructure.

- In order to determine the prices of materials necessary for the studied buildings, we analyzed the building material market in Vaslui.
- The Tables below feature the consumption of materials in the usual order [13].

Table 8. Estimate of material consumption for the confined masonry structure (placed in Romania – county of Vaslui)

Element name	Material	Quantity/ Volume	Units of measurement	Cost (RON)
Tie-columns	Concrete C16/20	52.31	m³	260
Tie-beams	Concrete C16/20	47.52		
Slabs	Concrete C16/20	115.44		
Masonry wall	Brick	265.985		803.64
Tie-columns reinforcement	PC52	5936.37	kg	2.3
	OB37	2512.67		
Tie-beams reinforcement	PC52	4671.27		
	OB37	1649.52		
Slabs reinforcement	PC52	8081.07		
Total volume of concrete C16/20		**215.27**	m³	55970.2
Total weight of reinforcement PC52		**18688.71**	kg	42984.03
Total weight of reinforcement OB37		**4162.19**		9573.04
Total volume of masonry		**265.985**	m³	213756.19
TOTAL COST (RON)				**322283.46**
TOTAL COST (EURO)				**70902.36**

Table 9. Estimate of material consumption for the confined masonry structure (placed in The Republic of Moldova – department of Ungheni)

Element name	Material	Quantity/ Volume	Units of measurement	Cost (RON)
Tie-columns	Concrete C16/20	24.18	m³	260
Tie-beams	Concrete C16/20	58.83		
Slabs	Concrete C16/20	88.8		
Masonry wall	Brick	282.8		803.64
Tie-columns reinforcement	PC52	4282.19	kg	2.3
	OB37	1161.77		
Tie-beams reinforcement	PC52	3577.36		
	OB37	1112.48		
Slabs reinforcement	PC52	5328.18		
Total volume of concrete C16/20		**171.81**	m³	44670.6
Total weight of reinforcement PC52		**13187.73**	kg	30331.779
Total weight of reinforcement OB37		**2274.25**		5230.775
Total volume of masonry		**282.8**	m³	227269.39
TOTAL COST (RON)				**307502.55**
TOTAL COST (EURO)				**67650.56**

DIFFERENCE	RON	EURO
	-14780.91	**-3251.8**

Figure 12. Difference in total cost for the superstructure of buildings following the economic analysis

4. CONCLUSIONS AND RECOMMENDATIONS

The proposed study led to the following conclusions:

- In both cases, certain short walls stressed by shear force have not been verified, but the building as a whole can successfully bear loads of the seismic action;
- The minimum strengths causing the $V_{Ed} > V_{Rd(0-1)}$ phenomenon is the design strengths to failure mechanism per inclined section for walls;
- Because the density of active walls was preserved, in both cases (RO, RofM) the values of $V_{Rdi(0-1)}$ (design strengths to failure mechanism per inclined section) are the same;
- Due to the rigid structure loads more from the horizontal action (earthquake), without consuming the energy of the earthquake by deforming, it results that for the Vaslui-based building the shearing forces are higher than those for the other region. Therefore, the number of walls non-resistant to shearing force is higher;
- In both cases, the structure is more loaded in the transverse direction with horizontal action because of the structural geometry (the short side is more loaded).
- From the perspective of structure behaviour in a seismic area with a_g=0.30g and of spatial-structural compliance, the building designed pursuant to the NCMF.03.02 – 2005 regulations has a better response;
- In addition, following an economic analysis, we concluded that such building is more budget-friendly because of the reduced number of tie-columns, of less thick flooring, of proper reinforcement according to design sections etc. Thus, the overall price difference is 3,250 Euros in favour of the building designed in The Republic of Moldova.

Recommendations:

- In order to solve the issue related to the design strengths per inclined section for slabs, one can use walls reinforcing in horizontal joints, at a height difference of three bricks;

- The use of seismic shock absorbers for certain walls.

REFERENCES

1. CR6:2013 - Cod de proiectare pentru structuri din zidărie (in Romanian);
2. P100-1:2013 - Cod de proiectare seismică. Partea 1 – Prevederi de proiectare pentru clădiri (in Romanian);
3. NCM – Zidărie: 2005 - Normativ moldovenesc de proiectare a construcțiilor din zidărie (in Romanian);
4. Vasilache M., Pruteanu M., *Construcții din zidărie.Curs.Îndrumător de proiectare*, Ed. Soc. Acad. "Matei-Teiu Botez", Iași, 2014, (in Romanian);
5. Stratan A., *Dinamica structurilor şi inginerie seismică*, Ed. Orizonturi Univers, Timişoara, 2007 (in Romanian);
6. SR EN 1991-1-1:2004/NA-2006, Acțiuni asupra structurilor, Partea 1-1, Anexă națională;
7. SR EN 1991-1-3:2005/NA-2006, Acțiuni asupra structurilor, Partea 1-3: Acțiuni generale – Încărcări date de zăpadă, Anexă națională;
8. https://wiki.csiamerica.com/display/etabs/Home
9. Neophytou, V., Etabs Modelling, 2013;
10. http://storage0.dms.mpinteractiv.ro/media/1/186/3927/11538171/6/harta-romaniei-in-intensitati-infp.jpg
11. Pop M., *Inginerie seismică. Curs*, 2010 (in Romanian);
12. http://www.publika.md/siguranta-la--cutremur-o-prioritate-in-republica-moldova_1497171.html
13. Pruteanu M.,Crețu C.,Vasilache M., *Comparative Study Regarding the Choice of Structural System for Buildings with Regular Plan Configurations in Seismic Areas*, "Intersecții" Journal, pages 15-24, vol.13, 2016, No.1.

"Computational Civil Engineering 2017", International Symposium
Iasi, Romania, May 26, 2017

Simulating Panic Effect on Crowd Evacuation

Ioana Olteanu[1], Mihai Budescu[1], Lucian Soveja [1] and Gheorghe Ionica[2]
[1]*Structural Mechanics Department, Gheorghe Asachi University, Iasi, 700050, Romania*
[2]*S.C. ALTISCAD, Bucharest, Romania*

Summary

Panic is a condition in which an individual can arrive suddenly when in its environment different stimuli appear, meaning excitatory factors which may cause a reaction to the body, more or less controlled. This can be amplified by another person or by a group that is subject to the same stimuli, usually transforming it in a violent terror. In this case, the judgment of an individual comes to be dominated only by the primary instinct of survival forgetting about others.

In the category of stimuli that can cause panic are: fires, earthquakes, impossibility to leave a space, various transportation accidents, an outbreak infection etc.

That means that the spaces in which crowded situations appear must be designed so that emergency evacuation, when panic stimuli arise, to occur normally with no injuries or casualties. Such situations can be prevented by sufficient exits properly signposted and calibrated with respect to their maximum capacity and through education. Education is extremely important and must be repeated regularly in order to replace fear with individual judgment. Unfortunately, this is superficially considered by the authorities leaving everything to those who conceive the buildings. Moreover, there are some special buildings that are not taken into account, such as churches, which have only one exit.

Evacuation scenarios can be simulated only by specialised software in which certain parameters, such as stampede, the appearance of human or material obstacles, etc., are difficult to enter.

This paper proposes some ways of adapting the existing software sin order to meet specific requirements, leading to delays in people evacuation in case of panic stimuli.

KEYWORDS: evacuation, panic, software, stampede

1. INTRODUCTION

Mass evacuation has several definitions in the literature. All of them have some common factors like a mass of people is involved, a threat to life is perceived and there must be a reasonable chance that within a limited time to be able to escape from danger (Drury & Cocking, 2007). When analysing mass evacuation it is important

to consider people psychology and how their behaviour depends on several factors, as personal matters and if the person is alone or in a group when the danger occurs. At the same time, different individual factors can certainly be expected to vary with gender and the cultural, social and geographical environment.

Gender differences are found from the earliest stages. When a person first notice that there is a possible emergency going on, men usually search for more information than women do. Later women tend to warn others then leave the building. Women use to seek for help, in contrast to men, who more often try to search for people who are trapped (Canter, et al., 1980).

How a person handles a certain situation depends on a lot on the environment as well as the surrounding individuals. The social influence refers to the effect of surrounding people and their behaviour in the evacuation process. The fear of making a fool of themselves often leads to delayed decision times. Nevertheless as someone in the group takes the first step, and for example, begins to walk to an exit door or just stands up, others are likely to follow (Nilsson & Johansson, 2009).

When a person joins a high-density group of people, e.g. religious ceremonial, the individuals will most likely change their usual attitude and mentality. The article considers psychological crowd (people attending a religious ceremonial), without analysing the behaviour of an aggregate crowd (the occupants of a supermarket) (Friberg and Hjelm, 2014).

The panic effect will be considered in the analysis and several cases will be reviewed. Keating defined panic as a concept of four elements (Fahy, et al., 2009): hope to escape through dwindling resources, contagious behaviour, aggressive concern about one's own safety and irrational, illogical responses. Meanwhile, the Oxford English Dictionary considers panic: “a sudden feeling of alarm or fear of sufficient intensity or uncontrollableness as to lead to extravagant or wildly unthinking behaviour, such as that which may spread through a crowd of people; the state of experiencing such a feeling. Also: an instance or an episode of such feeling; a scare” (Panic, 2014).

2. CROWD MODELING

A crowd is not simply a collection of individuals. The behaviour of an individual may be affected by others in the crowd, which may depend on various physiological, psychological and social factors. In order to reduce casualties in case of mass gatherings research is being conducted all around the world. There have been implemented three modelling approaches: flow-based, particle/entity-based and agent-based (Zhou, S. et. al. 2010):

- *flow-based approach*: models a crowd as a continuous flow of fluid, neglects the features of individuals;
- *entity-based approach*: individuals are modelled as a set of homogeneous entities, some global emerging phenomena such as jamming and flocking can be generated by these models;
- *agent-based approach*: models each individual in a crowd as an intelligent and autonomous agent, which may have capabilities to behave in the simulated world ranging from reacting to certain events to adapting to the complex dynamic environment. This approach also allows for more behavioural factors to be considered.

Another important aspect is the behavioural factors which were divided into three categories. The *physical factors* refer to those external tangible characteristics of an individual such as position, moving speed, appearance and gesture, etc. The *social factors* are also tangible factors, which considers that human behaviour is also influenced by a wide variety of social factors, such as culture, social norms, family ties and leadership etc. The computational models that incorporate these factors are usually based on social theories and observations from social studies. The *psychological factors* such as emotion play an important role in human decision making.

Several phenomena can be identified when evacuating a crowd. Some of the most common ones is reviewed below.

Counterflows is arisen when different flows meet each other. Lanes are often formed when humans are walking in the same direction (Helbing, et al., 2002).

When the natural flow of pedestrians cannot continue due to an obstacle (door, corridor) that does not allow the entire flow to get through at once, a *bottleneck* situation occurs (Drury & Cocking, 2007). If the pressure over a bottleneck gets too high, the opportunities to evacuate can be paralysed. When this actually happens, it can also be very difficult to reduce the already built up pressure, as well as to release the people who have been trapped. The people in the back do not know how the situation actually looks, the pressure often continues. This was the cause of the very tragic disaster, which occurred during the discotheque fire in Colectiv, Bucharest, 2015.

When density variation occurs, *stop and go waves* are formed. In the areas where the density in lower, the speed is higher, meanwhile, where the density increases the flow speed decreases significantly.

When the density of a crowd becomes even larger than what has been presented under stop and go waves, *turbulence* sometimes occurs. This can be compared with the aftermath of an earthquake, where various forces randomly are distributed in all the different directions (Ma, et al., 2013). With a density of about 8 persons per

square meter, there is no longer any space between the persons, at this stage waves can move the individuals up to 3 meters in lateral directions. Crowd turbulence has for example been proven to be the cause of the Love Parade disaster (Helbing & Mukerji, 2012).

Stampede is another main cause of crowd disasters. It represents a collective rush of people towards either united direction or destination or in a random manner (Still, 2014).

3. CASE STUDY

3.1. General information about structures

A general classification of the structural typology of Romanian Orthodox churches based on the plan view shows three major types: rectangular, trefoil and Greek cross, fig. 1. According to the specific architectural conception, the typical spatial structure of an Orthodox church consists of a well-established sequence: narthex, nave and altar.

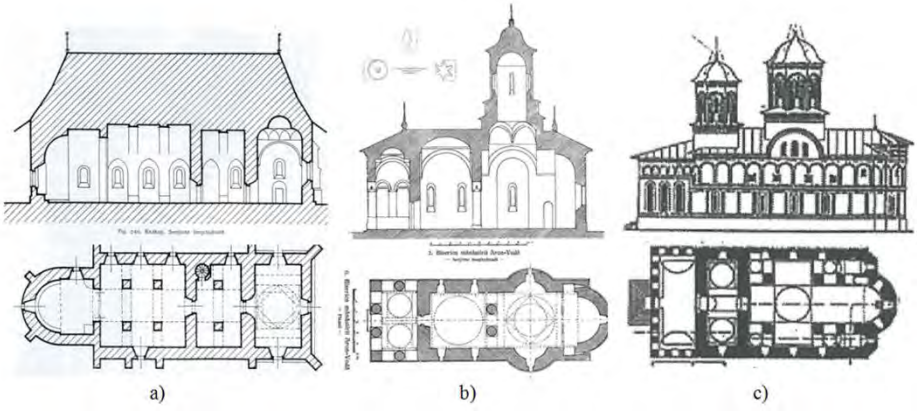

Figure 1. Structural typology of orthodox churches

The orientation of the church is symbolical, with the altar to the east. After the nave, the altar apse follows delimiting the church to the east. The altar is slightly elevated compared to the nave being separated from the latter by the iconostasis. Compared with the initial/classic orthodox structure, architectural innovations have resulted in slightly alteration of spatial configuration of the nave, in adding spaces with specific functions (crypt, exonarthex) or by the presence of a symbolic number of domes or towers.

On average, the areas for visitors in Romanian Orthodox churches varies from 85 m^2 to 160 m^2 depending on their size and the presence of the closed porch.

The case study was performed on Aroneanu church which was previously analysed by the authors (Budescu et al., 2016). The structure of the church, Figure 2 respects the classic plan of churches from that era. To the west, the nave is extended by a porch. The church tower rises above the nave, resting on a star which is supported by a square base. The church has an area of 110 m^2, from which the only 93m^2 is for the visitors.

It is considered that during the main religious ceremonies like Easter, Christmas and other important celebrations, the number of Christians attending the mass increases significantly. Among these elders or people with disabilities may be present. In the case of an imminent need for evacuation this category may represent real obstacles or may only slow down the process. Another specific category is represented by the participants which are very focused on the ceremony and do not get the dangerous event happening next to them. The case studies focus on different restrains in the evacuation process. These were introduced in order to simulate to bottleneck effect, the pre-movement stage in which the announcement about the stringent evacuation due to a natural disaster (earthquake), the different behaviour of the crowd and so on.

Figure 2. Aroneanu Church – exterior view

3.2. Software characteristics and input data

Pathfinder, which is an evacuation simulating computer program, is one of the latest tools that have been developed and are used by today's engineers. Pathfinder uses

Agent-Based Modelling. The purpose of the program is to facilitate the work, but also to improve the results and the validity of simulations that regards mass evacuation. The program can treat tens of thousands of spectators. It is based on simulations with a large number of spectators, all with their own individual characteristics. The subjects are assigned goals, characteristics and perceptions. This can be applied to larger groups as well as to each individual. The program is based on artificial intelligence, which means that the individuals also are able to adjust, based on other peoples' movement. This allows people to avoid colliding with each others. It also means that the subjects do not strictly need to follow the shortest path principles. Something that naturally gives a better flow of the pedestrians compared to other models, which are based on different calculations. Pathfinder is built from a coordinate system in 3D, the structure of the system can be created directly from the program, but can also be imported from other applications, such as CAD software. During a simulation, the user can follow the progress, pause or rewind, just like in a regular movie (Thornton, et al., 2010).

The total number of an occupant, 85, was divided unequally into three groups, justified mainly by the fact that people tend to clutter as close as possible to the altar where the religious ritual takes place. Group 1, G1, contains 10 persons with a density of 1.3pers/m^2 and it was the closest to the door. The second group, G2, has a density of 1.5pers/m^2 with a total of 25 people and is located in the middle. Group 3, G3, is located in front, in front of the altar and contains 50 people with a density of 1.8pers/m^2, Figure 3. The density represents the number of occupant per area and can be controlled by the user.

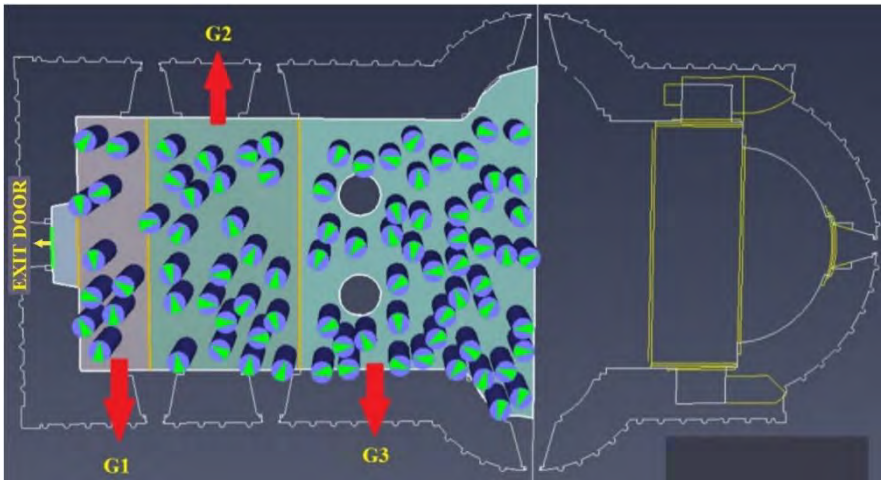

Figure 3. Crowd distribution

The following input data were considered: average walking speed - 1.19m/s, one narrow exit (0.88m) and a person shoulder width of 45.58cm. Among the considered

parameters are the ones specific to the steering mode: acceleration time of 1.1s, persist time of 1s, collision response time 1.5s and comfort distance of 0.08m.

The acceleration time specifies the amount of time it takes for the occupant to reach maximum speed from rest or to reach rest from maximum speed. The resulting forward acceleration of each occupant is max_speed/accel_time. The occupant uses a separate reverse acceleration of 2*forward_acceleration and a separate lateral acceleration of 1.5*forward_acceleration (Pathfinder, user manual)). The persist time refers to the amount of time an occupant will maintain an elevated priority when trying to resolve movement conflicts. The collision response time controls the distance at which an occupant will start recording a cost for colliding with other occupants when steering. The comfort distance specifies the desired distance one occupant will try to maintain with others in a queue. This may be entered explicitly as a distance, an occupant area, or an occupant density.

Seven cases were analysed. The first one, C1, represents also the initial condition, performs the analysis without any supplementary adjustment.

In case 2, C2, the authors considered a delay of the 30s for G2 in order to simulate the specific pre-movement actions of the people in the considered group (supplementary questions, the search of relatives or close friends, waiting for others to start moving and so on). It was considered that in the case of a dangerous event, for example, earthquake, the first to evacuate will be G1 and G3, which being close to the altar will hear and react faster to the priest directions.

In C3 two obstacles with the dimension of 0.88m were introduced as doors between G1 and G2, G2 and G3 respectively, Figure 4. The same delay was considered for G2.

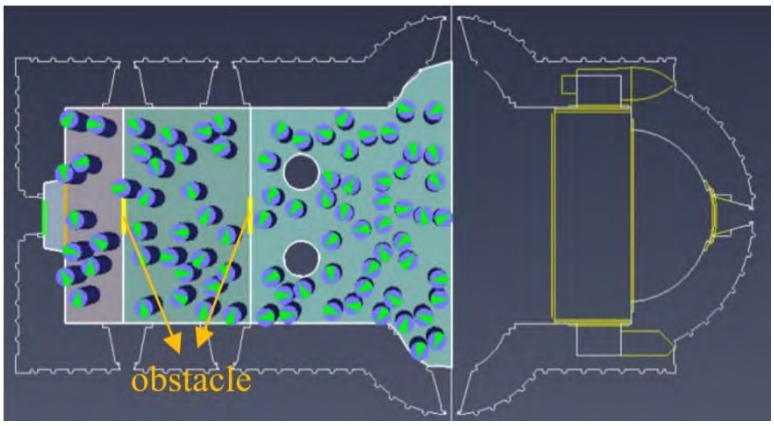

Figure 4. Obstacle distribution

For cases 4, 5, 6 and 7 a smaller speed was considered for G2, 0.5m/s^2. C4 does not use obstacle nor delay, meanwhile, C5 considers also the delay, but it ignores the

obstacles. C6 and C7 focus on the effect of the obstacles, C6 ignoring the delay and C7 considering it.

3.3. Results and discussions

A synthesis of the total required time to evacuate the entire crowd for each case is presented in Figure 5. It can be noticed, that C1, when no restrictions were applied leads to the minimum necessary time. Even though this maximum evacuation time is not realistic. It can be concluded that in order to fully evacuate the church in case of a disaster more than two minutes would be necessary for the most unfavorable case, C7. If we consider this information it can be stated that is possible that some of the Christians attending the ceremony might not be able to evacuate safely.

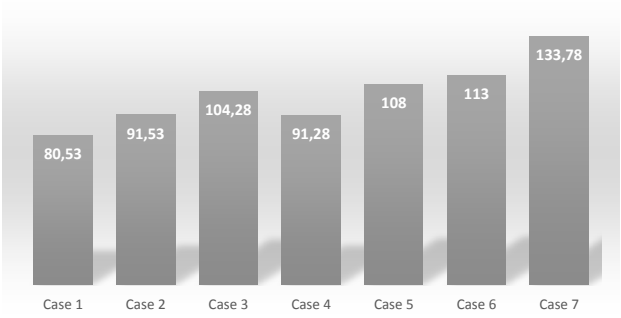

Figure 5. Total evacuation time synthesis in seconds

From Figure 6 in can be concluded that the most dangerous situation would be for C7, where only 21 people will be evacuated in the 30s and 33people will be evacuated in 60s. It is also noticed, that if the number of exited persons would be considered, for the 30s, C5 gets closer to C1. This is because G1 evacuates first (10 people) and in this time people from the G3 approach the door and the flow evacuation is constant until a bottleneck effect is produced.

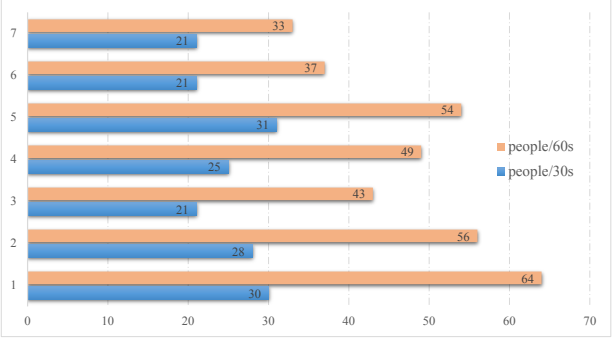

Figure 6. Number of people evacuated in the 30s and 60s

Other important comparisons which can give relevant information regarding the evacuation process refer to the flow rate through the main exit door and the intermediate doors/obstacles placed between the considered groups. Figure 6 presents the flow rates for the analysed cases.

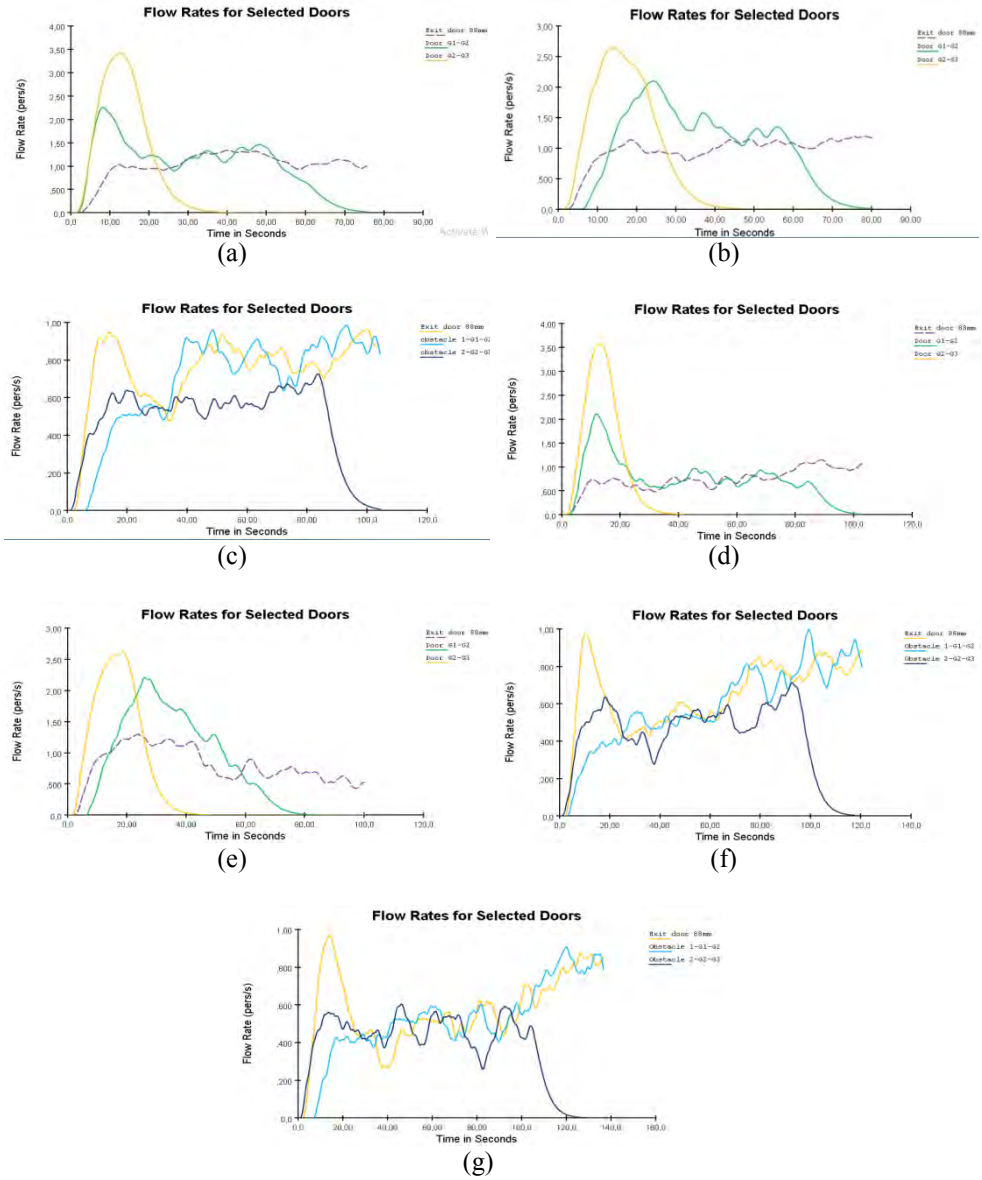

Figure 6. Flow rate for: (a) C1; (b) C2; (c) C3; (d) C4; (e) C5; (f) C6; (g) C7

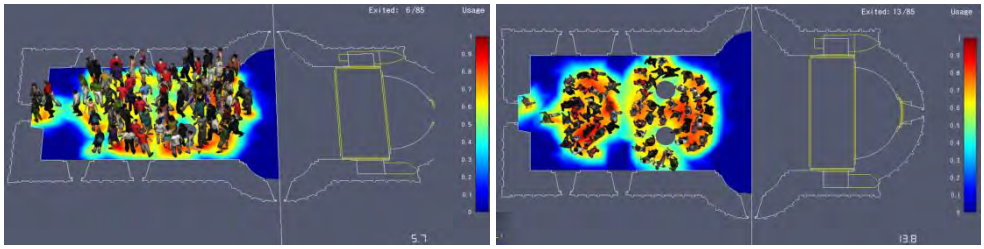

(a) (b)

Figure 7. Instantaneous usage for: (a) C3 and (b) C6

Figure 7 presents some print screens taken from the evacuation process with the instantaneous usage of the surface. Only two cases are presented due to lack of space. These photos show how the crowd is going to the exit and how they are distributed in the considered area. The effect of the bottleneck caused by the introduced obstacles is obvious in Figure 7(b).

4. CONCLUSIONS

Pathfinder software is among the most used software for simulating evacuation situations. The software allows the introduction of several parameters: number of people, speed, direction, delays and so on. With all this, there are some particularities that are not yet implemented in the software - stampede or bottleneck effect, or panic.

Based on the heterogeneity of people attending the mass gathering in general, religious ceremonial in particular several situations may occur that might slow the evacuation process. In order to simulate these obstacles were introduced. More detailed analysis is taken into consideration in order to modify parameters of each person, and not for an entire group.

Also, the human behaviour in cases of panic or disaster can lead to jams in the evacuation process. The changes in the human behaviour in case of a limit situation - the desire to survive, the fear for own life, should be also considered in further studies.

The current study shows that the characteristics of this type of structure – one narrow exit, might lead to severe human losses in case of a disaster due to difficulties to evacuate.

More complex studies should be done on structures with the same functionality in order to obtain some common lines. Based on the building vulnerability, estimates on the evacuation time required are targeted by the authors. Justified limitations should be imposed regarding the number of people who can enter a building at once

in order to allow a constant evacuation flow with reducing to a minimum the number of causalities.

ACKNOWLEDGEMENTS:

The authors are grateful to Thunderhead Engineering Consultants Inc. USA for providing Pathfinder.

References

1. Drury, J. & Cocking, C., 2007. The mass psychology of disasters and emergency evacuations: A research report and implications for practice, Brighton: Univeristy of Sussex.
2. Canter, D., Breaux, J. & Sime, J., 1980. Domestic, Multiple Occupancy, and Hospital Fires. In: D. Canter, ed. *Fires and Human Behaviour.* New York: John Wiley & Sons, pp. 117-136.
3. Nilsson, D. & Johansson, A., 2009. Social Influence during the Initial Phase of a Fire Evacuation - Analysis of Evacuation Experiments in a Cinema Theatre. *Fire Safety Journal,* 44(1), pp. 71-79.
4. Markus Friberg and Michael Hjelm, Mass evacuation - human behavior and crowd dynamics - What do we know?, Department of Fire Safety Engineering, Lund University, Lund 2014
5. Fahy, R. F., Proulx, G. & Aiman, L., 2009. *'Panic' and Human Behaviour in Fire,* London: Interscience Communications Ltd.
6. Panic, 2014. *Oxford English Dictionary.* [Online] Available at: http://www.oed.com/view/Entry/136852?rskey=Zi9sKJ&result=2&isAdvanced=false#eid
7. Zhou, S., Chen, D., Cai, W., Luo, L., Low, M. Y. H., Tian, F., Tay, V. S-H., Ong, D. W. S., Hamilton, B. D., 2010, Crowd modeling and simulation technologies, ACM Transactions on Modeling and Computer Simulation, http://hdl.handle.net/10149/118022.
8. Helbing, D., Farkás, I. J., Molnár, P. & Vicsek, T., 2002. Simulation of Pedestrian Crowds in Normal and Evacuation Situations. In: M. Schreckenberg & S. D. Sharma, eds. *Pedestrian and Evacuation Dynamics.* Berlin: Springer, pp. 21-58.
9. Helbing, D. & Mukerji, P., 2012. *Crowd disasters as systematic failures: analysis of the Love Parade disaster,* Zurich: Springer.
10. Ma, J., Song, W. G., Lo, S. M. & Fang, Z. M., 2013. New insights into turbulent pedestrian movement pattern in crowd-quakes. *Journal of Statistical Mechanics: Theory and Experiment.*
11. Still, G. K., 2014. *Crowd Risk Analysis and Crowd Safety Training.* [Online] Available at: http://www.gkstill.com/CV/ExpertWitness/CrowdDisasters.html
12. Budescu M., Soveja L., Olteanu I. (2016) Some Remarks Regarding Seismic Vulnerability for Orthodox Churches. In: Vacareanu R., Ionescu C. (eds) *The 1940 Vrancea Earthquake. Issues, Insights and Lessons Learnt. Springer Natural Hazards. Springer, Cham*
13. Thornton, C., O'Konski, R., Hardeman, B. & Swenson, D., 2010. Pathfinder: An Agent-Based Egress Simulator. In: J. D. Averill, E. D. Kuligowski & R. D. Peacock, eds. *Pedestrian and Evacuation Dynamics 2010.* New York: Springer, pp. 889-892.
14. Pathfinder 2015 – User Manual, http://www.thunderheadeng.com/downloads/pathfinder/users_guide.pdf

Assessment of internal forces from stress state by means of ANN

Alexandrina-Elena Pandelea, Mihai Budescu and Lucian Soveja
"Gheorghe Asachi" Technical University of Iaşi
Faculty of Civil Engineering and Building Services

Summary

ISANNIF is an image processing program (.png, .jpg, .bmp, .jpeg) using artificial neural network. The program can be used in Civil Engineering to determine the geometrical characteristics of the internal forces from a section taken as an image.

The input parameters of ANN are an image of the section with related dimensions, a chromatic map of the stresses and stresses values specific to each colour.

KEYWORDS: internal forces, neural network, stresses, chromatic map of the stresses, image processing.

1. INTRODUCTION

Most of the structural analysis programs with the finite element are designed to determine the values of stresses and specific deformations.

In the design of building structures is insufficient the knowing of tensions, so that it is necessary to integrate the stresses on the characteristic sections to obtain the efforts that are needed for the specific verifications in civil engineering. The intervention in the software part of these programs for this operation is sometimes very difficult, requiring specific programming knowledge.

A theory concerning the integration of normal or tangential stresses in a given area, which underlies these analysis programs with finite element consists in the approximation of surfaces with linear elements. This approximation leads to approximate numeric values of the internal forces in a section.

The *ISANNIF* software (*Intelligent System Artificial Neural Network Internal Forces*) was designed from the need to know the state of effort in any section of a structural element. The software is based on the processing of an image as .png, .jpg, .bmp, .jpeg, using an artificial neural network in Matlab programming language.

The program can determinate the state of efforts in any section of a structural element based on maps provided by the analysis programs with finite elements, without any kind of restriction. More, the program provides the state of internal force (moments) beside any axis imposed on a section.

2. THE SEQUENCE OF STAGES IN THE PROGRAM ISANNIF

2.1 Artificial Neural Network

In classical theories of image recognition issues, artificial neural networks of the feedforward type through local connection have been shown to have an advantage in extracting local features and combining them to form higher order features.

The receiving field of neurons from the hidden layer (which simplifies the processing without calculation) is not the same for the input layer, but it must be at best adjacent to avoid the possibility of losing information from the input layer. It is recommended to use two-dimensional squares layers and reception fields.

The ISANNIF program uses for the image processing a feedforward type artificial neural network, with three layers, which is free of feedback and is not recurrent. ANN consists of 3 neurons in the input layer, 3 neurons in the hidden layer and one neuron in the output layer.

The architecture of the artificial neural network for the ISANNIF program is shown in figure 1.

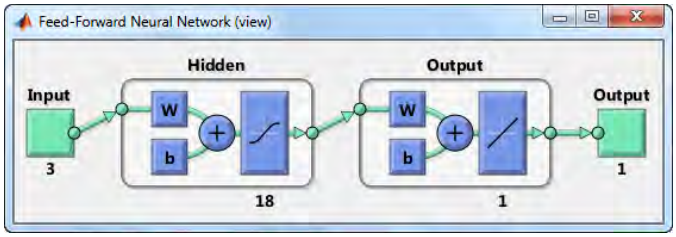

Figure 1. The architecture of neural network

Neural network input consists of an *RGB* matrix consisting of 3 lines and *n* columns M_{3xn}, where *n* is in the range [2,18] and represents the number of colours encountered on the image.

Neural network output is a matrix formed by one line and *m* columns, M_{1xm}, where *m* represents the numerical values of the internal forces associated with the colours of the matrix M_{3xn}. The numerical values number specific to tensions is one greater than the number of colours, since each colour is assigned both the maximum and the minimum values of stress level.

The activation functions used are tansigmoidal from the input layer on the hidden layer and linear from the layer hidden on the output layer.

2.2 The work steps of ISANNIF program

The graphical user interface of the program has been created with MATLAB GUIDE (*Graphical User Interface Development Environment*). *The initialize variables* require that to each object has to be assigned *handles* that allow the manipulation of the object properties. The program ISANNIF contain:

- the object named *„load tension image"*, an object that generates, after cutting the section from the image of the stresses, a colour matrix;
- the object named *„load colour map"*, an object that generates, following colour selection from the colour map, a matrix of colour-specific stresses.

With the resulting matrices and section sizes, the neural network is trained. The sequence of work steps is presented in the logic scheme of figure 2.

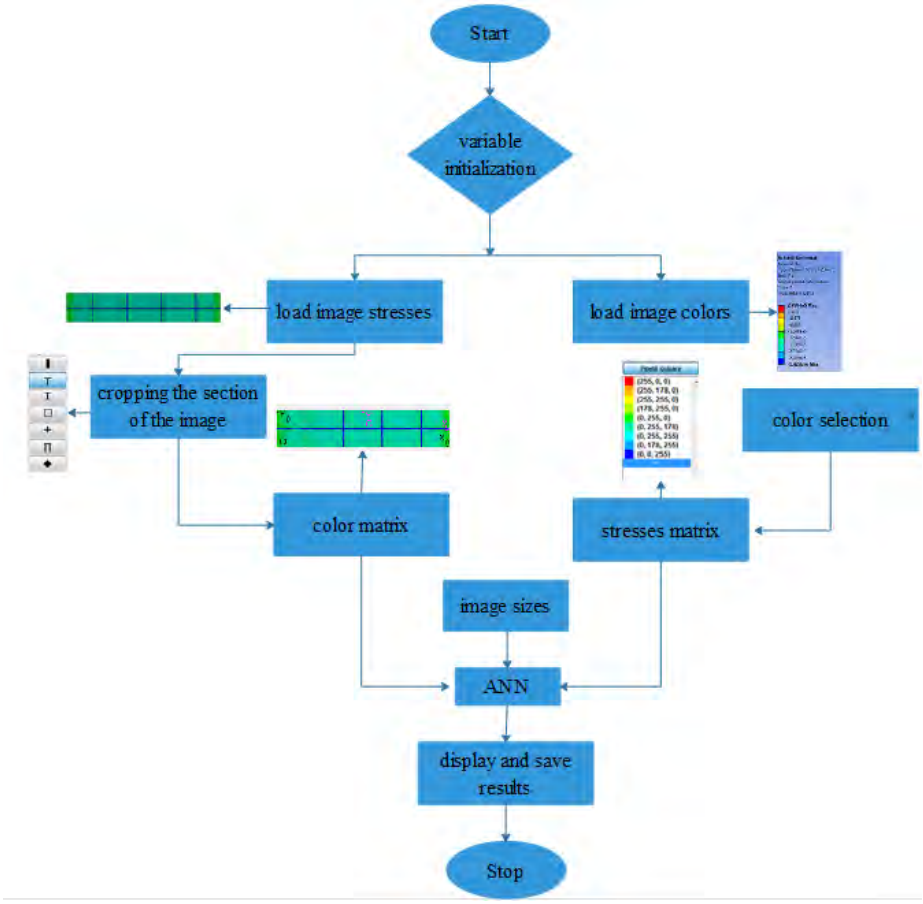

Figure 2. The logic scheme of program ISANNIF

2.3 The calculation stage of ISANNIF program

Using the results generated by the neural network we can determine:

- the gravity centre position (X_{OG} , Y_{OG})

The coordinates of the gravity centre are calculated as the arithmetic mean of x and y coordinates specific to all pixels in the section area.

- moments of axial inertia (I_x, I_y)

Calculation formulas specific to moments of inertia for a homogeneous section are taken from the Theoretical Mechanics. They are customised within the IASNNIF program being expressed in pixels. The section area is the product of the area of a pixel expressed in meters and the number of all the pixels from which the image is formed.

Moments of inertia are calculated by:

$$I_x = \frac{b_{pixel} \times h_{pixel}^3}{12} \times k + \sum_{n=1}^{k} (\left(x_{G_n} - x_G \right)^2 \times ratio(1) \times ratio(2)) \quad (1)$$

$$I_y = \frac{h_{pixel} \times b_{pixel}^3}{12} \times k + \sum_{n=1}^{k} (\left(y_{G_n} - y_G \right)^2 \times ratio(1) \times ratio(2)) \quad (2)$$

where:

b_{pixel} = the length of pixel expressed in meters;

h_{pixel} = the height of pixel expressed in meters;

k = the number of pixels from which the section is formed;

ratio(1) = the height of one pixel, in meters;

ratio(2) = the length of one pixel, in meters;

X_{G_n} = the position of the gravity centre of the n pixel in the x direction, related to the XOY system;

y_{G_n} = the position of the gravity centre of the n pixel in the y direction, related to the XOY system;

x_G = the position of the gravity centre of the section, in the x direction;

y_G = the position of the gravity centre of the section, in the y direction;

– the moment of centrifugal inertia (Ixy)

The moment of centrifugal inertia is calculated as the sum of the products of the four area specific terms: the differences in both directions between the position of the gravity centre of the n pixel and the section, and the pixel area expressed in meters on the x and y directions. The centrifugal moment, I_{xy}, can be determined with relation 3:

$$I_{xy} = \sum_{n=1}^{k}(\left(x_{G_n} - x_G\right) \times \left(y_{G_n} - y_G\right) \times ratio(1) \times ratio(2)) \tag{3}$$

– the main directions (α) and the main moments of inertia (I_1, I_2)

Both the main moments of inertia and their main directions are determined in the ISANNIF program with the formulas according to the literature.

- axial force (N), shear forces (V_x, V_y) and the bending moments (M_x, M_y)

The formulas of the internal forces in a section, used in the ISANNIF program, are highlighted as:

$$N = \sum_{i=1}^{k} \sigma^{k}_{medie\ norm,i} \times ratio(1) \times ratio(2) \tag{4}$$

$$M_x = \sum_{n=1}^{k} \left(y_{G_n} - y_G\right) \times \sigma^{k}_{medie\ norm,i} \times ratio(1) \times ratio(2) \tag{5}$$

$$M_y = \sum_{n=1}^{k} \left(x_{G_n} - x_G\right) \times \sigma^{k}_{medie\ norm,i} \times ratio(1) \times ratio(2) \tag{6}$$

$$V_x = \sum_{i=1}^{k} \sigma^{k}_{medie\ tang,i} \times ratio(1) \times ratio(2) \tag{7}$$

$$V_y = \sum_{i=1}^{k} \sigma^{k}_{medie\ tang,i} \times ratio(1) \times ratio(2) \tag{8}$$

where:

$\sigma^{k}_{medie\ norm,i}$ = the mean normal tension specific to k pixel;

$\sigma^{k}_{medie\ tang,i}$ = the mean tangential tension specific to k pixel;

the bending moments on a particular system (M'_x, M'_y)

In order to calculate the bending moments on a particular system, we need the position of the axes system $X'O'Y'$ in relation to the axes system X_OOY_O and the rotation of the system $X'O'Y'$. The formulas are expressed with:

$$M_x' = \sum_{n=1}^{k} y' \times \sigma_{medie\ norm,i}^{k} \times ratio(1) \times ratio(2) \tag{9}$$

$$M_y' = \sum_{n=1}^{k} x' \times \sigma_{medie\ norm,i}^{k} \times ratio(1) \times ratio(2) \tag{10}$$

The distances x' and y' are calculated using the relations:

$$y' = x\cos\beta - y\sin\beta \tag{11}$$

$$x' = x\sin\beta - y\cos\beta \tag{12}$$

where:

x = the position of the particular system in relation to the axes system X_OOY_O on x direction;

y = the position of the particular system in relation to the axes system X_OOY_O on y direction;

β = the angle of inclination of the particular axes system;

x' = the distance in the x-direction, calculated from the origin of the particular system to the centre of the i pixel;

y' = the distance in the y-direction, calculated from the origin of the particular system to the centre of the i pixel;

The program trains the artificial neural network with numerical values of normal stresses generating numerical values of the geometric characteristics (position of the gravity centre, moments of inertia, the moment of centrifugal inertia, main moments of inertia and main directions) and the internal forces from a certain section (axial force and the bending moments).

It is important to note that the particular calculus axes system can only be used after the neural network has generated the geometric characteristics.

Figure 3 shows the result after the first stage of training with the map of normal stresses for a T section.

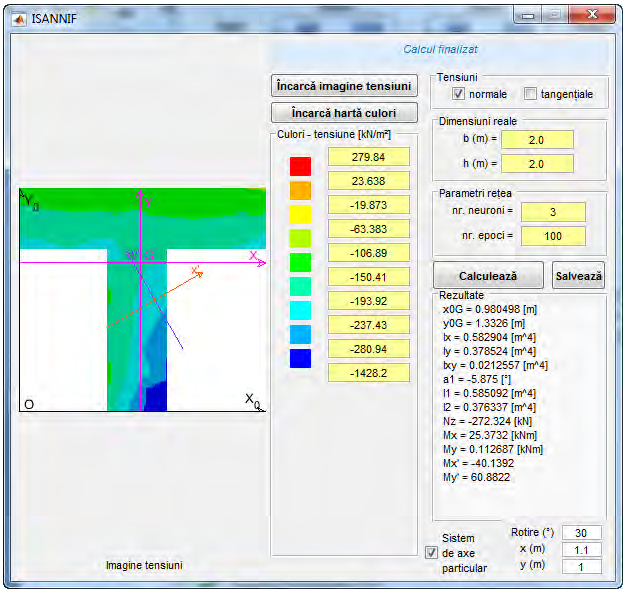

Figure 3. The results of the ISANNIF program for the first phase with the map of normal stresses

The training of the artificial neural network with numerical values of tangential stresses generates as results the shear force on the cross section. Figure 4 shows the calculation of the shear force for the T section presented above.

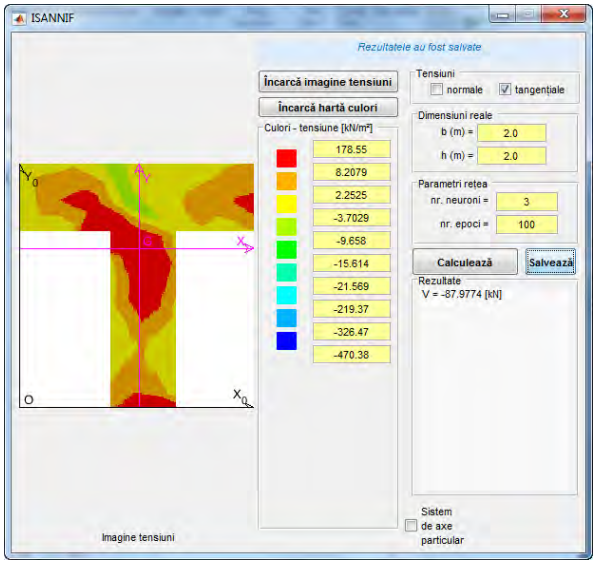

Figure 4. The results of the ISANNIF program for the second phase with the map of tangential stresses

3. CONCLUSIONS

In the design of building structures is insufficient the knowing of stresses, so that it is necessary to integrate the stresses on the characteristic sections to obtain the internal forces that are needed for the specific verifications in civil engineering.

The ISANNIF program offers the possibility to determine the internal forces (axial force, shear force, bending moment) in any section of any form, from a structural element based on the stress maps provided by the finite element analysis programs, with no restriction. The program allows the determination of bending moments in relation to an axes system positioned at any point of the section.

References

1. Beale M.H., Hagan M.T., Demuth H.B., *Matlab - Neural Networks Toolbox* – user guide, Mathworks Inc, 2015
2. Constantin Vertan, *Prelucrarea şi Analiza imaginilor*, Editura Printech, Bucureşti, 2000
3. Farnood Ahmadi F., Valadan Zoej M.J., Ebadi H.,. Mokhtarzade M., *The application of neural networks, image processing and cad-based environments facilities in automatic road extraction and vectorization from high resolution satellite images*, The International Archives of the Photogrammetry, Remote Sensing and Spatial Information Sciences. Vol. XXXVII. Part B3b., 2008.
4. Hage S., Hamade R., *Micro-FEM orthogonal cutting model for bone using microscope images enhanced via artificial intelligence*, Sciverse sciencedirect, pag.385-390, 2013.
5. Matcovschi M., Păstrăvanu O., *Aplicaţii ale reţelelor neuronale în automatică*, Ed. Politehnium, Iaşi, 2008

"Computational Civil Engineering 2017", International Symposium
Iasi, Romania, May 26, 2017

A numerical study on the behaviour of eccentrically braced frames in seismic areas using finite element analysis

Adina Vătăman[1], Adrian Ciutina[1] and Daniel Grecea[1, 2]
[1]*Department of Steel Structures and Structural Mechanics, Politehnica University of Timişoara, 300224, Romania*
[2]*Romanian Academy Timişoara Branch, 300223, Romania*

Summary

Eccentrically braced frames are a common structural typology in areas with seismic activity due to seismic energy dissipation capacity by deformation of the dissipative "link". The presence of the dissipative element allows the frame to withstand large seismic lateral forces by facilitating the formation of a plastic hinge in the link. In the case of short links failure occurs through shear of the web panel, in the case of long links failure occurs in bending, and in the case of intermediate link lengths, there is a combined effect. The current study is focused on eccentrically braced frames with short steel link element. There are many parameters that can influence the behaviour of the link, such as its length and slenderness of the steel profile, the presence of intermediate stiffeners or the presence of the concrete slab with or without shear connectors.

The current numerical study analyses the behaviour of eccentrically braced frames (EBFs) in the case of seismic loading, based on previous experimental data. The calibration of the numerical model is done by means of FEM software Abaqus while subjecting the model to both monotonic and cyclic loading. Due to the complex nature of the problem, different modelling solutions are investigated and compared.

KEYWORDS: EBF, Steel, Link, FEM.

1. INTRODUCTION

In the case of seismic loading, the steel Eccentrically Braced Frames (EBF) represent structures recognized for their good dissipation capacities. Such systems are characterised design by high values of the behaviour factor (q greater than 6 in ductility class high case), the seismic energy being dissipated by the formation of plastic hinges in the link elements. They represent elements highly loaded in shear and/or bending, in the case of lateral loads resisted by the triangulated adjacent systems. The formation of a plastic hinge in the link element allows for the other frame components to remain in the elastic domain, thus achieving local failure rather than a global failure of the structure.

The general philosophy in the design of steel structures states that the main concern in the case of the ultimate limit state is the limitation of deformations, in order to avoid important second order effects and other instabilities [1]. However, the formation of the plastic mechanism is aimed by design, in such a way that the plastic hinges form in elements with ductile behaviour. Thus, the ductility of the dissipative zones became of high importance in such cases, in order to allow plastic redistribution of forces [2].

In accordance with the European seismic norm – Eurocode 8 [3], short links are defined by their length $e_s < 1.6(M_{pl}/V_{pl})$ [mm] and are subjected preponderantly to shear. As proven by other authors [4], the link elements behaviour is very ductile proving high values of distortion of the order 120 to 200 mrad. On the other hand, structural simulations [5] on structures subjected to dynamic incremental analyses with accelerograms have proven that the limiting value proposed by EC8-1, § 6.8.2., of 80 mrad for short links in EBF might be insufficient for structures in high seismicity zones. However, as proven by Degee et al [6], the short links (vertical in this case) can assure adequate global structural dissipation capacities, having behaviour factors q as high as 6. Considering the stiffening of the dissipative link working in shear, Yurisman et al. [7], based on experimental tests performed numerical simulations on links with diagonal web stiffeners, showing their improved capacity in resistance. The experimental study performed by Okazaki et al. [8] in function of several parameters affecting the disposition and general form of web stiffeners leads to interesting results regarding link flange slenderness and the importance of an appropriate loading protocol.

Unlike the simple definition of the short link elements offered by EN 1998-1, the above-mentioned studies show that other parameters can influence the dissipative capacities of eccentrically braced frames, such as different loading conditions, the presence of stiffeners on the link element web, the length of the element or the slenderness of the link profile. The current paper is aimed at presenting the calibration of an experimental model using finite element analysis in order to investigate the influence of such details on the overall response of EBF with short steel link elements.

2. CALIBRATION OF NUMERICAL MODEL

2.1. Experimental Basis

A large experimental study was undertaken at the CEMSIG laboratory of the Politehnica University of Timisoara [9] concerning the behaviour of eccentrically braced frames with short link elements in different solutions (steel/composite) and

with different loading patterns (monotonic/cyclic). The reference specimen for the study was a steel EBF with a fixed short link element, loaded monotonically, EBF-LF-M. This is also the specimen that was used for the numerical calibration.

The testing sub-assembly was part of a larger dual frame structure (moment resisting frames + eccentrically braced frames) with five storeys and three bays (outer bays of 6m and an inner bay of 4.5m). The design has taken the seismic zone of Bucharest into consideration, using the following design details: $a_g = 0.24g$, $T_C = 1.6$ sec; a permanent load of 4 kN/m^2 and a live load of 3 kN/m^2.

The reference EBF specimen (denoted as EBF-LF-M) represents the first storey central bay of this structure. The beam is an HE200A profile (including the link zone of 300mm), columns are HE260B profiles, and braces are HE180A profiles, as it can be distinguished in Figure 1a. Although not required by design, the beam-to-column joints were designed as full-resistant (extended end-plate bolted connections) in view of transmitting the axial load. The columns were pinned at the base in order to reduce the lateral force in the actuators, see Figure 1b) for loading lay-out.

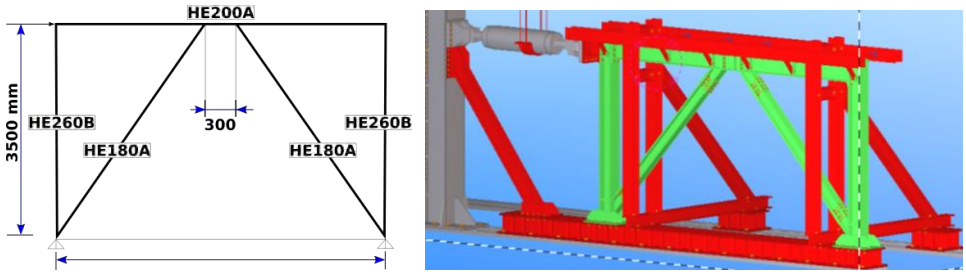

a) b)

Figure 1. a) Dimensions of the steel EBF specimen; b) Experimental lay-out

The loading of the sub-assembly was made using displacement control by means of a loading actuator placed at the top left corner of the frame on the column flange. The displacement of the frame was monitored by means of multiple displacement transducers. The maximum recorded displacement was 180mm and the testing procedure ended due to limitations of the technological equipment. The maximum displacement of 180 mm corresponds to a link rotation greater than 250 mrad, four times higher than the value mentioned in the norm (80 mrad in EN 1998-1). At maximum deflection, the web of the link suffered significant crippling due to shear force, as is shown in Figure 3d).

Figure 2a) shows the resulting force - lateral displacement curve, derived from the pushing load of the actuator and the lateral displacement of the left frame corner, monitored by means of a displacement transducer. Figure 2b) shows the derived V (shear force) – γ (distortion angle) curve of the link element, where V is computed

according to the static schema of the frame and γ represents the distortion angle of the link web, computed on the basis of displacement transducers located on the link itself (diagonal on the web panel). It should be mentioned that for the configuration presented, only the dissipative area of the link element has undergone plastic deformations, all other elements such as braces, columns and beams within the triangulated zone, as well as their connections exhibited elastic behavior. However, noticeable deformation was recorded in the brace and brace connections up to 4mm per brace, due to sliding of the connection elements.

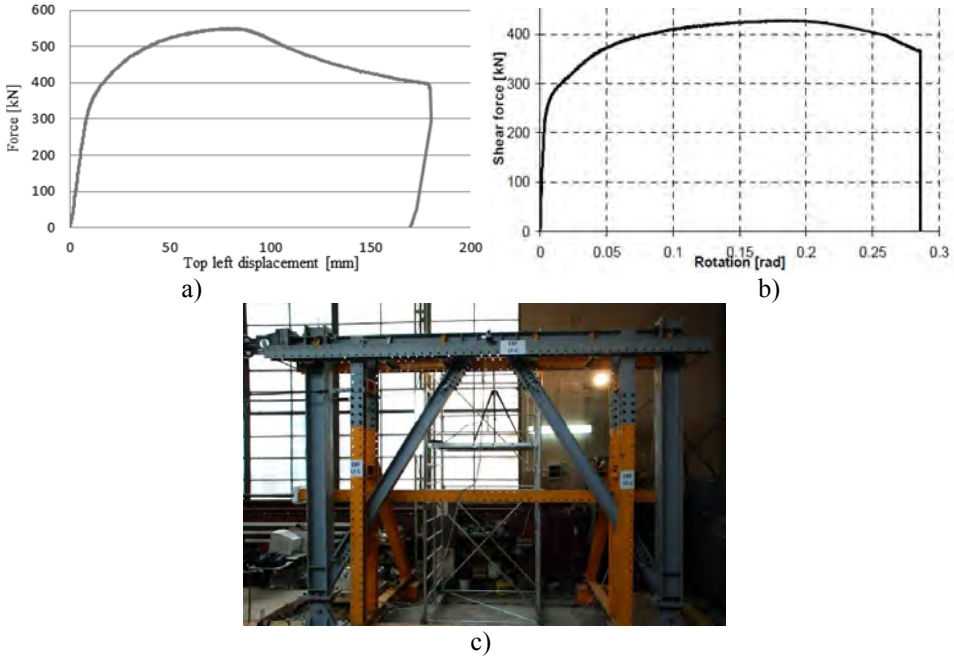

Figure 2. a) Force-displacement curve for steel EBF; b) Shear force-rotation curve of dissipative element; c) Experimental set-up

2.2. Finite element model and calibration

The numerical study which will be presented further was based on the initial experimental results. The numerical finite element model of the reference frame EBF-LF-M was created using finite element software ABAQUS 6.11-1 [10] by considering 3D solid frame elements, as shown in Figure 3. The model was assigned the name LS3-H0-M, corresponding to short steel link with the length of 300mm, with an H profile (HE200A) undergoing a monotonic loading procedure.

The model was assigned the same geometrical properties as the tested specimen. The link element was considered fixed as well and the column base connections

were considered to be pinned connections. The assigned material properties were corresponding to nominal values of materials, in compliance with the specifications from Eurocode 3 Part 1-3 [11], considering the results of coupon tests (see Figure 3b), but transformed in true stress-strain curves in case of the beam, including dissipative link [12]. These true stress-strain material properties were assigned only for the beam because initial analyses were in accordance to experimental testing proving that the rest of the frame elements remained in the elastic domain.

The analysis procedure used was Dynamic Explicit with a monotonically applied displacement of 180 mm on the top of the left column, similar to the maximum recorded displacement for the corresponding displacement transducer in experimental testing.

Hex type C3D8R finite elements have been used for meshing using a sweep technique and mixed medial axis and advancing front algorithms. Different finite element sizes have been used. An element size of 6mm was used for the dissipative part of the frame (link element and adjacent beam ends) as shown in Figure 3a). The frame components, which were expected to remain in the elastic domain, were assigned larger size elements: 25mm for columns and column stiffeners, 20mm for beam and beam stiffeners and respectively 15mm for braces.

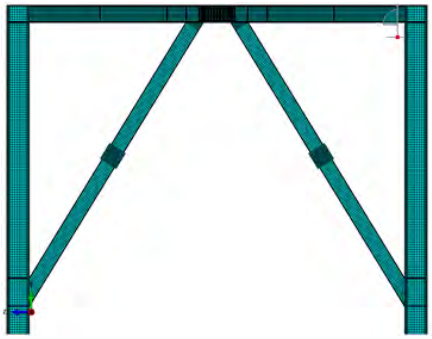

a)

Element profile		Measured steel yield strength	Tensile strain at break
		[N/mm²]	[%]
Beam web	HE200A	304	32.24
Beam Flange	HE200A	323	35.01
Column	HE260B	355	15
Brace	HE180A	355	15

b)

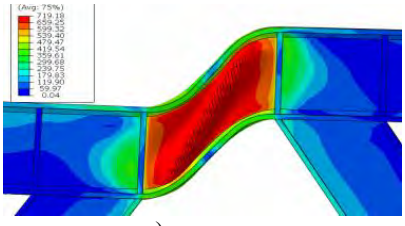

c)

d)

Figure 3. a) Mesh of the finite element EBF model; b) material characteristics used in calibration; The deformed shape of the dissipative link elements: c) FE Model d) Laboratory test

The resulting force-displacement curve (denoted as FEModel) followed the experimental response appropriately, as it could be observed in Figure 4a), however, the initial stiffness of the numerical model was slightly higher than that of the experimental model.

The displacement transducers recorded a slip of the bolted connections of the braces during experimental testing, so this was further integrated into the numerical model by a using a connector and a sliding element at the middle of the braces (Figure 4c). The connector was assigned a displacement law according to recorded values of elastic deformation considering a maximum 1.5mm slip at a force of 300kN. The finite element response corresponding to this situation is shown as curve FEModel+Slip in Figure 4 a).

As this additional effect was shifting the maximum resistance point, adjustments on the applied constraints and boundary conditions were considered for re-fitting the experimental results. The lateral supporting system of the beam consisted of 4 separate vertical parts assigned as rigid body along the length of the beam, positioned on the edge of the flanges.

As a consequence, the lateral supporting system of the beam had to be re-positioned along the length of the beam with a clearance of 2mm on each side of the beam. This allowed a limited out-of-plane displacement of the beam to take place as in the case of experimental testing.

The final numerical model containing all of these modifications can be seen in Figure 4a) as the force-displacement curve LS3-H0, which closely follows the experimental curve EBF-LF-M-DHTL, with less than 1% difference in values compared to experimental results.

Figure 4 b) shows the resulting deformed shape of the same eccentrically braced frame model. A comparison between the deformed shapes of the dissipative link element at the end of the analysis and at the end of experimental testing can be seen in Figure 3 c) and Figure 3 d) respectively. Similar failure modes can be observed, as the shear of the link web panel is quite obvious and distortion of the dissipative element takes place similarly.

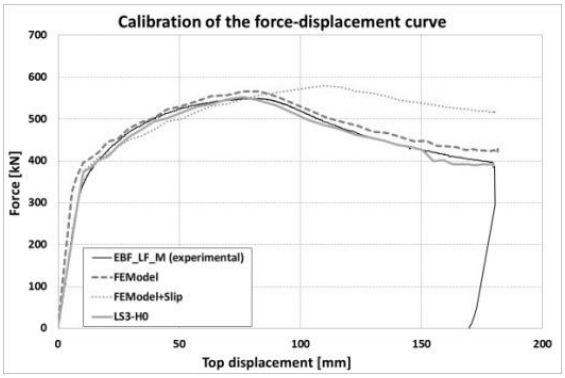

a)

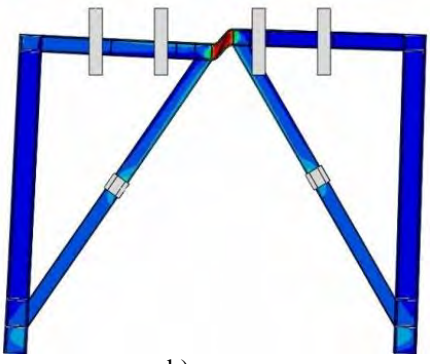

b)

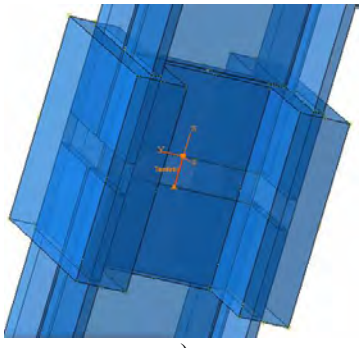

c)

Figure 4. a) Calibration of the force-displacement curve;
b) Deformed shape of calibrated EBF model; c) Detail of slip connector.

3. PARAMETRIC STUDY

After the initial calibration was achieved, a parametric study was performed in order to reveal the behaviour of the EBF when considering different parameters such as different link lengths, different configurations for link web stiffening, different link slenderness. Table 1 presents the different numerical models with notations and explanations of the parameters used for each model.

Based on the good initial results which were obtained, an additional model was created using a cyclic loading procedure, in order to quantify the difference in resistance and link distortion in the case of alternant lateral loads.

Table.1 Configurations of analysed EBF models under monotonic loading

Name of FE model	Number of stiffeners	Link section	Link length e [mm]	Name of FE model	Number of stiffeners	Link section	Link length e [mm]
LS3-H0 (Reference)	0	HE200A	300	LS4-H0	0	HE200A	400
LS3-H1	1	HE200A	300	LS5-H0	0	HE200A	500
LS3-H2	2	HE200A	300	LS6-H0	0	HE200A	600
LS3-I0	0	IPE240	300	LS7.5-H0	0	HE200A	750
LS3-I1	1	IPE240	300	LS4-I0	0	IPE240	400
LS3-I2	2	IPE240	300	LS5-I0	0	IPE240	500
				LS6-I0	0	IPE240	600
				LS7.5-I0	0	IPE240	750

3.1. Link length parameterization:

The first analysed parameter was the length of the link, taking into consideration five different lengths. All of the lengths were within the limitations for short link elements, which in this particular case meant a maximum length of 760 mm. For lengths superior to this value, the dissipative element would be subjected to both shear and bending. The lengths which were used were 300, 400, 500, 600 and 750 mm respectively. The models were adapted in order to keep the original bay of 4.5m and changing only the angle of braces in order to accommodate the new link lengths.

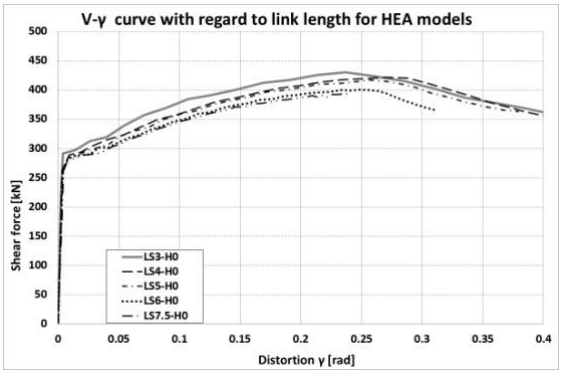

Figure 5. Shear force-distortion curve for different link lengths

Figure 5 shows the response V- γ curves in function of link lengths. A general trend could be observed, where the link length has little influence on elastic and post-elastic ranges: the elastic and ultimate strengths are decreasing with the

length, but the difference between the resistances is less than 10% for ultimate and elastic strengths respectively. However, by passing to larger lengths, such as 750 mm, the web loses its stability earlier, thus having a limited ultimate resistance and ductility.

This can also be seen in the case of the failure modes, presented in Figure 6. The links with shortest dimensions (300 to 400 mm) are characterized by a global-type shear plasticization while the longer link elements (500 to 750 mm) are characterized by web crippling on sides of the panel, while the other side remaining plain but with high levels of shear stresses.

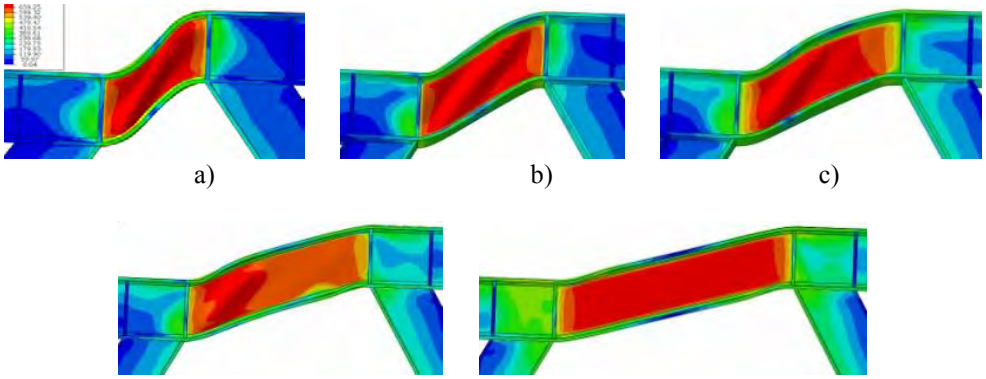

Figure 6. Deformed link shapes at the end of the numerical analysis:
a) 300mm length; b) 400mm length; c) 500mm length; d) 600mm length; e) 750mm length.

3.2. Link web stiffness parameterization:

The second parameter which was analysed was the influence of the stiffness of the link's web on the overall behaviour of the steel frame by comparing three configurations of web stiffening: one model considering no stiffeners on the dissipative link, a second model with one stiffener in the middle of the link (representing the normative solution) and a third model with 2 stiffeners on the link, at equal intervals from the centre and from the end of the link.

According to EN 1998-1 the link elements should be provided with intermediate stiffeners at maximum intervals in millimetres of ($30t_w$-d/5), with t_w being the web thickness and d the height of the cross-section of the link. Consequently, a maximum distance of 155 mm results in the case of an HE200A profile.

Figure 7 shows that the elastic behaviour, initial stiffness and the point of plasticization are practically independent of the number of stiffeners. However, there are important differences in the plastic range: the ultimate resistance of the

models' increases with the number of stiffeners and the same happens with the post-elastic stiffness (hardening stiffness).

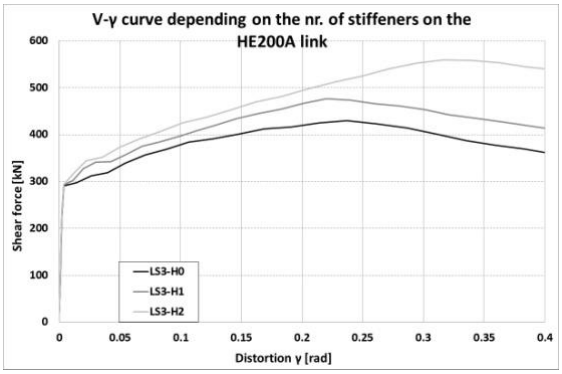

Figure 7. Shear force-distortion curves for different configurations of link web stiffening.

Considering the distortion capacity, all models showed high capacities, up to 0.4rad. The rotation of maximum load shifts from 0.24 to 0.32rad in the case of two intermediate web stiffeners, while for the other two models the difference is visible only in terms of resistance.

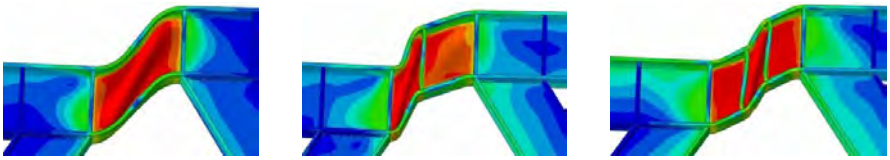

a) b) c)

Figure 8. Deformed shapes of the link elements at the end of analysis:
a) No stiffener; b) One stiffener; c) Two stiffeners.

It could be observed that in both cases additional stiffeners leads to division of the original shear panel into multiple panels, each of these having its own web deformation, as shown in Figure 8. The initial elastic deformations are shared among the panels, but in the post-elastic range the plasticization becomes concentrated in one of the panels, the other contributing only partially to the global deformation

3.3. Link web slenderness parameterization:

The third parameter, link web slenderness, was taken into consideration by transitioning from an HE200A profile to an IPE240 steel profile for the whole beam. The modification was made by considering the close shear areas of the two

profiles, but also the different web slenderness. The value for shear area A_v was computed according to Chapter 6.8 on design and detailing rules for eccentrically braced frames from EN 1998: Part 1. The resulting values for the shear area of the link of 1170mm2 for HE200A and 1427mm2 for IPE240 which represent reduced values for dissipative links, compared to the standard shear area of the two profiles of 1808mm2 respectively 1910mm2 as used for normal gravitational shear verifications. The web slenderness parameter was addressed by changing the profile from HE200A having a nominal web of 7x180 mm with a more slender profile IPE 240 with a web of 6.2x232,9 mm.

The other sections of the frame elements and the global geometrical dimensions remained unchanged. A comparison of the response of the two models is shown in Figure 9 in terms of shear force-distortion curves. Both responses are characterized by a three-linear behaviour:

- an initial elastic behaviour up to plasticization;
- a linear post-elastic hardening branch with important stiffness;
- a discharging branch with similar stiffness as for hardening.

An identical elastic behaviour could be observed when comparing the two responses, with the main difference present in the post-elastic zone: the model with the slender web (IPE profile) showed a slightly smaller maximum resistance, explained by a smaller shear area. This was accompanied by an important reduction in the distortion values corresponding to the maximum load. The local instability appeared earlier in the case of the slender web. For the initial HE200A profile the resistance is slightly higher than for the IPE240 profile, approximately 4%, but at much larger distortion values, of 0.236rad compared to 0.123rad for the slender web.

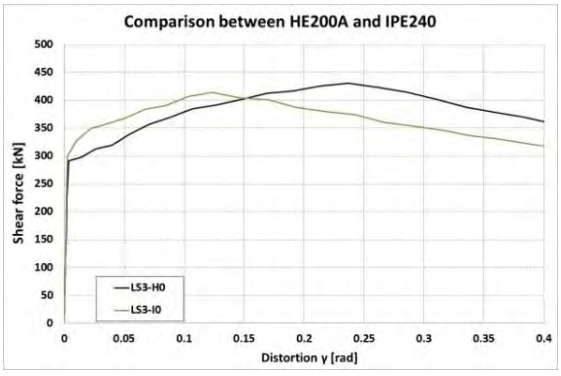

Figure 9. Shear force-distortion curve with regard to the web slenderness of the link element

In both models, a similar shear hinge formed and there was noticeable web crippling due to large horizontal differences of the two lateral sides of the dissipative element. The stress amplitudes outside the link panel were much smaller than those of the internal web itself. The deformed shape of the link elements is presented in Figure 10.

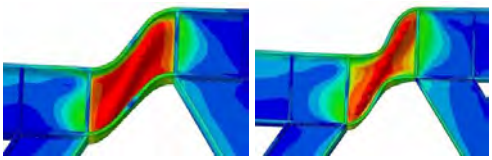

a) b)

Figure 10. Deformed shape of the link element at the end of analysis:
a) HE200A link; b) IPE240 link.

3.4. Monotonic versus cyclic loading:

A final parameter was considered during the study, the influence of cyclic loading compared to monotonic loading on the behaviour of the short dissipative element.

The reference model LS3-H0-M was loaded by displacement control up to 180mm as was done during experimental testing. For the cyclically loaded numerical model, it was necessary to perform a new calibration based on the experimental specimen EBF-LF-C, which was part of the same experimental study described earlier.

The cyclic loading procedure used during experimental testing followed the ECCS loading procedure [13]. Accordingly, three different amplitudes of 0.25Dy, 0.5Dy and 0.75Dy were applied in the elastic range. In the plastic range amplitudes of 1Dy, 2Dy, 4Dy, 6Dy and 8Dy were applied. In all of the above, Dy represents the yield displacement resulted from the interpretation of monotonic tests, in accordance with the ECCS procedure. The load application point is identical to monotonic testing, at the top of the frame and applied in displacement control.

The results from testing can be observed in Figure 11. The experimental response of EBF-LF-C specimen showed a ductile behaviour with good dissipation capacity of the link element with high values of distortion exceeding 150 mrad (Figure 11c). The maximum resistance was of 550 kN, as can be observed in Figure 11b). The failure mode was by alternate shear buckling of the link web panel in positive and negative cycles followed by tearing of the web panel (Figure. 12a).

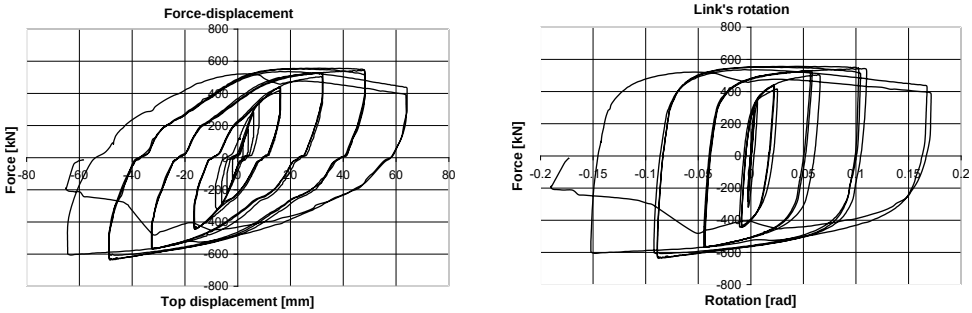

a) b)

Figure 11. a) Force-displacement curve; b) Shear force-rotation curve.

The numerical model LS3-H0-C of the tested frame EBF-LF-C, was created based on the previous numerical model LS3-H0-M by adding certain modifications characteristic for a cyclic loading procedure. The geometry and monotonic material properties of the reference specimen were maintained, but specific cyclic parameters were accounted for:

-Plastic material properties were assigned in order to provide a combined isotropic and kinematic hardening for beam steel material, including the dissipative link element;

-The cyclic material model adopted considered 5 back-stresses in order to accurately model the material behaviour, as suggested by Chaboche [14].

All frame members were modelled using solid finite elements. Hex type elements were used for meshing, considering a sweep technique with a mixed median axis and advancing front algorithms. The finite element size ranged from a fine mesh with 6 mm elements on the dissipative area of the frame (link element and adjacent beam area) to larger element sizes of 15 mm for braces, 20 mm for beam and beam stiffeners and 25 mm for columns and column stiffeners.

The same loading procedure was used as during experimental testing. As in the case of monotonic models, the slip in the brace connections had to be included in the analysis. This meant considering a rigid body element, which allowed the sliding (translation) of the brace and a connector that allows for an elastic spring elongation of the braces, using a behaviour law corresponding to experimentally recorded values. These values were different compared to those recorded during monotonic testing. The change in slip values from monotonic loading to cyclic has led to an increased initial stiffness, and also a better accuracy with the experimental restoring stiffness.

Figure 12 presents the experimental frame top-displacement curves for the experimental response (EBF-LF-C curve) and the finite element calibration (LS3-

H0-C curve). The numerical model was considered calibrated when a maximum 6% difference between experimental and numerical values was reached.

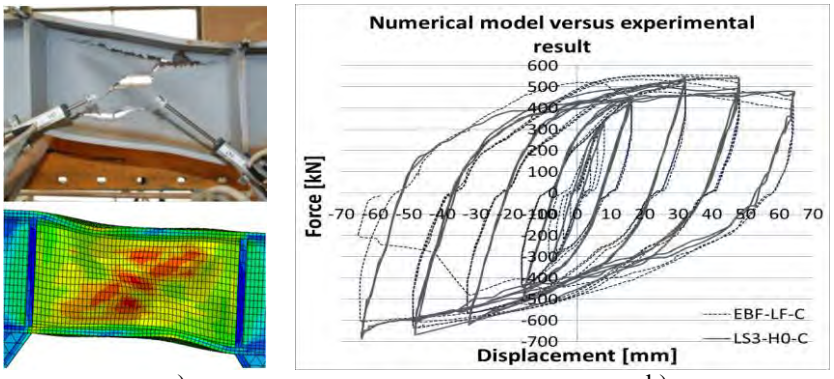

a) b)

Figure 12. a) Deformed shape of the link element at the end of experimental testing of specimen EBF-LF-C; b) Force-displacement calibration curve-experimental versus numerical response.

By comparing the values from monotonic and cyclic analyses it can be observed that the cyclic behaviour introduces a slight limitation in distortion capacity as compared to monotonic responses. However, these values remained higher than the limit value recognised by EN1998-1 of 80 mrad.

As in the case of experimental testing, the cyclic model showed similar values of elastic stiffness to the monotonically loaded model. The rotation of the link element in the case of cyclic loading is smaller than in the case of monotonic loading, but the model reaches higher values resistance for smaller values of link distortion.

4. CONCLUSIONS

The present study was focused on the seismic behaviour of eccentrically braced frames with short steel link elements. Based on a previously existing experimental study on a one-storey specimen, including both monotonic and cyclic loading, two numerical models were developed and calibrated on these experimental results. Further, a parametric study was accomplished based on different parameters: variation of link length, the variation of numbers of vertical intermediate stiffeners on the linked web, different loading procedures.

The study showed that numerically reproducing experimental results is achievable only by carefully defining geometric properties, material laws and testing details,

both in the case of monotonic and cyclic analysis. Details such as brace elongations or out of plane displacement of the element, though small (under 2mm) need to be accounted for.

The analysing of different parameters showed interesting results. The increase in the number of stiffeners induced higher shear resistances and improved the overall ductility of the frame, without influencing the elastic stiffness of the system.

The increase in link length (while still remaining in the range of short links) led to smaller maximum resistances and affected the elastic stiffness of the system significantly. Very short links presented a stiffness almost double compared to the links with a length bordering to intermediate length links.

The change of the beam steel profile from HEA to a more slender IPE profile had little influence on the initial elastic domain. The maximum resistance suffered a small decrease, but the major influence was noticeable in terms of distortion levels, which decreased to almost half the initial values for HEA.

In the case of cyclic loading, additional material parameters should be considered in order to control the cyclic behaviour of the entire frame. The Chaboche material model seems to be adequate in accurately modelling the cyclic material response.

The use of a cyclic loading procedure instead of a monotonic one induced both a reduction in maximum shear resistance and distortion capacity of the system. The reduction in shear resistance was up to 5%, while the reduction in distortions was approximately 10%.

However, in all the numerically analysed models the maximum link distortions satisfied the minimum normative requirements of 80 mrad, in accordance with EN 1998-1.

The current study was only focused on analysing the behaviour of short steel elements in eccentrically braced frames and could be broadened to investigate additional parameters, such as different types of stiffeners, longer link lengths exceeding the normative limitations for short link elements, detachable dissipative elements, the influence of the presence of a reinforced concrete slab over the beam, etc. Finite element numerical models seem to be a very accurate solution in predicting such behaviour.

ACKNOWLEDGEMENTS

The research was partially supported by the Sectorial Operational Program Human Resources Development POSDRU/159/1.5/S/137516 financed from the European Social Fund and by the Romanian Government.

References

1. Vayas I., Design of braced frames, *Seismic resistant steel structures*, Chapter 5, CISM Courses and Lectures, 420, 241-288, Springer Verlag Wien GmbH, , 2000
2. Gioncu V., Mazzolani F., *Seismic design of steel structures*, CRC Press Taylor and Francis Group, 2014.
3. European Committee for Standardization – CEN. EN 1998-1, *Eurocode 8: Design of structures for earthquake resistance - Part 1, General rules, seismic actions and rules for buildings*, 2004.
4. Stratan, A., Studiul Comportării Clădirilor Multietajate cu Cadre Metalice Duale Amplasate În Zone Seismice, PhD thesis, Universitatea Politehnica Timişoara, 1998.
5. Danku G., Ciutina A., Dubina D., Influence of steel-concrete interaction in dissipative zones of frames: II – Numerical study, *Steel and Composite Structures*, Vol. 15, No. 3 , ISSN 1229-9367, pp: 323-348, 2013.
6. Degée H., Lebrun N., Plumier A., Considerations on the design, analysis and performances of eccentrically braced composite frames under seismic action, *Proceedings of SDSS 2010 Conference –Stability and Ductility of Steel Structures*, 337-344, 2010.
7. Yurisman Y., Budiono B., Moestopo M., Suarjana, M., Behavior of shear link of WF section with diagonal web stiffener of Eccentrically Braced Frame (EBF) of steel structure, *International Journal of. Engineering Science*, 42(2), 103-128, 2010.
8. Okazaki, T., Arce, G., Ryu H.C., Engelhardt M.D., Experimental study of local buckling, overstrength, and fracture of links in eccentrically braced frames, *J. Struct. Eng*. – ASCE, 131(10), 1526-1535, 2005.
9. Danku G., *Study of the development of plastic hinges in composite steel-concrete structural members subjected to shear and/or bending*, Ph.D. Thesis, Politehnica University of Timisoara, 2011.
10. Dassault Systèmes Simulia Corp, Abaqus 6.11-1, 2011.
11. European Committee for Standardisation – CEN. EN 1993-1, 2005. *Eurocode 3: Design of steel structures*.
12. Arasaratnam P., Sivakumaran K.S., Tait M.J., True stress-strain models for structural steel elements, *International Scholarly Research Notices (ISRN) Civil Engineering*, Volume 2011, Article ID 656401, 2011.
13. ECCS TWS 1.3 N.45/86, 1986. Recommended Testing Procedure for Assessing the Behaviour of Structural Steel Elements under Cyclic Loads.
14. Chaboche J.L., A review of some plasticity and viscoplasticity constitutive theories, *International Journal of Plasticity,* 24(10), 1642-1693, 2008.

Benchmark Analysis between a Two-Zone Fire Model and a CFD Fire Model

Zeno-Cosmin Grigoraș, Mihaela Ibănescu
Faculty of Civil Engineering and Building Services, "Gheorghe Asachi" Technical University, Iasi, 700050, Romania

Summary

This paper presents the benchmark analysis between a two-zone fire model and a CFD (Computational Fluid Dynamics) fire model.

A fire from a conference room is modelled using CFAST and FDS computer software. Both computer programs use advanced fire models based on energetic equilibrium.

The HRR (Heat Release Rate) curve is modelled according to the European legislation.

The aim of this benchmark analysis is to compare the temperatures computed by different fire models.

KEYWORDS: two-zone fire model, CFD fire model, FDS (Fire Dynamics Simulator), CFAST (Consolidated Model of Fire and Smoke Transport), fire safety engineering.

1. INTRODUCTION

The computer programs are tools that offer the possibility of "numerical experiments" in "virtual laboratories" at lower cost (compared to "physical experiments" in "testing laboratories") and with the credibility of the obtained results within the limits of the engineering acceptability [1].

The fire safety engineering approach uses complex mathematical models that describe the fire development.

This paper is based on a benchmark analysis between two different fire models: a two-zone fire model and a CFD (Computational Fire Dynamics) fire model. Both models use the energetic equilibrium to describe the fire development.

This study is performed in a conference hall located at the Faculty of Civil Engineering and Building Service from Iasi, Romania. The geometry of the analysed space is presented in Fig. 1, and the interior of the considered space is presented in Fig. 2 and Fig. 3.

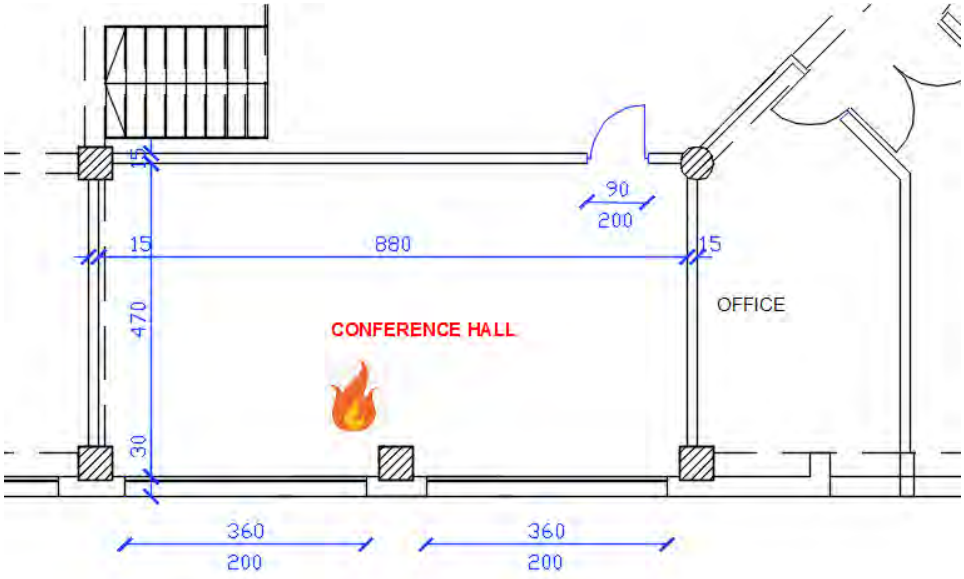

Figure 1. The geometry of the analyzed space – conference hall

Figure 2. The interior of the conference hall

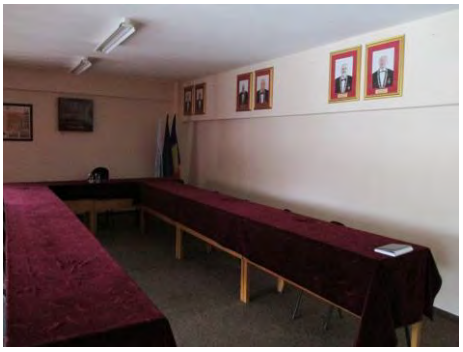

Figure 3. The interior of the conference hall

The walls of the analysed space are made of 15 cm brick; the upper and lower slabs are made of 15 cm of reinforcing concrete, 15 cm in thickness. The main combustible material is wood.

2. FIRE DEVELOPMENT AND COMBUSTION MODELING

The fire load density was considered in compliance with the European codes [2,3] 420 MJ/m^2, corresponding to office type spaces. The fire development was

modelled by considering different scientific works [4], in addition to Eurocodes. The Heat Release Rate (HRR) curve is shown in Fig. 4: one stage fire development fire (growth stage) with a peak HRR of 456 kW at 202 seconds.

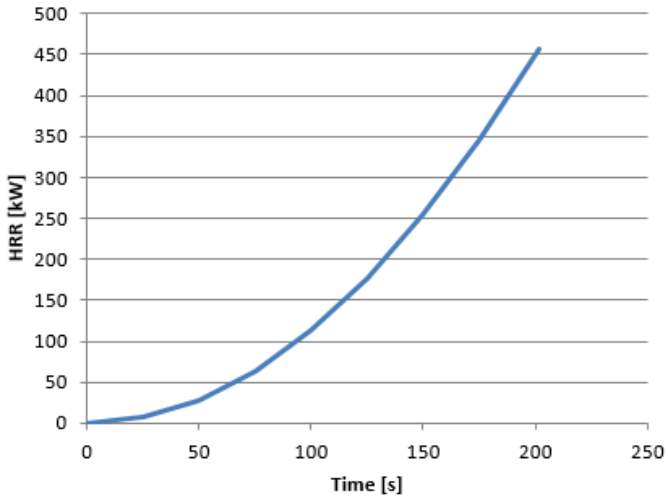

Figure 4. The geometry of the analysed space – conference hall

For this case study, the burning reaction of wood was simulated according to [4]. The combustion model involves the existence of a single fuel that is composed primarily of C, H, O and N that react with oxygen in one mixing-controlled step to form H_2O, CO_2, CO and soot [4]. The fuel properties are described in Tab. 1.

Table 1. The fuel properties

User input data	Value
Carbon atoms	1
Hydrogen atoms	1.7
Oxygen atoms	0.72
Nitrogen atoms	0.001
Heat of combustion [kJ/kg]	17500
The fraction of fuel mass converted into CO	0.004
The fraction of fuel mass converted into smoke particles	0.015

Another important aspect considered during the performed simulations is the thermal transfer to walls and slabs. The considered thermal properties are presented in Tab.2.

Table 2. Thermal properties of walls and slabs

User input data	Unit	Walls	Slabs
Material	-	brick	concreate
Thickness	cm	15	15
Density	kg/m^3	2000	2500

User input data	Unit	Walls	Slabs
Specific Heat	kJ/(kg·K)	0.87	0.84
Conductivity	W/(m·K)	1.16	1.74
Emissivity	-	0.94	0.95

3. FIRE MODELS

The scientific understanding of fires has created the possibility of treating them as phenomena and subsequently, led to the engineering approach to fire safety. This field uses scientific and engineering principles for and controlling the burning process involved in fires and the structural effects in fire situations, as well.

3.1. Two-zone fire model

The scientific literature [5] defines the zone models in the assumption of uniform distribution of temperature in the fire compartment. The two-zone fire models assume the existence of two layers: an upper layer consisting of hot gases and a lower layer consisting of cooler gases. Both layer temperatures vary in time.

For the current case study, CFAST (Consolidated Model of Fire and Smoke Transport) software was used. CFAST is a two-zone fire model used to calculate the evolving distribution of smoke, fire gases and temperature throughout compartments of a building during a fire [6].

3.2. CFD fire model

The most advanced computational models describing the fire development are the CFD models. Based on numerical analysis of fluid dynamics, CFD fire models provide a high degree of credibility.

A 3D mesh is used for solving the mathematical equations describing the spread of smoke and hot gases together with the heat transfer for each mesh cell [7].

Conceptually, CFD fire models represent an extension of the two-zone fire models.

For the current case study, FDS (Fire Dynamics Simulator) software was used. FDS is a CFD model of fire-driven fluid flow. FDS solves numerically a form of the Navier-Stokes equations, appropriate for low-speed (Ma<0.3), thermally-driven flow with an emphasis on smoke and heat transport from fires [8].

4. NUMERICAL SIMULATIONS

For both fire models, the input data consist of: analysed space geometry (for FDS a 40x40x40 cm mesh was used), thermal properties of the walls and slabs, HRR curve, fuel properties and the simulation time.

For the current case study, the two-zone model is presented in Fig. 5 and the CFD model is presented in Fig. 6.

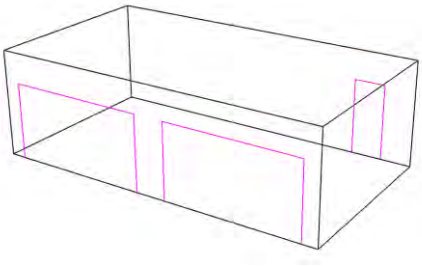

Figure 5. Two-zone model for the analysed space

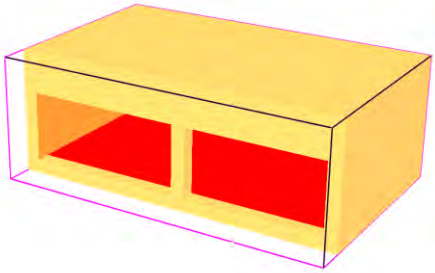

Figure 6. CFD model for the analysed space

5. RESULTS

According to the numerical analysis, Fig. 7 and Fig. 8 present the maximum temperature inside the analyzed space.

For the two-zone fire model, CFAST computed a maximum temperature of 45 °C.

For the CFD fire model, FDS computed a maximum temperature of 65 °C.

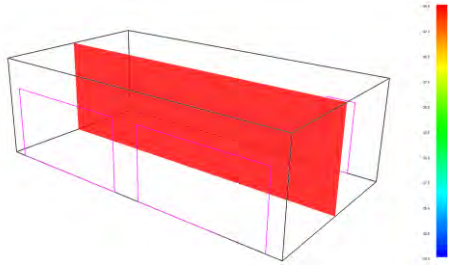

Figure 7. Two-zone model for the analysed space

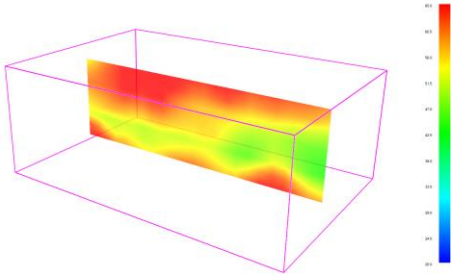

Figure 8. CFD model for the analysed space

6. CONCLUSION

For the considered fire scenario: peak HRR (456 kW), total burning time (202 s) and maximum temperature of the interior space (45°C and 65°C), it can be concluded that the fire has a low effect on the building structural elements.

It can be also concluded that the temperature difference, representing 20 °C, lies within the limits of engineering acceptability.

The temperature computed by CFD fire model is closer to the reality, but the two-zone fire model can be used for a quick simulation. In the case of a two-zone fire model, it is much easier to define the input data and the computational time is shorter.

ACKNOWLEDGEMENTS

The authors are grateful to Thunderhead Engineering Consultants Inc. USA for providing the free educational license for PyroSim (graphical user interface for FDS).

References

1. Diaconu-Sotropa D., *Ingineria securităţii la incendiu în construcţii - suport de curs*, *(http:// http://server.ce.tuiasi.ro/~ddiaconu/)* Accessed: 12-01-2015 (in Romanian).
2. ***, *Actions on Structures. Part 1-2: General Actions – Actions on Structures Exposed to Fire. Annex E: Fire Load Densities. Eurocode 1, EN 1991-1-2 Annex E.*
3. Grigoraş Z.C., Diaconu-Şotropa D., *Definirea focului de calcul conform SR EN 1991-1-2 Anexa E*, Revista Asociaţiei Inginerilor Constructori Proiectanţi de Structuri - AICPS REVIEW 1-2/2014 (2014) 150-155 (in Romanian).
4. DiNenno, P., Drydale D., Beyler C., Douglas Walton W., Custer R., Hall J., Watts J., *SFPE Handbook of Fire Protection Engineering*, Third Ed., Published by the National Fire Protection Association Massachusetts, USA, 2002.
5. Zaharia R., *Calculul structurilor la acţiunea focului. Partea I-a: Eurocoduri – Note de curs*, (http://www.ct.upt.ro/users/RaulZaharia/Curs_foc.pdf) Accesed: 12-01-2015 (in Romanian).
6. Peacock R., Reneke P., Forney G., *CFAST – Consolidated Model Fire Growth and Smoke Transport (Version 7) Volume 2: User's Guide*, National Institute of Standards and Technology, 2006.
7. Yeoh G. H., Yeun K. K., *Computational Fluid Dynamics in Fire Engineering – Theory, Modelling and Practice*, Butterworth-Heinemann, Elservier Science and Technology, USA, 2009. McGrattan K., Hostikka S., McDermott R., Floyd J., Weinschenk C., Overholt K., *Fire Dynamics Simulator User's Guide*, NIST Special Publication 1019, Sixth Edition, National Institute of Standards and Technology, 2017.
8. McGrattan K., McDermott R., Weinschenk C., Hostikka S., Floyd J., *Fire Dynamics Simulator – User's Guide*, National Institute of Standards and Technology Special Publication 1019, USA, 2017.

"Computational Civil Engineering 2017", International Symposium
Iasi, Romania, May 26, 2017

Uncertainties in seismic hazard probabilistic analysis

Dan Cretu[1], Andrei Pricopie[1], Liviu Crainic[2]
[2]*Department of Strength of Materials, Bridges and Tunnels, Technical University of Civil Engineering, Bucharest, 020396, Romania*
[2]*Department of Reinforced Concrete Structures, Technical University of Civil Engineering, Bucharest, 020396, Romania*

Summary

Structural codes for seismic analysis and design imply an accurate (as far as possible) assessment of the parameters which quantify the severity of seismic action as felt on each location of the national territory. Probabilistic seismic hazard analysis (PSHA) is nowadays preferred by most codes. Cornell-McGuire methodology is usually accepted.

Although PSHA seems to be an advanced and logical approach, its intensive use along many years evidenced intrinsic sensitivities leading to unexpected distortions with respect to a real phenomenon.

The goal of the paper is to examine the sensitivity of PSHA, according to the model used within the Romanian Seismic Design Code P100, for different input data. A MATLAB program has been written for this purpose, which allowed determining the mean recurrence interval (MRI) for different earthquake magnitudes.

KEYWORDS: structural code, seismic analysis, seismic hazard, probabilistic seismic hazard analysis (PSHA), mean recurrence interval (MRI), earthquake magnitude.

1. INTRODUCTION

Parameters which describe earthquake features and their effects within a seismic zone show a pronounced random character. Consequently, the use of statistic/probabilistic concepts and methods was a logical trend in quantifying the seismic hazard for structural analysis and design. For the last decades, probabilistic seismic hazard analysis (PSHA) according to Cornell-McGuire methodology ([2],[15]) is preferred by most structural codes.

Although PSHA seems to be an advanced and logical approach, its intensive use along many years evidenced intrinsic sensitivities leading to unexpected distortions with respect to a real phenomenon. Two families of uncertainties define the random character of the PSHA: (a) aleatory uncertainties related to the variability

of natural phenomena and (b) epistemic uncertainties - due to the insufficient accuracy of the modelling. Epistemic uncertainties can be improved through alternative assumptions, better theoretical models or use of more reliable parameters within an accepted model.

Romanian seismic design codes [5] and [6] are based on "modern" PSHA procedure for seismic hazard assessment. The PSHA model implemented in these codes is the "classical" Cornell-McGuire one. The recurrence relationships and the predictive (attenuation) relations are those proposed by Lungu [9], [12].

In an attempt to suggest a further way to enhance the actual codes version, the present paper aims to identify some sources of sensitivity of the PSHA model implemented within them. A MATLAB program was compiled and thoroughly tested for this purpose. The influence of the following parameters was examined: the value of the maximum credible earthquake moment magnitude, the site distance to the hypocenter, the focal depth, the site distance to the epicentre and the standard deviation of the ground motion attenuation relationship.

Only the seismic hazard due to Vrancea sub-crustal earthquakes has been investigated.

2. THEORETICAL BACKGROUNDS

According to Cornell-McGuire methodology ([2], [11], [15]), the probability that a ground shaking parameter Y exceeds a certain threshold y^* can be determined using the total probability theorem:

$$P\left[Y > y^*\right] = P\left[Y > y^* | X\right] P[X] = \int P\left[Y > y^* | X\right] f_x(X) dx \tag{1}$$

where X is a vector of the random variable Y.

The following parameters have been considered within the vector X: the moment magnitude M_w, the epicentre distance R and the focal depth H. These are accepted to be independent variables and, as consequence, the probability density function $f_x(X)$ can be determined as a product of three independent functions, i.e. the product of three independent integrals:

$$P\left[Y > y^*\right] = \int\int\int P\left[Y > y^* | m, r, h\right] f_M(m) f_R(r) f_H(h|m) dm\, dr\, dh \tag{2}$$

$P\left[Y > y^* | m, r, h\right]$ is obtained from the predictive (attenuation) function itself depending on the three random independent functions $M(m)$, $R(r)$ and $H(h)$. The Lungu's relationship has been accepted ([12]):

$$\ln PGA = b_0 + b_1 M_w + b_2 \ln R + b_3 R + b_4 h + \varepsilon \tag{3}$$

where:

$PGA = y^*$ is the peak ground acceleration at the site,

M_w - the earthquake moment magnitude,

$R = \sqrt{h^2 + d^2}$ - the site distance to the focus,

h, d - the focal depth and the site distance to the epicentre, respectively,

$b_0 \div b_4$ - regression coefficients,

ε - random variable with zero mean value and the standard deviation $\sigma_{ln,PGA}$.

Using the records of the earthquakes of 1977, 1986 and 1990, Lungu determined through multiple regression the follow coefficients for Bucharest [9]:

$$b_0 = 1.685 \quad b_1 = 1.181 \quad b_2 = -1.0 \quad b_3 = 0.002 \quad b_4 = -0.005 \quad \varepsilon = 0.461 \tag{4}$$

It should be noted that d represents the site distance to any point of the seismogenic zone. It is assumed that any point within the seismogenic zone has the same occurrence probability of an earthquake having the moment magnitude between $M_{w,\min} = 6.3$ and $M_{w,\max} = 8.1$.

$f_M(m)$, $f_R(r)$, $f_H(h|m)$ are normal probability density functions for moment magnitude, epicentre distance and focal depth.

Recurrence function $f_H(h|m)$ shows the relationship between moment magnitude and focal depth. Using the linear regression of data for M_w within domain 6.3-8.1, one gets:

$$\ln h = -0.866 + 2.846 \ln M_w \tag{5}$$

with a standard deviation $\sigma_{\ln,h} = 0.18$.

For a site with N_S zones with potential occurrence of earthquakes, each of them having a magnitude exceeding mean rate of

$$\nu_i = e^{\alpha_i - \beta_i M_{w,\min}} \tag{6}$$

$$\alpha_i = 8.657 \quad \beta_i = 1.687$$

$$M_{w,\min} = 6.3$$

the number of earthquakes in one year is

$$n = 10^{3.76 - 0.73m} \tag{7}$$

The mean rate of exceeding for all considered seismogenic zones will be

$$\lambda_y = \sum_{i=1}^{N_S} \nu_i \int\int\int P\left[Y > y^* \middle| m, r, h\right] f_{Mi}(m) f_{Ri}(r) f_{Hi}(h|m) dm\, dr\, dh \tag{8}$$

In order to solve the integrals, each density functions is accepted to be a normal distribution. Functions h and Y are supposed to be lognormal, but applying the logarithm they become a normal distribution.

The integrals are solved through numerical procedure accepting that the functions are constant over the integral steps $\Delta m, \Delta r, \Delta h$. Accordingly, the mean exceeding rate is:

$$\lambda_y = \sum_{i=1}^{N_S} \sum_{j=1}^{N_M} \sum_{k=1}^{N_R} \sum_{l=1}^{N_H} \nu_i P\left[Y > y^* \middle| m_j, r_k, h_l\right] f_{Mi}(m_j) f_{Ri}(r_k) f_{Hi}\left(h_l \middle| m_j\right) \Delta m \Delta r\, \Delta h \tag{9}$$

relationship equivalent with:

$$\lambda_y = \sum_{i=1}^{N_S} \sum_{j=1}^{N_M} \sum_{k=1}^{N_R} \sum_{l=1}^{N_H} \nu_i P\left[Y > y^* \middle| m_j, r_k, h_l\right] P(M = m_j) P(R = r_k) P\left(H = h_l \middle| m_j\right) \tag{10}$$

The procedure accepts that each source generates only N_M earthquakes of moment magnitude m_j, over only N_R distances source-site r_k and only N_H focal distances h_l.

For a single seismogenic source results:

$$\lambda_{y,i} = \sum_{j=1}^{N_M} \sum_{k=1}^{N_R} \sum_{l=1}^{N_H} \nu_i P\left[Y > y^* \middle| m_j, r_k, h_l\right] P(M = m_j) P(R = r_k) P\left(H = h_l \middle| m_j\right) \tag{11}$$

The Gutenberg-Richter truncated probability density function has been implemented:

$$f_M(m) = \frac{\beta e^{-\beta\left(m - M_{w,\min}\right)}}{1 - e^{-\beta\left(M_{\max} - M_{w,\min}\right)}} \tag{12}$$

where $\beta = 1.687, M_{w,\min} = 6.3$ and $M_{w,\max} = 8.1$.

3. COMPUTER MATLAB PROGRAM

The probabilistic seismic hazard analysis (PSHA) performed within the present research uses a MATLAB program specifically developed for this purpose. The program involves two modules: POZITIE and PSHA01.

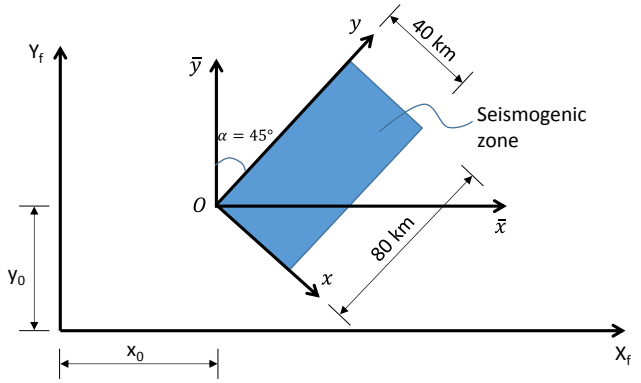

Figure 1. Seismogenic zone Vrancea

The first module, POZITIE, provides the coordinates of potential epicentres which could be developed within the seismogenic zone VRANCEA, supposed to be a rectangle of 40 x 80 km x km according to [9] (Figures 1 and 2).

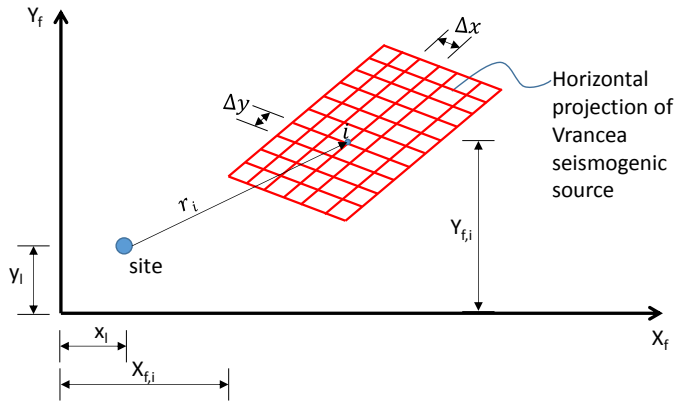

Figure 2. Horizontal projection of fault rupture surface

The second module, PSHA01, determines the probability that the peak ground acceleration (PGA) in a location exceeds a certain threshold, according to the Cornell-McGuire methodology above described. In a first step, the PGA probability density function is determined as a product of three random independent functions, i.e. the site distance to the epicentre *d*, the site distance to the hypocenter *r* and the focal depth *h* (Figure 3):

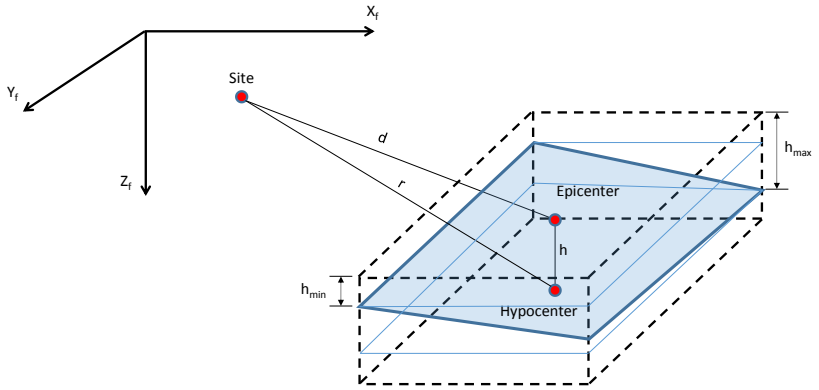

Figure 3. Three dimensional seismogenic zone

The next program step determines the temporal distribution of earthquakes using the Gutenberg-Richter recurrence law with the parameters α and β according to [9]. Supposing that the moment magnitude is a random function of normal distribution within the interval $M_{w,\min} - M_{w,\max}$, the density moment function is determined through Gutenberg-Richter truncated relationship.

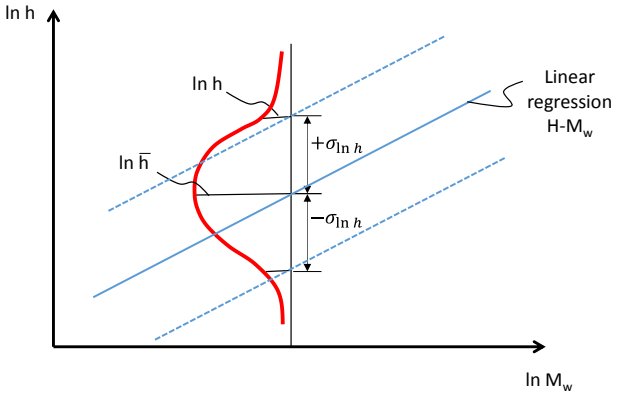

Figure 4. Linear regression between focal depth and moment magnitude

The random variable H of the focal depth is accepted to be a lognormal function (Figure 4). The relative frequency of the ratio h/m is obtained after applying the logarithm of the function H with the relationship:

$$f_H(h|m)\Delta h = \frac{\Delta h}{\sqrt{2\pi}\cdot h\cdot \sigma_{\ln,h}} e^{-\frac{1}{2}\left(\frac{\ln h - \ln \bar{h}}{\sigma_{\ln,h}}\right)^2} \tag{13}$$

The peak ground acceleration (PGA) is a random variable too, having a spatial distribution quantified through attenuation (predictive) relationships. Within present study, the attenuation relationship deduced by Lungu [9] has been used.

The mean rate of exceeding for all considered seismogenic zones is obtained through probability's summation of all random variables involved, according to the theorem of total probability. The result is the value of mean exceeding the rate for each discrete magnitude of PGA. The inverse of this value is the mean recurrence interval (MRI).

Thus, the program calculates the seismic hazard curve $PGA = f(MRI)$ and then, trough linear interpolation, the discrete PGA magnitudes for MRI = 50, 100, 225, 475, and 975 years, respectively.

4. PERFORMED INVESTIGATIONS AND COMMENTS

The uncertainties in determining the parameters magnitude which defines the ground movement are generally associated with the location on which earthquake of significant magnitude occur, to the moment magnitude of potential earthquakes, to their recurrence rate, and to the accepted attenuation (predictive) relationship.

Other uncertainties are generated by the adopted calculation algorithm i.e. are of mathematical nature. Accordingly, the first step in the present research was to elaborate a computer program using the Cornell-McGuire Methodology [11] and to test it thoroughly. The attenuation relationships and the coefficients of nonlinear regression are those described in [9].

Table 1 contains the values of PGA for different MRI given by the computer program and, between brackets, the reference values taken from [20]. A difference of 5-15% between these values can be noticed.

In modern approach, PSHA uses, in attenuation relationship, the constant ε which expresses the uncertainty in prediction of PGA through independent random variables

$$ln(PGA) = f(M,R,h) + \varepsilon = f(M,R,h) + n\sigma_{ln,PGA} \tag{14}$$

The magnitude of the standard deviation has a significant influence on the prediction of PGA, being a source of underestimation or overestimation of the parameters which define the seismic movement of the ground.

The step size of the numerical integration, namely Δm , Δr , Δh and ΔPGA have a small influence on the value of PGA, around 1%.

Table 1. Calculated and reference PGA values for different MRI

Site-city	MRI =50	MRI=100	MRI=225	MRI=475	MRI=975	Data
Bucharest	158.9754	208.0345	271.6799	335.7867	402.2741	Bucharest
	158.3220	203.3545	261.0905	319.5041	380.7808	All data
	130.0899	157.6611	191.2836	222.8324	253.7478	0.50ε
	142.1885	176.7198	219.8386	261.8401	304.6103	0.75ε
	201.1098	280.1626	388.8639	506.6457	637.9049	1.50ε
	259.4	395.2	598.8	836.9	1119.600	2.00ε
		(213.97)	(289.54)			
Focşani	31.5139	41.8058	55.1549	69.6843	84.2528	Moldova
	55.6168	325.7026	414.1323	502.8896	595.6003	All data
	216.0891	277.5522	356.1851	435.5087	518.2142	Bucharest
		(292.487)	(392.6)			
Craiova	122.7789	162.4327	213.9023	265.6092	318.9603	Bucharest
	91.5325	118.4423	152.9939	188.2252	225.0098	All data
		(130.54)	(175.69)			
Caracal	126.2931	166.9326	219.8266	272.7046	327.3241	Bucharest
	98.6700	127.5023	164.6501	202.4717	242.1101	All data
		(140.36)	(189.43)			
Alexandria	134.2207	177.0261	232.5675	288.4301	345.9634	Bucharest
	113.6824	146.8124	189.4942	232.5494	277.8805	All data
		(163.91)	(214.95)			
Giurgiu	137.1806	180.8080	237.2512	294.0542	352.7319	Bucharest
	119.2197	153.6020	198.0142	242.9569	290.2834	All data
		(165.87)	(223.78)			
Ploieşti	186.7080	242.1606	313.5630	385.6461	460.6751	Bucharest
	205.3517	262.9570	336.1176	410.0404	487.3537	All data
		(261.08)	(343.53)			
Iaşi	18.1899	24.3180	33.2640	42.6143	52.5674	Moldova
	129.4446	166.6598	214.5745	263.2086	314.2280	All data
		(169.8)	(229.67)			
Bacău	24.4484	33.1260	44.4248	56.3256	69.4168	Moldova
	191.5639	245.2579	313.7019	382.8400	455.3249	All data
		(247.34)	(321.93)			
Suceava	15.2868	21.6276	30.1162	37.8275	46.4803	Moldova
	108.1574	139.6631	180.0319	220.8840	263.6801	All data
		(145.262)	(196.3)			
Galaţi	172.1986	224.2652	291.6845	359.6702	430.1375	Bucharest
	180.4735	231.0209	295.4076	360.6649	429.0020	All data
		(229.671)	(291.506)			
Constanţa	105.5233	136.1400	175.4553	215.3162	257.1190	All data
	107.4000	143.4325	189.8742	235.0499	280.8351	Dobrogea
		(147.225)	(194.337)			
Mangalia	94.5187	122.2251	157.7652	193.7246	231.5442	All data
	124.1572	164.2037	216.2364	268.5336	322.2857	Dobrogea
		(154.096)	(192.374)			

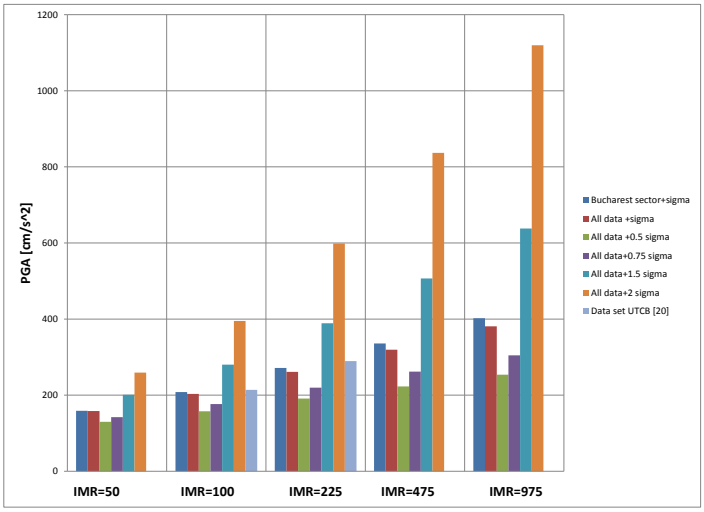

Figure 5. PGA values for different MRI and uncertainty levels ε in Bucharest

Figure 5 shows the PGA values for different MRI and uncertainty levels ε in Bucharest.

The inferior moment magnitude doesn't have a significant influence on the calculated PGA while the considered maximum moment magnitude is particularly important (see Figure 6). For this reason, it would be important to accept $M_{w,\max} = 7.9$ as Cliff Frohlich suggests [10] instead of $M_{w,\max} = 8.1$.

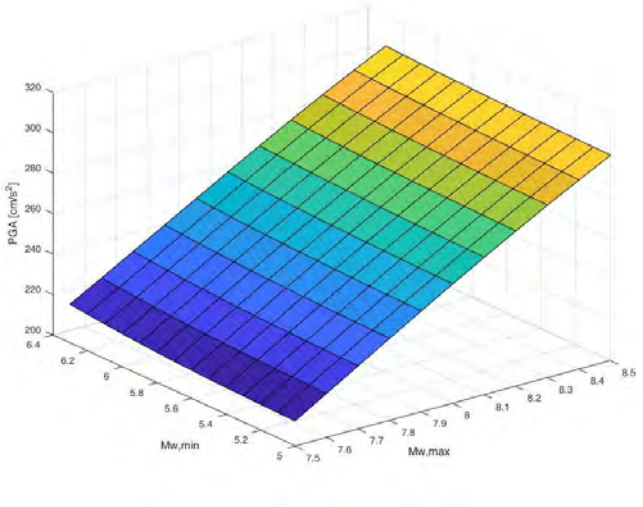

Figure 6. Variation of PGA with $M_{w,min}$ and $M_{w,max}$

5. DIRECTIONS FOR FURTHER RESEARCHES

The research described in the paper, limited to the zones prone to the Vrancea earthquakes, should be considered as the first step in a more comprehensive effort aimed to improve the quantification of design seismic hazard to be implemented in next generations of codes. For this purpose, the next step is intended to be an extended research on the seismic hazard of the seismogenic zones of the Transylvanian Basin.

The Transylvanian Basin, spanning over about 40% of the Romanian territory, shows a moderate toward low seismic activity. However, it requires a specific attention. In contrast with the zones subjected to Vrancea earthquakes, the Transylvanian Basin seismicity is generated mainly by seismogenic crustal sources even though the effect of Vrancea subcrustal earthquakes could be felt (with moderate intensity) within its Eastern part. Consequently, for Transylvania, appropriate new predictive laws (attenuation relations) have to be developed in order to accurately apply PSHA. Moreover, for certain Transylvanian sites, two or more seismogenic zones should be considered according to appropriate procedures.

6. POTENTIAL ALTERNATIVE APPROACHES FOR DESIGN SEISMIC HAZARD ASSESSEMENT

The use of PSHA for seismic design codes is nowadays almost generalised throughout Europe countries as well as in the USA. However, its use along many years evidenced some important shortcomings of this approach. They have to be addressed.

A first issue which has been remarked was expressed in the following question [1]: *"Why Do Modern Probabilistic Seismic-Hazard Analyses often Lead to Increased Hazard Estimates?"*. The first paper about that was followed by substantial comments [21]. It can be added that in the last version of the Romanian code the hazard estimation according to PSHA approach led to a substantial increase of design seismic force justified by an MRI transition from 100 to 225 years [4]. It is behind the scope of the present paper to extend more the discussion about this issue but it has to be mentioned.

In Italy, a country with strong seismic activity, the forecast of destructive earthquake occurrence according to seismic hazard maps compiled through PSHA procedures was dramatically contradicted by the reality of the last decades [17]. In zones considered with low seismicity according to seismic zonation maps, destructive earthquakes occurred with numerous causalities.

Similar situations have been encountered in Japan (Tohoku earthquake of 2011 with a Richter magnitude of 9 in a zone considered with low seismicity produced 15.000 victims and severe damage to Fukushima nuclear plant) and in Haiti - 2010.

The shortcomings of PSHA approach led to a trend of reconsidering the deterministic methods, obviously in a modern, improved manner. The NDSHA (Neo-Deterministic Seismic Hazard Analysis) developed at the University of Trieste / Italy [17] is a good example of such approach. It capitalises the updated knowledge about the Earth Geophysics and modern computational methods in Geodynamics for developing an original method to analyse the local seismic hazard which could be directly implemented in structural codes.

7. CONCLUSIONS

The accurate prediction - as far as possible - of the severity of earthquakes which potentially occur in a location within a given recurrence period is a basic key to improving the seismic structural design.

PSHA is the up-to-date approach to seismic hazard analysis implemented almost generalised in codes. However, its use along many years evidenced several shortcomings of this approach.

The present paper is focused on identify some sources of PSHA epistemic uncertainties, to quantify them, and to suggest implicitly ways to mitigate them.

The USA project Next Generation of Ground Motion Attenuation Models, a multidisciplinary research program, can be considered as a model approach to a key problem of the seismic hazard analysis for design purposes [19]. In order to mitigate the inherent subjectivity of approaches, five sets of ground motions models were developed by five teams working independently. However, interaction meetings were organised between the teams aimed to lead gradually to a consensual decision.

It is supposed that extending this research in several ways suggested within the paper could contribute to a better understanding and a more accurate assessment of the seismic hazard for design purposes.

References

1. Bommer, J., Abrahamson, N. A., *Why Do Modern Probabilistic Seismic-Hazard Analyses often Lead to increased Hazard Estimates?*, Bulletin of the Seismological Society of America, Vol. 96, No. 6, pp. 1967–1977, December 2006.
2. Cornell, C., *Engineering seismic risk analysis*, Bulletin of the Seismological Society of America, 58, 1968.

3. Chen W.F., Lui E.M., *Earthquake engineering for structural design,* CRC Press, Taylor & Francis, 2006.
4. *Cod de proiectare seismică – Partea I – Prevederi de proiectare pentru clădiri, indicativ P100-1/2013*, Monitorul Oficial al ROMÂNIEI, 2013, nr. 338 bis/3.IX.2013. (in Romanian)
5. *Cod de proiectare seismică – Partea I – Prevederi de proiectare pentru clădiri, indicativ P100-1/2006*, R. A. Monitorul Oficial, 2006. (in Romanian)
6. *Cod de proiectare seismică – Partea a III-a – Prevederi pentru evaluarea seismică a clădirilor existente, indicativ P100-3/2008*, Monitorul Oficial al ROMÂNIEI, nr. 647 bis/1.X.2009. (in Romanian)
7. Douglas, J., *Ground-motion prediction equations 1964-2010*, PEER Report 2011/102, BRGM.
8. Douglas J., *Estimation of Strong Ground Motion: Aleatory Variability and Epistemic Uncertainty,* Proceedings of 5-th National Conference on Earthquake Engineering and 1-st National Conference on Earthquake Engineering and Seismology Bucharest, Romania, 19-20 June 2014, Conspress.
9. Dubină, D., Lungu, D. (coordinators), *Construcţii amplasate în zone cu mişcări seismice puternice*, Ed. Orizonturi Universitare, Timişoara, 2003. (in Romanian)
10. Frohlich, C., *Deep Earthquake,* Cambridge University Press, 2009.
11. Kramer, S. L., *Geotechnical Earthquake Engineering,* Prentice Hall, 1996.
12. Lungu, D., Mazzolani, F. &. Savidis, S., (coordinators), *Calculul structurilor în zone seismice - EUROCODE 8, Exemple de calcul*, BRIDGEMAN Ltd. Timişoara, 1997.
13. Mărmureanu, G., Cioflan, C.O., Mărmureanu, Al., Ionescu, C., *How long time will we go with linear seismology?*, Romanian Journal of Physics, vol. 60, pg. 613-625, Bucureşti, 2015.
14. Mândrescu, N., Mărmureanu, G., Radulian, M., Ionescu C., *Studiul integrat al datelor geologice, geodezice şi seismice pentru evaluarea răspunsului local în zona oraşului Bucureşti,* Ed. Academiei Române, 2008.
15. McGuire, R., *FORTRAN computer program for seismic risk analysis.* U.S. Geological Survey Openfile Report 76-67, 1976.
16. McGuire, R. L., *Seismic Hazard and Risk Analysis*, edited by Earthquake Engineering Research Institute, 2004.
17. Peresan, A., Panza, G. E., *Improving Earthquake Hazard Assessments in Italy: An Alternative to "Texas Sharpshooting"*, EOS, no. 51, American Geophysical Union, 18 December 2012.
18. Sokolov, V. Yu, Wenzel, F., Mohindra, R., *Probabilistic seismic hazard assessment for Romania and sensitivity analysis: A case of joint consideration of intermediate-depth (Vrancea) and shallow (crustal) seismicity*, Soil Dynamics and Earthquake Engineering 29, pp. 364-381, Elsevier, 2009.
19. Tapan, K. Sen, *Fundamentals of Seismic Loading on Structures*, John Wiley&Sons, 2009.
20. Văcăreanu, R., Pavel, F., Aldea, A., Arion, C., Neagu, C., *Noi perspective şi rezultate ale analizei probabilistice de hazard seismic pentru România - partea I*, AICPS Review, nr. 3/2015.
21. Wang, Z., Mai, Z., *Comment on "Why Do Modern Probabilistic Seismic-Hazard Analyses often Lead to Increased Hazard Estimates?" by Julian J. Bommer and Norman A. Abrahamson, Bulletin of the Seismological Society of America, Vol. 96, No. 6,* Bulletin of the Seismological Society of America, Vol. 97, No. 6, pp. 2212–2214, December 2007.
22. Wang, Z., *Seismic Hazard and Risk Assessment and Mitigation Policy in USA,* ICTP Advanced Conference on Seismic Risk Mitigation and Sustainable Development, 10-14 May 2010.

"Computational Civil Engineering 2017", International Symposium
Iasi, Romania, May 26, 2017

Expert systems in the BIM environment

Oleksiy Levchenko[1], Tetyana Kashchenko[2]
[1]*Department of Informational Technologies in Architecture, Architectural Faculty, Kyiv National University of Construction and Architecture, 03680, Ukraine*
[2]*Department of Architectural Design of Civil Buildings and Structures, Architectural Faculty, Kyiv National University of Construction and Architecture, 03680, Ukraine*

Summary

In modern architectural practice, it is important the availability of software that makes it possible to compare design alternatives, gives quickly assessment of the architectural object - comprehensive or by individual components, makes energy modelling and resource balance, thermal parameters, optimises the form. System quality assessment of project increases with the expansion of technologies, the introduction of Building Information Model (BIM) and Building Energy Model (BEM). According to qualimetric analysis this project evaluation allows operating with the value of the floor space standard unit to the total building area, attractiveness and the level of investment risk.

The analysis is carried out at the level of 3D inspection of architectural and structural elements and at the level of structural parametric data that accompany these three-dimensional data for architectural, structural and engineering components of buildings and structures.

Expert System Allcheck in BIM-design environment allows to search "collisions", errors and to perform rapid analysis of structural elements incorporated in accordance with the regulations and requirements of government control and examination.

On a base, Allcheck ("Allbau Software") is executed verification of additional data (attributes) filling in accordance with the detailing project degree of LOD (Levels of Detail) according to interaction standard BIM-software based on data format IFC.

The development of Allcheck plugin would expand the number of inspections and the options: to add a groups of audits by regulatory requirements on the AX-3000 basis, to supplement verifying of thermal performance, the functional properties of space - regulatory indoor temperature and energy consumption, which enables approach to "zero energy" and rapid formation of energy passport of the building.

KEYWORDS: informational technologies in architecture, Nemetschek Allplan, Allcheck, Building Information Model (BIM), Building Energy Model (BEM).

INTRODUCTION

The end of the 20th - early 21-st centuries, connected with the rapid development of information technologies, was marked by the appearance of a fundamentally new approach to architectural and construction design.

The BIM (Building Information Modelling) concept allows a team of authors - architects and engineers - to work together on a project, creating a computer model of a new building that carries all the information about a future site.

Leading developments in the field of BIM in the territory of the European Union belongs to Nemetschek concern and their partner Allbau Software GmbH (the head - Vladimir Shkatov [1]), in Ukraine it is the "Allbau Software Competence Center in Ukraine" (the head - Yuri Smirnov [2]). The company develops researchers in the field of BIM and is engaged in its own projects, both the creation of expert systems and the expansion of Allplan functionality in accordance with government regulations.

Experience in the study and implementation of BIM Allplan Nemetschek is presented in the manual "Collection Allplan. A short course of the BIM. Theory and Practice" [3] and displays the fullness and the need for this concept in a modern design.

When using BIM technologies, the amount of information processed increases significantly. With information modelling, an object-oriented digital model of the whole object is created, and a model of its construction process can also be developed. Given the complexity of such models, a large number of elements, a variety of requirements for them there is a need for control.

The control provides for synchronous or post-project analysis of compliance with the tasks, architectural and construction norms and rules. This function is performed by the Allcheck module developed for Allplan and Planbar [4].

DESCRIPTION OF THE SOFTWARE SOLUTION

Allplan is a comprehensive solution that unites all the sections of the building design: architecture, reinforced concrete structures, engineering systems of buildings, general layout, construction volumes, cost estimation and estimates, metal structures, design.

Work on the project is carried out simultaneously, it is possible to see the changes made by engineers of related specialities, and also some changes can be applied to the whole complex project.

Intelligent building objects are interconnected, therefore it is possible to effectively design engineering systems, to check the heat losses of the building when changing the planning decision, transform the architectural model into a calculation model for SCAD, LIRA and the program from Nemetschek - SCIA Engineer, for constructive calculations in accordance with the norms [5].

Allcheck is a customizable expert system for monitoring architectural and design solutions in Allplan.

Allcheck is a plugin, which allows finding errors in projects before the beginning of construction and installation works. The program is able to perform a thorough check of the information model of the object, identify collisions, check the model's compliance with the requirements of the BIM standard and regional design standards, compare models and extract all necessary information.

Allcheck's capabilities allow for automated testing, analysis and quality control of information models. It is also possible to partially correct models according to specified rules. The plugin is intended for both designers and experts.

Most often, errors are considered in such situations:

- collisions between elements;
- design errors in violation of design standards;
- errors in filling in the attributes [6].

A working group of Allbau Software specialists, led by A. Baranetsky, E. Medyanik, O. Levchenko developed a new version of "Checks in Allcheck, AllPlan 2016-2017".

This Allcheck plugin allows you to validate the BIM model for the Allplan environment, and verify compliance with the current rules and regulations of the regional architectural and structural design.

Prior to the conversion of "Checks in Allcheck, AllPlan 2016-2017" included:

- Architectural checks;
- Structural checks;
- Precast checks.

To the Architectural checks are included 33 control positions, to the Structural checks- 13, to the Precast checks – 8.

The main positions of Architectural checks include: door opening area, rooms situation, height of elements and rooms (fig. 1), area of passages to openings (fig. 2), rooms without openings (fig. 3), rooms without doorways (fig. 4), rooms without window openings, intersections (fig. 5), analysis of identical rooms, identical rooms in groups (fig. 6), rooms without finish floor, wall, ceiling (fig. 7), specification of attributes for window openings and for doorways, elements in openings (fig. 8).

Structural checks mainly control thus positions: vertical and horizontal load-bearing elements, walls and beams parameters, curvilinear architectural elements, starter bars, concrete cover, load-bearing elements with no reinforcement in it.

Precast checks mostly control the multiplicity of sizes of walls, floor slabs and openings in them, erection joint between walls, the general rule for checking the attributes, fixtures are within the formwork of the element, correspondence between 3d attributes and catalogue.

General rules determine the general procedure for verification.

For the analysis accuracy by controlling positions it is defined:
- Description of checked element or collision;
- Checked elements;
- Exceptions (no exceptions or exceptions with their respective descriptions);
- The purpose of checking the mutual collision.

In the case of finding an error, a detailed description of the error will be displayed in the lower part of the "Results" window and the image in the Allplan window is scaled to the invalid element, which is highlighted in red. The degree of criticality of the checks is output after the description of the error.

Every user can add and edit both the list of rules and the check criteria (tolerances) in each rule, and the check criteria can also be edited.

Thus, the structure of this plugin allows conducting a comprehensive verification of the project, as accurately as possible to take into account the requirements of architectural and building standards, as well as flexibly respond to individual requirements when designing.

CASE STUDY INVOLVING BEM (BUILDING ENERGY MODELING)

The plugin is planned to be developed in future and supplement the list of possible checks. The current direction of development of the plugin is checking the parameters of buildings related to energy efficiency.

The main categories of inspections can be:
- exposition of areas or rooms, which is related to the solar radiation gains;
- compactness of building;
- thermal characteristics of structures according to the type of building;
- heat bridges;
- checking for collisions of engineering systems associated with energy efficient equipment - heat pumps, heliocollectors, heat exchangers and others.

Additions to the plugin, related to energy-efficiency, are focused on the use of new standards for thermal insulation of buildings in Ukraine. Also in the plugin, it can be taken into account typological features of the building - residential or public buildings.

This type of inspection in systems of BIM-design should be important in the development of BEM (Building Energy Modeling) for the design of energy-efficient buildings.

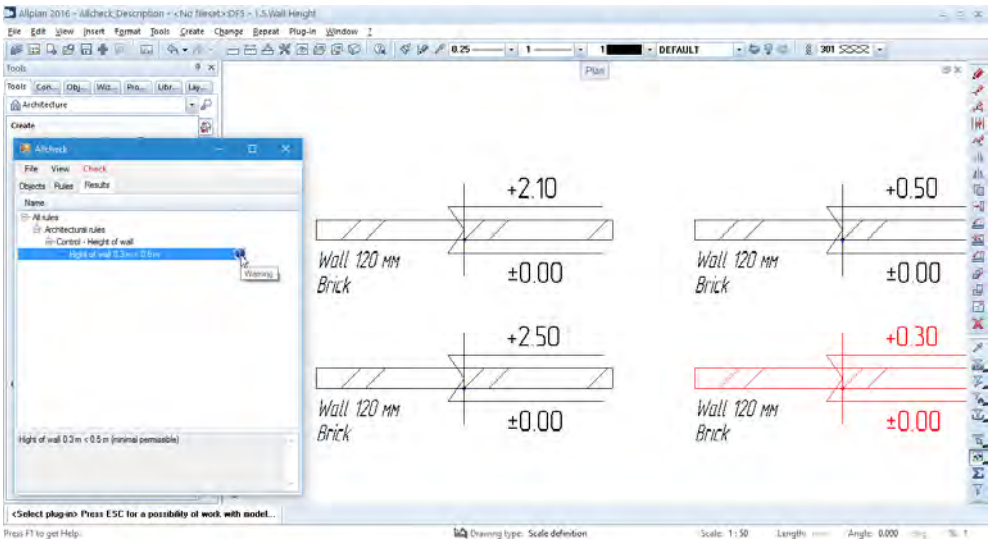

Figure 1. Architectural checks. 1.5. Wall Height

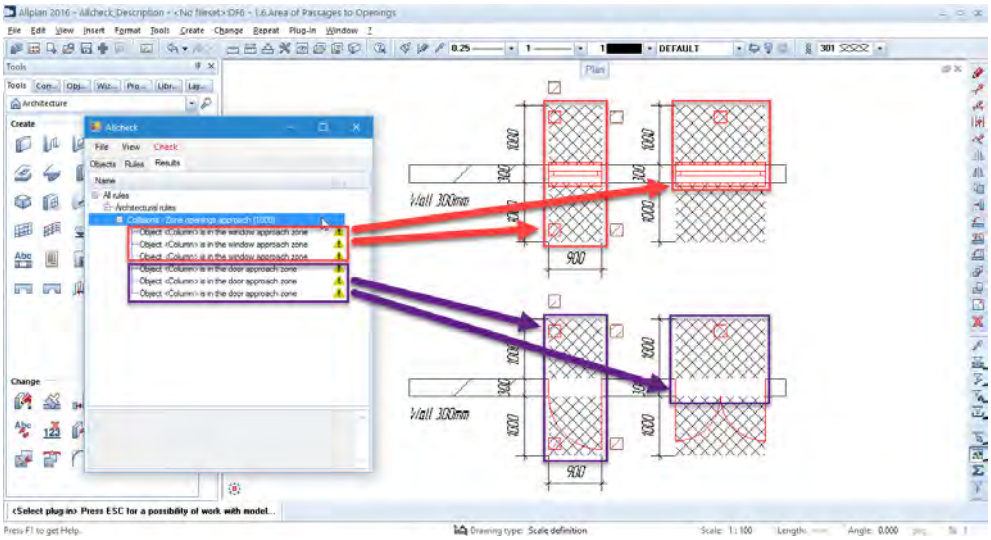

Figure 2. Architectural checks. 1.6. Area of Passages to Openings

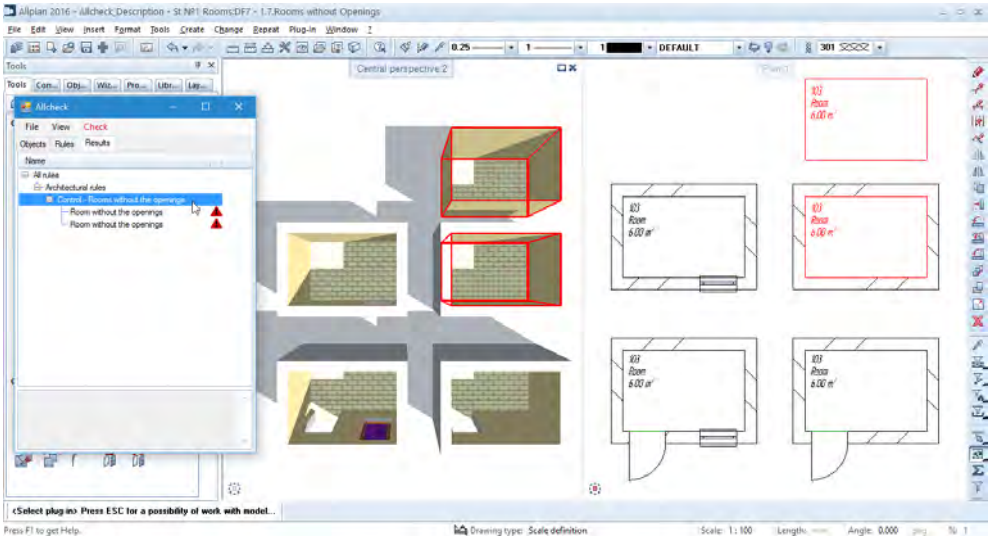

Figure 3. Architectural checks. 1.7. Rooms without Openings

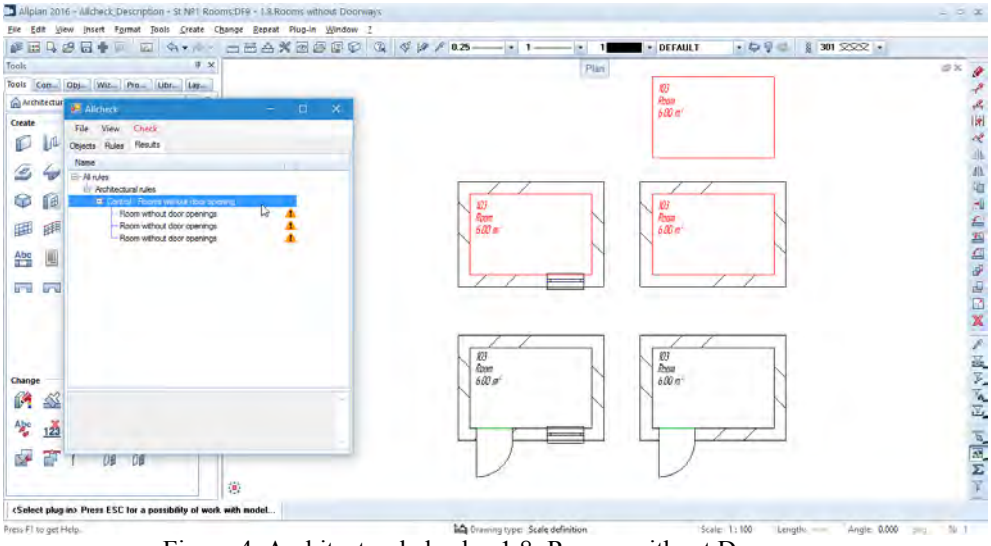

Figure 4. Architectural checks. 1.8. Rooms without Doorways

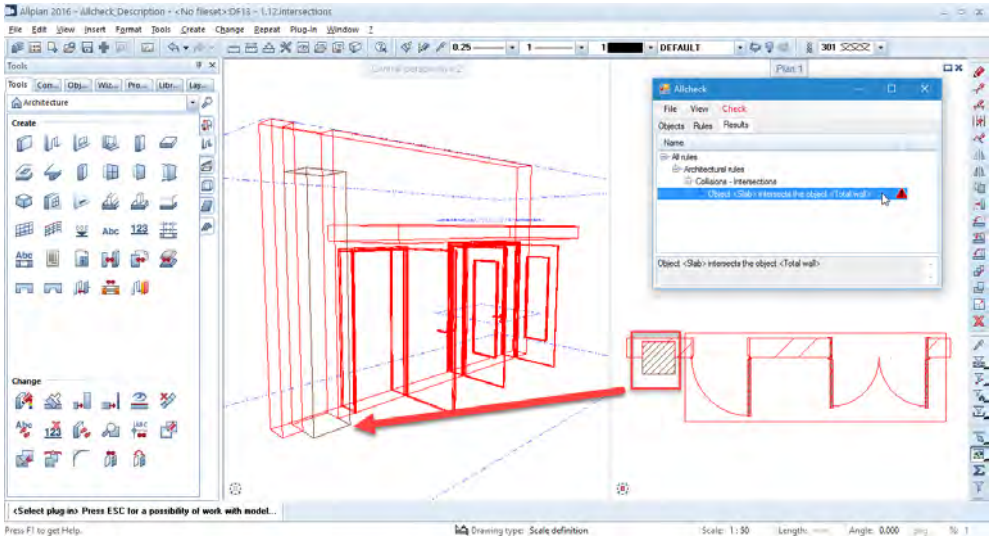

Figure 5. Architectural checks. 1.12.Intersections

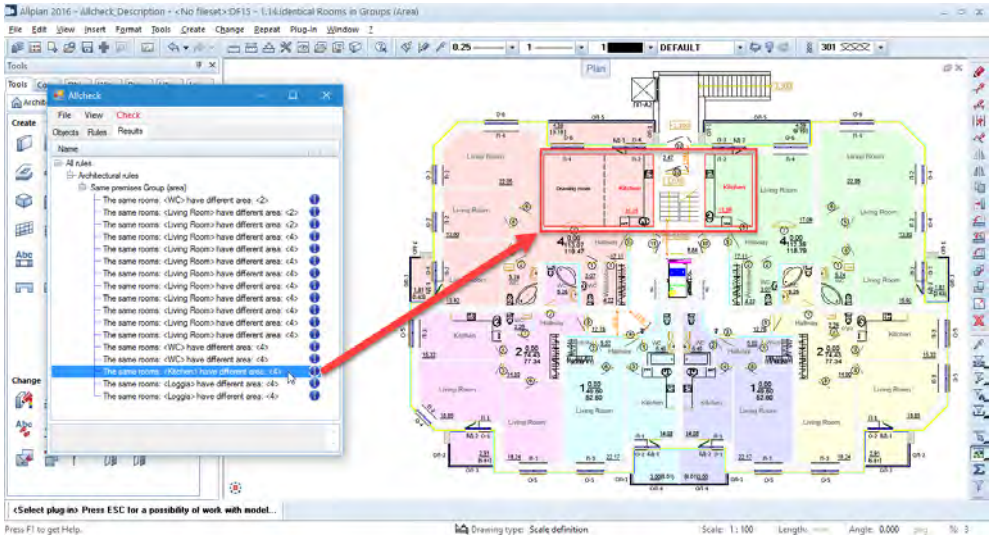

Figure 6. Architectural checks. 1.14.Identical Rooms in Groups (Area)

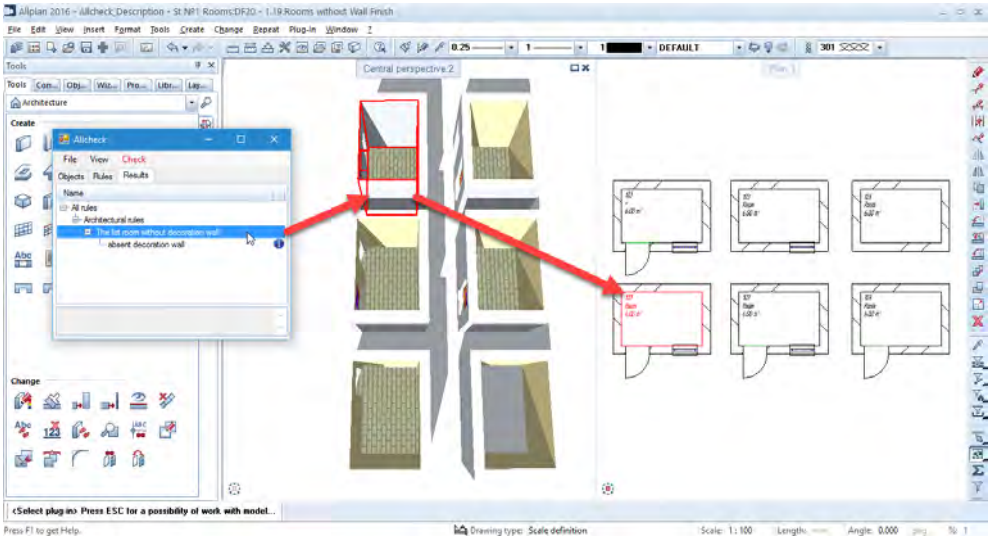

Figure 7. Architectural checks. 1.19. Rooms without Wall Finish

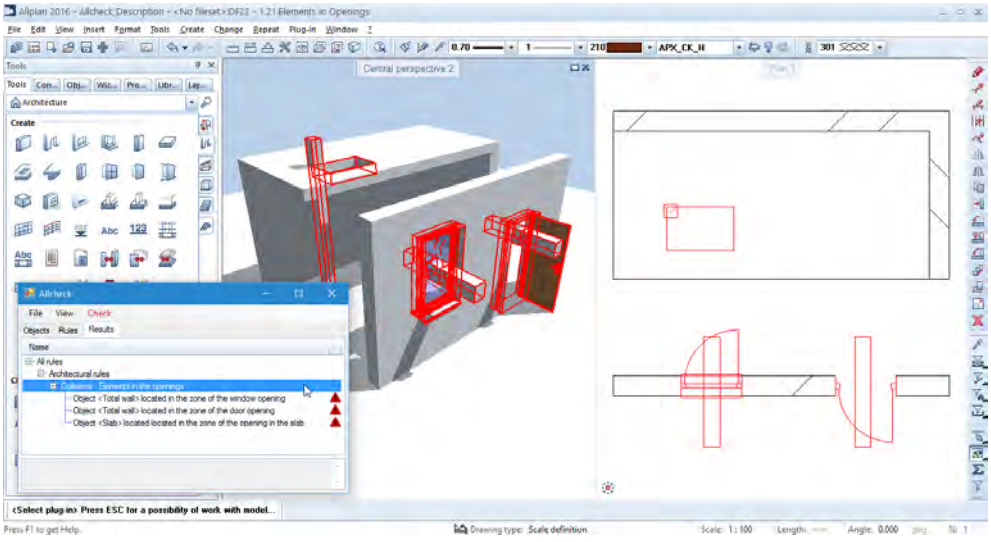

Figure 8. Architectural checks. 1.21.Elements in Openings

CONCLUSIONS

Proposed Allcheck plugin "Checks in Allcheck. AllPlan 2016-2017" allows an operative analysis of the design solution or project analysis for the presence of design errors ("Human Factor"). The analysis of the design solution can be carried out at different stages, including at the early stages of project development, which significantly improves the design quality. This plugin is a multifunctional tool for architects, engineers, experts. The ability to customise the rules and parameters of the assessment allows you to adapt it to local architectural and construction norms and rules. Using plugin "Checks in Allcheck. AllPlan 2016-2017" significantly speeds up the design process, improves the accuracy and overall quality of the project documentation, helps to design modern complex architectural objects.

ACKNOWLEDGEMENTS

The authors are grateful for the help and support in the work of Allbau Software GmbH Director V. Shkatov and the head of the Allbau Software Competence Center in Ukraine, Y. Smirnov.

References

1. http://www.allbau-software.de
2. http://www.allbau-software.de/index.php/kontakt.html
3. http://www.allbau-software.de/index.php/podderzka/download/dokumentatsiya/file/141-sbornik-allplan-kratkij-kurs-bim-teoriya-i-praktika.html
4. http://www.allbau-software.de/index.php/produkty/allcheck.html
5. http://www.allbau-software.de/index.php/produkty/allplan.html
6. http://www.allbau-software.de/index.php/produkty/allcheck.html
7. Levchenko O. *BIM concept and demoecological approach as architectural and landscaping aspect of the formation of the urban environment*. - Modern problems of architecture and urban planning, Scientific-technical edition. - K .: KNUCA, 2016.- #46.- p.107-111.
8. Levchenko O. *Using IFC format in BIM technology. "Information technologies of modern architectural design"* - Modern problems of architecture and urban planning, Scientific-technical edition. - K .: KNUCA, 2015.- #39.- p.106-111.
9. Kashchenko O.V., Mikhailenko A.V., Kashchenko T.O., Antao A. *Information technologies at architectural education*. — Kharkiv: “Operativnaya poligrafiya”, 2015. — 120 p.

Communicating through the use of Computer Aided Design to improve design skills for Civil Engineering students

Adelina Manea
School of Energy, Construction and Environment, Coventry University, Coventry, CV1 5FB, United Kingdom

Summary

Professionals in the construction industry use certain methods to communicate. In recent years, the term BIM has become more popular but fundamentally all professions from Architects to Quantity surveyors use drawings to show and demonstrate buildings or structures. The perception of students training to become civil engineers is that they will not have to produce drawings but only calculations. This paper investigates how Civil Engineering students can improve their communication skills by developing 3D modelling, 2D drafting and hand drawing skills. The findings show that student satisfaction and overall module attendance have improved therefore student engagement has improved.

KEYWORDS: CAD, Communication, AutoCAD, 3D Modelling, Civil Engineering, 2D Drafting, Visualisation, learning by instruction.

1. INTRODUCTION

Students enrolling on to Civil Engineering seem to believe that the profession involves no design or creativity. They find it hard to come up with solutions on the spot and to communicate ideas. One of the main reasons for this is the fact that they cannot visualize a three dimensional structure when only provided with two dimensional drawings or orthographic projections and vice versa. The Institute of Civil Engineers states this about civil engineering:

> *Civil engineering is all about helping people and shaping the world. It's the work that civil engineers do to make our lives much easier.*
>
> *They keep us switched on and powered up by supplying electricity and gas to our homes. They give us clean water and purify it so we can use it again. They build all sorts of things so we can get around, from roads and bridges to railways and airports.*

> *Civil engineers also do lots of other things like finding clever ways of recycling our waste, and finding solutions to problems like pollution (ICE, 2017).*

Civil engineers design solutions to existing problems, thus in order for a student to qualify as a civil engineer they have to learn to design things that would work in the 3D world. The workplace has changed for the civil engineer in the last 50 years, with the birth of Computer Aided Design and the extinction of the draftsman, nowadays engineers having to produce, modify and fundamentally understand a 2D drawing as a representation of a 3D object.

Spatial visualisation ability or skill has been defined as "the ability to mentally manipulate, rotate, twist or invert pictorially presented stimulus objects" (McGee, 1979, p. 893). This skill enables engineers and engineering students to conceptualise links between the real world and an abstract model of this same world (Sorby & Baartmans, 1996). This versatile ability helps students and practitioners with picturing, expecting, planning and checking for the worst case scenario of loading on a certain structure. (Alias, 2002) Battista and Winkel have found that spatial visualisation ability is also a vital part of a student's success in subjects such as calculus and mathematics (Winkel, 1997) (Battista, 1989).

Duesbury describes how students that have the facility to manipulate a virtual 3D model understand the two-dimensional aspects of the structure better than students who do not have that option. Research also talks about how this spatial and three-dimensional visual ability can be significantly improved by exercise that lets the student understand the relationship between two-dimensional and three-dimensional features of structures or objects. (Ben-Chaim et al, 1988) (Alias et al, 2002). Research at Onn University College in Malaysia also used test groups to prove that manipulating objects and sketching improves students' spatial visualization ability, irrespective of gender or interaction effect with significant increases in students' abilities (Department of Technical Education, 1990).

2. CIVIL ENGINEERING AT COVENTRY UNIVERSITY

The Civil Engineering course at Coventry University is a multi-path course where all the students get the same information in the first year, branching out into different paths of the discipline later. There are approximately 200 students in the first year and they take the following modules over 2 semesters

- Construction Industry and Practice – Integrated Group Project

This is taught over two semesters, concentrating on the teamwork element in the first semester and on an execution plan in the second semester. Students spend one

hour in tutorials for the first semester and four hours split between lectures and tutorials in the second semester. The module requires students to work in groups of seven to nine and is assessed on a 50% coursework and 50% exam basis (Coventry University, 2017)

- Engineering Analysis and Materials

This module is taught over one semester in four hours split between lectures, laboratories and tutorials, and is assessed on a 100% exam basis. Students are required to 'formulate an engineering approach to solving problems by applying appropriate mathematical methods of analysis' to successfully pass this module (Coventry University, 2017)

- Structural Analysis and Mathematics

This module is taught over one semester in four hours split between lectures and tutorials and is assessed on a 50% coursework and 50% exam basis. Students are required to 'apply the fundamental principles of statics and mathematical principles to solve engineering problems' and to 'Analyse experimental data relating to material behaviour for use in structural design processes' to successfully pass this module (Coventry University, 2017)

- Highways and Surveying

This module is taught over one semester in six hours split between lectures, laboratories and tutorials and is assessed on a 25% coursework and 75% exam basis. Students are required to 'Demonstrate a practical competence in the use of an ordinary level and theodolite/total station including setting up and taking and recording field observations' and to 'Demonstrate an understanding of the concepts behind safety engineering and the impact upon highway design' to successfully pass this module (Coventry University, 2017)

- Design studies

This module is taught over one semester in eight hours split between short lectures and tutorials, and will be the focus of this paper. Students are required to demonstrate a high level of understanding of construction practices and practicalities, construction methods and the ability to understand innovative design though the use of sketches, 3D models, virtual models and drawings both 2D and 3D. The module is assessed on a 10% Exam, 10% Group work and 80% coursework basis. (Coventry University, 2017)

3. DESIGN STUDIES AT COVENTRY UNIVERSITY

We have found that civil engineering students at Coventry University have difficulties understanding how 2D drawings relate to real life buildings or structures. Less than 10% of students have done any technical drawing before university and know what parallel projection is. The design studies module helps to accommodate the student with a 3D and 2D drawing environment, teaching by example and by instruction. Students are required to produce designs for the other modules described above.

One of the modules asks that they produce a design for a footbridge. They have to show a representation of this bridge by any means available, but most civil engineering students at level one have no hand drawing skills, so in order to pass this module they have to either learn how to produce high quality hand drawings in a short period of time or learn a 3D modelling/ 2D drafting software.

This changes the students' perspective on the civil engineering profession as the expectation for the majority is that they will only be doing calculations as part of their future jobs. They soon realize that creating producing, amending and fundamentally understanding 3D and 2D drawings is part of day to day work as a civil engineer. This realisation makes the student engaged with the design studies module. Another aspect of the module is the 10% Phase test, an online based exam assessing the students' ability to use AutoCAD to an advanced level. The test has had a positive impact on the module.

4. TEACHING MATERIALS USED

In the process of the module a series of instructional exercises was used. These help the students learn basic commands that help them develop their own creative designs. In certain instances, the learner starts with a base document and needs to manipulate the objects in the model, following the steps aiming for an end product similar to the provided example. This makes the end result more attainable.

Figure 1 - Example of finished exercise

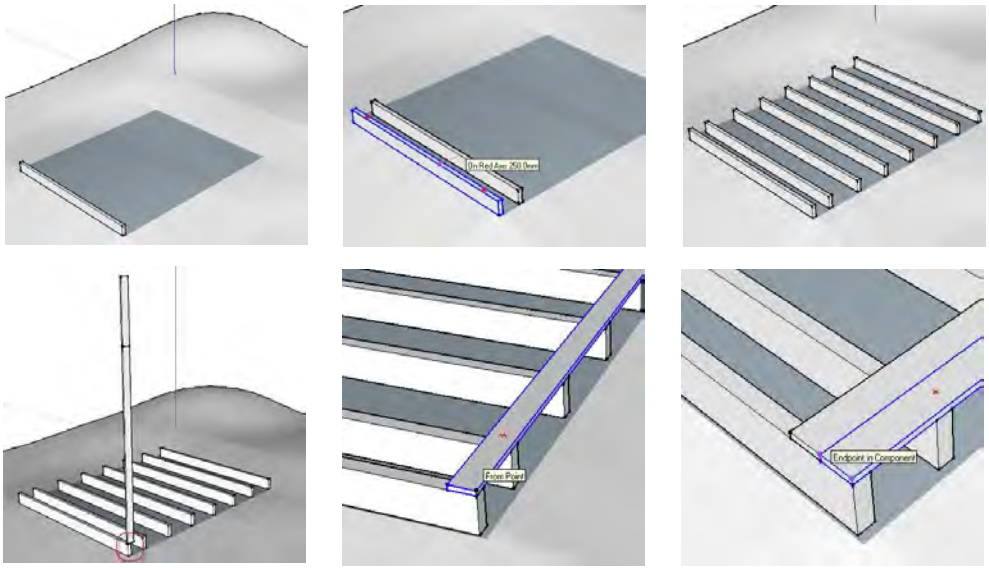

Figure 2 - Step by step instruction

5. METHODOLOGY

The following questions were investigated:

1. Can students communicate better though the use of drawings?
2. Does a virtual 3D environment help students understand 2D drawings better?
3. Does the practice of drafting develop student's design skills?

The variables for the group of students are:

4. The group is gender mixed
5. The group is culturally diverse meaning that for some students English is not the first language
6. The group has a wide age range
7. The group has varied levels of computer literacy.

6. CASE STUDIES

6.1. Case study A

Student A is a mother wanting to start a career in her mid-40s. She is not used to operating a computer and English is not her first language. She found it extremely difficult to integrate with the group because of language and age barriers. She also had to work as part of a group for the integrated module and communicate her ideas in a coherent and logical manner. Even though she found the learning curve extremely steep, as she had to learn computer skills in addition to 3D modelling and 2D drafting skills. She was helped by the provision of step by step instructional sheets and videos available at all times. She had good results in the submitted coursework and a passing mark in the AutoCAD phase test, due to English being her second language.

6.2. Case study B

Student B is a university age student with dyslexia. He is showing signs of mild autism. He has not integrated well with the group as he doesn't seem to have the patience to interact with his peers. He finds it difficult to communicate ideas in writing. The student was very enthusiastic about the use of software and seems comfortable using computers. He developed his skills very quickly and started to help his peers which further helped him develop verbal communication skills as well as using drawings as means of communication. He had an exceptional result in the AutoCAD phase test and excellent marks overall in the module

7. RESULTS

As seen from the case studies above, learning Computer Aided Design software helps students improve their communication skills in a university environment,

with most evidence in those with a disadvantage. As the Civil Engineering cohort at Coventry University has a large number of international students, or individuals who don't have English as a first language this is common. Several methods have been discussed to be implemented, such as pre sessional English lessons and a good level of English as an entry requirement onto the course as proved by a certified test such as IELTS or Cambridge, but developing the skill of hand drawing, 3D modelling and 2D drafting seems to be most effective with civil engineering students.

A large portion of the module is based around the use of digital simulations, enabling students to visualise their ideas, also encouraging peer feedback and participation, process though which overcomes the "far from help" issue that most international students face (Eggen & Kauchak, 2011). By peer feedback and review, the whole cohort integrates; therefore, they act as a design community and start using social media for learning, and through this they gain a global perspective over the construction sector, also gaining useful contact for their future careers (Eaves, 2011).

The AutoCAD Certification test is marked as 10% of the design studies module and was introduced in the 2014/15 academic year. A sample of the test can be found in Appendix B. From the introduction of the AutoCAD Certification test in the 2014-2015 academic year, it can be seen in the graph below how the percentage of satisfactory results helps increase the overall module mark for the Design Studies module.

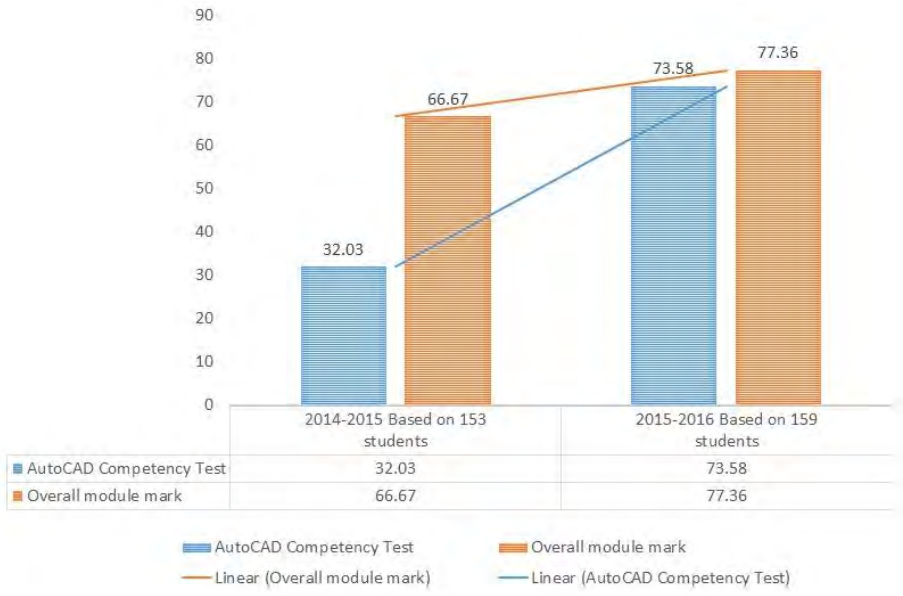

Figure 3 - Student performance in AutoCAD test in relationship with the mark

Another significant change observed was that student attendance had increased significantly as per the chart below

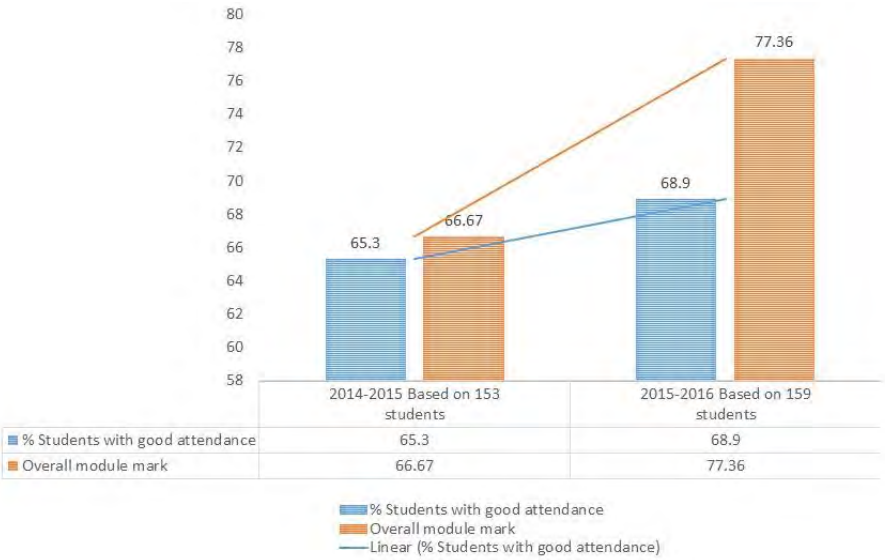

Figure 4 – Student Attendance

The student satisfaction is measured with a Module Evaluation Questionnaire (MEQ) performed by an external body. The questionnaire can be seen in Appendix C. Below are the results from the 2013-2014 to 2016-2017 academic year. In Appendix C can be found more results from the MEQ.

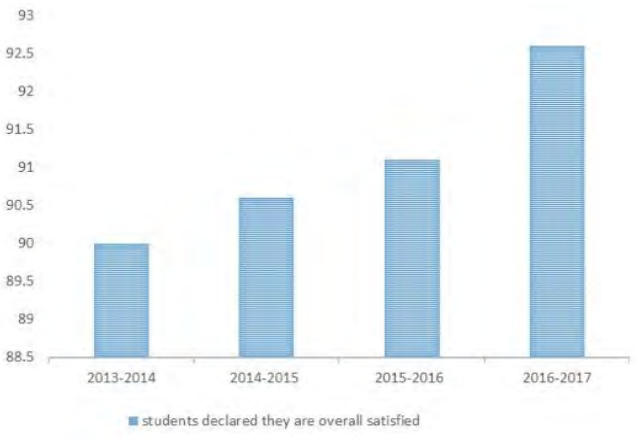

Figure 5 - Student Satisfaction

8. COMPARISON TO ARCHITECTURE AND ARCHITECTURAL TECHNOLOGY STUDENTS

The university environment is very different for different courses. Taking two different environments, an architectural studio and a large lecture theatre. Architecture students are expected to learn from their peers, research and gain skills in their free time. For this they are generally provided with a creative space equipped with specialised computers and equipment. Civil engineering students are generally taught in lecture theatre, a unidirectional space where information is given to students for them to apply and process at a later date.

The environment provided in the above-mentioned design studies module is a combination of both of these. It provides a semi-formal space, where students are expected to listen to short lectures but also help their peers, communicate ideas and improve their skills. This is emphasised by the presence of student proctors. Student proctors are second and third year students from civil engineering or building courses that have had excellent results on the same tasks and have shown an interest in the position. They interact with the students answering questions, clarifying issues and giving informal feedback. The student proctors give the students an insight into their course and future profession as well as keep the students motivated and focused on the task at hand. As the class sizes vary from 20 to 55, student proctor help is vital in ensuring that the sessions run smoothly.

9. CONCLUSION

This paper is set out to establish a relationship between developing a three dimensional modelling and two dimensional drafting skill and improving communication in civil engineering students. The results show that with the introduction of step by step instruction, a certification test in AutoCAD student satisfaction has risen as well as student attendance and the overall module mark. These results also show that by improving the students' ability to visualise three dimensional structures from two dimensional drawings helps improve their design skills as well as their communication skills making them work better in a team and increase their overall performance in other civil engineering modules.

In addition to gaining valuable skills for the construction industry, by the end of the Design Studies module a significant change in the students' mind-set and perception of the industry and work life after university has been observed. The presence of student proctors, some of which have done industrial placements, helps the students get an unique experience of the engineering profession, helping people and shaping the world (ICE, 2017)

10. REFERENCES

1. Alias, M (2000) Spatial visualisation ability and civil engineering problem solving. Unpublished doctoral thesis, University of Surrey. Guildford, United Kingdom
2. Alias, M., Black, T.R. and Gray, D. (2002) Effect of Instructions on Spatial Visualisation Ability in Civil Engineering Students. International Education Journal Vol 3, No 1. [Online] https://ehlt.flinders.edu.au/education/iej/articles/v3n1/Alias/paper.pdf [25 March 2017]
3. Baartmans, B.G. and Sorby, S.A. (1996a) Making connections: Spatial skills and engineering drawings. The Mathematics Teacher, 89 (4), 348-357
4. Battista, M.T., Wheatley, G.H. and Talsma, G. (1989) Spatial visualisation, formal reasoning, and geometric problem-solving strategies of pre-service elementary teachers. Focus on Learning
5. Problems in Mathematics, 11 (4), 17-30
6. Ben-Chaim, D., Lappan, G. and Houang, R.T. (1988) The effects of instruction on spatial visualisation skills of middle school boys and girls. American Educational Research Journal, 25 (1), 51-71
7. Coventry University (2017) Civil Engineering BEng (Hons) [Online] www.coventry.ac.uk/course-structure/engineering-environment-and-computing/undergraduate-degree/2017-18/civil-engineering-beng-hons [15 March 2017]
8. Department of Technical Education (1990) C201: Engineering Drawing Syllabus. Malaysia: Ungku Omar Polytechnic
9. Eaves, M. (2011) The relevance of learning styles for international pedagogy in higher education, Teachers and Teaching, 17(6), 677-691
10. Eggen, P. D., & Kauchak, D. P. (2011) Strategies and models for teachers: Teaching content and thinking skills, London: Pearson Higher Ed
11. McGee, M.G. (1979) Human spatial abilities: Psychometric studies and environmental, genetic, hormonal, and neurological influences. Psychological Bulletin, 86 (5), 889-918
12. Institution for Civil Engineers (2017) What is Civil Engineering [Online] https://www.ice.org.uk/careers-and-professional-development/what-is-civil-engineering [5 April 2017]
13. Sorby, S.A. and Baartmans B.G. (1996a) Improving the 3-D spatial visualisation skills of women engineering students. 1996 ASEE Annual Conference Proceedings. [Online] www.asee.org/conferences/searches/01361.PDF [20 March 2017]
14. Sorby, S.A. and Baartmans B.G. (1996b) A course for the development of 3-D spatial visualisation skills. Engineering Design Graphics Journal, 60 (1), 13-20
15. Winkel, B.J. (1997) In plane view: An exercise in visualisation. International Journal of Mathematics Education Science and Technology, 28(4), 599-607

Appendix A

This is a sample of the teaching literature used in step by step instructional tutorials

To Start

1. Launch AutoCAD
2. START > PROGRAMS > AUTODESK > AUTOCAD > AUTOCAD -ENGLISH

TIP

3. With the brand new drawing its good practice to Zoom Extents - **DC** the middle mouse wheel to zoom to the extents: or **Z** ↵ **E** ↵ will do the same thing.

The only status toggles you really need for 2D CAD.

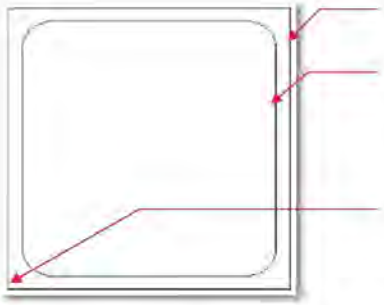

4. Draw the square outline of the watch face [1]:
   Ribbon: Home tab: Draw Panel
   Menu Browser > Draw > Rectangle >
   `Command line` : **<rectangle> or <rec>** ↵

   - Enter start point: **50, 50**
   - Specify other corner point: **100,100**

   Note - the other corner point is the Size of the thing you are going to draw and NOT the point from the Origin.

5. Draw the inner rectangle and then Fillet the corners [2]:
   Ribbon: Home tab: Draw Panel

Figure 6 - Step by step tutorial sheet with additional explanation

Appendix B

These are a couple of examples of phase test questions used in the AutoCAD Phase test

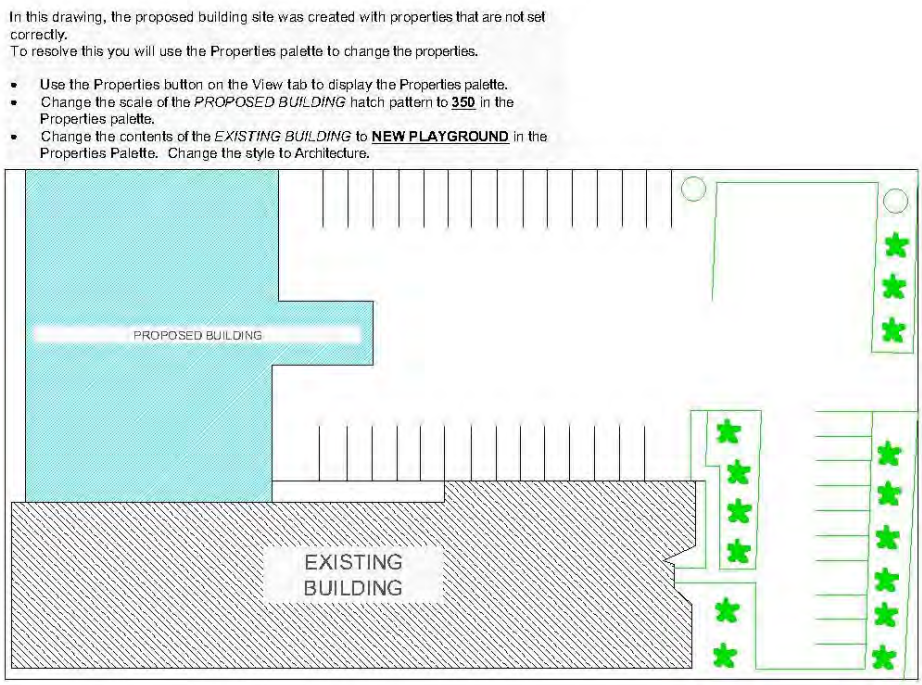

Figure 7 - Example of AutoCAD question 1

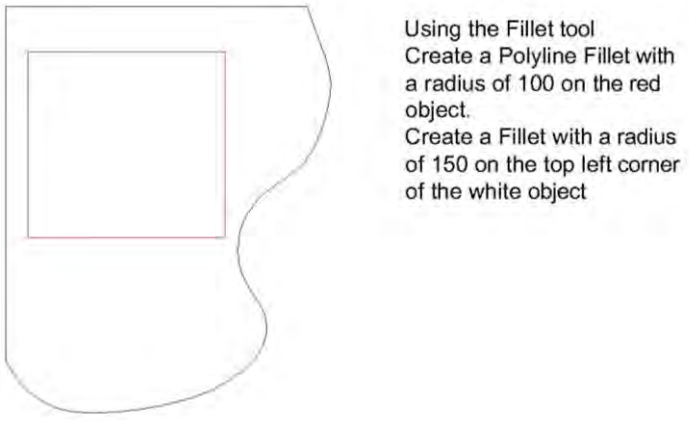

Figure 8 - Example of AutoCAD question 2

Appendix C

This is an example of the Module Evaluation Questionnaire used with this group of students. It has been designed to work across all the courses, modules and universities by the National Student Survey.

Table 1 - Module Evaluation Questionnaire Example

	Question	Definitely Agree	Mostly Agree	Neither Agree Nor Disagree	Mostly Disagree	Definitely Disagree
1	Staff teaching on this module are good at explaining things clearly					
2	Staff teaching on this module make the subject interesting					
3	The module is intellectually stimulating and engaging					
4	Staff teaching on this module are enthusiastic about what they are teaching					
5	The materials used by the staff have enhanced my learning					
6	Module information (module guide, timetable and assessment requirements) is available on CUOnline					
7	CUOnline is used effectively to support my learning					
8	Staff teaching on this module are well prepared					
9	Classes usually start and finish on time					
10	The assessment requirements on this module are clear					
11	Hand-in dates and coursework return dates are clearly defined					
12	Feedback on any returned work has been useful to develop my understanding of					

	the module content	
13	Sufficient academic advice and support on this module are available	
14	Staff teaching on this module are available when they say they will be	
15	The module timetable operates as expected and changes are communicated clearly in advance	
16	Library resources and services are sufficient for my needs on this module	
17	There is adequate access to specialist computer hardware and software required for this module	
18	There is adequate access to specialist equipment required for this module	
19	Overall the quality of this module is satisfactory	

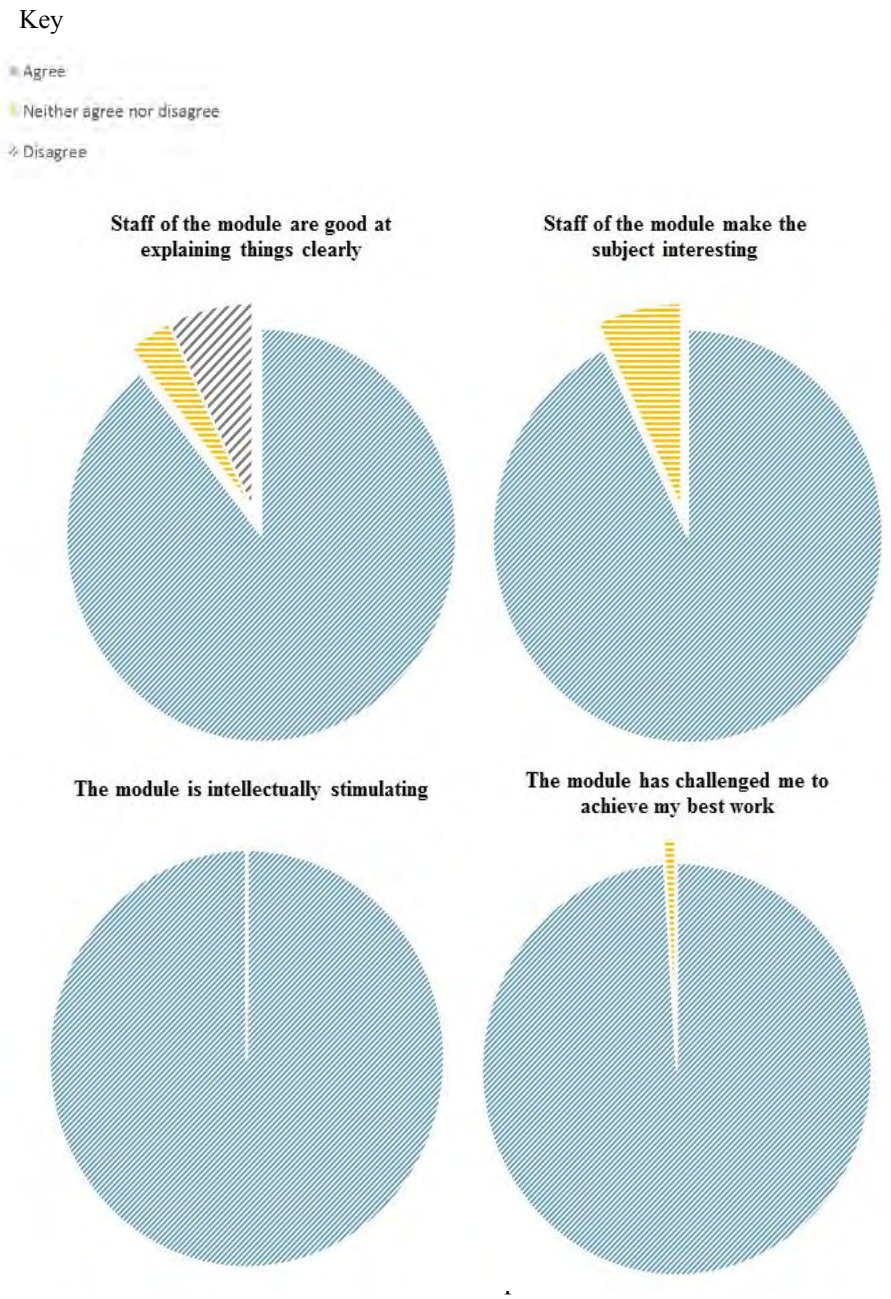

Figure 9 - Pie charts showing student responses

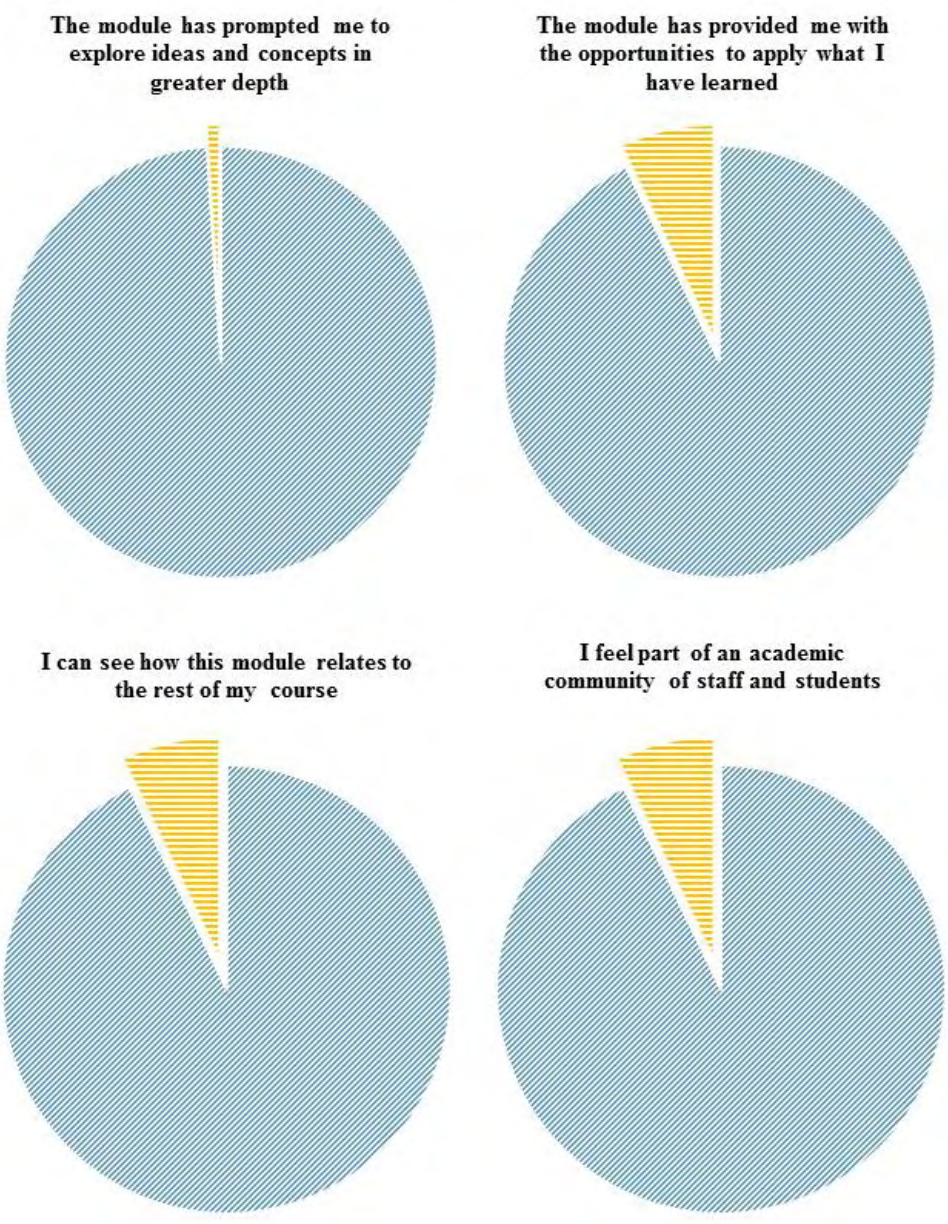

Figure 10 - Pie charts showing student responses

Analysis of software gamification for teaching architects in immersive virtual reality

Olga Kysil
Department of Information Technology in Architecture, Kyiv National University of Construction and Architecture, Kyiv-037, 03680, Ukraine

Summary

The progressive tendencies of education computerization are analysed in the article. Gamification of this process accelerates the time of understanding and consolidation of educational material are proved. The author examines the prospects of using virtual reality as an effective method of teaching architectural composition course. The results provide an opportunity for students to operate with abstract concepts through the immersion virtual world where they can visualise any geometric shapes as well as to do conceptual models in real time. The future architects begin to create an architectural space based on many factors, including abstract, which usually have a graphical representation. Using a powerful database platform game software, which allows building mental models for incorporation of the virtual world of immeasurable concept. This article is devoted to the features and functionality of Unity 3D Engine and Unreal Engine for creation on this basis the gamification education of conceptual architectural modelling.

KEYWORDS: immersive virtual reality, gamification software, composition analysis, architectural education.

1. INTRODUCTION

Recently, computer modelling volumes, processes and mechanisms became the highest relevance, because it gives the user the clearest picture. Virtual reality technology further expanded the possibilities of design. The number of computer programs that enables design anything in real time are growing every day. For the success of construction industry, these technologies are gradually implemented in education. Many institutions of secondary and higher education establish computer-learning methods simulating future professional work of students. Also global approach to learning via the Internet becoming popular. All these innovations are concerning in architectural education. An example is OIKODOMOS i OIKONET: The aim of the OIKODOMOS and OIKONET virtual campus training and research projects is the development, research and

application of new methods of study of housing and housing design, implementation of innovative education methodology in the field of architectural education (in its different forms and multidisciplinary perspectives), joint international actions addressing housing issues in contemporary Europe (in cooperation with local councils) and the creation of European educational programs compatible with the Bologna Process, which should combine physical and virtual mobility of students and teachers. In addition, these projects deal with topical issues of housing, and with innovative global dwelling solutions corresponding to social, economic and technological challenges of contemporary society. Finally, they create opportunities for active collaboration between universities and other stakeholders, such as with municipalities and social organisations, addressing complex housing problems [1].

The author believes that an essential aspect of online distance learning is Gamification of the study process. McGonigal defines four basic traits that can be found in any game: clear goals that give the player a sense of purpose, rules that define the limitations how to achieve the goal, a feedback system giving the player the promise that the goal in question is definitely reachable and, ultimately, a voluntary participation, i.e., the user accepts the goals, rules, and feedback of the system voluntarily. Everything else, such as interactivity, narrative context, graphics, or rewards are enhancements or reinforcements of these defining features [2]. All these factors transform the learning process an interesting and exciting experience.

Future architects, above all, have developed spatial imagination. In the language of psychology, they are "visual" people, who had better perceive data from visual information channel. Therefore, immersive virtual reality, based on game software, is ideal for training of this industry specialists. This research proves the possibility of creating a software platform that will combine all strengths of the above technologies.

2. METHOD

Architectural composition course has a high level of abstraction in many aspects. Classic architectural education programs offer a multifaceted analysis of existing works of art and works of the architects of the past. Methods of this analysis have inductive and deductive nature expressed through graphic language. Breakdown the shapes or flat picture on the modules, composite axis’s, bundling zones of any type - this entire are required the support tools. The study provides a software environment for teaching composition, which has the following specific, purely conceptual elements. It can look like this: a student receives a task - for example, to

do a compositional analysis of the Italian Renaissance palazzo. On the above software developed basis, it can:

- to integrate 3D model of the Palazzo into the virtual gaming environment;
- to look and move in real time inside and outside the model, put VR glasses;
- by optimising facilities student will have the opportunity to see different levels of model detail.

Using a set of tools for conceptual modelling, the student performs compositional analysis models, 3D designs modular grid system used by the author of Palazzo project finds the proportioning system, notes nodes, etc. The main game point is checked compositional analysis by comparing the executed task with existing proportioning system.

In addition, the presence of such a model allows a comparative computer analysis, for example, the evolution of forms of Italian Renaissance palazzo compared with medieval buildings.

The student plays the peculiar "3D puzzles": computer provides conceptual diagrams of buildings, which must inscribe in the buildingţs model. Therefore, two scientific cognition methods - induction and deduction are realised. The virtual environment is allowed to select any view to building a holistic perception of volume and finding a right decision.

Further work with the platform of research is execution a conceptual stage of their design tasks. This can be called "virtual sketching" with having specific digital indicators, and possibilities of computer analysis. Game component implemented by comparing the set design factors with those embodied in the model of the learner.

To realise the above objectives of the study have been found needful key points relative to choice a software for application development of conceptual modelling in VR [5]:

- Usability (UI, how easy it was to learn and develop with)
- Functionality (What exactly the engine can do)
- Price Point
- Cross-platform

According to the above factors, the author was made a conclusion that Unity 3D and Unreal Engine have the greatest functionality, usability for architectural purpose and cross-platform feature. Other important features of this software are indicated in Table 1.

These game engines have free versions for individual work. Scripting for Unity 3D can be performed in Visual Studio, which is also free. Additionally, it should be noted that in Unreal Engine scripting is done by using visual programming language Blueprint. There are plugins for Unity 3D engine that allow programming

so also (Uscript). This technology can prescribe algorithms without dipping into writing codes through text nodes - a graphic representation of software elements.

Table 1. Comparative analysis important for this study Unity 3D and Unreal Engine features.

Type of software	Optimisation	Scripting	Possibilities in VR	3D file formats	Cross-platform
Unity 3D	Level of Detail	C#	Unity VR lets you target virtual reality devices directly from Unity, without any external plug-ins in projects. It provides a base API and feature set with compatibility for multiple devices. It has been designed to provide forward compatibility for future devices and software [3].	.3ds, .max, .obj, .fbx, .dae, .ma, .mb, .blend	Windows, OS X, Windows Phone, Android, Apple iOS, Linux, Wii, PlayStation 3, PlayStation 4, Xbox 360, Xbox One, MotionParal-lax3D
Unreal Engine	Node count is the number of nodes on the screen or in the game space in general. The number of nodes simultaneously visible on the screen affects the performance when rendering the scene.	C++	Rendering pipeline that gets you to 90 Hz stereo frame rate or faster at high resolutions, no code changes required. Tools that scale from simple to extremely detailed scenes, environments and characters. Low friction startup and rapid iteration [4].		Microsoft Win-dows, Linux, Mac OS и Mac OS X; Xbox, Xbox 360, Xbox One, PlayStation 2, PlayStation 3, PlayStation 4, PSP, PS Vita, Wii, Dreamcast, GameCube, Apple (iPad, iPhone).

The method of transferring mathematical meanings and relationships in a visual plane is the best fit to the general hypothesis of the study, which is to present the abstract model graphically. In addition, the above-listed software runs on object-

oriented programming, on the main provisions of which is lying model component hierarchy. Besides both platforms implemented the principle of optimisation game geometry, which is crucial in the assembly the build of the game. Moreover, the implementation of the optimisation principle, which makes image more detail when the user came closer, offers to users different levels of model details. He can manage this system through a specially designed UI. That is if the user is close to a particular piece of the model the fragment is automatically detailed. In case the user wants to see a generalised image of close, he gives the appropriate command from the menu, and vice versa. The concept of “Level of Detail” is very important for this study. Development of analysis tools and architectural compositions in virtual reality requires flexible interface, for maximum comfort and clearness for the user.

The relevance of the study is also confirmed by various developments of inexpensive equipment for training specialists. For example, the system of 3D-visualization I-Space FGUP NIIR. I-Space is a multifaceted cubic environment in which the observer is completely "immersed" in a virtual Scene. The main components of the system are projection screens, projectors, interactive feedback (tracking) system, audio system and software for creating interactive 3D visualisation [6].

CONCLUSIONS:

Virtual space - is a boundless field to implement any ideas that have a graphical representation. Human sees in the imagination of even abstract concepts, and thinking, in fact, is the consequence of this view. Research makes the assumptions that among immersive virtual reality environment, as in the human mind, it is possible to visualise any concept, to create a concept model, and make from it a specific architectural conceptual model later. The Educational Conceptual design of architectural spaces on the first stage is performed from archetype shapes that have mutual relationships and connections. Executing of educational tasks from this "virtual designer" according to the proportions and other factors is interesting professional experience and the development of abstract and spatial imagination. The game principle of the gradual complication of tasks by increasing the number of influencing factors and increasing structural elements are training architects to design large multifunctional complexes. However, mastering the study material comes from the possibility of constant checks on the raw data in the a not stressful atmosphere. The teacher has the ability to distance observe and adjust the process in real time with the appropriate equipment.

It should be noted that the above gamification-learning platform widens the boundaries the classical concept of architectural space. Optionally, by changing the

program code of physics engine, space stops to obey earthly physical laws. This provides an opportunity for students to create new virtual architectural measurements, experiment with algorithmic shaping in the absence of the usual gravity force and explore multidimensional mathematical spaces. One of the hypotheses of this study is understanding the virtual environment not as a simulation of a real environment, but as a new real architectural space. Architects create virtual offices for business meetings of various experts, virtual stores and 3D social networks pages interior with the same importance of representative value as an own home décor. These spaces can be radically different in structure, but open and bring unexpected compositional novelty into the real physical world. This will contribute to "go beyond" the standard of the imagination - one of the main principles of gamification, which immersive virtual reality is provided.

References

1. Innovation in architectural education - OIKONET experience - Viera Joklová & Henrich Pifko, Volume 17, Number 3, 2015 © WIETE 2015 Global Journal of Engineering Education – 124-130 p.
2. Reality Is Broken: Why Games Make Us Better and How They Can Change the World, Jane McGonigal, Published February 1st 2011 by Jonathan Cape - 400 p.
3. Unity для VR и AR во главе революции, URL: https://unity3d.com/ru/unity/multiplatform/vr-ar (in Russian).
4. VR requires performance & fidelity, URL: https://www.unrealengine.com/vr
5. Game Engine Analysis and Comparison, Jamie O’ Flanagan, June, 2014, URL: https://www.gamesparks.com/blog/game-engine-analysis-and-comparison/#comment-1441388923
6. Анализ перспектив использования технологий виртуальной реальности в дистанционном обучении Я.Г. Подкосова, О.О. Варламов, А.В. Остроух, М.Н. Краснянский «Вопросы современной науки и практики.» Университет им. В.И. Вернадского. №2(33), Москва, 2011. (in Russian)

Appendix

Gamification is the application of game-design elements and game principles in non-game contexts. Huotari, K., & Hamari, J. (2012). "Defining Gamification – A Service Marketing Perspective" (PDF). Proceedings of the 16th International Academic MindTrek Conference 2012, Tampere, Finland, October, 3–5.

VR (virtual reality); **Immersion** into virtual reality is a perception of being physically present in a non-physical world.

https://en.wikipedia.org/wiki/Immersion_(virtual_reality).